Instability and Receptivity of Boundary Layers on Concave Surfaces and Swept Wings

A thesis presented for the degree of

Doctor of Philosophy of Imperial College London

and the

Diploma of Imperial College

by

Difei Zhao

Department of Mathematics

Imperial College

180 Queen's Gate, London SW7 2BZ

September 2011

I certify that this thesis, and the research to which it refers, are the product of my own work, and that any ideas or quotations from the work of other people, published or otherwise, are fully acknowledged in accordance with the standard referencing practices of the discipline.

Signed:

Copyright

Copyright in text of this thesis rests with the Author. Copies (by any process) either in full, or of extracts, may be made **only** in accordance with instructions given by the Author and lodged in the doctorate thesis archive of the college central library. Details may be obtained from the Librarian. This page must form part of any such copies made. Further copies (by any process) of copies made in accordance with such instructions may not be made without the permission (in writing) of the Author.

The ownership of any intellectual property rights which may be described in this thesis is vested in Imperial College, subject to any prior agreement to the contrary, and may not be made available for use by third parties without the written permission of the University, which will prescribe the terms and conditions of any such agreement. Further information on the conditions under which disclosures and exploitation may take place is available from the Imperial College registry.

TO MY PARENTS

Abstract

This thesis studies the instability and receptivity of boundary layers over a concave wall and a swept Joukowski airfoil. The main interest is in excitation of relevant instability waves by free-stream vortical disturbances and in their subsequent linear development.

We first consider excitation of Görtler vortices in a Blasius boundary layer over a concave wall. Attention is focused on disturbances with long streamwise wavelengths, to which the boundary layer is most receptive. The appropriate initial-boundary-value problem describing both the receptivity process and the subsequent development of the induced perturbation is formulated for the generic case where the Görtler number G_Λ (based on the spanwise wavelength Λ of the disturbance) is of order one. The impact of free-stream disturbances on the boundary layer is accounted for by the far-field boundary condition and the initial condition near the leading edge, both of which turn out to be the same as those given by Leib, Wundrow and Goldstein (J. Fluid Mech. vol. 380, 1999, p.169) for the flat-plate boundary layer.

Numerical solutions of the initial-value problem show that for a sufficiently small G_Λ, the induced perturbation exhibits essentially the same characteristics as streaks occuring in the flat plate case: the streamwise velocity undergoes considerable amplification and then decays. However, when G_Λ exceeds a critical value, the induced perturbation exhibits (quasi-)exponential growth. Comparison with local parallel and non-parallel instability theories reveal that the perturbation acquires the modal shape of Görtler vortices rather quickly, but its growth rate differs appreciably from that predicted by local instability theories before the convergence at large downstream distances. Nevertheless, the overall agreement is close enough to indicate that Görtler vortices have been excited by free-stream disturbances. The amplitude of excited Görtler vortices is found to decrease with the fre-

quency. Steady vortices, generated by steady components of free-stream disturbances, tend to be dominant. Detailed quantitative comparisons with experiments were performed. It is found that the eigenvalue approach predicts the modal shape adequately, but only the initial-value approach can accurately predict the evolution of the amplitude as well as the modal shape.

An asymptotic analysis is performed on the assumption of $G_\Lambda \gg 1$ to map out distinct regimes through which a disturbance of a fixed spanwise wavelength evolves. The centrifugal force enters the play to influence the generation of the pressure when $x^* \sim \Lambda R_\Lambda G_\Lambda^{-2/3}$, where R_Λ denotes the Reynolds number based on Λ. The induced pressure leads to full coupling of the momentum equations when $x^* \sim \Lambda R_\Lambda G_\Lambda^{-2/5}$. This is the crucial regime linking the pre-modal and modal phases of the perturbation because the governing equations admit a countable set of growing asymptotic eigensolutions, which develop into fully fledged Görtler vortices of inviscid nature when $x^* \sim \Lambda R_\Lambda$. From this position onwards, local eigenvalue formulations are mathematically justified. The generated Görtler vortices continue to amplify and enter the so-called most unstable regime when $x^* \sim \Lambda R_\Lambda G_\Lambda$, and ultimately approach the right-branch regime when $x^* \sim \Lambda R_\Lambda G_\Lambda^2$.

We then extend our study to the receptivity of a three-dimensional boundary layer over a swept wing to free-stream vortical disturbances. The base flow is taken to be the boundary layer over a swept Joukowski airfoil. In contrast to the two-dimensional boundary layer, external disturbances with comparable streamwise and spanwise wavelengths are relevant to receptivity. The appropriate initial-boundary-value problem consists of linearised boundary-layer equations supplemented by the initial condition at the leading edge and the boundary condition in the far field, which are derived by applying the rapid distortion theory, and matching the resultant inviscid solution with the boundary-layer solution. It is found that the linearised boundary-layer equations support spatially growing eigenmodes despite the absence of a pressure gradient. The modes may be first excited by free-stream disturbances, and eventually evolve into fully fledged crossflow vortices.

Acknowledgements

I would like to thank my supervisor, Prof. Xuesong Wu, for his guidance over the last four years. Without him, this work would not have been possible. I would also like to thank my PhD student friends for helpful discussions. Special thanks are given to my parents for their unconditional support and love.

Difei Zhao

Table of contents

Abstract **5**

1 Introduction **14**
1.1 Laminar-turbulent transition and hydrodynamic instability 14
1.2 General approach to hydrodynamic instability 15
1.3 Important instability mechanisms 17
1.4 Transition routes and receptivity 20

2 Görtler Vortices **23**
2.1 Introduction 23
2.2 Formulation and scaling 29
2.3 The base flow 31
2.4 Perturbation equations 31
2.4.1 The upstream and far-field boundary conditions 34
2.5 Eigensolution formulation: $G_\Lambda = O(1)$ 38
2.5.1 Non-parallel eigenvalue problem 38
2.5.2 Parallel-flow approximation 39
2.6 Asymptotic analysis for $G_\Lambda \gg O(1)$ 40
2.6.1 Pre-modal stage I: $\hat{x} = O(G_\Lambda^{-2/3})$ 40
2.6.2 Pre-modal stage II: $\hat{x} = O(G_\Lambda^{-2/5})$ 41
2.6.3 Inviscid regime: $\hat{x} = O(1)$ 47
2.6.4 Most unstable regime: $\hat{x} = O(G_\Lambda)$ 50
2.7 Numerical methods 52
2.7.1 Numerical method for the initial-boundary-value problem 52
2.7.2 Numerical method for solving the local eigenvalue problem 54
2.7.3 Validation 54
2.8 Results and comparisons with experiments 55
2.8.1 Steady Görtler vortices 55
2.8.2 Unsteady Görtler vortices 71
2.9 Summary and discussions 77

3 Crossflow Vortices **79**
3.1 Introduction 79
3.2 Formulation and scalings 86
3.3 The base flow 88

3.3.1 The inviscid external flow . . . 88
3.3.2 The boundary layer flow . . . 97
3.4 Perturbation equations . . . 105
3.4.1 General governing equations . . . 107
3.4.2 The linear inviscid solution . . . 110
3.4.3 The linearised boundary layer equations . . . 116
3.5 Eigenvalue formulation . . . 124
3.5.1 Non-parallel boundary-layer eigenvalue formulation . . . 124
3.5.2 Parallel boundary-layer eigenvalue formulation . . . 125
3.5.3 Non-parallel Navier-Stokes eigenvalue formulation . . . 125
3.6 Numerical results . . . 131
3.6.1 Validation of the eigenvalue solver . . . 131
3.6.2 Initial-value and eigenvalue solutions . . . 135
3.6.3 The intermediate regime . . . 139
3.7 Summary and discussion . . . 142

4 Further discussions and future work **144**
4.1 Summary of conclusions and further discussions . . . 144
4.2 Topics for future study . . . 146

A Approximation for $S - \theta$ relation for $\pi - \theta = O(b/a)$ **148**

B Evaluation of drift function **151**

References **164**

List of Figures

2.1 Influence of FST on the occurrence of Görtler vortices (Kottke 1988). Left: adjusting the distance of the grid to the leading edge with fixed mesh size. Right: adjusting the mesh size with fixed distance. 27

2.2 Schematic illustration of the physical problem and the asymptotic flow structure. Also shown are the main stages: pre-modal, inviscid and the 'most unstable' regimes, through which the induced perturbation evolves when $G_\Lambda \gg 1$ (Courtesy of Dr. P. Ricco). 32

2.3 Matching of different regimes. Dashed lines: asymptotic eigen mode; solid lines: inviscid modes; dotted lines: the large-$\hat{x}$ limit of inviscid modes, i.e. (2.6.41) with $n = 2, 3$. 49

2.4 $|\bar{u}|$ at $\eta = 1.64$ calculated from different values of $\kappa \leq 1.0$ with $\kappa_2 = -\kappa$ using equations (2.4.9)–(2.4.12). 55

2.5 Profiles of the streamwise and spanwise velocities of the perturbation at the indicated values of $\bar{x}$ for $\kappa = 1.0$, $\kappa_2 = -1.0$. 56

2.6 Profiles of $|\bar{u}|/|\bar{u}|_{\max}$ at indicated $\bar{x}$ for $\kappa = 1.0$, $\kappa_2 = -1.0$. 56

2.7 $|\bar{u}|_{\max}$ and ln $|\bar{u}|_{\max}$ calculated for different values of Görtler number G_Λ with $\hat{k}_1 = 0.0$, $k_2 = -1.0$ and $k_3 = 1.0$. 57

2.8 Comparison of the growth rates as predicted by nonparallel eigenvalue approach (σ, dashed line) and by initial-value approach ($\frac{1}{\bar{u}}\frac{d\bar{u}}{d\hat{x}}$ at $\eta = 1.64$, solid line) for $\hat{k}_1 = 0.0$, $k_2 = -1.0$, $k_3 = 1.0$ and different values of G_Λ as indicated in the plot. 57

2.9 Comparison of streamwise and spanwise perturbation velocity profiles predicted by nonparallel eigenvalue and initial-value approaches. Top row: $\hat{x} = 1.0$; bottom row: $\hat{x} = 4.0$. The parameters are $\hat{k}_1 = 0.0$, $k_2 = -1.0$, $k_3 = 1.0$ and Görtler number $G_\Lambda = 20.0$ 58

2.10 Comparison of the streamwise and spanwise velocity profiles (at $\hat{x} = 1.0$) predicted by the nonparallel eigenvalue and initial-value approaches. The parameters are $\hat{k}_1 = 0.0$, $k_2 = -1.0$, $k_3 = 1.0$ and Görtler number G_Λ = 200.0 (top), and 100.0 (bottom). 59

2.11 Downstream development of normalised streamwise and spanwise velocities at indicated values of $\hat{x}$, with $\hat{k}_1 = 0.0$, $k_2 = -1.0$, $k_3 = 1.0$ and Görtler number G_Λ= 100.0 59

2.12 Growth rates predicted by different parallel and nonparallel theories as well as by initial-value calculation, when $\hat{k}_1 = 0.0$ and G_Λ=89.5 (corresponding to $G_b \approx 15$ in the paper of Boiko et al. (2007, 2010)) 61
2.13 Normalised streamwise and spanwise velocity profiles predicted by different parallel and nonparallel theories at $\hat{x} = 0.6241494$ (top) and $\hat{x} = 8.0$ (bottom) for G_Λ=89.5, which corresponds to $\Lambda_b = 149$ in Boiko et al. (2010). 63
2.14 Normalised streamwise and spanwise velocity profiles of the second mode predicted by parallel and nonparallel theories at $\hat{x} = 0.6241494$ (top) and $\hat{x} = 8.0$ (bottom), for G_Λ=89.5, which corresponds to $\Lambda_b = 149$ in Boiko et al. (2010). 64
2.15 Comparison of the downstream development of the maximum streamwise velocity predicted by the initial-value approach with the experiment data of Tani (1962). The parameters are $G_\Lambda = 1765.0$, $\hat{k}_1 = 0.0$, $k_2 = -1.0$ and $k_3 = 1.0$. 68
2.16 Comparison of the growth rate predicted by the initial-value approach and by the nonparallel eigenvalue theory. The parameters are $G_\Lambda = 1765.0$, $\hat{k}_1 = 0.0$, $k_2 = -1.0$ and $k_3 = 1.0$. 68
2.17 Comparison of normalised streamwise velocity obtained from the initial-value and eigenvalue calculations with the experiment data of Tani (1962). The parameters are $G_\Lambda = 1765.0$, $\hat{k}_1 = 0.0$, $k_2 = -1.0$ and $k_3 = 1.0$ at $\hat{x} = 0.03906$ (top left), $\hat{x} = 0.065$ (top right), $\hat{x} = 0.1172$ (bottom left) and $\hat{x} = 0.1562$ (bottom right). 69
2.18 Comparison of downstream development of the maximum streamwise velocity predicted by initial-value approach with experiment data of Finnis and Brown (1997) for $U_\infty = 10$m/s (left) and $U_\infty = 7.5$m/s (right). The parameters are $G_\Lambda = 2192$ (left), $G_\Lambda = 1222$ (right), $\hat{k}_1 = 0.0$, $k_2 = -1.0$ and $k_3 = 1.0$. 70
2.19 Comparison of the growth rate predicted by initial-value approach, nonparallel eigenvalue theory, inviscid approach and the experiment data of Finnis and Brown (1997). The parameters are $G_\Lambda = 2192$ (left), $G_\Lambda = 1222$ (right), $\hat{k}_1 = 0.0$, $k_2 = -1.0$ and $k_3 = 1.0$. 70
2.20 ln $|\bar{u}|_{\max}$ v.s. $\hat{x}$ for different frequencies with $G_\Lambda = 89.5$. The frequencies in the plot (top to bottom) correspond to 0, 5.67, 8.0, 12.0, 20.0 and 40.0 in Boiko et al. (2007, 2010) 71
2.21 Growth rates predicted by local instability theories and comparison with the initial-value prediction. The parameters are taken to be $\hat{k}_1 = 3.33604$, G_Λ=89.5 (corresponding to $\Lambda_b = 149$ and $F = 5.67$ in Boiko et al. (2007, 2010)). 72
2.22 Comparison of the streamwise and spanwise velocity profiles predicted by the initial-value approach with the eigenfuctions of different parallel and non-parallel theories at $\hat{x} = 0.624$, 4.0 and 8.0. The parameters are G_Λ=89.5 and $\hat{k}_1 = 3.336$ (corresponding to $\Lambda_b = 149$ and $F = 5.67$ in Boiko et al. (2007, 2010) 73

2.23 Comparison of the streamwise velocity profiles predicted by the initial-value, parallel and non-parallel theories with the measurements of Boiko et al. (2010) at $\hat{x} = 0.378$ (left), 0.749 (right) for $\hat{k}_1 = 3.336$ and $G_\Lambda = 89.5$ ($\Lambda_b = 149$, $F = 5.67$). 74
2.24 Development of unsteady Görtler vortices and comparison with the experiment of Boiko et al. (2010). The parameters are $G_\Lambda = 89.5$ and $\hat{k}_1 = 3.336$ ($\Lambda_b = 149$ and $F = 5.67$). 74
2.25 Growth rates (a) and phase speeds (b) of unsteady Görtler vortices predicted for different frequencies and comparison with the experimental data at $\hat{x} = 0.62$. The parameters are $G_\Lambda = 89.5$ and $\Lambda_b = 149$. 75

3.1 Joukowski transformation $\zeta(z) = z + c^2/z$ from the exterior of the circle to the exterior of the airfoil. 90
3.2 Geometry of Joukowski airfoil for different ratios of b/a. 91
3.3 Characteristic length scales of symmetric Joukowski airfoil for $b/a = 0.035$. 92
3.4 Comparison of the asymptotic approximations with the exact solution (theory) for u_e $(b/a = 0.035)$. 95
3.5 The relation between u_e and S, and comparison of the asymptotic approximation with the exact numerical solution $(b/a = 0.035)$. 97
3.6 The distribution of the slip velocity along the airfoil surface for different values of b/a. 98
3.7 Solution to Falkner-Skan equation for different values of m. 102
3.8 Velocity profiles for different ratios of b/a at $S = 0.05$. 102
3.9 Velocity profiles for different ratios of b/a at $S = 0.99$. 103
3.10 Velocity profiles of Falkner-Skan-Cooke boundary layer with $m = 1$. 106
3.11 Chordwise and spanwise velocity profiles at different downstream locations with $b/a = 0.035$. 106
3.12 Velocity profiles at the stagnation point. The parameters used are $\omega = 0.12$, $k_3 = 1.0$, $\Lambda = 0.05$, and $b/a = 0.1$. 121
3.13 The distribution of $R_1 = \delta/\delta_s$ and R_1/R_0 along the airfoil for $b/a = 0.1$. . 130
3.14 The growth rate and chordwise wavenumber of crossflow vortices at different chordwise locations. Parameter values: $\omega = 0.1071$, $R_\Lambda = 1428.57$ and $\Lambda/a = 2.9 \times 10^{-4}$. 134
3.15 Non-parallel eigenvalue calculation for different frequencies at $x = 35$ with $\Lambda/a = 0.005$, $k_3 = 1.0$, and $b/a = 0.1$. 135
3.16 The growth rates $(\mathrm{Re}(\sigma))$ and chordwise wavenumber $(\mathrm{Im}(\sigma))$ of the non-parallel eigenmodes for different spanwise wavelengths for $\omega = 0.12$, $k_3 = 1.0$, and $b/a = 0.1$. 138
3.17 Non-parallel eigenvalue and comparison with the theoretical result . Parameter values: $\omega = 0.12$, $\Lambda/a = 0.001$, $k_3 = 1.0$, and $b/a = 0.1$. 138
3.18 Comparison between non-parallel and parallel eigenvalue calculations with the theoretical result for $\omega = 0.12$, $\Lambda/a = 0.001$, $k_3 = 1.0$, and $b/a = 0.1$. 139
3.19 The local growth rate predicted by the initial-value calculation for FST and comparison with the non-parallel eigenvalues. Parameter values: $\omega = 0.12$, $\Lambda/a = 0.001$, $k_3 = 1.0$, and $b/a = 0.1$. 140

3.20 The local growth rate predicted by the initial-value calculation for suction and comparison with the non-parallel eigenvalues. Parameter values: $\omega = 0.12$, $\Lambda/a = 0.001$, $k_3 = 1.0$, and $b/a = 0.1$. 140

A.1 Comparison of the $s - \theta$ relation obtained by numerical integration with the asymptotic approximation (A.0.5) $(b/a = 0.035)$. 150

B.1 Drift function for $b/a = 0.1$, and $\Lambda/a = 0.001$. 155

Chapter 1

Introduction

1.1 Laminar-turbulent transition and hydrodynamic instability

Flow motions exhibit different degree of spatial and temporal complexity. Laminar flows refer to those which display relatively simple variations in both space and time, whereas turbulent flows refer to those which display no discernable spatial pattern or temporal repeatability at all; the flow field appears chaotic and random. When the controlling parameters vary, a laminar flow may change to a turbulent state, usually through a sequence of increasingly more complex intermediate states. Transition to turbulence may take place in physical space, from one part of the flow field to another, rather than with respect to change of an overall controlling parameter.

A simple example is the so-called thermal convection, a horizontal layer of quiescent fluid being heated from below. When the temperature difference is small enough, the fluid remains motionless and the heat exchange between the top and bottom is through conduction, which is a very inefficient process. When the temperature difference is raised beyond a critical value, the resulting buoyancy may cause the fluid particles near the bottom to overcome the viscous resistance and move upwards. A pattern of steady convection cells is formed. When the temperature difference is increased further, the cells may become unsteady and be eventually replaced by an apparently turbulent state. The non-dimensional parameter controlling the process is the so-called Rayleigh number, which measures the ratio of the buoyancy to the viscous resistance. Another example is the flow through a circular pipe, which was first studied by Reynolds (1883) in his well-known experiment. By visualising the flow via injected dye, he observed that at relatively low speeds, the flow is

steady and all fluid particles move parallel to each other along the axial direction. However, when the speed exceeds a critical value, the flow becomes time dependent and three-dimensional, i.e. a state of turbulence prevails. Crucially, Reynolds established that the transition was determined by the dimensionless parameter UD/ν, which was later referred to as the Reynolds number, where D is the diameter of the pipe, and ν is the kinematic viscosity of the fluid. The work of Reynolds has been credited as the first to discover and systematically document two flow states: laminar and turbulent, and it marked the beginning of turbulence research.

Transition also takes place in the flow around an airfoil. In this case, a Reynolds number Re based on the airfoil length can be defined. However, unlike the flows mentioned above, the parameter Re does not dictate the entire flow field provided that Re is sufficiently large. No matter how large Re is, the flow near the leading edge of the airfoil is laminar, but is turbulent further downstream. There is an extended region in between where transition takes place.

Transition between from one state to another, especially transition to turbulence, is not only of fundamental importance in science, but also of great practical relevance to engineering and technology. For instance, transition in thermal convection is closely related to heat transfer and mixing, while transition in the pipe flow and in the flow around an airfoil is closely related to drag that the fluid exerts on the surfaces. At supersonic speeds, transition in the flow around the airfoil affects the aerodynamic heating.

1.2 General approach to hydrodynamic instability

Hydrodynamic stability is concerned with when and how a laminar flow loses its stability, and how it evolves subsequently. The eventual transition to turbulence is of particular interest. The topic has been regarded as one of the central problems in fluid mechanics. Research activities in this area in the past few decades were driven by modern technology needs, especially those in aeronautical and astronautical engineering.

The field of hydrodynamic instability has attracted many of great physicists, including Lord Kelvin, Lord Rayleigh, Sommerfeld and Heisenberg, whose work laid down the theoretical foundation.

The flow whose stability is of concern is referred to as the base flow. It is characterized by a velocity field $\mathbf{U}(\mathbf{x}, \mathbf{t})$, and other quantities, such as pressure $P(\mathbf{x}, t)$ and temperature

$\Theta(\mathbf{x}, t)$, which are all specified at each point $\mathbf{x}$ and time t. In order to study its stability, the base flow is perturbed by small disturbances such that the perturbed flow can be represented as a superposition of

$$\mathbf{u}(\mathbf{x}, t) = \mathbf{U} + \mathbf{u}', \quad p(\mathbf{x}, t) = P + p', \quad \theta(\mathbf{x}, t) = \Theta + \theta'.$$

Substitution into the Navier-Stokes equations then yields the equations governing the evolution of the perturbation. The instability of the base flow can be determined according to whether the perturbation grows in time or in space. If a disturbance amplifies to a significantly higher level, the flow is deemed to be unstable. If all permissible initial disturbances are found to decay or remain bounded, the flow is said to be stable. This is the so-called *initial-value approach* to stability. While the basic idea looks simple and most general, its implementation involves many complications. It has to be decided whether temporal or spatial evolution of the perturbation should be considered. Temporal evolution is appropriate for bounded flows, and semi-bounded flows which are homogeneous in the unbounded direction. In such cases, the interest is in whether a new state would ultimately emerge at large time. The short-time transient evolution is of little relevance because it is not repeatable and cannot be observed in experiments. For example, in the case of a pipe flow, at a fixed Reynolds number one observes either a laminar state or a turbulent state, but not the transient process from laminar to turbulence. Temporal evolution is not always appropriate. In open flows such as the boundary layer type of flow around an airfoil, it is more appropriate to follow the spatial development of a perturbation. In this case, it is important to prescribe physically realistic boundary conditions as well as initial conditions to be imposed at a suitable upstream location. This would ensure that the resulting formulation describe correctly the so-called receptivity, an important issue which we shall discuss further later. Unlike the temporal evolution, the spatial transient evolution from the upstream laminar state to the downstream turbulent stage can be observed in laboratory. It is indeed the main focus of transition research, and has been studied extensively.

The perturbation equations are nonlinear in general, and so the initial-value approach is mostly implemented by direct numerical simulations (DNS). For small perturbations, products of the perturbation $\mathbf{u}'$ can be neglected to obtain a linear system of partial differential equations, which serve as a first approximation. If a base flow is steady and homogenous in certain direction(s), the equations may be Fourier transformed with respect to time and the

homogenous direction(s). This leads to normal mode analysis, in which each perturbation quantity is written into independent components or modes, which vary with time t and homogenous direction(s), x say, like $e^{i(\alpha x-\omega t)}$, where α and ω may be complex numbers. The formulation is referred to as being temporal if α is assumed to be real and $\omega = \omega_r + i\omega_i$ complex, or spatial if ω is taken to be real and $\alpha = \alpha_r + i\alpha_i$ complex (Gaster 1962). The equations and the homogeneous boundary conditions form an eigenvalue problem to determine the complex frequency ω for a given wavenumber α in the temporal instability formulation, or the complex wavenumber α for a given real frequency ω in the spatial instability formulation. If $\omega_i > 0$ ($\alpha_i < 0$) for any α (ω), then the perturbation will grow with time (in the homogenous direction), and the flow is said to be unstable. If $\omega_i < 0$ ($\alpha_i > 0$) for all α (ω), then the perturbation will decay exponentially with time (in space), and the flow is said to be asymptotically stable or stable; if $\omega_i = 0$ or $\alpha_i = 0$, the mode neither grows nor decays, and is referred to as a neutral mode. The flow is said to be neutrally stable if all modes decay except neutral modes (Drazin and Reid 1981). The condition $\omega_i = 0$, or $\alpha_i = 0$, defines in the parameter space a neutral curve or surface. The mathematical procedure described above forms the so-called *eigenvalue approach*, which was pioneered by Lord Rayleigh (1880) and Lord Kelvin (1880), and has now become the standard tool for predicting instability.

1.3 Important instability mechanisms

While the theoretical approaches described in the previous section are general, they have not been able to give a criterion for the onset of instability in an arbitrarily base flow. Instability has therefore been studied for relatively simply flows which include, in addition to the quiescent state, plane Poiseuille flow and boundary layer type of flows. Several important fundamental physical mechanisms of instability have been identified. These include thermal instability induced by the buoyancy effect; inertial instability induced purely by the background shear or by the combined effect of viscosity and shear, which are usually referred to as Rayleigh and Tollmien-Schlichting (T-S) instabilities respectively; centrifugal instability induced by the centrifugal force. The first of these mechanisms is well understood. In this section, we shall summarise the main results concerning inertial and centrifugal instabilities, which are directly relevant to the investigation in this thesis.

The simplest flow in which inertial or shear instability can arise is a uni-directional

parallel flow with a velocity profile $U_B(y)$. The variation of the velocity is with respect to the transverse variable y, which is normalised by a characteristic length scale δ^*. The relevant parameter is the Reynolds number $U_0\delta^*/\nu$, where U_0 is a typical velocity. Lord Rayleigh (1880) first studied the stability of such a base flow bounded by two parallel planes. With the Reynolds number being taken to be infinite, i.e. the viscous effects being neglected, he showed that if instability is to occur, the basic velocity profile must have an inflectional point y_c interior to the flow, that is

$$U_B''(y_c) = 0. \tag{1.3.1}$$

This result is commonly called Rayleigh's inflection-point theorem, which states that (1.3.1) is a necessary condition for inviscid instability. A stronger form of the Rayleigh's inflection-point theorem was proved by Fjørtoft. He showed that the necessary condition for instability is

$$U_B''(y_c) = 0, \quad \text{and} \quad U_B''[U_B - U_B(y_c)] < 0, \tag{1.3.2}$$

somewhere interior to the flow. Later, Tollmien (1935) showed that for bounded flows with symmetric profiles, and unbounded flows with monotonic velocity profile, condition (1.3.2) is both necessary and sufficient for instability (Drazin and Reid 1981). For a general unbounded flow, however, the condition (1.3.1) is not sufficient to guarantee the occurrence of instability. The instability is of inviscid nature and is customary referred to as Rayleigh instability, and the associated waves are called Rayleigh waves/modes, the phase speeds of which are bounded by the maximum and minimum of the base velocity. The temporal (spatial) growth rate has an order of magnitude of U_0/δ^* ($1/\delta^*$). Due to large growth rates, the instability can lead to rapid breakdown to turbulence (Reed et al. 1996).

According to Rayleigh's theorem, velocity profiles without an inflection point ought to be stable, at least when Reynolds number is sufficiently high. However, instability and transition do occur in many flows with non-inflectional velocity profiles (e.g. the plane Poiseuille flow and Blasius boundary layer). This prompted the formulation of viscous instability theory. For parallel shear flows, the normal-mode analysis led to the eigenvalue problem governed by the Orr-Sommerfield (O-S) equation. Applying this theory to the plane Poiseuille flow, Heisenberg (1924) showed that provided the Reynolds number is sufficiently large, viscosity may cause instability despite that it dissipates energy. The eigenvalue problem was later solved by highly accurate numerical method, and the critical

Reynolds number for linear instability was found to be 5772.2 (Orszag 1971).

Viscous instability theory formulated for exactly parallel flows has been frequently adapted to boundary layers, where the base flow consists of a transverse component V_B and the streamwise component varies with the streamwise coordinate. The normal-mode analysis is, strictly speaking, not applicable. A remedy is making the local parallel-flow approximation, first suggested by Prandtl. In this approximation, the streamwise variation and V_B are ignored, and the streamwise profile is frozen at each location allowing a normal-mode solution to be sought. This approach was first taken by Tollmien (1929) and Schlichting (1933) for the Blasius boundary layer. They demonstrated boundary layer is unstable, which was later confirmed by experiments (Schubauer and Skramstad 1947). The viscous shear instability then became known as Tollmien-Schlichting instability. Refined analysis of the O-S equation was carried out by Lin (1945, 1955), and the equation was solved numerically by numerous researchers to map out the neutral curve, which consists of lower and upper branches. The predicted characteristics of the instability are broadly in agreement with experiments.

The non-parallel-flow effects have been investigated following two different approaches. The first is the composite approximation, in which the O-S equation serves as the first approximation. The non-parallel-flow corrections, associated with V_B and the streamwise variations of the base flow and the eigenfunction, were taken into account at $O(R^{-1})$ (Gaster 1974). Comparison with experimental data suggests that this approach gives more accurate prediction, especially at moderated Reynolds numbers (Saric and Nayfeh 1975). The alternative approach is the systematic high-Reynolds-number asymptotic expansion. At leading order, the instability near the lower branch is governed by the well-known triple-deck structure (Lin 1945), and the wavelength is of order $R^{1/4}$ times the boundary layer thickness, much longer than what was implicitly assumed in the composite approximation. As a result, non-parallelism appears as an $O(R^{-3/4})$ correction to the growth rate (Smith 1979). The accuracy of this approach is unfortunately rather poor at moderate Reynolds number. However, it provides the precise asymptotic estimate of the characteristic length scale of the instability, an insight crucial for understanding receptivity.

Centrifugal instability is best illustrated in the flow between two concentric rotating cylinders, known as the Taylor-Couette problem. Detailed theoretical and experimental studies were carried out by Taylor (1923). The instability leads to the formation of toroidal vortices, an periodic array of doughnut-shaped cells, along the axial direction. A simi-

lar mechanism operates in a boundary layer over a concave wall. The imbalance between the centrifugal force and the pressure gradient in the wall-normal direction leads to formation of longitudinal counter rotating vortices, which are now called Görtler vortices, as Görtler (1940) was the first to investigate them theoretically. Realising the analogy with Taylor-Couette flow, Görtler considered temporal instability and formulated an eigenvalue problem. However, it was realized later that Görtler instability differs considerably from Taylor instability in many aspects. A detailed introduction will be given in chapter 2 of this thesis.

The base flow for the aforementioned instabilities is two dimensional. In practical applications, of which the boundary layer over a swept wing is a typical example, the base flow is three-dimensional, and the characteristics of stability will be affected substantially by the additional velocity component in the crossflow direction. A multitude of instabilities may operate in different regions of the flow, including (temporal) viscous instability along the attachment line, and crossflow instability in the region of favourable pressure gradient (i.e. near the leading edge), streamwise T-S type instability in the adverse pressure region and Görtler instability in the concave section of the wing (Reed and Saric 1989, Saric et al. 2003). The occurrence of crossflow instability is often attributed to the fact that the crossflow velocity is zero at the wall and at the outer edge of the boundary layer so that an inflectional point must exist in the profile, and inviscid instability may be possible and instability modes must propagate in the direction nearly coinciding with the crossflow direction. In this sense, crossflow instability is in essence a Rayleigh instability. This simple interpretation holds in the majority of the flow region where the wavelength of instability modes is comparable with the local boundary layer thickness. However, near the leading edge, crossflow instability has a viscous origin. We will give, in chapter 3, a detailed introduction to crossflow instability and the issues related to receptivity and transition.

1.4 Transition routes and receptivity

Transition of a laminar flow to turbulence is caused by the intrinsic instability, but it is also influenced by external disturbances. This is the case especially for open flows. The information of instability alone is not sufficient for predicting transition. Depending on the level of external disturbances, transition may take different routes. In order to be specific, we

consider two-dimensional boundary-layer transition as an example. When the free-stream turbulence level is low, the growth of T-S waves is instrumental and ensuing transition is referred to as natural transition. When the free-stream turbulence level is high, transition occurs without apparently involving T-S waves. Transition of this kind is referred to as bypass transition (Morkovin 1969).

The natural transition is a complicated process consisting of five different stages: receptivity where external disturbances excite intrinsic instability (i.e. T-S) waves; linear growth where T-S waves amplify exponentially as predicted by linear stability theory, nonlinear saturation, secondary instability leading to eventual breakdown to turbulence. It has been observed in experiments that the final transition location varies significantly with the level of free-stream disturbances and surface roughness. This has been attributed to different initial amplitudes of T-S waves that are excited through the receptivity. Clearly, transition cannot be predicted without accounting for receptivity.

Receptivity is concerned with how the boundary layer responds to external disturbances and how the instability waves develop from the response. This means that mathematically receptivity must be described by an initial-boundary-value problem (Reshotko 1976). In order to formulate such a problem, it is necessary to consider first physical nature of the disturbances present in the ambient environment. In the case of boundary layer, unsteady external disturbances consist of vortical and acoustical disturbances in the free stream. The former represents vorticity fluctuation being advected by the uniform background flow so that there is no associated pressure fluctuation at leading order, while the latter is an irrotational motion representing pressure waves propagating through the fluid with the speed of sound. Steady disturbances come from surface roughness, which may be isolated or distributed. None of these disturbances alone could excite T-S waves because the time and length scales of each of these disturbances cannot be the same simultaneously as the corresponding intrinsic characteristic scales of the instability. As was pointed out by Goldstein (1983), crucial to receptivity is the scale conversion, which tunes the external scales to match the intrinsic scales. Several scale conversion mechanisms have been identified (Goldstein and Hultgren 1989).

The first is the the so-called ‘leading-edge adjustment’ mechanism, discovered first by Goldstein (1983). He demonstrated that while T-S waves are governed by the O-S equation or triple-deck theory, this eigenvalue formulation becomes invalid near the leading edge, where non-parallelism is a leading-order effect so that the perturbation must be governed by

linearised boundary layer equations. These equations admit the so-called Lam-Rott asymptotic modes. Acoustic disturbances, appearing as the inhomogeneous boundary condition of the boundary layer equations, excite Lam-Rott modes, among which the most rapidly decaying one undergoes wavelength shortening and eventually evolves into a T-S wave.

The second scale-conversion mechanism was identified by Ruban (1984) and Goldstein (1985). It involves interaction of an acoustic wave with a local roughness. The frequency of the acoustic wave and the length scale of the roughness are chosen to be comparable to the frequency and wavelength of an amplifying T-S mode respectively. The acoustic wave interacts with the local mean-flow induced by the roughness to generate an unsteady forcing, which has time and length scales matching the intrinsic scales. A T-S wave is generated as a result. A similar mechanism has been described by Duck et al. (1996) for receptivity to vortical disturbances. Wu (2001a,b) later formulated receptivity theory for distributed roughness, and also extended the theory of Duck et al. (1996) to second order. Detailed quantitative comparison was made with experimental data, and a good agreement was found.

In summary, the seminal work of Goldstein (1983, 1985) and Ruban (1984) marks a breakthrough in our understanding of receptivity. The receptivity process in the two-dimensional flat-plate boundary layer has been thoroughly understood at least in incompressible flows. The key idea and existing mathematical formalisms can be generalised, in a rather straightforward manner, to many other flows including certain forms of crossflow receptivity.

In this thesis, we shall tackle two of remaining receptivity problems for which the solutions are far from being obvious or straightforward. One is concerned with generation of steady and unsteady Görtler vortices by free-stream vortical disturbances, while the other is excitation of non-stationary crossflow vortices in three-dimensional boundary layers by free-stream vortical disturbances. Both problems require a detailed examination of the instability properties of the underlying base flows in the leading-edge region. These two problems will be investigated in chapter 2 and chapter 3 respectively. In chapter 4, we give an overall summary and highlight a few topics for future study.

Chapter 2

Görtler Vortices

2.1 Introduction

Görtler instability is an important type of centrifugal instability. It occurs in a boundary layer over a concave wall due to the imbalance between the centrifugal force and the normal pressure gradient. The instability leads to formation of counter-rotating vortices with axes parallel to the free stream. Usually the vortex pattern appears more-or-less periodic in the spanwise direction with a discernible wavelength λ_z. While the underlying physical mechanism is essentially the same as that of Taylor instability in a flow between two concentric rotating cylinders, the mathematical theory for Görtler instability is more complex because of the non-parallelism associated with the streamwise growth of the boundary layer. As the instability occurs in an open domain, it is also crucially affected by ambient perturbations, making an accurate prediction a considerable challenge. The problem of Görtler instability and the resulting transition to turbulence has been a subject of active research for several decades. Comprehensive reviews have been given by Hall (1990), Floryan (1991) and Saric (1994).

The problem was first studied by Görtler in 1940 (Görtler 1940). In his original formulation, two assumptions were made: (a) the boundary-layer thickness is much smaller than the radius of curvature; (b) the base flow is nearly parallel to the wall with its dependence on the streamwise coordinate and the transverse velocity both being neglected. The second assumption is referred to as the quasi-parallel approximation, which allows us to seek normal-mode solution for the perturbation so that the instability can be treated as an

eigenvalue problem. The relevant parameter controlling the instability is

$$G_\theta = (U_\infty \theta/\nu)\sqrt{\theta/r_0^*},$$

where U_∞ is the free-stream velocity, θ is the momentum thickness of the boundary layer, ν is the kinematic viscosity, and r_0^* is the radius of curvature. This parameter was later referred to as the Görtler number in recognition of Görtler's pioneering work.

Görtler (1940) formulated and solved a temporal instability problem, in which the perturbation was assumed to amplify with time. Improvements to Görtler's work were made over several decades since. Smith (1955) formulated a spatial instability problem, in which vortices grow with the streamwise position. The normal velocity and the variation of the streamwise velocity of the base flow were retained. However, Smith neglected the streamwise derivative of the normal velocity as result of assuming that all three velocity components of the perturbation have the same order of magnitude. This assumption was erroneous as was first recognised by Floryan and Saric (1982, 1984), who pointed out that the streamwise velocity of the perturbation has magnitude greater than that of the normal and spanwise velocities by factor of $O(R_\theta)$, where $R_\theta = U_\infty\theta/\nu$ is the Reynolds number based on θ. With this correct scaling, the streamwise derivative of the normal velocity of the base flow appears at leading-order and must be retained in the stability equations. In all eigenvalue formulations, for a given wavenumber $k = (2\pi/\lambda_z)\theta$, a Görtler number G_θ may be found such that the mode is neutral, i.e. a unique neutral curve in the (k, G_θ) plane may be identified. The neutral curve indicates that vortices of a given wavelength begin to amplify at some distance downstream but decay near the leading edge.

In conjunction with theoretical studies, many experiments have been conducted. Early investigations include hot-wire measurements (Tani 1962, Tani and Sakagami 1962, Tani and Aihara 1969) and visualization of the vortex pattern (Wortmann 1969, Bippes and Görtler 1972). The result of Tani (1962) supports the theoretical assumption that the spanwise wavelength of Görtler vortices remains constant as they evolve downstream. The measurements were compared with the theoretical prediction of Smith (1955), and a relatively good agreement was obtained for the normalised streamwise velocity profile, but the agreement for growth rates was unsatisfactory. A relatively recent experimental study focusing on the linear regime of vortices was that of Finnis and Brown (1997). They carried out detailed measurements of the velocity profile and amplitude of steady Görtler vortices

at different streamwise locations. The measured streamwise growth rate was found to be nearly a constant. A comparison with the local eigenvalue approach indicated that the eigenvalue approach over-predicted the growth rate considerably.

Hall (1982) and Hall (1983) pointed out that the normal-mode approach amounts to an *ad-hoc* treatment that cannot be justified mathematically for a weak curvature corresponding to $G_\theta = O(1)$. This is because vortices grow weakly in the streamwise direction over the same length scale as that of the underlying boundary layer, which means that the dependence of the coefficients in the perturbation equations cannot be treated as being parametric, and seeking a normal-mode solution is therefore inappropriate. Instead, one has to formulate the Görtler instability as an initial-value problem. The eigenvalue approach may be justified only when the Görtler number G_θ is asymptotically large, in which case distinguished regimes that may arise at a fixed downstream location have been identified for different spanwise wavelength λ_z, relative to the local boundary-layer thickness δ. In asymptotic analyses of Görtler instability, one usually uses, following Hall (1982) and Hall (1983), the Görtler number $G_H = (2L/r_0^*)(U_\infty L/\nu)^{\frac{1}{2}}$, which is related to G_θ via the relation $G_\theta = \frac{0.664^{3/2}}{\sqrt{2}} G_H^{\frac{1}{2}}$, i.e. $G_H \propto G_\theta^2$, where L is the distance to the leading edge. In order to provide an asymptotic characterisation of the neutral curve obtained by the eigenvalue approach, Hall (1982) first considered the regime pertaining to the right branch of the neutral curve. He showed that the ratio of the spanwise wavelength to the boundary-layer thickness δ is of $O(G_\theta^{-1/2})$, i.e. $\lambda_z/\delta = O(G_\theta^{-1/2})$. The typical growth rate, normalised by L , is of $O(G_\theta)$. Neutral modes with a zero growth rate fall into this regime. The eigenfunction concentrates in a thin viscous layer located in the main bulk of the boundary layer. Two further regimes emerge as λ_z/δ is increased. When $\lambda_z/\delta = O(G_\theta^{-2/5})$, the growth rate raises to $O(G_\theta^{6/5})$, and this is referred to as the most unstable regime (Timoshin 1990, Denier et al. 1991). The eigenfunction is confined in a thin viscous sub-layer adjacent to the wall. The inviscid regime operates when $\lambda_z/\delta = O(1)$. Görtler vortices spreads across the main boundary layer and have a growth rate of $O(G_\theta)$. In all these regimes, the nonparallel-flow effect appears as a high-order correction, which can be accounted for either by a formal asymptotic expansion or by a successive approximation (Bottaro and Luchini 1999) ; the latter assumes $G_\theta \gg 1$ but is not strictly asymptotic because viscous terms are retained at leading order despite being of smaller magnitude.

For $G_\theta = O(1)$, the growth rate of Görtler vortices is dependent on the upstream condition and as well as on ambient disturbances. A unique growth rate is thus not tenable and

neither is a unique neutral curve. This conclusion was made by Hall (1983), who solved the initial-value problem by applying a marching procedure, starting from a more or less arbitrarily imposed initial condition. Day et al. (1990) compared eigenvalue (normal mode) and marching (initial-value) solutions with the initial (upstream) disturbance being taken to be either a local eigenmode or its distorted form. It was found that solutions starting from different initial conditions evolve differently, but eventually approach the local eigen solution sufficiently downstream. The total accumulated growth is different albeit by a moderate amount.

The asymptotic analyses mentioned earlier imply that if vortices are initiated sufficiently near the leading edge, they must necessarily evolve through a regime in which $\lambda_z/\delta = O(1)$ or larger, and $G_\theta = O(1)$ so that the initial-value problem is the only correct formulation. Specifying relevant initial conditions is therefore vital if the entire evolution of Görtler vortices is to be described. Such a condition can only be provided by investigating how Görtler vortices are generated by external disturbances present in the environment. This is the so-called receptivity process, i.e. the process by which external disturbances enter the boundary layer to initiate unstable waves.

One important source of external disturbances is surface roughness, and the process by which Görtler vortices are generated was analysed by Denier et al. (1991) and Bassom and Hall (1994). An array of surface roughness element with a spanwise wavelength smaller than the local boundary-layer thickness was found to be extremely inefficient in exciting Görtler vortices as the coupling coefficient (the ratio of the amplitude of the vortices to that of the roughness) turned out to be exponentially small. For surface roughness with a wavelength comparable to the boundary-layer thickness, the coupling coefficient was of order one. However, for a streamwise isolated roughness the vortices decay first before the eventual growth at large distances. Interestingly, vortices generated by a streamwise distributed roughness amplify from outset. Further details can be found in the review by Bassom and Seddougui (1995).

Another important type of external disturbances is free-stream turbulence (FST), which usually consists of acoustic, vortical and entropy modes (Kovasznay 1953). Evidence of its effect on Görter vortices was indicated in the experiments of Bippes and Görtler (1972) and Swearingen and Blackwelder (1987), where it was found that the preferred wavelength, the pattern and onset locations as well as the amplitude of vortices all depend rather sensitively on the characteristics of FST. Employing grid-generated turbulence, Kottke (1988) investi-

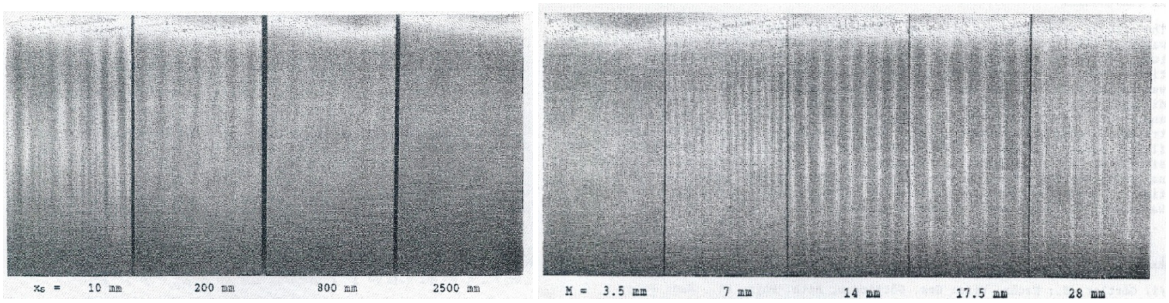


Figure 2.1: Influence of FST on the occurrence of Görtler vortices (Kottke 1988). Left: adjusting the distance of the grid to the leading edge with fixed mesh size. Right: adjusting the mesh size with fixed distance.

gated in detail how FST influences the occurrence and characteristics of Görtler vorticies. By adjusting the mesh size and/or the distance of the grid to the leading edge, he could alter the intensity and length scale of FST impinging on the boundary layer. When the distance is too large and hence FST intensity is almost diminished due to dissipation, Görtler vortices do not arise in the boundary layer. Clear vortex patterns are observed if the grid is relatively close to the leading edge (see figure 2.1 left), and the wavelength increases with the mesh size (see figure 2.1 right). These results provide the most convincing evidence that FST may excite Görtler vortices. This receptivity problem is of particular importance to turbo-machinery, where the oncoming flow is characterised by high turbulence intensity Tu (about 1–10 %). Since blade surfaces are curved, Görtler instability operates to affect transition (Volino and Simon 1995). Steady Görtler vortices were observed at moderate Tu of about 1% (Kim et al. 1992). At high Tu (8%), it was speculated that unsteady Görtler vortices may be present (Schultz and Volino 2003). Hot-wire measurements indicate that significant low-frequency fluctuations, reminiscent of unsteady streaks or vortices, reside in the boundary layer (Volino and Simon 2000).

Despite its importance, the initiation of Görtler vortices by free-stream disturbances has received very little theoretical attention. Hall (1990) considered the receptivity to a steady disturbance in the form of a spanwise-varying streamwise velocity superimposed on the oncoming flow. In this case, vortices in the boundary layer are driven by the streamwise slip velocity. This mechanism may be inefficient because vortices excited experience considerable decay before the eventual amplification. Schrader et al. (2011) attempted to simulate numerically the excitation of Görtler vortices by free-stream vortical disturbances and the subsequent transition process. In their work, which was published after ours, the free-

stream vortical disturbances were represented by continuous spectra of Orr-Sommerfeld and Squire equations. These equations were solved numerically, and the eigenfunctions obtained were imposed at the inlet of the computation domain. This is the only place where the external forcing acts on the boundary layer since a zero-disturbance condition is imposed on the upper calculation domain. Numerical results indicate that unstable modes are generated. However, the inlet condition is chosen for computational convenience rather than for having any physical significance. Further more, eigenfunctions of continuous spectra, which are based on the local parallel-flow approximation, cannot describe the entrainment of the most relevant long-wavelength disturbances because the latter have the same length scale as that of the base flow and are influenced by non-parallelism at leading order. Therefore, we believe that the receptivity process is not properly accounted for in the numerical simulations of Schrader et al. (2011).

The aim of this chapter is to provide a mathematical formulation which describes both the excitation of Görtler vortices by FST and their linear development. The relevant components in FST are long-wavelength steady or unsteady vortical disturbances. The effect of such disturbances on the pre-transitional flat-plate boundary layer was investigated by Leib et al. (1999) (referred to hereinafter as LWG). They showed that the boundary-layer signature is governed by the linearised unsteady boundary-region equations (LUBR), i.e. the linearised Navier-Stokes (N-S) equations with the viscous diffusion and pressure gradient in the streamwise direction being neglected, and derived appropriate initial and boundary conditions, which account for the action of the free-stream disturbance. Numerical solutions show that the boundary layer acts as a filter, allowing low-frequency fluctuations to penetrate into the shear layer and amplify downstream to form streamwise elongated streaks, while blocking high-frequency components. The problem formulated by LWG for a flat-plate boundary layer will be extended to a boundary layer over a concave wall, where the centrifugal force induces Görtler instability. The LUBR equations are modified by taking the centrifugal force into consideration.

The rest of this chapter is organized as follows. In §2.2–§2.4, we formulate the problem of Görtler instability and receptivity for the generic case corresponding to $G_\Lambda = O(1)$. The initial and boundary conditions, derived by LWG for the flat-plate case, are found to be applicable. In order to characterise the nature of the perturbation excited by FST, and to assess the validity and accuracy of *ad-hoc* eigenvalue approaches, the parallel and non-parallel instability equations are presented in §2.5 for $G_\Lambda = O(1)$. The limiting case

$G_\Lambda \gg 1$ is considered in §2.6, where an asymptotic analysis of the initiation and subsequent development of Görtler vortices was performed to map out the regimes, through which vortices with a fixed spanwise wavelength evolve. In §2.7, we describe the numerical methods used to solve the initial-value and eigenvalue problems. Numerical solutions and extensive comparisons with experimental data are presented in §2.8. A summary and concluding remarks are given in §2.9.

2.2 Formulation and scaling

We consider a boundary-layer flow over a concave wall with a local radius of curvature r_0^*, which varies slowly. The oncoming flow is assumed to be uniform with a speed U_∞, on which FST is superimposed. The FST has a characteristic spanwise length scale Λ. In order to include the curvature effect, we describe the fluid motion in a curvilinear system (x^*, y^*, z^*) with its origin at the leading edge, where x^* measures the streamwise distance to the leading edge along the wall, y^* is the distance normal to the wall, and z^* the spanwise coordinate normal to both x^* and y^*. Let

$$(x, y, z) = (x^*, y^*, z^*)/\Lambda, \quad \bar{r}_0 = \frac{r_0^*}{\Lambda}, \quad t = \frac{U_\infty t^*}{\Lambda},$$

where t^* is the dimensional time. The Reynolds number is defined as

$$R_\Lambda = \frac{U_\infty \Lambda}{\nu}, \tag{2.2.1}$$

with ν being the kinematic viscosity.

The current research interest lies in FST with long streamwise wavelengths $2\pi/k_1^* \gg \Lambda$, where k_1^* is the dimensional streamwise wavenumber. They are either steady or have low frequencies of $O(R_\Lambda^{-1} U_\infty/\Lambda)$. In the special case of a flat plate, FST are known to penetrate into the boundary layer to generate streamwise elongated streaks (LWG). The latter attain their maximum amplitude at $x^* \sim 2\pi/k_1^*$ (and decay further downstream). The local boundary-layer thickness becomes comparable with Λ when streaks are fully developed if $2\pi/k_1^* = O(\Lambda R_\Lambda)$; this is the distinguished scaling because the spanwise elliptic effect must be considered. In the case of a curved plate with a suitable curvature, streaks are expected to take on the character of Görtler vortices when $x^* \sim 2\pi/k_1^* \sim \Lambda R_\Lambda$. The above consideration suggests the introduction of the slow streamwise and time

variables

$$\hat{x} = \frac{x}{R_\Lambda}, \quad \hat{\tau} = \frac{t}{R_\Lambda}. \tag{2.2.2}$$

Let the dimensional velocity and pressure fields, (u^*, v^*, w^*) and p^*, be written as

$$(u^*, v^*, w^*)/U_\infty = (u, R_\Lambda^{-1}v, R_\Lambda^{-1}w), \quad \text{and} \quad \frac{p^*}{\rho U_\infty^2} = \frac{p}{R_\Lambda^2}. \tag{2.2.3}$$

Substitution of (2.2.2)–(2.2.3), and the Lamé coefficients (Tobak 1971)

$$h_1 = \frac{\bar{r}_0 - y}{\bar{r}_0}, \quad h_2 = 1, \quad h_3 = 1,$$

into the Navier-Stokes equations written in the body-fitted coordinates yields the leading order equations (Hall 1988)

$$\left.\begin{aligned} \frac{\partial u}{\partial \hat{x}} + \frac{\partial v}{\partial y} + \frac{\partial w}{\partial z} &= 0, \\ \frac{\partial u}{\partial \hat{\tau}} + u\frac{\partial u}{\partial \hat{x}} + v\frac{\partial u}{\partial y} + w\frac{\partial u}{\partial z} &= \frac{\partial^2 u}{\partial y^2} + \frac{\partial^2 u}{\partial z^2}, \\ \frac{\partial v}{\partial \hat{\tau}} + u\frac{\partial v}{\partial \hat{x}} + v\frac{\partial v}{\partial y} + w\frac{\partial v}{\partial z} + G_\Lambda u^2 &= -\frac{\partial p}{\partial y} + \frac{\partial^2 v}{\partial y^2} + \frac{\partial^2 v}{\partial z^2}, \\ \frac{\partial w}{\partial \hat{\tau}} + u\frac{\partial w}{\partial \hat{x}} + v\frac{\partial w}{\partial y} + w\frac{\partial w}{\partial z} &= -\frac{\partial p}{\partial z} + \frac{\partial^2 w}{\partial y^2} + \frac{\partial^2 w}{\partial z^2}. \end{aligned}\right\} \tag{2.2.4}$$

The essential influence of the wall curvature is contained in the term $G_\Lambda u^2$, where

$$G_\Lambda = \frac{R_\Lambda^2}{\bar{r}_0} \tag{2.2.5}$$

is called Görtler number, which is the ratio of the centrifugal force to the viscous force in the boundary layer. Use of G_Λ is convenient and natural since our interest is in tracing the development of vortices of a fixed wavelength. The relation between G_Λ and G_θ is

$$G_\Lambda = \frac{R_\Lambda^2}{\bar{r}_0} = \frac{(\frac{U_\infty \Lambda}{\nu})^2}{r_0^*/\Lambda} = \Big(\frac{U_\infty}{\nu}\Big)^2 \frac{\Lambda^3}{r_0^*} = \Big(\frac{U_\infty \theta}{\nu}\sqrt{\frac{\theta}{r_0^*}}\Big)^2 \Big(\frac{\Lambda}{\theta}\Big)^3 = G_\theta^2 \Big(\frac{\Lambda}{\theta}\Big)^3. \tag{2.2.6}$$

We assume that $G_\Lambda = O(1)$, which is the most generic scaling. The resulting equations (2.2.4) are most general. They are the Navier-Stokes equations with the streamwise dif-

fusion and pressure gradient being neglected. Following Kemp (1951), Davis and Rubin (1980) and LWG, we refer to (2.2.4) as the boundary-region equations. Equations (2.2.4) are valid for perturbations of any kind provided their streamwise length scale and frequencies are of $O(\Lambda R_\Lambda)$ and $O(R_\Lambda^{-1} U_\infty/\Lambda)$ respectively.

2.3 The base flow

In this study, the base flow is taken to be the Blasius boundary layer, for which velocity components have the similarity solution,

$$U = F'(\eta), \qquad V = (\frac{1}{2\hat{x}})^{\frac{1}{2}}(\eta F' - F), \tag{2.3.1}$$

where a prime denotes the differentiation with respect to the similarity variable

$$\eta = y(\frac{1}{2\hat{x}})^{\frac{1}{2}}.$$

The Blasuis function F is determined by (Schlichting 1955)

$$F''' + FF'' = 0,$$

subject to the boundary conditions $F(0) = 0, \quad F'(0) = 0$. As $\eta \to \infty$, $F' \to 1$, $F \to \eta - \beta$ with $\beta \approx 1.217$.

2.4 Perturbation equations

As in LWG, we assume that FST is statistically stationary and homogenous, and consists of small-amplitude convected vortical disturbances. In general, FST can be treated as a superposition of harmonic disturbances, but due to linearity, it suffices to consider a single component

$$\mathbf{u} - \hat{\mathbf{i}} = \epsilon \mathbf{u}^\infty e^{i(\boldsymbol{k}\cdot\boldsymbol{x} - k_1 t)} = \epsilon \mathbf{u}^\infty e^{i(\boldsymbol{k}\cdot\boldsymbol{x} - \hat{k}_1 \hat{\tau})}, \tag{2.4.1}$$

where $\hat{\mathbf{i}}$ is the unit vector in the streamwise direction, $\epsilon \ll 1$ is a measure of the turbulence intensity, $\mathbf{u}^\infty = \{\hat{u}_1^\infty, \hat{u}_2^\infty, \hat{u}_3^\infty\}$ is the scaled velocity perturbation, $\boldsymbol{k} = \{k_1, k_2, k_3\}$ is the non-dimensional wavenumber vector, and $\hat{k}_1 = k_1 R_\Lambda = O(1)$.

For the flat-plate case, LWG showed that the flow domain can be divided into four

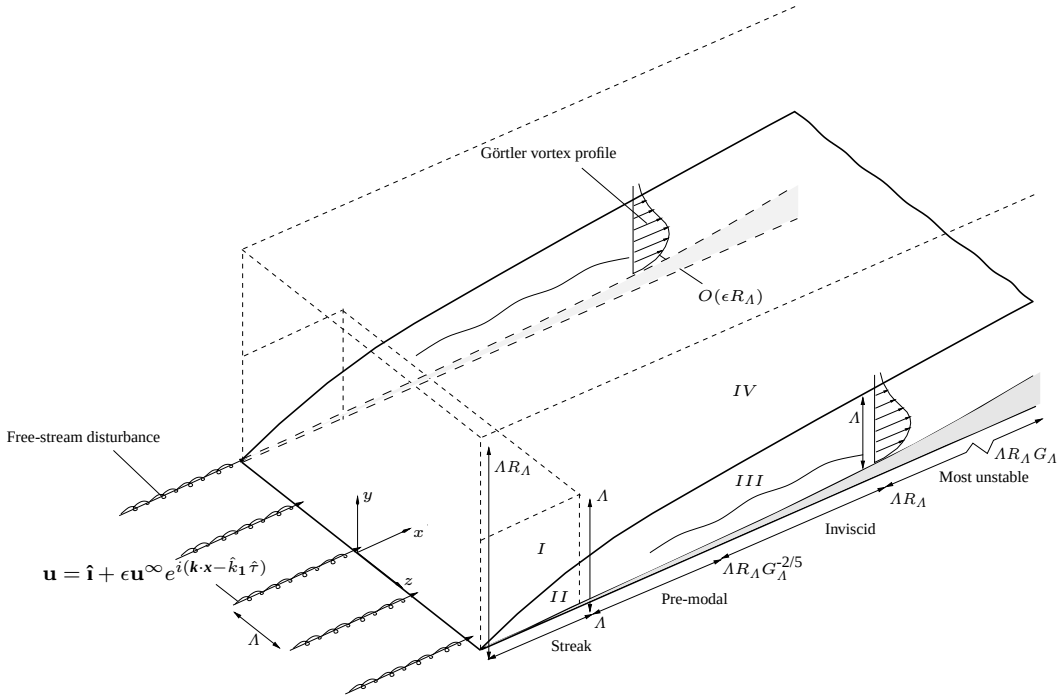


Figure 2.2: Schematic illustration of the physical problem and the asymptotic flow structure. Also shown are the main stages: pre-modal, inviscid and the 'most unstable' regimes, through which the induced perturbation evolves when $G_\Lambda \gg 1$ (Courtesy of Dr. P. Ricco).

asymptotic regions. The asymptotic structure holds for a concave wall and is illustrated in figure 2.2. Over the $O(\Lambda)$ distance to the leading edge is an inviscid region (I), which has $O(\Lambda)$ dimensions in the wall-normal and spanwise directions. The disturbance is treated as a small perturbation to the oncoming uniform flow. An analysis of the perturbation gives the stream- and spanwise slip velocities

$$u_1(0) = \hat{u}_1^\infty + \frac{ik_1}{\gamma}\hat{u}_2^\infty, \quad u_3(0) = \hat{u}_3^\infty + \frac{ik_3}{\gamma}\hat{u}_2^\infty, \tag{2.4.2}$$

where $\gamma = \sqrt{k_1^2 + k_3^2}$. The slip velocities are reduced to zero across region (II), the viscous boundary layer beneath the inviscid region. The perturbation is governed by the quasi-steady boundary-layer equations. Both the streamwise and spanwise components of the free-stream fluctuation are the leading-order forcing acting on the boundary layer to generate an $O(\epsilon)$ response. However, as in LWG, the response to the streamwise slip velocity remains bounded, and only the streamwise velocity driven by the spanwise slip velocity has amplitude in proportional to x and develops into larger amplitude streaks and eventually to Görtler vortices further downstream.

As the boundary-layer thickness grows with x, it becomes comparable to the spanwise length scale when $x = O(R_\Lambda)$ or $\hat{x} = O(1)$, at which point the spanwise derivative in the viscous terms becomes of the same order as the normal derivative. The perturbation is governed by the so-called boundary-region equations for the flat-plate case. In the case of a curved wall, the centrifugal force appears in the wall-normal momentum equation so that Görtler vortices emerge in this region (III). In order to provide the appropriate boundary condition in the far field, it is necessary to consider the outer region (IV).

In region III, the perturbed flow can be written as

$$\begin{aligned}(u,\, v,\, w,\, p) = &\Big(U(\hat{x}, y),\, V(\hat{x}, y),\, 0, -\tfrac{1}{2}\Big) \\ &+\epsilon R_\Lambda \Big(\hat{u}(\hat{x}, y, z, \hat{\tau}),\, \hat{v}(\hat{x}, y, z, \hat{\tau}),\, \hat{w}(\hat{x}, y, z, \hat{\tau}),\, \hat{p}(\hat{x}, y, z, \hat{\tau})\Big), \end{aligned} \tag{2.4.3}$$

where $\hat{u}$, $\hat{v}$, $\hat{w}$ and $\hat{p}$ are all of $O(1)$. Obviously the disturbance is fully nonlinear if the turbulent Reynolds number $r_t \equiv \epsilon R_\Lambda = O(1)$, but linear if $r_t \ll 1$, which is assumed to be the case in the present thesis. Inserting (2.4.3) into (2.2.4), and linearising, one obtains the leading-order perturbation equations (Hall 1983),

$$\hat{u}_{\hat{x}} + \hat{v}_y + \hat{w}_z = 0, \tag{2.4.4}$$

$$\hat{u}_{\hat{\tau}} + \hat{u}_{\hat{x}} U + \hat{u} U_{\hat{x}} + V \hat{u}_y + \hat{v} U_y = \hat{u}_{yy} + \hat{u}_{zz}, \tag{2.4.5}$$

$$\hat{v}_{\hat{\tau}} + U \hat{v}_{\hat{x}} + \hat{u} V_{\hat{x}} + V \hat{v}_y + \hat{v} V_y + 2 G_\Lambda \hat{u} U = -\hat{p}_y + \hat{v}_{yy} + \hat{v}_{zz}, \tag{2.4.6}$$

$$\hat{w}_{\hat{\tau}} + \hat{w}_{\hat{x}} U + V \hat{w}_y = -\hat{p}_z + \hat{w}_{yy} + \hat{w}_{zz}. \tag{2.4.7}$$

The essential influence of the wall curvature is contained in the term $2 G_\Lambda \hat{u} U$.

The slip velocities (2.4.2) suggest that it would be convenient to decompose the boundary-region solution for the perturbation as (Gulyaev et al. 1989, LWG)

$$\begin{aligned}(\hat{u}, \hat{v}, \hat{w}, \hat{p}) = &\Big[R_\Lambda^{-1} u_1(0) \Big(\bar{u}^{(0)},\, (2\hat{x})^{\frac{1}{2}} \bar{v}^{(0)},\, 0,\, \bar{p}^{(0)}\Big) \\ &+ \mathrm{i} k_3 u_3(0) \Big(\bar{u},\, (2\hat{x})^{\frac{1}{2}} \bar{v},\, \bar{w}/(\mathrm{i} k_3),\, \bar{p}\Big)\Big] e^{\mathrm{i}(k_3 z - \hat{k}_1 \hat{\tau})}, \end{aligned} \tag{2.4.8}$$

where $\{\bar{u}^{(0)}, \bar{v}^{(0)}, 0, \bar{p}^{(0)}\}$ is the two-dimensional part driven directly by the streamwise slip velocity $u_1(0)$, and $\{\bar{u}, \bar{v}, \bar{w}, \bar{p}\}$ is the three-dimensional part driven by the spanwise slip velocity $u_3(0)$. We only need to focus on the latter, which will evolve into dominant Görtler

vortices; the much smaller two-dimensional part is of no concern to us. Substituting (2.3.1) and (2.4.8) into (2.4.4)–(2.4.7) and rewriting the equations in terms of η, we obtain

$$\frac{\partial \bar{u}}{\partial \hat{x}} - \frac{\eta}{2\hat{x}}\frac{\partial \bar{u}}{\partial \eta} + \frac{\partial \bar{v}}{\partial \eta} + \bar{w} = 0, \tag{2.4.9}$$

$$-i\hat{k}_1\bar{u} + F'\frac{\partial \bar{u}}{\partial \hat{x}} - \frac{F}{2\hat{x}}\frac{\partial \bar{u}}{\partial \eta} - \frac{\eta F''}{2\hat{x}}\bar{u} + F''\bar{v} = \frac{1}{2\hat{x}}\frac{\partial^2 \bar{u}}{\partial \eta^2} - k_3^2\bar{u}, \tag{2.4.10}$$

$$-i\hat{k}_1\bar{v} + F'\frac{\partial \bar{v}}{\partial \hat{x}} - \frac{F}{2\hat{x}}\frac{\partial \bar{v}}{\partial \eta} - \frac{1}{(2\hat{x})^2}[\eta(\eta F')' - F]\bar{u} + \frac{(\eta F')'}{2\hat{x}}\bar{v} + 2G_{\Lambda}F'\bar{u}(\frac{1}{2\hat{x}})^{\frac{1}{2}}$$
$$= -\frac{1}{2\hat{x}}\frac{\partial \bar{p}}{\partial \eta} + \frac{1}{2\hat{x}}\frac{\partial^2 \bar{v}}{\partial \eta^2} - k_3^2\bar{v}, \tag{2.4.11}$$

$$-i\hat{k}_1\bar{w} + F'\frac{\partial \bar{w}}{\partial \hat{x}} - \frac{F}{2\hat{x}}\frac{\partial \bar{w}}{\partial \eta} = k_3^2\bar{p} + \frac{1}{2\hat{x}}\frac{\partial^2 \bar{w}}{\partial \eta^2} - k_3^2\bar{w}. \tag{2.4.12}$$

2.4.1 The upstream and far-field boundary conditions

The linearised boundary-region equations (2.4.9)–(2.4.12) must be solved subject to proper far-field and upstream boundary conditions. The former may be derived by considering the flow in region IV, which is above region III. The large–η asymptotic solution of (2.4.9)–(2.4.12) that matches the solution in region III then provides the correct boundary condition. Using the large-η form of the Blasius solution in (2.4.9)–(2.4.12), and rewriting these equations in terms of $y^{(0)}$, we have

$$\frac{\partial \bar{u}}{\partial \hat{x}} - \frac{\beta}{(2\hat{x})^{1/2}}\frac{\partial \bar{u}}{\partial y^{(0)}} + (2\hat{x})^{1/2}\frac{\partial \bar{v}}{\partial y^{(0)}} + \bar{w} = 0, \tag{2.4.13}$$

$$-i\hat{k}_1\bar{u} + \frac{\partial \bar{u}}{\partial \hat{x}} = \frac{\partial^2 \bar{u}}{\partial {y^{(0)}}^2} - k_3^2\bar{u}, \tag{2.4.14}$$

$$-i\hat{k}_1\bar{v} + \frac{\partial \bar{v}}{\partial \hat{x}} + \frac{1}{2\hat{x}}\bar{v} - \frac{\beta}{(2\hat{x})^2}\bar{u} + \frac{2G_{\Lambda}\bar{u}}{(2\hat{x})^{\frac{1}{2}}} = -\frac{1}{(2\hat{x})^{1/2}}\frac{\partial \bar{p}}{\partial y^{(0)}} + \frac{\partial^2 \bar{v}}{\partial {y^{(0)}}^2} - k_3^2\bar{v}, \tag{2.4.15}$$

$$-i\hat{k}_1\bar{w} + \frac{\partial \bar{w}}{\partial \hat{x}} = k_3^2\bar{p} + \frac{\partial^2 \bar{w}}{\partial {y^{(0)}}^2} - k_3^2\bar{w}, \tag{2.4.16}$$

where $y^{(0)} = (2\hat{x})^{1/2}(\eta - \beta)$. Note that the streamwise velocity of the perturbation within the boundary layer is of $O(\epsilon R_{\Lambda}\bar{u})$ (see (2.4.3)), while the perturbation in the free-stream only has an $O(\epsilon)$ streamwise velocity. The matching requirement is satisfied only if $\bar{u} = 0$ for $\eta \gg 1$.

Elimination of $\bar{v}$ and $\bar{w}$ among (2.4.14)–(2.4.16) yields the equation for $\bar{p}$, i.e.

$$\frac{\partial^2 \bar{p}}{\partial {y^{(0)}}^2} - k_3^2 \bar{p} = 0.$$

The solution is

$$\bar{p} = g(\hat{x}) e^{-|k_3| y^{(0)}}.$$

At the moment, the function $g(\hat{x})$ is as yet unknown, but its behaviour as $\hat{x} \to 0$ can be determined by matching with the solution in region (I).

The solution for $\bar{p}$ is inserted into (2.4.16) to find $\bar{w}$. The particular solution forced by $\bar{p}$ is found as

$$\bar{w}_p = k_3^2 e^{i\hat{k}_1 \hat{x} - |k_3| y^{(0)}} \int_0^{\hat{x}} g(\check{x}) e^{-i\hat{k}_1 \check{x}} d\check{x}.$$

Guided by the solutions in the outer region (IV) and the upstream region (I), we seek complementary solution of the form

$$\bar{w}_{cp} = h_1(\hat{x}) e^{i\hat{k}_1 \hat{x} + ik_2 y^{(0)}} + h_2(y^{(0)}) e^{i\hat{k}_1 \hat{x}},$$

where the first term represents the incident wave while the second is the reflected wave. Substitution into (2.4.16) yields the equations for $h_1(x)$ and $h_2(y^{(0)})$,

$$\frac{\partial h_1}{\partial \hat{x}} = -(k_2^2 + k_3^2) h_1, \qquad \frac{\partial^2 h_2}{\partial {y^{(0)}}^2} - k_3^2 h_2 = 0,$$

from which one finds

$$h_1 = A e^{-(k_2^2 + k_3^2)\hat{x}}, \quad h_2 = B e^{-|k_3| y^{(0)}}.$$

The constants A and B may be determined by matching.

As $\hat{x} \to 0$, matching with the solution in region (I) requires

$$(\hat{u}_3^\infty + \frac{ik_3}{\gamma} \hat{u}_2^\infty)(A e^{ik_2 y^{(0)}} + B e^{-|k_3| y^{(0)}}) \to \hat{u}_3^\infty e^{ik_2 y} + \frac{ik_3}{\gamma} \hat{u}_2^\infty e^{-\gamma y}.$$

It is deduced that

$$A = \frac{k_2}{k_2 - i|k_3|}, \quad \text{and} \quad B = -\frac{i|k_3|}{k_2 - i|k_3|},$$

where we have used the fact that $y^{(0)} \to y$ as $\hat{x} \to 0$, and $\gamma \approx |k_3|$ since $k_1 \ll 1$.

Therefore, the general solution for $\bar{w}$ can be written as

$$\bar{w} = \frac{e^{i\hat{k}_1\hat{x}}}{k_2 - i|k_3|}\left\{k_2 e^{ik_2 y^{(0)} - (k_2^2+k_3^2)\hat{x}} - i|k_3|e^{-|k_3|y^{(0)}}\right\} + k_3^2 e^{i\hat{k}_1\hat{x}-|k_3|y^{(0)}} \int_0^{\hat{x}} g(\check{x})e^{-i\hat{k}_1\check{x}}d\check{x}.$$

Similarly, inserting $\bar{w}$ into (2.4.13), and solving the resulting equation, we obtain

$$\bar{v} = \frac{ie^{i\hat{k}_1\hat{x}}}{(k_2 - i|k_3|)(2\hat{x})^{1/2}}\left\{e^{ik_2 y^{(0)} - (k_2^2+k_3^2)\hat{x}} - e^{-|k_3|y^{(0)}}\right\} + \frac{k_3 e^{i\hat{k}_1\hat{x}-|k_3|y^{(0)}}}{(2\hat{x})^{1/2}} \int_0^{\hat{x}} g(\check{x})e^{-i\hat{k}_1\check{x}}d\check{x}.$$

In conclusion, the solution to (2.4.13)–(2.4.16) that matches the outer solution turns out to be the same as that derived by LWG for the flat-plate case, namely

$$\bar{u} \to 0, \tag{2.4.17}$$

$$\bar{v} \to \frac{ie^{i\hat{k}_1\hat{x}}}{(k_2 - i|k_3|)(2\hat{x})^{1/2}}\left\{e^{ik_2 y^{(0)} - (k_2^2+k_3^2)\hat{x}} - e^{-|k_3|y^{(0)}}\right\} + \frac{k_3 e^{i\hat{k}_1\hat{x}-|k_3|y^{(0)}}}{(2\hat{x})^{1/2}} \int_0^{\hat{x}} g(\check{x})e^{-i\hat{k}_1\check{x}}d\check{x}, \tag{2.4.18}$$

$$\bar{w} \to \frac{e^{i\hat{k}_1\hat{x}}}{k_2 - i|k_3|}\left\{k_2 e^{ik_2 y^{(0)} - (k_2^2+k_3^2)\hat{x}} - ik_3 e^{-|k_3|y^{(0)}}\right\} + k_3^2 e^{i\hat{k}_1\hat{x}-|k_3|y^{(0)}} \int_0^{\hat{x}} g(\check{x})e^{-i\hat{k}_1\check{x}}d\check{x}, \tag{2.4.19}$$

$$\bar{p} \to g(\hat{x})e^{-|k_3|y^{(0)}}, \tag{2.4.20}$$

Elimination of the function $g(\hat{x})$ from (2.4.18)–(2.4.20) leads to mixed boundary conditions on the transverse velocity components and the pressure,

$$\left.\begin{aligned} \bar{u} &\to 0, \\ \frac{\partial\bar{v}}{\partial\eta} + |k_3|(2\hat{x})^{1/2}\bar{v} &\to -e^{i(\hat{x}+k_2(2\hat{x})^{1/2}\bar{\eta})-(k_2^2+k_3^2)\hat{x}}, \\ \frac{\partial\bar{w}}{\partial\eta} + |k_3|(2\hat{x})^{1/2}\bar{w} &\to ik_2\sqrt{2\hat{x}}e^{i(\hat{x}+k_2(2\hat{x})^{1/2}\bar{\eta})-(k_2^2+k_3^2)\hat{x}}, \\ \frac{\partial\bar{p}}{\partial\eta} + |k_3|(2\hat{x})^{1/2}\bar{p} &\to 0. \end{aligned}\right\} \tag{2.4.21}$$

As in LWG, the upstream condition may be derived by first considering the small-$\hat{x}$ solution of the boundary-region equations. The solution takes the form of a power series

$$\{\bar{u},\bar{v},\bar{w},\bar{p}\} = \sum_{n=0}^{\infty}(2\hat{x})^{n/2}\left\{2\hat{x}U_n(\eta), V_n(\eta), W_n(\eta), (2\hat{x})^{-\frac{1}{2}}P_n(\eta)\right\}. \tag{2.4.22}$$

Substituting (2.4.22) into (2.4.9)–(2.4.12), and collecting like powers of $\hat{x}$, one obtains a system of ordinary differential equations for the terms in the series (2.4.22). Since $\bar{u}$ tends to zero while $\bar{v}$ and $\bar{w}$ do not, the centrifugal force vanishes in the limit $\hat{x}\to 0$. As a result, the equations for (U_n, V_n, W_n) $(n = 0, 1)$ are the same as those given in LWG.

The upstream condition must be specified over the entire region $y = \eta(2\hat{x})^{\frac{1}{2}} = O(1)$, in order to account for the increased boundary-layer thickness in region III (LWG). The uniformly valid condition may be constructed by forming a composite solution from (2.4.17)-(2.4.20) and (2.4.22),

$$\bar{u} \to 2\hat{x}U_0 + (2\hat{x})^{\frac{3}{2}}U_1, \tag{2.4.23}$$

$$\begin{aligned}\bar{v} \to V_0 + (2\hat{x})^{\frac{1}{2}}V_1 + \frac{ie^{i\hat{k}_1\hat{x}}}{(k_2 - i|k_3|)(2\hat{x})^{\frac{1}{2}}}\left\{e^{ik_2(2\hat{x})^{\frac{1}{2}}\bar{\eta}-(k_3^2+k_2^2)\hat{x}} - e^{-|k_3|(2\hat{x})^{\frac{1}{2}}\bar{\eta}}\right\}\\ - \left(\frac{3\beta}{4} - \frac{1}{2}g_1|k_3|(2\hat{x})^{\frac{1}{2}}\right)e^{-|k_3|(2\hat{x})^{\frac{1}{2}}\bar{\eta}} - \bar{v}_c,\end{aligned} \tag{2.4.24}$$

$$\begin{aligned}\bar{w} \to W_0 + (2\hat{x})^{\frac{1}{2}}W_1 + \frac{e^{i\hat{k}_1\hat{x}}}{(k_2 - i|k_3|)}\left\{k_2e^{ik_2(2\hat{x})^{\frac{1}{2}}-(k_3^2+k_2^2)\hat{x}} - i|k_3|e^{-|k_3|(2\hat{x})^{\frac{1}{2}}\bar{\eta}}\right\}\\ - \frac{3\beta|k_3|}{4}(2\hat{x})^{\frac{1}{2}}e^{-|k_3|(2\hat{x})^{\frac{1}{2}}\bar{\eta}} - \bar{w}_c,\end{aligned} \tag{2.4.25}$$

where $\bar{\eta} = \eta - \beta$, and the common parts, $\bar{v}_c$ and $\bar{w}_c$, are given as

$$\bar{v}_c = -\eta + \frac{\beta}{4} + (2\hat{x})^{\frac{1}{2}}\left\{-\frac{i}{2}(k_2 + i|k_3|)\eta^2 + \beta(ik_2 - \frac{1}{4}|k_3|)\eta + c_1\right\},$$

$$\bar{w}_c = 1 + (2\hat{x})^{\frac{1}{2}}\left[i(k_2 + i|k_3|)\eta - \beta(ik_2 - \frac{1}{4}|k_3|)\right].$$

The normal and spanwise velocities of the initial condition (2.4.24)–(2.4.25), do not however vanish at the wall. They take non-zero values of $O(\hat{x})$. Though the error at the wall is comparable with that of the upstream condition for $y = O(1)$, it is preferable to have an initial condition satisfying the no-slip boundary condition exactly. This can be constructed by observing that the error was introduced by expanding the outer solution into a Taylor

series for both $\eta \ll 1$ and $\hat{x} \ll 1$ when matching it with the inner solution, and can be prevented if the expansion with respect to $\hat{x}$ is avoided. The resulting initial condition may then be written as (Wu et al. 2011)

$$\begin{aligned}\bar{v} \to \;& V_0 + (2\hat{x})^{\frac{1}{2}} V_1 + \tfrac{ie^{-ik_2(2\hat{x})^{\frac{1}{2}}\beta - (k_3^2+k_2^2)\hat{x}}}{(k_2 - i|k_3|)(2\hat{x})^{\frac{1}{2}}}\Big[e^{ik_2(2\hat{x})^{\frac{1}{2}}\eta} - e^{-|k_3|(2\hat{x})^{\frac{1}{2}}\eta}\Big] \\ & + e^{-|k_3|(2\hat{x})^{\frac{1}{2}}\eta}\big(\tfrac{\beta}{4} + \sqrt{2\hat{x}}c_1\big) - \bar{v}_c, \qquad (2.4.26)\\ \bar{w} \to\; & W_0 + (2\hat{x})^{\frac{1}{2}} W_1 + \tfrac{k_2 e^{-ik_2(2\hat{x})^{\frac{1}{2}}\beta - (k_3^2+k_2^2)\hat{x}}}{(k_2 - i|k_3|)}\Big[e^{ik_2(2\hat{x})^{\frac{1}{2}}\eta} - e^{-|k_3|(2\hat{x})^{\frac{1}{2}}\eta}\Big] \\ & + e^{-|k_3|(2\hat{x})^{\frac{1}{2}}\eta}\Big\{1 - \beta\Big[\mathrm{i}(k_2 + i|k_3|) + \tfrac{3}{4}|k_3|\Big]\sqrt{2\hat{x}}\Big\} - \bar{w}_c. \qquad (2.4.27)\end{aligned}$$

2.5 Eigensolution formulation: $G_\Lambda = O(1)$

2.5.1 Non-parallel eigenvalue problem

The initial boundary-value problem formulated in §2.3-§2.4 describes both the receptivity to FST and the evolution of the disturbance excited. As will be shown later, numerical solutions indicate that the disturbance exhibits exponentially growth that is characteristic of spatially growing eigenmodes. This prompts us to formulate a local eigenvalue problem for Görtler vortices. As usual, we seek a normal-mode solution

$$(\bar{u}, \bar{v}, \bar{w}, \bar{p}) = \Big[\tilde{u}(\eta), \tilde{v}(\eta), \tilde{w}(\eta), \tilde{p}(\eta)\Big] \exp\{\int^{\hat{x}} \sigma(\hat{x}) d\hat{x}\}, \qquad (2.5.1)$$

where σ is in general a complex quantity dependent on $\hat{x}$, with its real part representing the local growth rate. Substituting (2.5.1) into (2.4.9)–(2.4.12), and neglecting the streamwise variation of the eigenfunction, we obtain a set of ODEs. Upon introducing

$$\tilde{f} = \frac{\mathrm{d}\tilde{u}}{\mathrm{d}\eta}, \quad \tilde{g} = \frac{\mathrm{d}\tilde{w}}{\mathrm{d}\eta},$$

the resulting ODEs can be written as a first-order system,

$$\frac{\mathrm{d}\tilde{u}}{\mathrm{d}\eta} = \tilde{f}, \qquad (2.5.2)$$

$$\frac{\mathrm{d}\tilde{v}}{\mathrm{d}\eta} = -\sigma\tilde{u} - \tilde{w} + \frac{\eta}{2\hat{x}}\tilde{f}, \qquad (2.5.3)$$

$$\frac{\mathrm{d}\tilde{w}}{\mathrm{d}\eta} = \tilde{g}, \tag{2.5.4}$$

$$\frac{\mathrm{d}\tilde{f}}{\mathrm{d}\eta} = \left[(2\hat{x})(-i\hat{k}_1 + \sigma F' + k_3^2) - \eta F''\right]\tilde{u} + 2\hat{x}F''\tilde{v} - F\tilde{f}, \tag{2.5.5}$$

$$\frac{\mathrm{d}\tilde{p}}{\mathrm{d}\eta} = -\left[\sigma F - \frac{1}{2\hat{x}}(\eta F' - F) - \eta(-i\hat{k}_1 + \sigma F' + k_3^2)\right]\tilde{u} - \left[(2\hat{x})(-i\hat{k}_1 + \sigma F' + k_3^2) + F'\right]\tilde{v}$$
$$- F\tilde{w} + (\frac{1}{2\hat{x}} - \sigma)\tilde{f} - \tilde{g} - 2G_A F'\tilde{u}(2\hat{x})^{\frac{1}{2}}, \tag{2.5.6}$$

$$\frac{\mathrm{d}\tilde{g}}{\mathrm{d}\eta} = (2\hat{x})(-i\hat{k}_1 + \sigma F' + k_3^2)\tilde{w} + 2\hat{x}k_3^2\tilde{p} - F\tilde{g}. \tag{2.5.7}$$

Note that the normal velocities of the base flow and its streamwise derivative, $\partial V/\partial\hat{x}$, are included along with $\partial U/\partial\hat{x}$. Also, the normal mode is represented as $f(\eta)\exp\{\int^{\hat{x}}\sigma(\hat{x})d\hat{x}\}$, as opposed to $f(y)\exp\{\int^{\hat{x}}\sigma(\hat{x})d\hat{x}\}$ assumed in previous work. The present formulation will therefore be referred to as the η-based non-parallel theory in order to distinguish from the previous y-based non-parallel theory.

The system (2.5.2)-(2.5.7) along with the homogenous boundary conditions,

$$(\tilde{u},\tilde{v},\tilde{w}) = (0,0,0) \quad \text{at} \quad \eta = 0; \quad (\tilde{u},\tilde{v},\tilde{w},\tilde{p}) \to (0,0,0,0) \quad \text{as} \quad \eta \to \infty, \tag{2.5.8}$$

forms a local eigenvalue problem. The far-field boundary conditions may be replaced by

$$\tilde{u} \to 0, \quad \left[\frac{\mathrm{d}}{\mathrm{d}\eta} + |k_3|(2\hat{x})^{1/2}\right](\tilde{v},\,\tilde{w},\,\tilde{p}) \to 0. \tag{2.5.9}$$

2.5.2 Parallel-flow approximation

The non-parallel flow formulation can be reduced to a parallel formulation if we take the base flow velocity to be $\{F'(\eta),0,0\}$ and $\frac{\partial U}{\partial\hat{x}} = 0$. The governing equations then consist of

$$\frac{\mathrm{d}\tilde{u}}{\mathrm{d}\eta} = \tilde{f}, \tag{2.5.10}$$

$$\frac{\mathrm{d}\tilde{v}}{\mathrm{d}\eta} = -\sigma\tilde{u} - \tilde{w}, \tag{2.5.11}$$

$$\frac{\mathrm{d}\tilde{w}}{\mathrm{d}\eta} = \tilde{g}, \tag{2.5.12}$$

$$\frac{\mathrm{d}\tilde{f}}{\mathrm{d}\eta} = (2\hat{x})(-i\hat{k}_1 + \sigma F' + k_3^2)\tilde{u} + (2\hat{x})F''\tilde{v}, \tag{2.5.13}$$

$$\frac{\mathrm{d}\tilde{p}}{\mathrm{d}\eta} = -(2\hat{x})(-i\hat{k}_1 + \sigma F' + k_3^2)\tilde{v} - \sigma\tilde{f} - \tilde{g} - 2G_\Lambda F'\tilde{u}(2\hat{x})^{\frac{1}{2}}, \tag{2.5.14}$$

$$\frac{\mathrm{d}\tilde{g}}{\mathrm{d}\eta} = (2\hat{x})(-i\hat{k}_1 + \sigma F' + k_3^2)\tilde{w} + 2\hat{x}k_3^2\tilde{p}. \tag{2.5.15}$$

2.6 Asymptotic analysis for $G_\Lambda \gg O(1)$

It has been recognized since the work of Hall (1983) that any local eigenvalue formulation amounts to an *ad-hoc* approximation when the Görtler number is of order one. An eigenvalue approach is tenable only when the Görtler number is large. In most previous work, analysis of this kind was performed at fixed streamwise location for Görtler vortices of different wavelength. In the following, we will consider instead downstream development of Görtler vortices with a fixed physical wavelength Λ. In typical experimental situations $G_\Lambda = O(10^2)$ or larger, and so we may assume that $G_\Lambda \gg 1$, and map out the distinct regimes that the disturbance evolves through.

2.6.1 Pre-modal stage I: $\hat{x} = O(G_\Lambda^{-2/3})$

When $G_\Lambda \gg 1$, the induced perturbation evolves through two pre-modal stages in the region $\hat{x} \ll 1$.

Since $\bar{w}$ remains $O(1)$ as $\hat{x} \ll 1$ and $\eta = O(1)$, the continuity equation (2.4.9) implies that

$$\frac{\partial\bar{u}}{\partial\hat{x}} = O(1), \qquad \text{i.e.} \quad \bar{u} = O(\hat{x}), \quad \text{and} \quad \bar{v} = O(1).$$

From the normal momentum equation (2.4.11), the centrifugal force

$$G_\Lambda F'\frac{\bar{u}}{\sqrt{2\hat{x}}} \sim G_\Lambda\hat{x}^{\frac{1}{2}},$$

while the inertia and normal pressure gradient are both of $O(\frac{1}{\hat{x}})$. Thus, the centrifugal effect enters the play when

$$G_\Lambda\hat{x}^{\frac{1}{2}} = O(\frac{1}{\hat{x}}), \qquad \text{i.e.} \quad \text{when} \quad \hat{x} = O(G_\Lambda^{-\frac{2}{3}}),$$

but is negligible when $\hat{x} \ll G_\Lambda^{-\frac{2}{3}}$.

The scaling deduced above suggests the introduction of

$$x^\dagger = G_\Lambda^{\frac{2}{3}}\hat{x}, \quad u^\dagger = G_\Lambda^{\frac{2}{3}}\bar{u}. \tag{2.6.1}$$

It follows that

$$\frac{\partial}{\partial \hat{x}} = O(G_\Lambda^{\frac{2}{3}}\frac{\partial}{\partial x^\dagger}). \tag{2.6.2}$$

Substitution of (2.6.1) and (2.6.2) into (2.4.9)–(2.4.12) yields

$$\left.\begin{aligned} \frac{\partial u^\dagger}{\partial x^\dagger} - \frac{\eta}{2x^\dagger}\frac{\partial u^\dagger}{\partial \eta} + \frac{\partial \bar{v}}{\partial \eta} + \bar{w} = 0 \\ F'\frac{\partial u^\dagger}{\partial x^\dagger} - \frac{F}{2x^\dagger}\frac{\partial u^\dagger}{\partial \eta} - \frac{\eta F''}{2x^\dagger}u^\dagger + F''\bar{v} = \frac{1}{2x^\dagger}\frac{\partial^2 u^\dagger}{\partial \eta^2} \\ F'\frac{\partial \bar{w}}{\partial x^\dagger} - \frac{F}{2x^\dagger}\frac{\partial \bar{w}}{\partial \eta} = \frac{1}{2x^\dagger}\frac{\partial^2 \bar{w}}{\partial \eta^2} \end{aligned}\right\}, \tag{2.6.3}$$

and

$$\frac{1}{2x^\dagger}\frac{\partial^2 \bar{v}}{\partial \eta^2} + F'\frac{\partial \bar{v}}{\partial x^\dagger} - \frac{F}{2x^\dagger}\frac{\partial \bar{v}}{\partial \eta} + 2F'u^\dagger(\frac{1}{2x^\dagger})^{\frac{1}{2}} = \frac{1}{2x^\dagger}\frac{\partial \bar{p}}{\partial \eta}. \tag{2.6.4}$$

We call this regime, which operates in the region over $O(G_\Lambda^{-\frac{2}{3}}R_\Lambda\Lambda)$ distances to the leading edge, the pre-modal stage I. The induced velocity field is governed by the quasi-steady boundary-layer equations (2.6.3), and the pressure can be solved passively from the transverse momentum equation (2.6.4). Non-parallelism is at leading order, and the velocity response to FST remains identical to the flat-plate case. This regime is distinguished only in the sense that the centrifugal force influences the pressure distribution across the boundary layer, as is indicated by (2.6.4).

2.6.2 Pre-modal stage II: $\hat{x} = O(G_\Lambda^{-2/5})$

Since $\bar{u} \sim \hat{x}$, the balance in the normal momentum equation suggests that $\bar{p} = O(G_\Lambda \hat{x}^{\frac{3}{2}})$ for $\eta = O(1)$. The induced pressure affects the spanwise momentum equation (2.4.12) when

$$F'\frac{\partial \bar{w}}{\partial \hat{x}} = O(G_\Lambda \hat{x}^{\frac{3}{2}}), \quad \text{i.e. when } \hat{x} = O(G_\Lambda^{-\frac{2}{5}}),$$

and the perturbation enters a new regime. The scaling argument above suggests that we introduce

$$\breve{x} = G_\Lambda^{\frac{2}{5}} \hat{x}, \tag{2.6.5}$$

and write the solution for $\eta = O(1)$ as

$$\bar{u} = G_\Lambda^{-\frac{2}{5}} \Big(\breve{u} + O(G_\Lambda^{-1/5}) \Big), \quad \bar{p} = G_\Lambda^{\frac{2}{5}} \Big(\breve{p} + O(G_\Lambda^{-1/5}) \Big). \tag{2.6.6}$$

Inserting these into (2.4.9)–(2.4.12), we obtain

$$\frac{\partial \breve{u}}{\partial \breve{x}} - \frac{\eta}{2\breve{x}} \frac{\partial \breve{u}}{\partial \eta} + \frac{\partial \bar{v}}{\partial \eta} + \bar{w} = 0, \tag{2.6.7}$$

$$F' \frac{\partial \breve{u}}{\partial \breve{x}} - \frac{F}{2\breve{x}} \frac{\partial \breve{u}}{\partial \eta} - \frac{\eta F''}{2\breve{x}} \breve{u} + F'' \bar{v} = \frac{1}{2\breve{x}} \frac{\partial^2 \breve{u}}{\partial \eta^2}, \tag{2.6.8}$$

$$\frac{\partial \breve{p}}{\partial \eta} = -2\sqrt{2\breve{x}} F' \breve{u}, \tag{2.6.9}$$

$$F' \frac{\partial \bar{w}}{\partial \breve{x}} - \frac{F}{2\breve{x}} \frac{\partial \bar{w}}{\partial \eta} = k_3^2 \breve{p} + \frac{1}{2\breve{x}} \frac{\partial^2 \bar{w}}{\partial \eta^2}. \tag{2.6.10}$$

Since the non-parallel-flow effect appears at leading order, the regime is termed as pre-modal stage II. It is distinguished in that the pressure is fully coupled with the velocity field. As a result, Görtler instability starts to operate. We demonstrate this by showing that as $\breve{x} \gg 1$, the system (2.6.7)-(2.6.10) admits asymptotic eigen solutions of the form

$$(\breve{u}, \bar{v}, \bar{w}, \breve{p}) = \breve{x}^\gamma \left\{ \Big(\breve{x}^{-\alpha+1} U_E(\eta), V_E(\eta), W_E(\eta), \breve{x}^{-\alpha+\frac{3}{2}} P_E(\eta) \Big) + \ldots \right\} \mathrm{e}^{\breve{\sigma}(\breve{x})}, \tag{2.6.11}$$

where $\breve{\sigma}(\breve{x})$ expands as

$$\breve{\sigma} = \breve{\sigma}_0 \breve{x}^\alpha + \ldots, \tag{2.6.12}$$

with $\breve{\sigma}_0$, α, and γ being constants to be found. Inserting (2.6.11) with (2.6.12) into (2.6.10) yields at leading order, $\breve{x}^{\gamma+\alpha-1} \alpha \breve{\sigma}_0 F' W_E = k_3^2 \breve{x}^{\gamma-\alpha+\frac{3}{2}} P_E$, from which it may be deduced that

$$\alpha = 5/4, \tag{2.6.13}$$

$$\alpha \breve{\sigma}_0 F' W_E = k_3^2 P_E.$$

Substituting (2.6.11) into (2.6.7)–(2.6.9), we obtain at leading order

$$\alpha\breve{\sigma}_0 U_E + V_{E,\eta} + W_E = 0, \qquad \alpha\breve{\sigma}_0 F' U_E + F'' V_E = 0, \quad P_{E,\eta} = -2\sqrt{2}F'U_E.$$

Elimination of U_E, W_E, and P_E leads to the equation for V_E,

$$\frac{\partial^2 V_E}{\partial \eta^2} - \left[\frac{F'''}{F'} - \frac{2\sqrt{2}k_3^2 F''}{(\alpha\breve{\sigma}_0)^2 F'}\right] V_E = 0. \tag{2.6.14}$$

Since $F' = F''' = 0$ but $F'' \neq 0$ at $\eta = 0$, $\eta = 0$ is a regular singular point of the equation. The local solution can be constructed as a Fröbenus series

$$V_E = a(\eta + \tfrac{1}{2}\eta^2) + b\Big[1 - \eta^2 + \ldots + (\eta + \tfrac{1}{2}\eta^2)\ln\eta\Big].$$

We take $b = 0$ so that the no-penetration condition,

$$V_E(0) = 0, \tag{2.6.15}$$

is satisfied. Without losing generality, we set $a = 1$, which amounts to normalising the eigenfunction such that

$$V_{E,\eta}(0) = 1. \tag{2.6.16}$$

On the other hand, as $\eta \to \infty$, $\partial^2 V_E/\partial\eta^2 \to 0$ (see (2.6.14)). In order to keep V_E bounded, the boundary condition imposed is

$$V_{E,\eta} \to 0 \ \text{ as } \ \eta \to \infty. \tag{2.6.17}$$

With the normalisation (2.6.16), it follows that $U_E \to -1/(\alpha\breve{\sigma}_0)$ as $\eta \to 0$. The slip velocity is reduced to zero across a viscous sublayer, the width of which is $\eta \sim \breve{x}^{-5/12}$, as can be deduced by balancing the convection and diffusion in the momentum equations. We thus introduce the local transverse coordinate

$$\zeta = (2\lambda\alpha\breve{\sigma}_0)^{1/3}\breve{x}^{5/12}\eta.$$

For $\zeta = O(1)$, the viscous solution expands as

$$(\breve{u}, v, w, \breve{p}) = \breve{x}^{\gamma} \left\{ \left(\breve{x}^{-\frac{1}{4}} u_s(\zeta), \breve{x}^{-\frac{5}{12}} (2\lambda\alpha\breve{\sigma}_0)^{-1/3} v_s, w_s, (2\lambda\alpha\breve{\sigma}_0)^{-1/3} \breve{x}^{-\frac{1}{6}} p_s \right) + \ldots \right\} \mathrm{e}^{\breve{\sigma}(\breve{x})}, \tag{2.6.18}$$

where u_s, v_s, w_s and p_s functions of ζ. Their governing equations, obtained by inserting (2.6.18) into (2.6.7)–(2.6.9), are

$$\alpha\breve{\sigma}_0 u_s + v_{s,\zeta} + w_s = 0, \quad \alpha\breve{\sigma}_0(\zeta u_s - u_{s,\zeta\zeta}) + v_s = 0, \quad \alpha\breve{\sigma}_0(\zeta w_s - w_{s,\zeta\zeta}) = k_3^2 p_s,$$

and $p_{s,\zeta} = 0$. Elimination of u_s and w_s among these equations gives

$$(\frac{\mathrm{d}^2}{\mathrm{d}\zeta^2} - \zeta) v_{s,\zeta\zeta} = 0, \tag{2.6.19}$$

for v_s, while the boundary conditions, $u_s(0) = v_s(0) = 0$, and the matching requirement correspond to

$$v_{s,\zeta\zeta\zeta}(0) = k_3^2 p_s / \alpha\breve{\sigma}_0, \quad v_{s,\zeta}(0) = 0; \qquad v_{s,\zeta} \to 1 \quad \text{as} \quad \zeta \to \infty.$$

The solution is

$$v_s = c_0 \int_0^{\zeta} (\zeta - \tilde{\zeta}) Ai(\tilde{\zeta}) \mathrm{d}\tilde{\zeta}, \quad \text{with} \quad c_0 = 1 / \int_0^{\infty} Ai(\zeta) \mathrm{d}\zeta = 3, \tag{2.6.20}$$

where Ai denotes the Airy function. The solution to the pressure is

$$p_s = \frac{\alpha\breve{\sigma}_0}{k_3^2} c_0 Ai'(0). \tag{2.6.21}$$

It follows that as $\zeta \to \infty$,

$$v_s \to \zeta - c_0 \int_0^{\infty} \zeta Ai(\zeta) \mathrm{d}\zeta \equiv \zeta + v_\infty.$$

The transpiration velocity, v_∞, induces a correction of $O(\breve{x}^{-5/12})$ in the core of the boundary layer; see (2.6.18). It may be further deduced that the expansions (2.6.11)-(2.6.12) should proceed as

$$\breve{\sigma} = \breve{\sigma}_0 \breve{x}^{5/4} + \breve{\sigma}_1 \breve{x}^{5/6} + \breve{\sigma}_2 \breve{x}^{5/12}, \tag{2.6.22}$$

$$(\breve{u},\bar{v},\bar{w},\breve{p})=\breve{x}^{\gamma}\left\{\left(\breve{x}^{-1/4}U_E(\eta),V_E(\eta),W_E(\eta),\breve{x}^{1/4}P_E(\eta)\right)\right.$$
$$\left.+\sum_{n=1}^{3}\breve{x}^{-\frac{5n}{12}}\left(\breve{x}^{-1/4}U_E^{(n)}(\eta),V_E^{(n)}(\eta),W_E^{(n)}(\eta),\breve{x}^{1/4}P_E^{(n)}(\eta)\right)\right\}\mathrm{e}^{\breve{\sigma}(\breve{x})}. \tag{2.6.23}$$

The lowest-order correction satisfies a system of inhomogeneous equations,

$$\left.\begin{aligned}\alpha\breve{\sigma}_0U_E^{(1)}+V_{E,\eta}^{(1)}+W_E^{(1)}&=-\tfrac{5}{6}\breve{\sigma}_1U_E,\\ \alpha\breve{\sigma}_0F'U_E^{(1)}+F''V_E^{(1)}&=-\tfrac{5}{6}\breve{\sigma}_1F'U_E,\\ P_{E,\eta}^{(1)}+2\sqrt{2}F'U_E^{(1)}&=0,\\ \alpha\breve{\sigma}_0F'W_E^{(1)}-k_3^2P_E^{(1)}&=-\tfrac{5}{6}\breve{\sigma}_1F'W_E.\end{aligned}\right\} \tag{2.6.24}$$

These equations can be reduced to

$$\frac{\partial^2V_E^{(1)}}{\partial\eta^2}-\left[\frac{F'''}{F'}-\frac{2\sqrt{2}k_3^2F''}{(\alpha\breve{\sigma}_0)^2F'}\right]V_E^{(1)}=\frac{10\sqrt{2}k_3^2\breve{\sigma}_1}{3(\alpha\hat{\sigma}_0)^3}F''V_E/F'. \tag{2.6.25}$$

The boundary conditions are

$$V_E^{(1)}=(2\lambda\alpha\breve{\sigma}_0)^{-1/3}v_\infty\ \text{ at }\ \eta=0;\qquad V_{E,\eta}^{(1)}\to0\ \text{ as }\ \eta\to\infty.$$

Imposing the solvability condition on (2.6.25), we find that

$$\frac{10\sqrt{2}k_3^2\breve{\sigma}_1}{3(\alpha\breve{\sigma}_0)^3}\int_0^\infty F''V_E^2/F'\mathrm{d}\eta=(2\lambda\alpha\breve{\sigma}_0)^{-1/3}v_\infty, \tag{2.6.26}$$

which determines $\breve{\sigma}_1$. The higher-order corrections, $\breve{\sigma}_2$ and γ, can be obtained by considering $V_E^{(2)}$ and $V_E^{(3)}$ respectively.

It can be deduced that U_E, W_E and P_E all decay exponentially as $\eta\to\infty$, but V_E tends to a constant, indicating that the scaling (2.6.6) and the system (2.6.7)-(2.6.10) are not uniformly valid for all η. An outer layer must be introduced, where the inertia in the normal momentum equation, negligible when $\eta=O(1)$ (see (2.6.9)), comes into play. A scaling argument suggests that the width of this layer corresponds to $\eta\sim G_\Lambda^{1/5}/\sqrt{2\breve{x}}$, and

hence we introduce

$$y_o = G_\Lambda^{-1/5}\sqrt{2\breve{x}}\,\eta.$$

For $y_o = O(1)$, the solution expands as

$$(\bar{u},\bar{v},\bar{w},\bar{p}) = (G_\Lambda^{-3/5}\bar{u}_o, \bar{v}_o, G_\Lambda^{-1/5}\bar{w}_o, G_\Lambda^{1/5}\bar{p}_o). \tag{2.6.27}$$

It follows from the streamwise momentum equation (2.4.10) that $\partial\bar{u}_o/\partial y_o = 0$, and so $\bar{u}_o = 0$ in order to satisfies the boundary layer condition at the infinity. Substitution of (2.6.27) into (2.4.9) and (2.4.11)-(2.4.12) shows that

$$\sqrt{2\breve{x}}\frac{\partial\bar{v}_o}{\partial y_o} + \bar{w}_o = 0, \quad \frac{\partial\bar{v}_o}{\partial\breve{x}} + \frac{\bar{v}_o}{2\breve{x}} = -\frac{1}{\sqrt{2\breve{x}}}\frac{\partial\bar{p}_o}{\partial y_o}, \quad \frac{\partial\bar{w}_o}{\partial\breve{x}} = k_3^2\bar{p}_o. \tag{2.6.28}$$

The solution is found as

$$\bar{p}_o = g_o'(\breve{x})\,\mathrm{e}^{-|k_3|y_o}, \quad \bar{w}_o = k_3^2 g_o(\breve{x})\,\mathrm{e}^{-|k_3|y_o}, \quad \bar{v}_0 = \frac{|k_3|}{\sqrt{2\breve{x}}}g_o(\breve{x})\,\mathrm{e}^{-|k_3|y_o}\,.$$

The function g_o is found by matching with the main-deck solution as

$$g_o(\breve{x}) = \breve{x}^{\gamma+\frac{1}{2}}\Big(V_{E,\infty} + O(\breve{x}^{-5/12})\Big)e^{\breve{\sigma}(\breve{x})}, \tag{2.6.29}$$

where $V_{E,\infty} = \lim_{\eta\to\infty} V_E(\eta)$, which is determined once the eigenvalue problem, defined by (2.6.14) with (2.6.15) and (2.6.17), is solved.

The asymptotic eigenvalue problem, (2.6.14) with (2.6.15)–(2.6.17), is solved by a shooting method. A countable set of asymptotic eigen modes exist, and for the first four we find that $\breve{\sigma}_0 = 0.8209$, 0.5143, 0.3781 and 0.2996 while the viscous correction $\breve{\sigma}_1 = -1.6614$, -1.8047, -1.8122, -1.6729. The role of the asymptotic eigen modes in the receptivity of Görtler instability is analogous to that of the first Lam-Rott mode in the Tollmien-Schlichting instability (Goldstein 1983): they represent the earliest intrinsic characteristic motion that develops from the forced motion, and then evolves into fully fledged local eigen modes, i.e. Görtler vortices in the present case. On the other hand, unlike the damped Lam-Rott mode, the present eigen modes are unstable. Consequently, Görtler vortices are much more receptive to FST than Tollmien-Schlichting waves.

2.6.3 Inviscid regime: $\hat{x} = O(1)$

In the region where $\breve{x} = O(G_\Lambda^{2/5})$, i.e. $\hat{x} = O(1)$, the outer region merges with the main layer, and the spanwise wavelength becomes comparable with the local boundary-layer thickness, so that $G_\theta = O(G_\Lambda)$. As was suggested by (2.6.22)–(2.6.23), the solution now takes the WKBJ form

$$\begin{aligned}(\bar{u},\bar{v},\bar{w},\bar{p}) = \Big[&\Big(G_\Lambda^{-\frac{1}{2}} u_0(\hat{x},\eta), v_0(\hat{x},\eta), w_0(\hat{x},\eta), G_\Lambda^{\frac{1}{2}} p_0(\hat{x},\eta)\Big) \\ &+ G_\Lambda^{-\frac{1}{6}} \Big(G_\Lambda^{-\frac{1}{2}} u_1(\hat{x},\eta), v_1(\hat{x},\eta), w_1(\hat{x},\eta), G_\Lambda^{\frac{1}{2}} p_1(\hat{x},\eta)\Big) + \ldots \Big] E,\end{aligned} \tag{2.6.30}$$

where we have put

$$E = \exp\Big\{ G_\Lambda^{\frac{1}{2}} \int^{\hat{x}} \hat{\sigma}(\hat{x}) d\hat{x} \Big\} \tag{2.6.31}$$

with $\hat{\sigma}$ being expanded as

$$\hat{\sigma} = \hat{\sigma}_0 + G_\Lambda^{-\frac{1}{6}} \hat{\sigma}_1 + \ldots. \tag{2.6.32}$$

As will be shown later, the $O(G_\Lambda^{-\frac{1}{6}})$ correction is contributed by the viscous effect near the wall. Substituting (2.6.30) and (2.6.32) into (2.4.9)-(2.4.12), we obtain

$$\left.\begin{aligned} \hat{\sigma}_0 u_0 + \frac{\partial v_0}{\partial \eta} + w_0 &= 0, \\ \hat{\sigma}_0 F' u_0 + F'' v_0 = 0, \quad \hat{\sigma}_0 F' v_0 + \frac{2F'}{\sqrt{2\hat{x}}} u_0 &= -\frac{1}{2\hat{x}} \frac{\partial p_0}{\partial \eta}, \quad \hat{\sigma}_0 F' w_0 = k_3^2 p_0. \end{aligned}\right\} \tag{2.6.33}$$

These equations can be reduce to the equation for v_0,

$$\frac{\partial^2 v_0}{\partial \eta^2} - \left[\frac{F'''}{F'} + 2\hat{x} k_3^2 - \frac{2\sqrt{2\hat{x}} k_3^2 F''}{\hat{\sigma}_0^2 F'} \right] v_0 = 0, \tag{2.6.34}$$

subject to the boundary conditions:

$$v_0 = 0 \ \text{ at } \ \eta = 0; \qquad v_0 \to 0 \ \text{ as } \ \eta \to \infty. \tag{2.6.35}$$

The eigenvalue problem (2.6.34)-(2.6.35) corresponds to the inviscid limit of Görtler formulation. The eigenfunction is normalised such that

$$v_{0,\eta}(0) = 1. \tag{2.6.36}$$

The eigenvalue problem has an exact solution (Denier et al. 1991)

$$v_0 \sim F' \, \mathrm{e}^{-k_3\sqrt{2\hat{x}}\,\eta}, \qquad \hat{\sigma}_0 = \sqrt{k_3}, \tag{2.6.37}$$

for an arbitrary $\hat{x}$. Further numerical study of (2.6.34)–(2.6.35) shows that there exist infinitely many modes, of which (2.6.37) is the most unstable one.

When $\hat{x} \to 0$, the dominant balance in the equation (2.6.34) indicates that $\hat{\sigma}_0$ scales with $\hat{x}$ as

$$\sigma_0 \sim \hat{x}^{\frac{1}{4}}, \quad \text{so that} \quad \int^{\hat{x}} \hat{\sigma}(\hat{x}) d\hat{x} \sim \frac{4}{5}\hat{\sigma}_0 \hat{x}^{\frac{5}{4}}, \tag{2.6.38}$$

which is consistent with the large $\breve{x}$-limit of the asymptotic solution found in §2.6.2. Interestingly, the exact solution does not follow this scaling. As a result, this mode, though most unstable, is not excited by FST.

Denier et al. (1991) considered the limit $k_3 \gg 1$ for a fixed $\hat{x}$, and showed that the eigen modes become trapped in a wall layer. Since the limit $k_3 \gg 1$ for a fixed $\hat{x}$ is equivalent to the limit $\hat{x} \gg 1$ for a fixed k_3, the structure of the eigenfunction holds true for the latter. The simplified equation can be obtained by using the near-wall approximation for $F \approx \frac{1}{2}\lambda\eta^2 + O(\eta^4)$ in (2.6.34), leading to

$$\frac{\partial^2 v_0}{\partial \eta^2} - [2\hat{x} - \frac{2\sqrt{2\hat{x}}}{\hat{\sigma}_0^2 \eta}] k_3^2 v_0 = 0. \tag{2.6.39}$$

The dependence on $\hat{x}$ may be eliminated by introducing the substitutions $\hat{\zeta} = \sqrt{2\hat{x}}\,\eta = O(1)$ and $\hat{v}_0 = \sqrt{2\hat{x}}\, v_0$, in terms of which, equations (2.6.39) and (2.6.36) become

$$\frac{\partial^2 \hat{v}_0}{\partial \hat{\zeta}^2} - [1 - \frac{2}{\hat{\zeta}\hat{\sigma}_0^2}] k_3^2 \hat{v}_0 = 0, \quad \hat{v}_{0,\hat{\zeta}}(0) = 1. \tag{2.6.40}$$

Equation (2.6.40) is a form of Whittaker's equation, and it has a countable set of eigenvalues (Denier et al. 1991)

$$\hat{\sigma}_0 = \sqrt{k_3/n} \quad (n = 1, 2, 3, \ldots). \tag{2.6.41}$$

For $n = 1$, $\hat{v}_0 \sim \mathrm{e}^{-k_3\sqrt{2\hat{x}}\,\eta}$.

Similar to the asymptotic eigen solution, a viscous sublayer must be introduced to re-

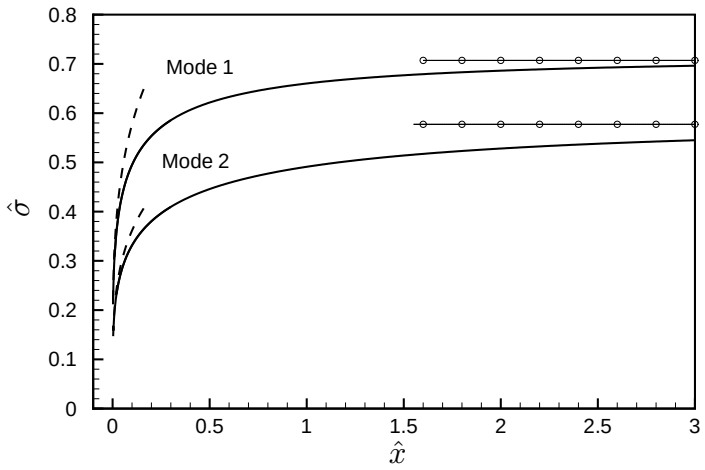


Figure 2.3: Matching of different regimes. Dashed lines: asymptotic eigen mode; solid lines: inviscid modes; dotted lines: the large-$\hat{x}$ limit of inviscid modes, i.e. (2.6.41) with $n = 2, 3$.

duce the slip velocity to zero. The normal velocity may be written as

$$\bar{v} = G_{\Lambda}^{-1/6}(2\lambda\hat{\sigma}_0\hat{x})^{-1/3}\bar{v}_s(\zeta), \quad \zeta = G_{\Lambda}^{1/6}(2\lambda\hat{\sigma}_0\hat{x})^{1/3}\eta,$$

with $\bar{v}_s$ satisfying the equation (2.6.19) and has the solution (2.6.20). The viscous effect induces a transpiration velocity, which in turn forces an $O(G_{\Lambda}^{-1/6})$ correction in the main layer; see (2.6.30). The equation for v_1 is

$$\frac{\partial^2 v_1}{\partial\eta^2} - \left[\frac{F'''}{F'} + 2\hat{x}k_3^2 - \frac{2\sqrt{2\hat{x}}k_3^2F''}{\hat{\sigma}_0^2F'}\right]v_1 = \frac{4\sqrt{2\hat{x}}k_3^2\hat{\sigma}_1}{\hat{\sigma}_0^3}\frac{F''v_0}{F'}, \tag{2.6.42}$$

subject to the boundary condition

$$v_1(0) = (2\lambda\hat{\sigma}_0\hat{x})^{-1/3}v_\infty, \quad v_{1,\eta} \to 0 \ \text{ as } \ \eta \to \infty.$$

From the solvability condition on (2.6.42), it follows that

$$(2\lambda\hat{\sigma}_0\hat{x})^{-1/3}v_\infty = \frac{4\sqrt{2\hat{x}}k_3^2\hat{\sigma}_1}{\hat{\sigma}_0^3}\int_0^\infty \frac{F''v_0^2}{F'}\mathrm{d}\eta \to \frac{2\sqrt{2}k_3^2\hat{\sigma}_1}{\hat{\sigma}_0^3}\hat{x}^{-1/2}\int_0^\infty \frac{\hat{v}_0^2}{\hat{\zeta}}\mathrm{d}\hat{\zeta} \quad \text{as} \quad \hat{x} \to \infty.$$

Note that $\hat{\sigma}_1 \sim \hat{x}^{1/6}$ as $\hat{x} \to \infty$, use of which in (2.6.32) suggests that the viscous correction to the growth rate becomes leading order when $\hat{x} = O(G_{\Lambda})$.

The inviscid eigenvalue problem (2.6.34)-(2.6.35) is solved by a shooting method. A countable number of inviscid modes are also identified, among which (2.6.37) is the most unstable one. The matching between different regimes is demonstrated in figure 2.3. All inviscid modes evolve from the upstream asymptotic modes, except the most unstable exact inviscid solution (2.6.37), which cannot be traced back to any of asymptotic modes.

2.6.4 Most unstable regime: $\hat{x} = O(G_\Lambda)$

As $\hat{x}$ increases, the wall layer in which eigen modes concentrate shrinks and becomes viscous when $\hat{x} \sim O(G_\Lambda)$. This new regime may be described by the variables

$$\tilde{x} = \hat{x}/G_\Lambda \sim O(1), \quad \tilde{\zeta} = \sqrt{2\hat{x}}\,\eta = G_\Lambda^{\frac{1}{2}}\sqrt{2\tilde{x}}\,\eta.$$

The eigen solution ($\bar{u}$, $\bar{v}$, $\bar{w}$, $\bar{p}$) expands as

$$(\bar{u},\, \bar{v},\, \bar{w},\, \bar{p}) = \Big[\tilde{u}_0(\tilde{x},\tilde{\zeta}),\, \tilde{v}_0(\tilde{x},\tilde{\zeta}),\, G_\Lambda^{\frac{1}{2}}\tilde{w}_0(\tilde{x},\tilde{\zeta}),\, G_\Lambda^{\frac{1}{2}}\tilde{p}_0(\tilde{x},\tilde{\zeta})\Big]E + \ldots, \tag{2.6.43}$$

where E is defined in (2.6.31) but can be rewritten as

$$E = \exp\Big\{G_\Lambda^{\frac{3}{2}}\int^{\tilde{x}}\hat{\sigma}(\tilde{x})d\tilde{x}\Big\}, \tag{2.6.44}$$

in terms of $\tilde{x}$. Substituting (2.6.43) into (2.4.9)–(2.4.12), we obtain at leading order

$$\left.\begin{aligned}
\hat{\sigma}\tilde{u}_0 + \sqrt{2\tilde{x}}\frac{\partial\tilde{v}_0}{\partial\tilde{\zeta}} + \tilde{w}_0 &= 0,\\
-i\hat{k}_1\tilde{u}_0 + \frac{\lambda\tilde{\zeta}}{\sqrt{2\tilde{x}}}\hat{\sigma}\tilde{u}_0 + \lambda\tilde{v}_0 &= \frac{\partial^2\tilde{u}_0}{\partial\tilde{\zeta}^2} - k_3^2\tilde{u}_0,\\
-i\hat{k}_1\tilde{v}_0 + \frac{\lambda\tilde{\zeta}}{\sqrt{2\tilde{x}}}\hat{\sigma}\tilde{v}_0 + \frac{\lambda\tilde{\zeta}}{\tilde{x}}\tilde{u}_0 &= -\frac{1}{\sqrt{2\tilde{x}}}\frac{\partial\tilde{p}_0}{\partial\tilde{\zeta}} + \frac{\partial^2\tilde{v}_0}{\partial\tilde{\zeta}^2} - k_3^2\tilde{v}_0,\\
-i\hat{k}_1\tilde{w}_0 + \frac{\lambda\tilde{\zeta}}{\sqrt{2\tilde{x}}}\hat{\sigma}\tilde{w}_0 &= k_3^2\tilde{p}_0 + \frac{\partial^2\tilde{w}_0}{\partial\tilde{\zeta}^2} - k_3^2\tilde{w}_0.
\end{aligned}\right\} \tag{2.6.45}$$

Elimination of $\tilde{w}_0$ and $\tilde{p}_0$ among these equations yields

$$\left.\begin{aligned}(\frac{\partial^2}{\partial\tilde{\zeta}^2}-\frac{\lambda\tilde{\zeta}}{\sqrt{2\tilde{x}}}\hat{\sigma}-k_3^2+i\hat{k}_1)(\frac{\partial^2}{\partial\tilde{\zeta}^2}-k_3^2)\tilde{v}_0 &= -\frac{\lambda\tilde{\zeta}}{\tilde{x}}k_3^2\tilde{u}_0,\\ (\frac{\partial^2}{\partial\tilde{\zeta}^2}-\frac{\lambda\tilde{\zeta}}{\sqrt{2\tilde{x}}}\hat{\sigma}-k_3^2+i\hat{k}_1)\tilde{u}_0 &= \lambda\tilde{v}_0.\end{aligned}\right\} \tag{2.6.46}$$

The boundary conditions are

$$\tilde{u}_0=\tilde{v}_0=0 \text{ at } \tilde{\zeta}=0; \quad \tilde{u}_0\to 0, \quad \tilde{v}_0\to 0 \text{ as } \tilde{\zeta}\to\infty. \tag{2.6.47}$$

For $\tilde{x}=O(1)$, the local boundary-layer thickness

$$\delta=(\nu x^*/U_\infty)^{\frac{1}{2}}=G_\Lambda^{\frac{1}{2}}\Lambda\tilde{x}^{\frac{1}{2}}, \quad \text{i.e.} \quad \delta/\Lambda\sim G_\Lambda^{\frac{1}{2}},$$

and the Görtler number defined in Denier et al. (1991) is

$$G_H=O(G_\theta^2)=O(G_\Lambda^{\frac{5}{2}}\tilde{x}^{\frac{3}{2}}).$$

Thus the spanwise wavenumber non-dimensionalised by δ is

$$\delta/\Lambda=O(G_H^{\frac{1}{5}}).$$

As is indicated by (2.6.44), the growth rate normalised by x^* is of $O(G_\Lambda^{\frac{3}{2}})=O(G_H^{\frac{3}{5}})=O(G_\theta^{\frac{6}{5}})$. Therefore, the present regime corresponds to the most unstable regime of Görtler vortices identified by Denier et al. (1991) and Timoshin (1990). The present formulation consists of a generalization to include the unsteadiness. It may be worthy noting that the growth rate non-dimensionalised by x^* acquires different orders of magnitude in different regimes. However, the growth rate normalised by the same reference length, Λ say, remains of the same order of magnitude, namely

$$\sigma^*\Lambda=O(G_\Lambda^{\frac{1}{2}}/R_\Lambda)=O(\sqrt{\Lambda/r_0^*}), \tag{2.6.48}$$

throughout the inviscid and the most unstable regimes.

Further downstream, when

$$\tilde{x} = O(G_\Lambda), \qquad \delta/\Lambda = O(G_H^{\frac{1}{4}}), \tag{2.6.49}$$

the perturbation enters the right-hand branch regime, in which Görtler vortices attenuate and finally decay (Hall 1982).

2.7 Numerical methods

2.7.1 Numerical method for the initial-boundary-value problem

For computational purpose, it is convenient to write $\bar{u} = 2\hat{x}\bar{\bar{u}}$. Then setting

$$\frac{\partial \bar{\bar{u}}}{\partial \eta} = \bar{f}, \quad \frac{\partial \bar{w}}{\partial \eta} = \bar{g},$$

equations (2.4.9)–(2.4.12) is recast as a system of six first-order partial differential equations, which may be written in the matrix form

$$\frac{\partial \mathbf{U}}{\partial \eta} = c_0 \mathbf{U} + c_1 \frac{\partial \mathbf{U}}{\partial \hat{x}}, \tag{2.7.1}$$

where $\mathbf{U} = \{\bar{\bar{u}}, \bar{v}, \bar{w}, \bar{f}, \bar{p}, \bar{g}\}^T$, c_0 and c_1 are 6×6 coefficient matrices,

$$c_0 = \begin{pmatrix} 0 & 0 & 0 & 1 & 0 & 0 \\ -2 & 0 & -1 & \eta & 0 & 0 \\ 0 & 0 & 0 & 0 & 0 & 1 \\ 2\hat{x}K + 2F' - \eta F'' & F'' & 0 & -F & 0 & 0 \\ K_0 & -2\hat{x}K + F' & -F & -1 & 0 & -1 \\ 0 & 0 & 2\hat{x}K & 0 & 2\hat{x}k_3^2 & -F \end{pmatrix},$$

$$c_1 = \begin{pmatrix} 0 & 0 & 0 & 0 & 0 & 0 \\ -2\hat{x} & 0 & 0 & 0 & 0 & 0 \\ 0 & 0 & 0 & 0 & 0 & 0 \\ 2\hat{x}F' & 0 & 0 & 0 & 0 & 0 \\ -2\hat{x}(F - \eta F') & -2\hat{x}F' & 0 & -2\hat{x} & 0 & 0 \\ 0 & 0 & 2\hat{x}F' & 0 & 0 & 0 \end{pmatrix}$$

with $K_0 = -3(F - \eta F') + (2\hat{x})\eta K - 2GF'(2\hat{x})^{3/2}$, and $K = -i\hat{k}_1 + k_3^2$.

We apply the second-order central difference scheme in the normal direction, i.e.

$$\mathbf{U}_{j+1} - \mathbf{U}_j = \frac{h}{2}(\mathbf{U}'_{j+1} + \mathbf{U}'_j) + O(h^3), \tag{2.7.2}$$

where $h = \eta_{j+1} - \eta_j$, and a prime indicates differentiation with respect to η. By using (2.7.2), equation (2.7.1) can be rewritten as

$$\left[I - \frac{h}{2}c_0^{j+1}\right]\mathbf{U}_{j+1} + \left[-I - \frac{h}{2}c_0^{j}\right]\mathbf{U}_j = \frac{h}{2}\left(c_1^{j+1}\frac{\partial \mathbf{U}_{j+1}}{\partial \hat{x}} + c_1^{j}\frac{\partial \mathbf{U}_{j}}{\partial \hat{x}}\right), \tag{2.7.3}$$

where I is the 6×6 identity matrix.

A second order accurate backward differencing scheme is used in the streamwise direction to approximate $\partial \mathbf{U}^{n+1}/\partial \hat{x}$,

$$\frac{\partial U^{n+1}}{\partial \hat{x}} = \gamma \mathbf{U}^{n+1} + \mathbf{f}_d^{n+1} + O((\Delta \hat{x})^2), \tag{2.7.4}$$

where $\Delta \hat{x} = \hat{x}_{n+1} - \hat{x}_n$, and

$$\mathbf{f}_d^{n+1} = -(\alpha_0 \mathbf{U}^n + \alpha_1 \mathbf{U}^{n-1}).$$

If we choose $\gamma = \frac{3}{2\Delta\hat{x}}$, $\alpha_0 = \frac{2}{\Delta\hat{x}}$, $\alpha_1 = -\frac{1}{2\Delta\hat{x}}$, then discretization is of second-order accuracy. For convenience, we rewrite the discretized equations in the following form,

$$\left[I - \frac{h}{2}c_{j+1}\right]\mathbf{U}_{j+1} + \left[-I - \frac{h}{2}c_j\right]\mathbf{U}_j = \frac{h}{2}(\mathbf{g}_{j+1} + \mathbf{g}_j), \tag{2.7.5}$$

where $c_{j+1} = c_0^{j+1} + \gamma c_1^{j+1}$ is evaluated at $\hat{x}_{n+1}$, $\mathbf{U}$ stands for $\mathbf{U}^{n+1}$ and $\mathbf{g}_j = c_1^j \mathbf{f}_d^{n+1}$.

In order to march downstream, the values of $\mathbf{U}$ at the first two steps are specified by using the composite solution (2.4.26)-(2.4.27) or (2.4.23)–(2.4.25). Alternatively, the composite solution is used to evaluate $\mathbf{U}^0$, while $\mathbf{U}^1$ is calculated by dividing the step $\Delta\hat{x}$ into ten sub-steps and using a first-order difference scheme (Euler's Method) for $\partial \mathbf{U}/\partial \hat{x}$, i.e. by choosing $\gamma = \frac{1}{0.1\Delta\hat{x}}$, $\alpha_0 = \frac{1}{0.1\Delta\hat{x}}$ and $\alpha_1 = 0$. Values of $\mathbf{U}$ at subsequent mesh points can be calculated using the second-order scheme. Typically, the marching starts from $\hat{x} = 0.003$, and the step size $\Delta\bar{x} = 10^{-3}$. The numerical solution overlaps (2.4.26)-(2.4.27) for $0.003 < \hat{x} \leq 0.005$, indicating that the choice of the starting point is appropriate.

2.7.2 Numerical method for solving the local eigenvalue problem

As with the initial-boundary-value problem, equations (2.5.2)–(2.5.7) (or (2.5.10)–(2.5.15)) can be written in the matrix form

$$\frac{\partial \tilde{\mathbf{U}}}{\partial \eta} = M\tilde{\mathbf{U}}, \tag{2.7.6}$$

where $\tilde{\mathbf{U}} = \{\tilde{u}, \tilde{v}, \tilde{w}, \tilde{f}, \tilde{p}, \tilde{g}\}$, and M denotes the coefficient matrix of the system of six first order ordinary differential equations. After applying the finite-difference scheme (2.7.2) to (2.7.6), the discretized system may be written as

$$(I - \frac{h}{2}M_{j+1})\tilde{\mathbf{U}}_{j+1} - (I + \frac{h}{2}M_j)\tilde{\mathbf{U}}_j = 0,$$

where M_j denotes the value of M at the mesh point j.

The eigenvalue σ can be found by the condition that the determinant of the block matrix, which is comprised of M_j, the far-field condition on the top and the wall condition at the bottom, must vanish. This is implemented by a numerical procedure consisting of Gaussian elimination to convert the block matrix to the upper triangular form, and a Newton-Raphson iteration on σ, which makes the last diagonal element of the upper triangular matrix equal zero.

2.7.3 Validation

As a check of our codes, we first reproduce the results of LWG, which were obtained by using a numerical method quite different from ours. LWG's formulation is for unsteady free stream turbulence interacting with the boundary layer over a flat plate, which corresponds to Görtler number being zero in our formulation. For the purpose of calculating both steady and unsteady Görtler vortices, the parameter κ and κ_2 in LWG's formulation are replaced by $\hat{k}_1$, k_2 and k_3 in our formulation. By replacing $\bar{u}$ with $\hat{k}_1\bar{u}$, k_3^2=$\hat{k}_1\kappa^2$, $\bar{x} = \hat{k}_1\hat{x}$, and setting the Görtler number $G_\Lambda = 0$, equations (2.4.9)–(2.4.12) reduces to (5.2)–(5.5) of LWG.

Figure 2.4 presents the downstream development of the maximum streamwise velocity, attained at $\eta = 1.64$ approximately, for different κ values. The maximum streamwise velocity initially increases with decreasing κ value; as κ reduced further, the maximum streamwise velocity also decreases. For a fixed κ (say $\kappa = 0.1$), the streamwise velocity grows linearly with $\bar{x}$ for relatively small $\bar{x}$, and decreases to zero rapidly. This kind of eventual decay is caused by the spanwise ellipticity effect. Figure 2.5 shows the dis-

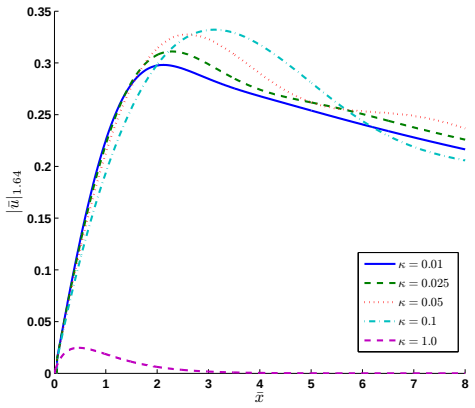


Figure 2.4: $|\bar{u}|$ at $\eta = 1.64$ calculated from different values of $\kappa \leq 1.0$ with $\kappa_2 = -\kappa$ using equations (2.4.9)–(2.4.12).

tributions of the streamwise and spanwise velocities at different downstream locations. It is known that the profile of the streamwise velocity given by LUBL is valid for relatively small $\bar{x}$. However, the shape of the profile does not change significantly when $\bar{x}$ becomes relatively large as indicated in figure 2.6

Figures 2.4–2.6 are in exact agreement with the results as shown in Figures 3-4 and Figures 6-7 of LWG, thereby giving us the confidence in our own codes.

2.8 Results and comparisons with experiments

Since the majority of experiments were conducted on a curved plate with a constant curvature, our calculations will be carried out for this special case, even though the numerical method is applicable to a curved wall with a varying curvature. With the non-dimensionalisation adopted, the spanwwise wavenumber $k_3 = 1$. We set $k_2 = -1$, which serves as a representative case.

2.8.1 Steady Görtler vortices

In this section, we present results on the response of the boundary layer over a curved plate with a constant curvature to steady free-stream disturbances ($\hat{k}_1 = 0.0$). The particular interest is in the generation of steady Görtler vortices. For the purpose of observing the effect of curvature on the boundary-layer response to free-stream disturbances, the downstream

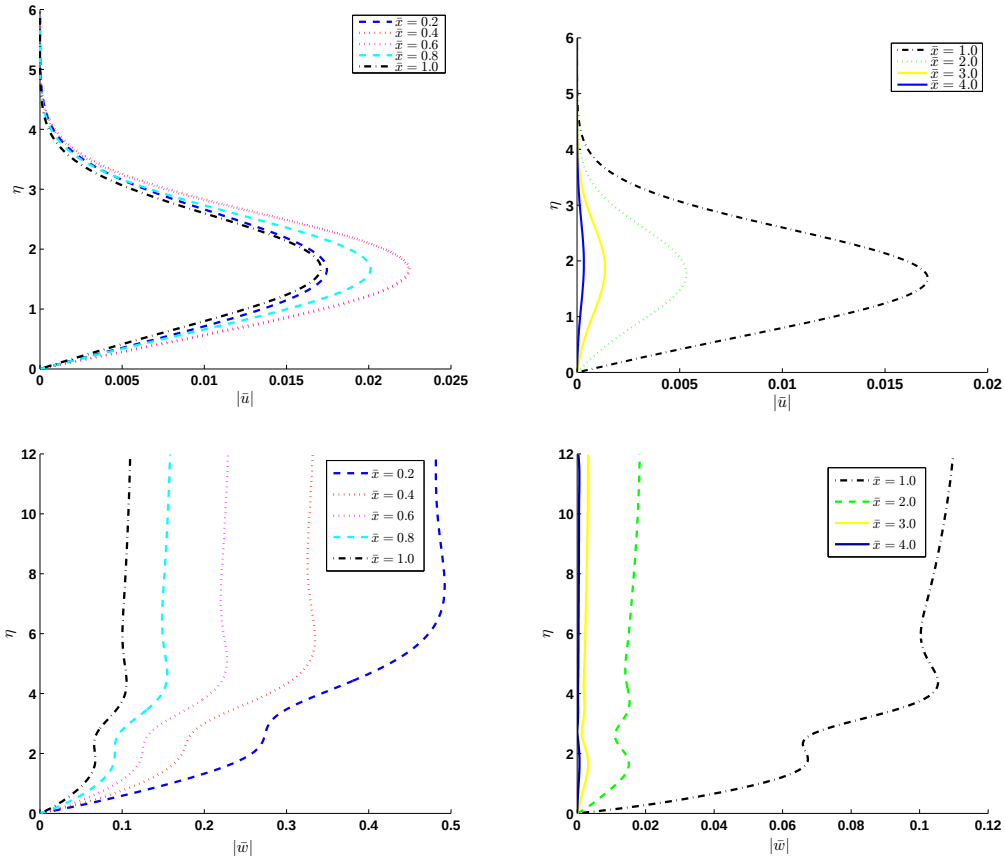


Figure 2.5: Profiles of the streamwise and spanwise velocities of the perturbation at the indicated values of $\bar{x}$ for $\kappa = 1.0$, $\kappa_2 = -1.0$.

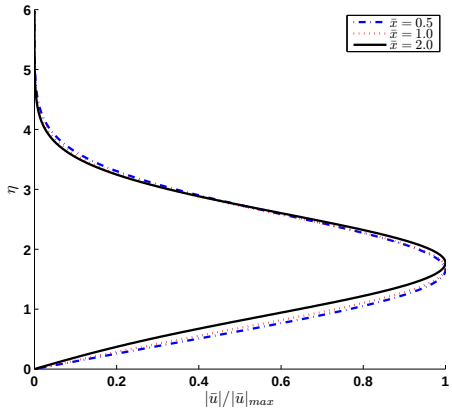


Figure 2.6: Profiles of $|\bar{u}|/|\bar{u}|_{\max}$ at indicated $\bar{x}$ for $\kappa = 1.0$, $\kappa_2 = -1.0$.

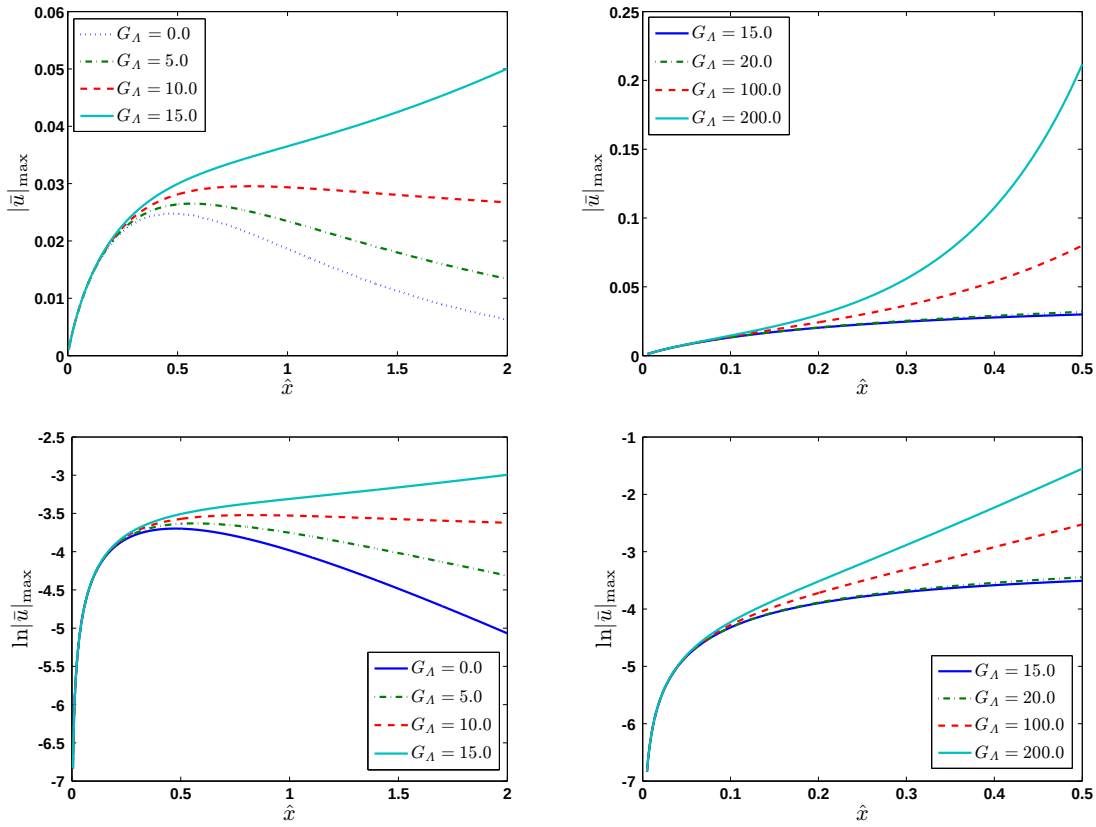


Figure 2.7: $|\bar{u}|_{\max}$ and $\ln|\bar{u}|_{\max}$ calculated for different values of Görtler number G_Λ with $\hat{k}_1 = 0.0$, $k_2 = -1.0$ and $k_3 = 1.0$.

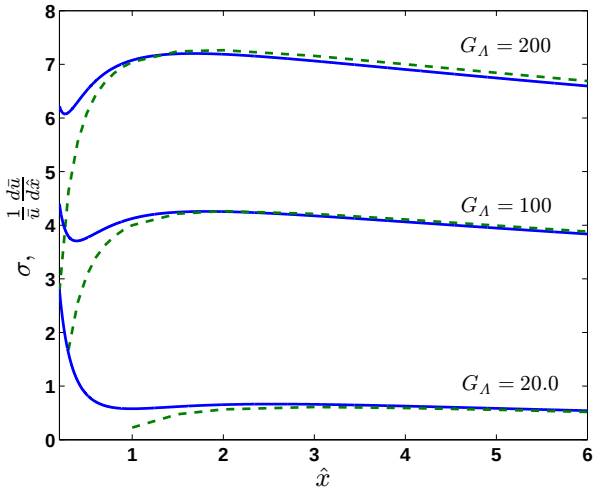


Figure 2.8: Comparison of the growth rates as predicted by nonparallel eigenvalue approach (σ, dashed line) and by initial-value approach ($\frac{1}{\bar{u}}\frac{d\bar{u}}{d\hat{x}}$ at $\eta = 1.64$, solid line) for $\hat{k}_1 = 0.0$, $k_2 = -1.0$, $k_3 = 1.0$ and different values of G_Λ as indicated in the plot.

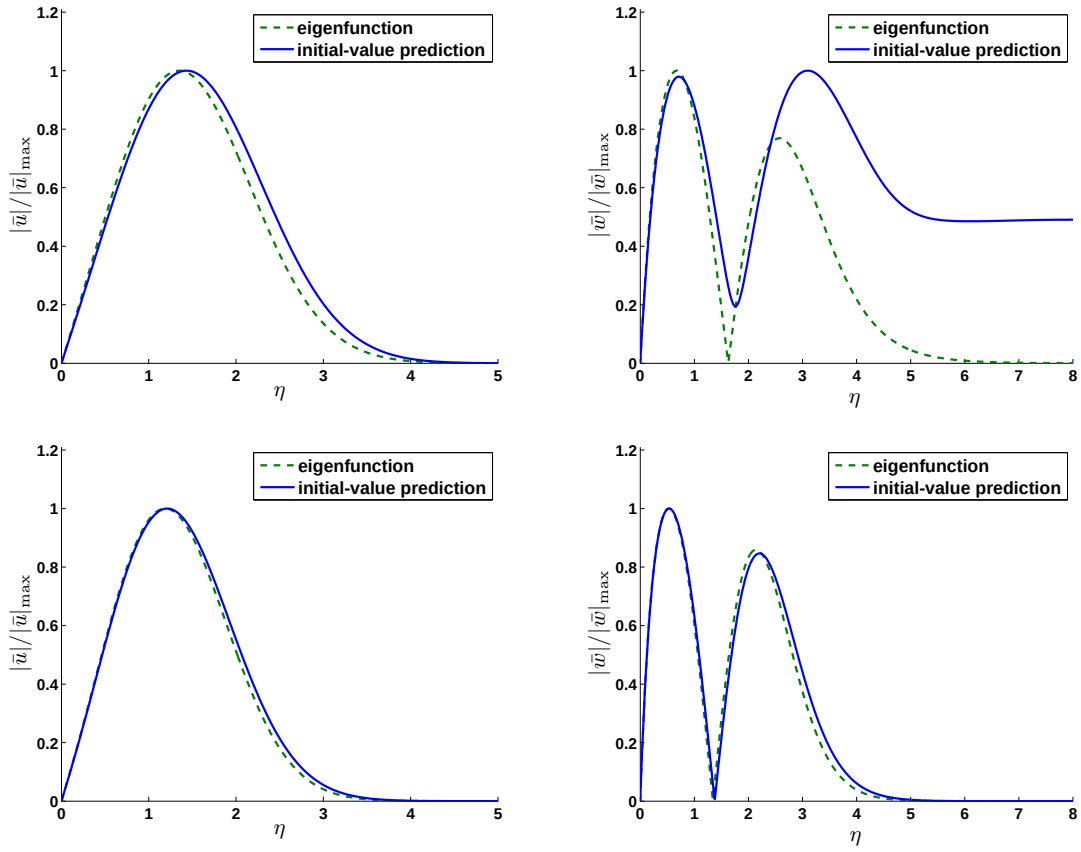


Figure 2.9: Comparison of streamwise and spanwise perturbation velocity profiles predicted by nonparallel eigenvalue and initial-value approaches. Top row: $\hat{x} = 1.0$; bottom row: $\hat{x} = 4.0$. The parameters are $\hat{k}_1 = 0.0$, $k_2 = -1.0$, $k_3 = 1.0$ and Görtler number $G_\Lambda = 20.0$.

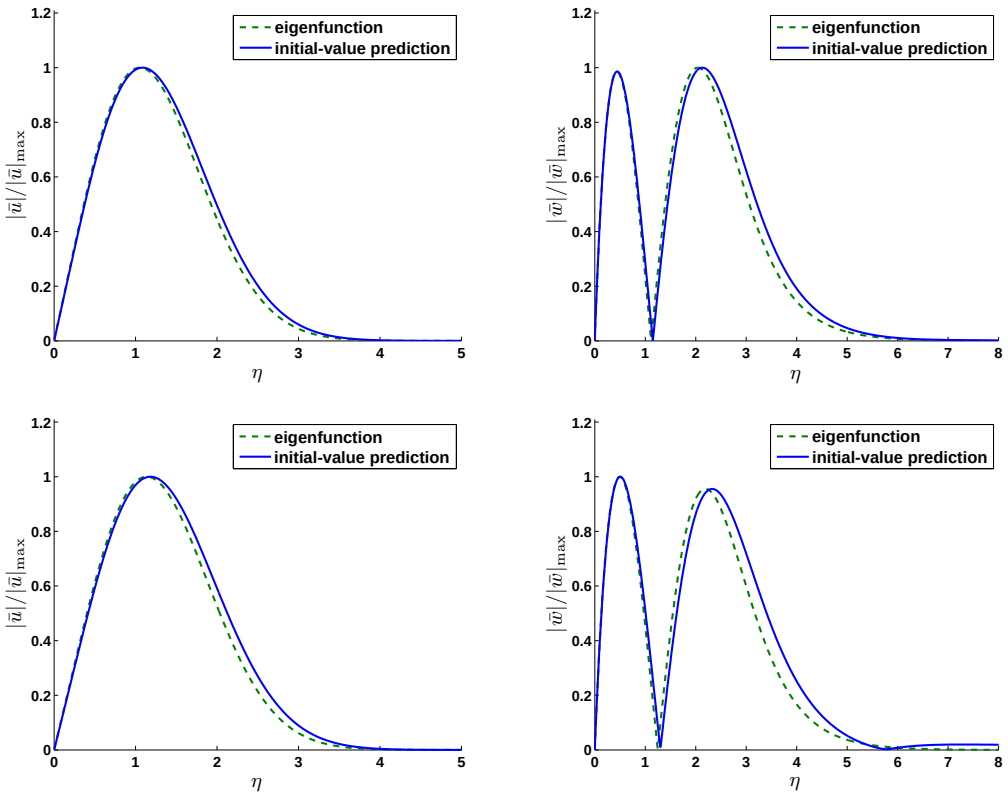


Figure 2.10: Comparison of the streamwise and spanwise velocity profiles (at $\hat{x} = 1.0$) predicted by the nonparallel eigenvalue and initial-value approaches. The parameters are $\hat{k}_1 = 0.0$, $k_2 = -1.0$, $k_3 = 1.0$ and Görtler number G_Λ = 200.0 (top), and 100.0 (bottom).

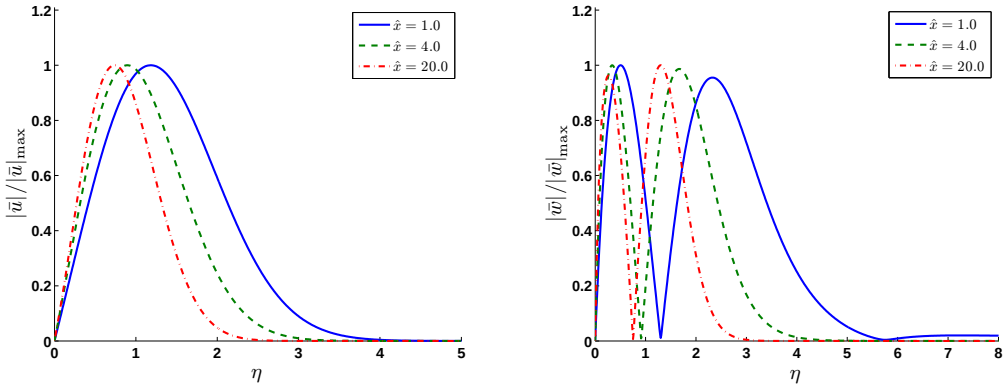


Figure 2.11: Downstream development of normalised streamwise and spanwise velocities at indicated values of $\hat{x}$, with $\hat{k}_1 = 0.0$, $k_2 = -1.0$, $k_3 = 1.0$ and Görtler number G_Λ= 100.0 .

development of the maximum streamwise perturbation velocity,

$$|\bar{u}|_{\max} = \max_{\eta} |u|,$$

for different Görtler numbers is displayed in figure 2.7. For sufficiently small Görtler numbers, the streamwise perturbation velocity initially grows then decreases to zero. The response is primarily streamwise streaks, enhanced by the centrifugal force. However, as the Görtler number G_Λ exceeds a critical value of about 12, the velocity exhibits continued growth with the downstream distance. The growth appears to be exponential as indicated by the corresponding logarithmic plots in figure 2.7. This prompts us to associate the amplifying disturbance with unstable Görtler vortices. In order to establish the link, we solve the (composite) local eigenvalue problem (2.5.2)–(2.5.7), in which the perturbation is assumed to be of the form $f(\eta)e^{\sigma\hat{x}}$, where σ represents the local growth rate.

Figure 2.8 shows the eigenvalue σ against $\hat{x}$, and the local growth rate, $\frac{1}{\bar{u}}\frac{d\bar{u}}{dx}$, obtained from the initial-value calculation (marching). The two converge as the disturbance develops downstream, confirming that the perturbation gradually develops into an eigenmode. The growth rate of the perturbation increases with the Görtler number, indicating that as the plate becomes more curved, the flow becomes more unstable as expected.

Figure 2.9 compares the local eigenfunctions with the velocity profiles predicted by the initial-value formulation at two different downstream locations. At $\hat{x} = 1.0$, the streamwise velocity has already acquired modal shape, but the spanwise velocity differs appreciably from the eigenfunction. At $\hat{x} = 4.0$, both velocity profiles become almost indistinguishable from the corresponding eigenfunctions. The agreement on eigenfunctions indicate that perturbation evolves into eigenmode and eigenvalue formulation is valid for relatively large downstream distances. For larger G_Λ, the perturbation acquires the character of eigenmodes earlier, as shown in figure 2.10. For instance, for $G_\Lambda = 100$, both spanwise and streamwise velocities have already converged to their eigenfunctions at $\hat{x} = 1$.

Figure 2.11 displays the streamwise velocity profiles at different $\hat{x}$. The peak position of the streamwise velocity approaches to the the wall as the flow develops downstream, in consistent with the analysis of §2.6 and Denier et al. (1991), which indicates that the perturbation tends to concentrate in a wall layer.

There exist somewhat different eigenvalue formulations. The parallel theory neglects the streamwise variation of the base flow as well as the small transverse velocity com-

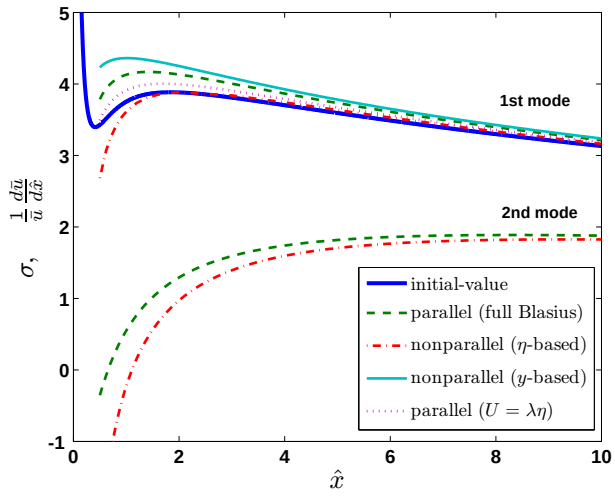


Figure 2.12: Growth rates predicted by different parallel and nonparallel theories as well as by initial-value calculation, when $\hat{k}_1 = 0.0$ and G_Λ=89.5 (corresponding to $G_b \approx 15$ in the paper of Boiko et al. (2007, 2010))

ponent, that is, the base flow is taken to be $\{F'(\eta),\ 0,\ 0\}$. For the so-called most unstable modes, which concentrate in the viscous sub-layer, the profile can be simplified to $\{\lambda\eta, 0, 0\}$, where λ refers to the wall shear (Denier et al. 1991). In the non-parallel flow formulation, both the streamwise variation of the base flow and the transverse velocity are included, i.e. the base flow is taken to be $\{F'(\eta), \frac{1}{R_\Lambda}(\frac{1}{2\hat{x}})^{\frac{1}{2}}(\eta F' - F), 0\}$. The perturbation may be assumed to be of the form $f(y)\exp\{\int^{\hat{x}}\sigma d\hat{x}\}$ or $f(\eta)\exp\{\int^{\hat{x}}\sigma d\hat{x}\}$, leading to the η-based and y-based non-parallel formulations respectively. None of these formulations are strictly justifiable for finite Görtler numbers, and so their relative merit can only be assessed by comparing with the initial-value calculation results.

Figure 2.12 displays the growth rates predicted by different local eigenvalue theories and the initial-value formulation where we choose $G_\Lambda = 89.5$ corresponding to one of the experimental condition of Boiko et al. (2010). For $\hat{x} \geq 0.3$, they all give qualitatively similar results, but there still exists appreciable quantitative difference. The η-based non-parallel theory appears to match with the initial-value prediction best. Somewhat surprisingly, the parallel theory, employing either the full Blasius solution or its approximation $U = \lambda\eta$, gives a more accurate result than the y-based non-parallel theory does. As expected, the difference between different formulations diminishes as $\hat{x}$ increases. The local eigenvalue problems admit multiple modes. The growth rates of the second mode calcu-

lated by using parallel and (η-based) non-parallel theories, are displayed in figure 2.12. Obviously, the second mode remains less unstable than the first mode at all distances. Figure 2.13 shows the comparison between the normalised eigenfunctions and normalised velocity profiles from initial-value calculation at the indicated values of $\hat{x}$, confirming again that the perturbation induced by FST develops into an eigenmode downstream.

Figure 2.12 indicates also that for a given G_Λ, the growth rate predicted by all local instability theories would decrease and eventually become negative as $\hat{x}$ decreases, implying that a critical local Görtler number G_θ exists for instability. As G_Λ is varied continuously, the loci of each critical G_θ and the corresponding local wavenumber forms the lower-branch of the neutral curve. However, these critical G_θ must be suspected because the eigenvalue approach becomes invalid close to the leading edge, where the initial-value formulation is needed. Different upstream conditions would then give arise to different critical G_θ (Hall 1983). With the present upstream and far-field conditions, appropriate for free-stream vortical disturbances, the boundary-layer signature amplifies monotonically, that is, a minimal G_θ is not required for instability and hence a lower-branch of the neutral curve does not even exist. In contrast, in the case of Görtler vortices developed from an artificially imposed upstream condition (Hall 1983), or from the forcing of surface roughness (Denier et al. 1991; Bassom and Hall 1994) or from spanwise non-uniformity of the oncoming flow (Hall 1990), a critical G_θ is identified, implying that the induced perturbation experiences a period of transient decay before it starts to amplify. It may therefore be inferred that FST is particularly effective in generating Görtler vortices. It is perhaps not surprising that there has never been any report of transient decay being observed in experiments.

The local eigenvalue problems admit multiple modes. The growth rates of the second mode predicted by using the parallel and (η-based) non-parallel theories, are displayed in figure 2.12. The second mode remains less unstable than the first mode at all distances. The eigenfunctions of the second mode are displayed in figure 2.14. The streamwise/spanwise profiles of the second mode have two/three maximas as opposed to one/two maxima for the first mode.

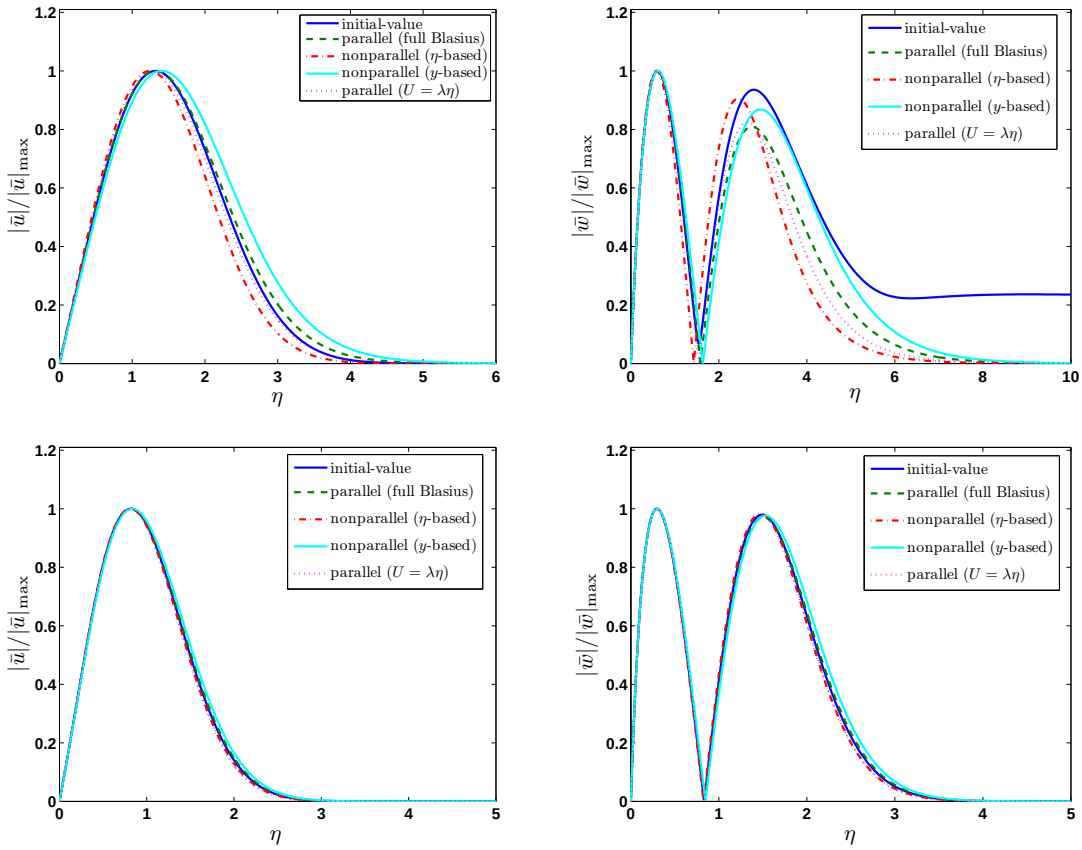


Figure 2.13: Normalised streamwise and spanwise velocity profiles predicted by different parallel and nonparallel theories at $\hat{x} = 0.6241494$ (top) and $\hat{x} = 8.0$ (bottom) for G_Λ=89.5, which corresponds to $\Lambda_b = 149$ in Boiko et al. (2010).

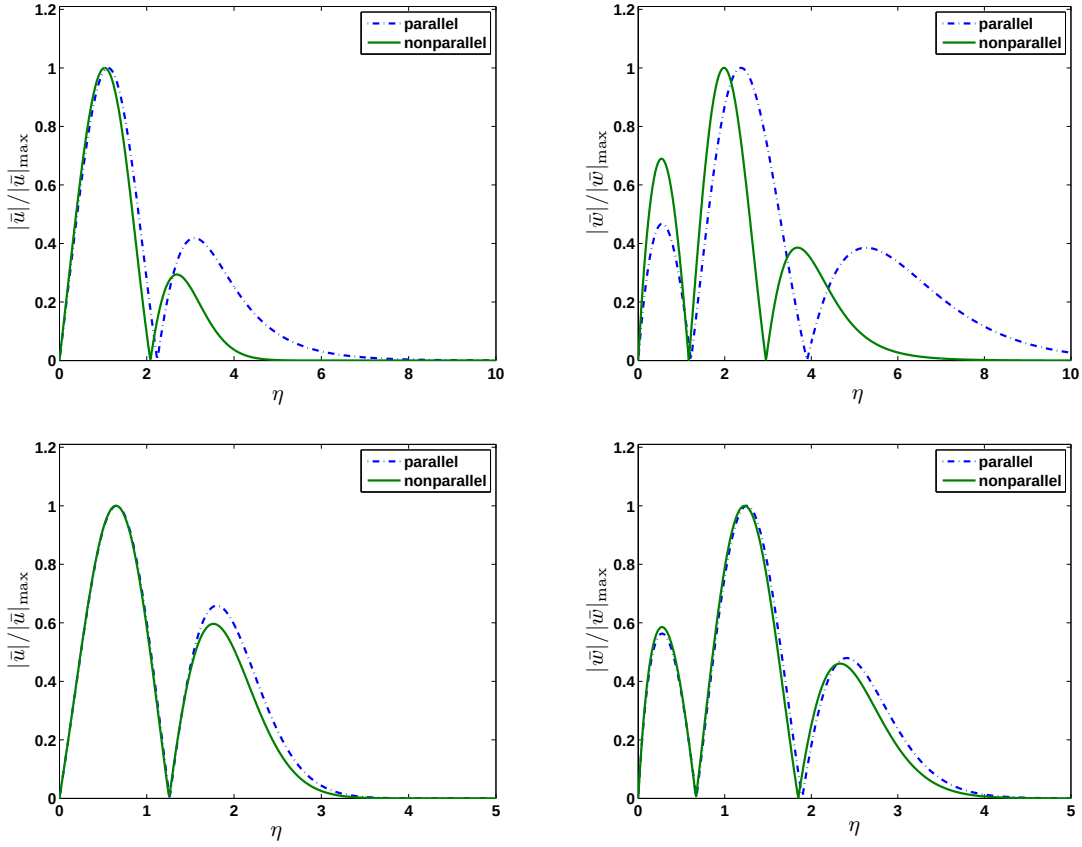


Figure 2.14: Normalised streamwise and spanwise velocity profiles of the second mode predicted by parallel and nonparallel theories at $\hat{x} = 0.6241494$ (top) and $\hat{x} = 8.0$ (bottom), for G_Λ=89.5, which corresponds to $\Lambda_b = 149$ in Boiko et al. (2010).

Detailed measurements of Görtler vortices were conducted by Tani (1962) on two concave-wall models, which have radii of curvature of 5 and 10 metres respectively. The streamwise gradient of the free-stream velocity was eliminated within the accuracy of measurements so that the base flow corresponds to a Blasius boundary layer. Stationary vortices were observed whose spanwise wavelength Λ remains fixed as the perturbation evolves downstream. When the radius of curvature is 10 meters, and the free stream velocity $U_\infty = 11\mathrm{m/s}$, a spanwise wavelength $\lambda_z = 2.1\mathrm{cm}$ was observed. The streamwise velocity of the vortices was measured at locations between $x^* = 30\mathrm{cm}$ and $x^* = 120\mathrm{cm}$. No vortex generator was employed, and it was most likely that vortices were excited by free-stream disturbances, which were later found to be a dominant source of Görtler vortices in addition to wall roughnesses (Swearingen and Blackwelder 1987, Kottke 1988, Crane and Sabzvari 1982). It is therefore appropriate to compare our theoretical results with the experiment data of Tani (1962). For that purpose, we need to figure out the corresponding Görtler number G_Λ and the downstream locations $\hat{x}$ in our formulation. We first calculate the Reynolds number pertaining to the experiment of Tani (1962), $R_\Lambda = U_\infty \Lambda/\nu = U_\infty \lambda_z/(2\pi\nu) = 2.298 \times 10^3$, where we take $\nu = 1.6 \times 10^{-5}\mathrm{m}^2/\mathrm{s}$, the kinematic viscosity coefficient of dry air at the pressure of one atmosphere at 30°C (Batchelor 1967). The Görtler number is $G_\Lambda = R_\Lambda^2/\bar{r}_0 = R_\Lambda^2 \lambda_z/(2\pi r_0^*) = 1765$. The dimensional downstream distance x^* is related to the dimensionless distance $\hat{x}$ via the relation

$$\hat{x} = x^*/(\Lambda R_\Lambda) = 2\pi x^*/(R_\Lambda \lambda_z). \tag{2.8.1}$$

The measurement locations at $x^* = 30\mathrm{cm}$, $50\mathrm{cm}$, $90\mathrm{cm}$ and $120\mathrm{cm}$ thus correspond to $\hat{x} =$ 0.03906, 0.065, 0.1172 and 0.1562 respectively.

The data in figure 5 of Tani (1962) is converted to $\ln(|\bar{u}|_{max}/|\bar{u}|_{30})$, and is compared in figure 2.15 with the theoretical prediction by the initial-value approach, where $|\bar{u}|_{30}$ denotes the maximum value of $\bar{u}$ at $x^* = 30$cm. A good agreement is noted. This indicates that the initial-value approach describes the development of Görtler vortices very well even at small distances to the leading edge. To the best of our knowledge, this is the first time that a quantitatively accurate prediction of the amplitude development of steady Görtler vortices is made. Crucial to the present success is the inclusion in our formulation of the relevant receptivity process. In figure 2.16, we compare the amplification rate given by the initial-value calculation with the non-parallel viscous and parallel inviscid eigen solutions.

U_∞(m/s)	R_Λ	G_Λ	Measurement locations ($\hat{x}$)					
10	1804	2192	0.0731	0.1158	0.1589	0.2012	0.2444	0.2854
7.5	1344	1222	0.0978	0.1549	0.2126	0.2692	0.3269	0.3819

Table 2.1: Parameters pertaining to the experiments of Finnis and Brown (1997).

The agreement is rather poor for $\hat{x} \leq 0.10$, but the discrepancy decreases rather rapidly as $\hat{x}$ increases, and a reasonably close agreement is observed for $\hat{x} > 0.12$. This feature is expected since the eigenvalue approach cannot describe the development of Görtler vortices at small distances, where an initial-value formulation is required. The eigenvalue approach becomes tenable only at large downstream distances, where non-parallelism becomes a secondary effect. Interestingly, the eigenvalue given by the inviscid parallel theory agrees better with the initial-value prediction. It is important to point out that the inviscid eigenvalue, to which the initial-value solution converges, is the second most unstable mode rather than the most unstable exact solution (2.6.37). The latter is not excited by FST because it cannot be traced back to any of asymptotic eigen modes. It may therefore be concluded that excitation of asymptotic modes is a vital necessary process in the receptivity of Görtler vortices to FST.

In figure 2.17, the normalised streamwise velocity profiles obtained from the initial-value and eigenvalue calculations are compared with the measurement of Tani (1962). As is illustrated, the agreement is excellent at all four measurement locations including even at the first one $\hat{x} = 0.039$, indicating that the disturbance acquires the modal shape fairly quickly.

A set of up-to-date experimental data was provided by Finnis and Brown (1997). Their measurements were made over a concave wall with radius of curvature of 4 meters for two free-stream velocities $U_\infty = 10$m/s and 7.5m/s. The kinematic viscosity extracted from their experiment is $1.50 \times 10^{-5}\mathrm{m}^2/\mathrm{s}$. and the spanwise wavelength λ_z was found to be approximately 17 mm. Finnis and Brown measured the amplitude of the maximum streamwise velocity of steady Görtler vortices at six downstream locations, $x^* = 356$mm, 564mm, 774mm, 980mm, 1190mm and 1390mm. The corresponding Reynolds and Görtler numbers as well as the non-dimensional streamwise locations are listed in table 2.1. In figure 2.18, we compare the amplitude evolution predicted by the initial-value approach with the experiment results for both $U_\infty = 10$m/s and $U_\infty = 7.5$m/s cases. Because the data on the free-streamwise disturbance in the experiment is not available, the absolute

amplitude of Görtler vortices cannot be predicted. The theoretical result was re-scaled to fit the measured value at the first location. There is a fairly good agreement up to the third measurement location. The disturbance evolves linearly during this stage. However, as it amplifies, nonlinearity comes into play causing the amplitude to saturate.

Finnis and Brown (1997) also extracted growth rates of Görtler vortices from the amplitudes (apparently at the first three measurement locations). Their data is compared with the linear growth rate of steady Görtler vortices predicted by various theories; see figure 2.19. For $\hat{x} \leq 0.05$, the initial-value prediction is quite different from the eigenvalue, which is rather expected since the disturbance has not yet acquired a modal character. All theories give qualitatively similar results as Görtler vortices emerge. In particular, the growth rate predicted by the initial-value approach is very close to the measurement within the first three locations. The error appears to be less than 10%, which is probably within the experimental uncertainty. The η-based non-parallel stability theory appreciably under predicts the growth rate, while the y-based stability calculation of Finnis and Brown (1997) over predicts. A similar observation was made by Bottaro and Luchini (1999). Interestingly, the inviscid instability theory, which neglects both viscosity and non-parallelism, outperforms either of the non-parallel theories in the range covering the first three measurement locations. Inspecting figures 2.16 and 2.19, one notes that the difference between the initial-value and the parallel inviscid approaches increases with G_Λ. This is because there is an $O(G_\Lambda^{1/3})$ error in the first-order expansion for the growth rate $G_\Lambda^{1/2}\hat{\sigma}$ as is indicated by (2.6.32).

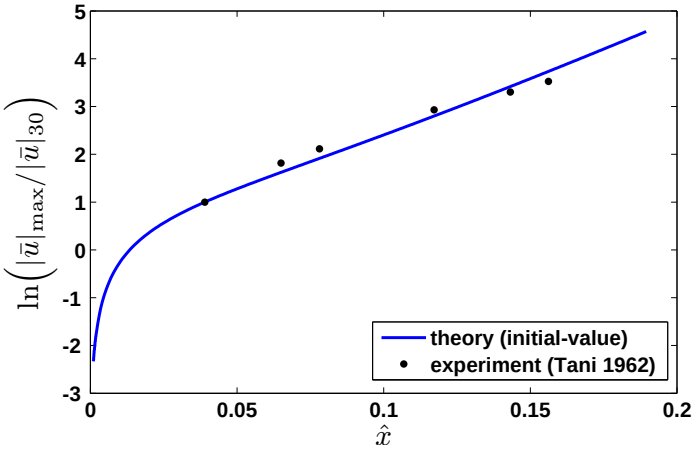


Figure 2.15: Comparison of the downstream development of the maximum streamwise velocity predicted by the initial-value approach with the experiment data of Tani (1962). The parameters are $G_\Lambda = 1765.0$, $\hat{k}_1 = 0.0$, $k_2 = -1.0$ and $k_3 = 1.0$.

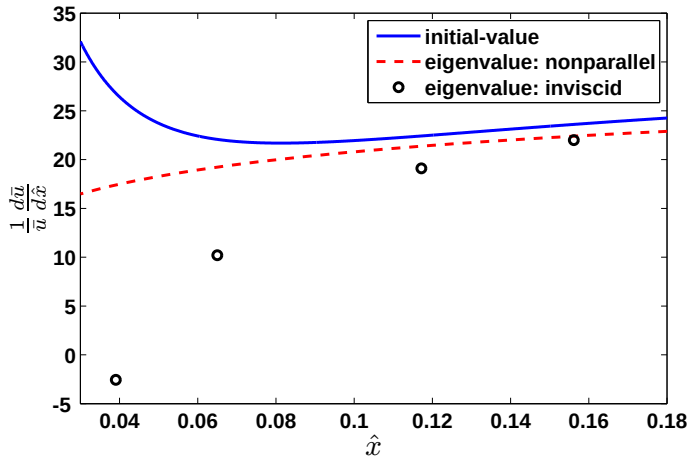


Figure 2.16: Comparison of the growth rate predicted by the initial-value approach and by the nonparallel eigenvalue theory. The parameters are $G_\Lambda = 1765.0$, $\hat{k}_1 = 0.0$, $k_2 = -1.0$ and $k_3 = 1.0$.

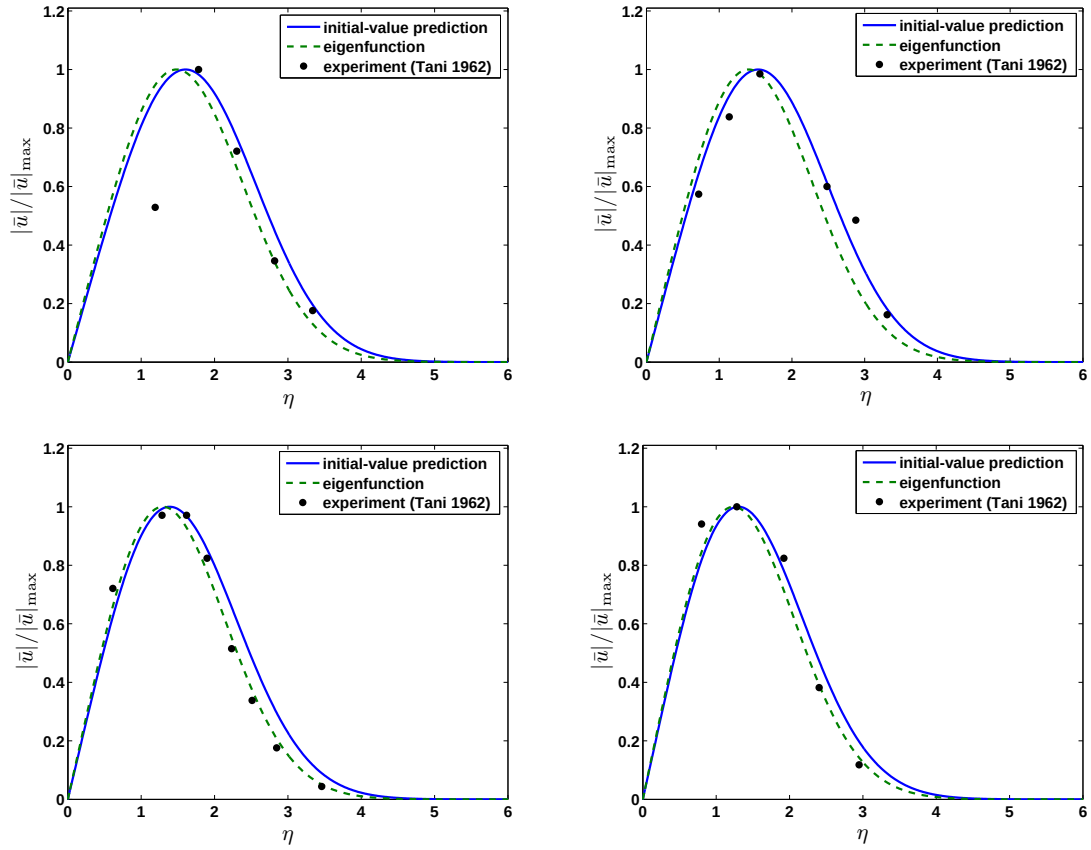


Figure 2.17: Comparison of normalised streamwise velocity obtained from the initial-value and eigenvalue calculations with the experiment data of Tani (1962). The parameters are $G_\Lambda = 1765.0$, $\hat{k}_1 = 0.0$, $k_2 = -1.0$ and $k_3 = 1.0$ at $\hat{x} = 0.03906$ (top left), $\hat{x} = 0.065$ (top right), $\hat{x} = 0.1172$ (bottom left) and $\hat{x} = 0.1562$ (bottom right).

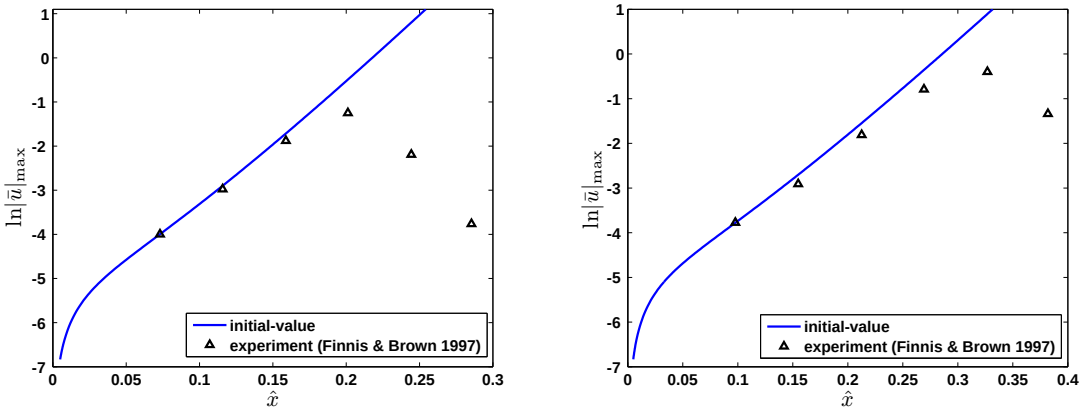


Figure 2.18: Comparison of downstream development of the maximum streamwise velocity predicted by initial-value approach with experiment data of Finnis and Brown (1997) for $U_\infty = 10$m/s (left) and $U_\infty = 7.5$m/s (right). The parameters are $G_\Lambda = 2192$ (left), $G_\Lambda = 1222$ (right), $\hat{k}_1 = 0.0$, $k_2 = -1.0$ and $k_3 = 1.0$.

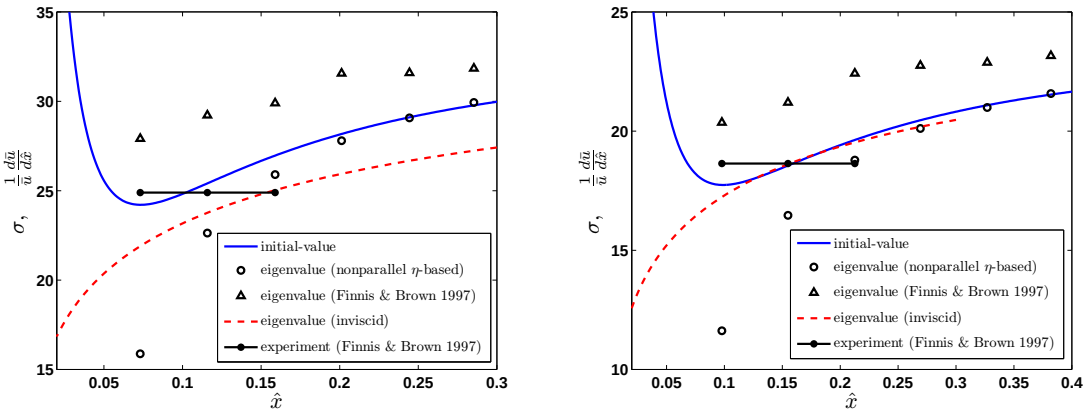


Figure 2.19: Comparison of the growth rate predicted by initial-value approach, nonparallel eigenvalue theory, inviscid approach and the experiment data of Finnis and Brown (1997). The parameters are $G_\Lambda = 2192$ (left), $G_\Lambda = 1222$ (right), $\hat{k}_1 = 0.0$, $k_2 = -1.0$ and $k_3 = 1.0$.

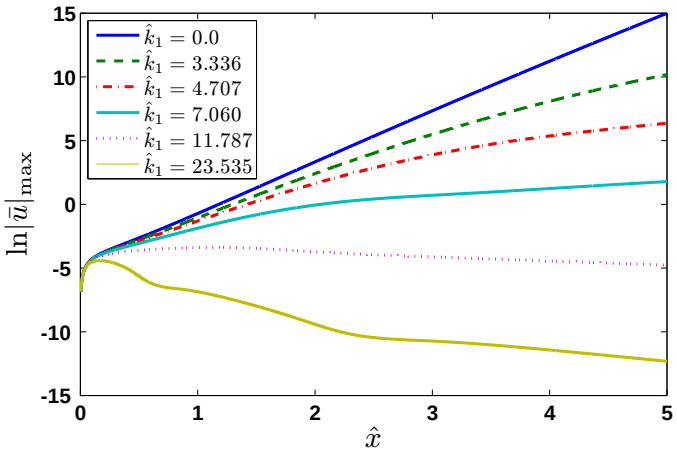


Figure 2.20: $\ln |\bar{u}|_{\max}$ v.s. $\hat{x}$ for different frequencies with $G_\Lambda = 89.5$. The frequencies in the plot (top to bottom) correspond to 0, 5.67, 8.0, 12.0, 20.0 and 40.0 in Boiko et al. (2007, 2010)

2.8.2 Unsteady Görtler vortices

In this section, we present results on the response of the boundary layer over a curved plate to unsteady free-stream disturbances ($\hat{k}_1 \neq 0$). The particular interest is in the generation of unsteady Görtler vortices. The parameters to be used in the calculation are chosen to correspond to those in the two recent papers of Boiko et al. (2007, 2010), who have carried out theoretical and experimental investigations of unsteady Görtler vortices. They define the Görtler number and the dimensionless spanwise wavelength by

$$G_b = \frac{U_\infty \delta^*}{\nu}\sqrt{\frac{\delta^*}{r_0^*}}, \quad \Lambda_b = \frac{U_\infty \lambda_z}{\nu}\sqrt{\frac{\lambda_z}{r_0^*}}, \tag{2.8.2}$$

where δ^* is the boundary-layer displacement thickness, and r_0^* the radius of the wall curvature. G_b and Λ_b are related to G_Λ and R_Λ via

$$G_\Lambda = \Lambda_b^2/(2\pi)^3, \quad R_\Lambda = \Lambda_b (r_0^*/\lambda_z)^{\frac{1}{2}}/(2\pi). \tag{2.8.3}$$

Using the definition for the boundary-layer displacement thickness,

$$\delta^* = \Lambda \int_0^\infty (1-U)dy = \Lambda\sqrt{2\hat{x}}\int_0^\infty (1-F')d\eta = \Lambda\beta\sqrt{2\hat{x}}, \tag{2.8.4}$$

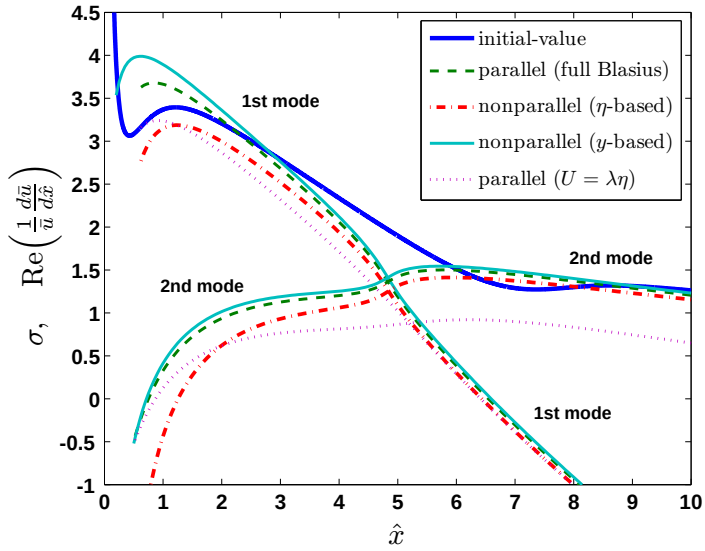


Figure 2.21: Growth rates predicted by local instability theories and comparison with the initial-value prediction. The parameters are taken to be $\hat{k}_1 = 3.33604$, G_Λ=89.5 (corresponding to $\Lambda_b = 149$ and $F = 5.67$ in Boiko et al. (2007, 2010)).

in (2.8.3), we find the relation between $\hat{x}$ and G_b,

$$\hat{x} = 2\pi^2 (G_b/\Lambda_b)^{4/3}/\beta^2. \tag{2.8.5}$$

In the experiment of Boiko et al. (2010), a non-dimensional frequency

$$F = 2\pi f^* \nu / U_\infty^2 \times 10^6$$

was used, where f^* is the dimensional frequency in Hertz. The frequency parameter $\hat{k}_1$ in our formulation is related to F by

$$\hat{k}_1 = R_\Lambda^2 F \times 10^{-6}. \tag{2.8.6}$$

Figure 2.20 shows the development of the maximum streamwise perturbation velocity for different frequencies. Clearly, the response becomes weaker as the frequency is increased. For zero and moderate frequencies, the perturbation induced within the boundary-layer experienced substantial amplification. The logarithmic plots indicate that the growth is exponential, suggesting that the perturbation evolves into unsteady Görtler vortices. This

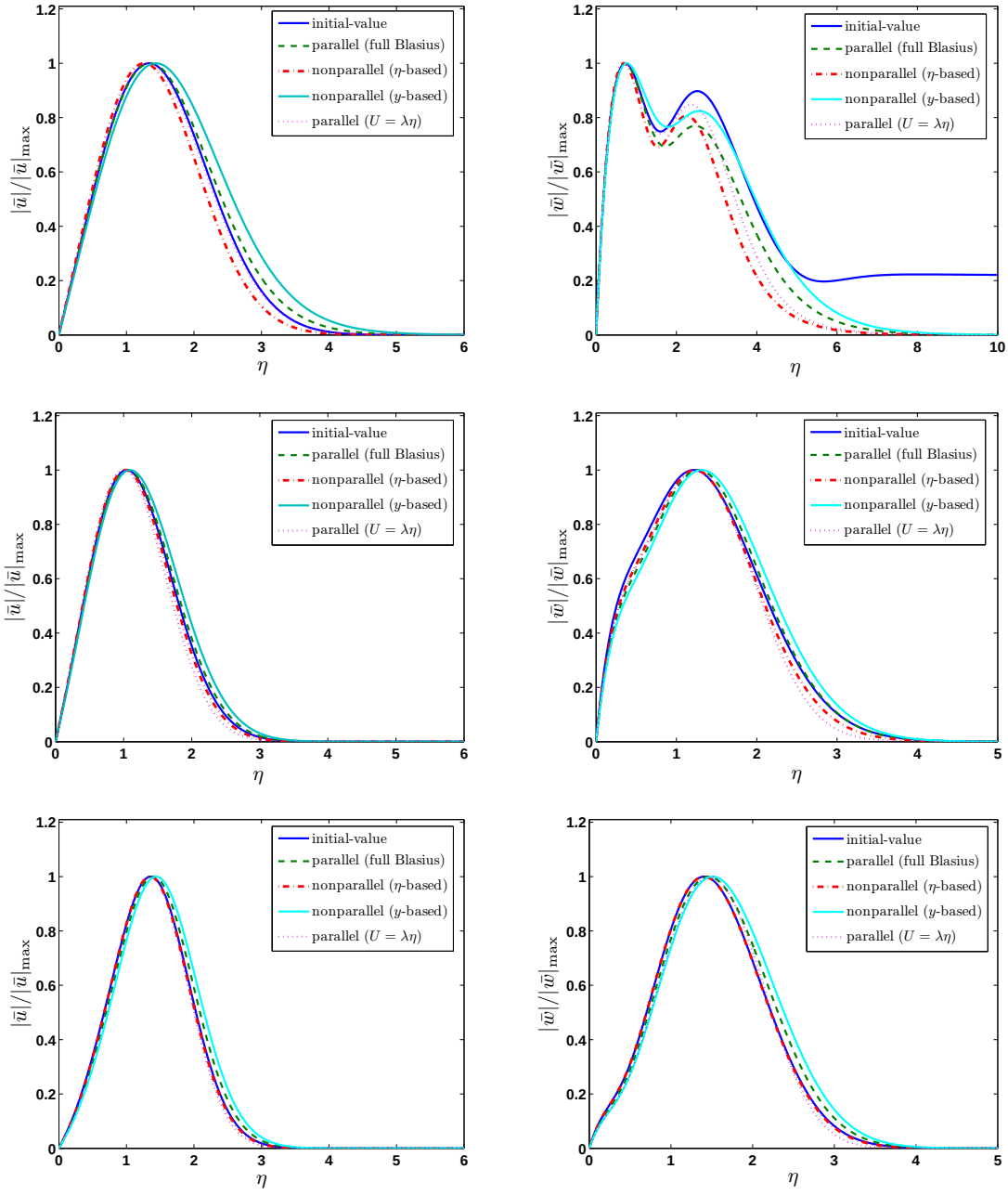


Figure 2.22: Comparison of the streamwise and spanwise velocity profiles predicted by the initial-value approach with the eigenfuctions of different parallel and non-parallel theories at $\hat{x} = 0.624$, 4.0 and 8.0. The parameters are G_Λ=89.5 and $\hat{k}_1 = 3.336$ (corresponding to $\Lambda_b = 149$ and $F = 5.67$ in Boiko et al. (2007, 2010)

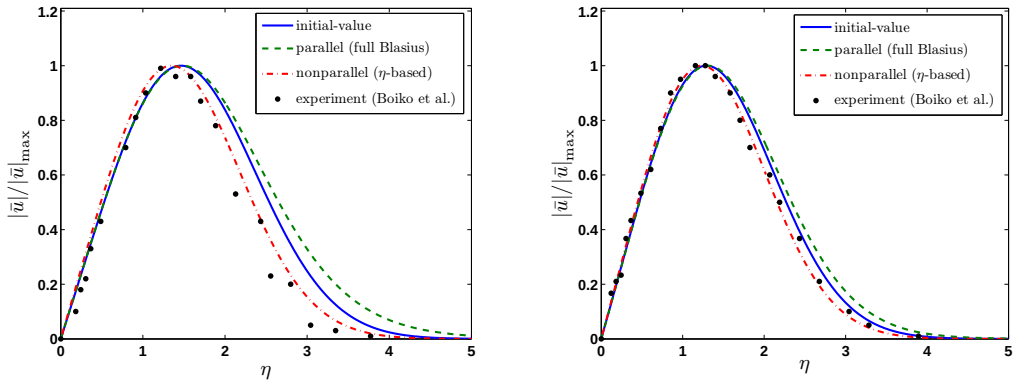


Figure 2.23: Comparison of the streamwise velocity profiles predicted by the initial-value, parallel and non-parallel theories with the measurements of Boiko et al. (2010) at $\hat{x} = 0.378$ (left), 0.749 (right) for $\hat{k}_1 = 3.336$ and $G_\Lambda = 89.5$ ($\Lambda_b = 149$, $F = 5.67$).

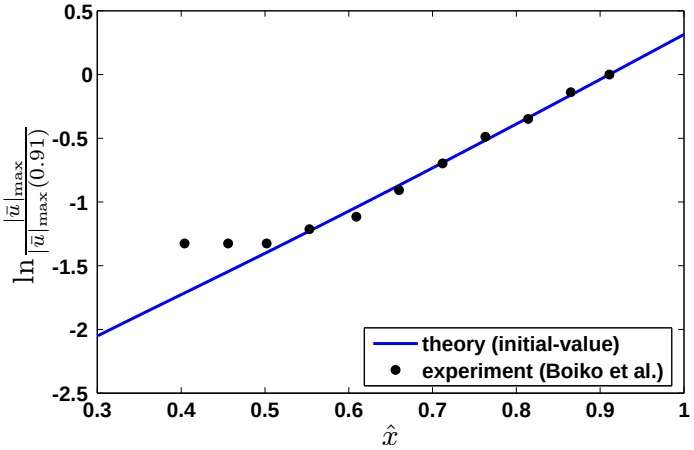


Figure 2.24: Development of unsteady Görtler vortices and comparison with the experiment of Boiko et al. (2010). The parameters are $G_\Lambda = 89.5$ and $\hat{k}_1 = 3.336$ ($\Lambda_b = 149$ and $F = 5.67$).

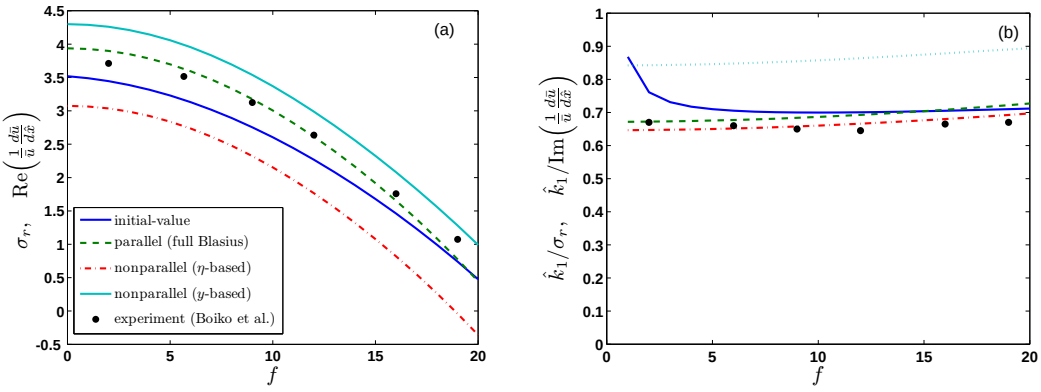


Figure 2.25: Growth rates (a) and phase speeds (b) of unsteady Görtler vortices predicted for different frequencies and comparison with the experimental data at $\hat{x} = 0.62$. The parameters are $G_\Lambda = 89.5$ and $\Lambda_b = 149$.

will be confirmed by comparing with eigenvalues and eigenfunctions.

The growth rates of unsteady Görtler vortices, predicted by different theories, are displayed in figure 2.21. As with the steady case, higher modes exist. For moderate values of $\hat{x}$ ($\hat{x} \leq 5$), they have much smaller growth rates than the first mode, as has been found by Boiko et al. (2010). However, further downstream ($\hat{x} \geq 5$), the second mode becomes more unstable. The amplification rate predicted by the initial-value approach is seen to be reasonably close to those given by the eigenvalue approaches for $0.5 \leq \hat{x} \leq 4.0$. Over this region, the boundary-layer signature is dominated primarily by the first mode. The second-mode is of course also excited, but is negligibly small owing to its small amplification rate in the upstream region. However, for the unsteady case, the residual second-mode will eventually overtake the first mode at modestly large downstream distances, since it becomes more unstable while the latter starts to decay. As a result, the perturbation approaches asymptotically the second-mode at large downstream distances as shown in the figure.

Figure 2.22 shows the profiles of the streamwise and spanwise velocities at three different locations. At $\hat{x} = 0.62$, the streamwise velocity profile has already acquired the character of the local eigenfunction, but the spanwise velocity is still influenced by the forcing from the free-stream, as is indicated by its finite amplitude at large η. At $\hat{x} = 4.0$, both streamwise and spanwise profiles are well represented by the eigenfunctions of the first mode. At $\hat{x} = 8.0$, the velocity profiles acquired the character of the second mode.

We now focus on the disturbance with $F = 5.67$ or $\hat{k}_1 = 3.336$, for which Boiko et al. (2010) measured the streamwise velocity profiles at locations corresponding to $\hat{x} = 0.378$, 0.526 and 0.749 as well as the amplitude development. We calculated the streamwise velocity profiles at these locations using the parallel and non-parallel (η-based) instability theories. The results are compared with the experimental data in figure 2.23. The agreement is fairly good even for quite small downstream distance $\hat{x} = 0.378$ and improves as $\hat{x}$ increases. It is hardly possible to tell which theory is the best. The close agreement indicates that the modal shape of the streamwise velocity is only slightly affected by non-parallelism. Figure 2.24 presents the evolution of the amplitude of unsteady Görtler vortices. The theoretical prediction by the initial-value approach is compared with the experimental data. The agreement is good when the perturbation has acquired the character of Görtler vortice, which is signaled by the exponential growth. The initial phase of the development is however not captured by the theory. This is because in the experiment Görtler vortices are excited by spanwise periodic blowing/suction imposed on the wall rather than by a free-stream convected gust assumed by the theory. The discrepancy highlights once again the importance of including the receptivity process in the formulation if the entire evolution of the boundary-layer signature is to be predicted.

Finally, we computed the instability characteristics of unstable Görtler vortices for a range of frequencies, and the results are shown and compared with the experiment in figure 2.25 for $\hat{x} = 0.62$, where the perturbation just enters the phase of modal development as figure 2.24 implies. The growth rate decreases with the frequency with steady vortices being the most unstable. The predictions by the initial-value approach and the parallel instability theory are in reasonable agreement with the experiment data with an error less than 10% (figure 2.25a). The η- and y-based nonparallel theories are both are less accurate with an error of about 15%, and they under- and over-predict the growth rate respectively. The predictions by different approaches for the phase speed exhibit closer agreement (figure 2.25b). Overall, the phase speed is less sensitive to the non-parallel-flow effect.

Our theoretical results suggest that unsteady Görtler vortices can be excited by FST. Surprisingly, only a few laboratory observations of such vortices have been reported. These include the laser-Doppler measurements carried out by Winoto and Crane (1980) and Crane and Sabzvari (1982), which revealed that vortices may undergo slow, small-amplitude spanwise meandering, and the hot-wire measurements of Volino and Simon (2000), which detected a significant level of low-frequency fluctuations. Floryan (1991) mentioned a similar

finding by Ito in 1991 (unpublished). In typical experimental settings, vortices oscillate in the frequency band below 10Hz, and hence are distinctively different from the secondary instability of Görtler vortices, whose characteristic frequency is about two orders of magnitude higher. However, such low-frequency fluctuations are not readily detected by usual surface visualisation techniques (Schultz and Volino 2003). We hope that the present theoretical work would stimulate further investigations of the possible unsteady nature of Görtler vortices.

2.9 Summary and discussions

It is well known that Görtler instability should, in the generic regime where the spanwise wavelength is comparable with the local boundary-layer thickness, be formulated as an initial-value as opposed to an eigenvalue problem (Hall 1983). This implies that specification of appropriate initial and boundary conditions is of fundamental importance. Those conditions could only be provided by studying the receptivity of the boundary layer to relevant external disturbances. In this chapter, we considered the receptivity to steady and unsteady vortical disturbances in the free stream, which experiments show to be a key agent exciting Görtler vortices. The present work relies heavily on that of LWG, which is concerned with generation of streaks in a flat-plate boundary layer by FST. As in LWG, attention is focussed on components with a long streamwise wavelength because they are entrained into the boundary layer most effectively. The initial-boundary-value problem describing both the excitation and subsequent evolution of Görtler vortices consists of the linearised boundary-region equations (but including the centrifugal force), and the upstream and far-field boundary conditions, which turn out to be the same as those given by LWG.

The initial-value problem was solved numerically for different values of the Görtler number G_Λ. For a sufficiently small G_Λ, the induced boundary-layer signature exhibits essentially the same characteristics as streaks occurring in the flat-plate case: the streamwise velocity amplifies and then decays. When G_Λ exceeds a critical value, the induced perturbation undergoes (quasi-)exponential growth. By comparing with the predictions by *ad-hoc* local parallel and non-parallel instability theories, it is found that the perturbation evolves to acquire the modal shape of Görtler vortices rather quickly, but its growth rate differs appreciably from that given by the local eigenvalue approach. Nevertheless, the overall agreement with, and the eventual convergence to, the eigenvalue at large distances

downstream indicate that Görtler vortices have been excited by free-stream disturbances. The amplitude of the Görtler vortices excited is found to decrease with the frequency with steady vortices generated by steady components of free-stream disturbances being dominant. The present free-stream vortical disturbances turn out to be more effective in generating Görtler vortices than other forms of external disturbances (e.g. surface roughness or spanwise non-uniformity of the oncoming flow) because the induced boundary-layer signature amplifies monotonically without going through transient decay.

In order to provide useful insights into the initiation and evolution of Görtler vortices, an asymptotic analysis is performed on the assumption that $G_\Lambda \gg 1$. Distinct regimes through which a disturbance with a fixed spanwise wavelength evolves were mapped out. Over the distance $x^* \ll \Lambda R_\Lambda G_\Lambda^{-2/3}$ to the leading edge, the signature induced by free-stream disturbances is the same as streaks in the flat-plate boundary layer. The centrifugal force enters the play at $x^* \sim \Lambda R_\Lambda G_\Lambda^{-2/3}$ by influencing the generation of the pressure but without affecting the velocity field to leading order. When $x^* \sim \Lambda R_\Lambda G_\Lambda^{-2/5}$, the induced pressure leads to full coupling of the momentum equations with non-parallelism appearing at leading order. This is the crucial regime linking the pre-modal and modal phases of the perturbation because the governing equations admit a countable set of growing asymptotic eigen solutions, which develop into fully fledged Görtler vortices of inviscid nature when $x^* \sim \Lambda R_\Lambda$. From this position onwards, local eigenvalue formulations are mathematically justified because the non-parallelism becomes a secondary effect. The generated Görtler vortices continue to amplify and enter the most unstable regime when $x^* \sim \Lambda R_\Lambda G_\Lambda$, and ultimately approach the right-branch regime when $x^* \sim \Lambda R_\Lambda G_\Lambda^2$.

In this chapter, we have made comprehensive quantitative comparisons with available experimental data. Satisfactory agreements were noted, indicating that the initial-value approach can accurately predict the entire evolution of the amplitude as well as the modal shape. The initial-value formulation provides an appropriate yardstick against which the validity and relative merit of the *ad hoc* local parallel and non-parallel instability theories can be assessed. The latter become valid at sufficiently large distances downstream, and are found to predict the modal shape adequately at moderate distances for G_Λ values typical of experiments. The growth rate is however predicted less accurately. Interestingly, it is found that inclusion of non-parallelism in the eigenvalue formulation does not necessarily lead to an improved result; the non-parallel theory in which the eigen function is taken to be dependent on y is less accurate than the parallel theory.

Chapter 3

Crossflow Vortices

3.1 Introduction

In this chapter, we consider instability and receptivity of three-dimensional boundary layers, which exist on swept surfaces or rotating disks. The inviscid streamline at the edge of the boundary layer is usually curved due to the combined effects of the sweep and the chordwise pressure gradient, or in the case of a rotating disk, due to the imposed circumferential motion. Crossflow appears in boundary layers on swept surfaces or rotating disks due to the imbalance between the centripetal force and the pressure gradient in the so-called crossflow direction, i.e. the direction perpendicular to the inviscid streamline (Saric et al. 2003). In the inviscid region, the centripetal force is balanced with the pressure gradient so that the crossflow velocity is zero. Inside the boundary layer, the pressure remains unchanged, however the centripetal force decreases approaching the wall. Due to the imbalance between the two forces, a crossflow must be formed. At the wall, the crossflow velocity is also zero due to the no-slip boundary condition. Therefore, between the wall and the far field, an inflectional point will exist in the crossflow profile. According to the inflection point theorem in linear inviscid stability theory of parallel flows, established first by Rayleigh (1880) and extended later by Tollmien (1935), instability may occur in the presence of a crossflow (Gregory et al. 1955). The instability leads to the formation of crossflow vortices. Similar to Görtler vortices, the crossflow vortex pattern also appears more-or-less periodic in the spanwise direction with a discernable wavelength, which is, for fully developed vortices, of the same order of magnitude as the local boundary layer thickness. But, unlike Görtler vortices which are counter rotating, crossflow vortices all ro-

tate in the same direction with the axes being nearly parallel to the free streamline. While the instability mechanism sustaining the vortices is well understood qualitatively at least over the majority of the flow field, a quantitative prediction of crossflow instability is quite a challenge because of three-dimensional nature of the base flow and the non-parallelism associated with the streamwise growth of the boundary layer. The latter effect is particularly significant in the region close to the leading edge, where the wavelength of the vortices may be much longer than the local boundary layer thickness. The research on crossflow instability and the resulting transition to turbulence has continued for decades, and comprehensive reviews have been given by Reed and Saric (1989), Reed et al. (1996), Bippes (1999), Saric et al. (2003), Theofilis (2003), and Theofilis (2011). In the following, only major historic developments and key results will be summarised.

The stability study of crossflow instability and transition has focused on two prototypes of flows: the boundary layer flow on the surface of a rotating disk, and boundary layer flow on a swept wing. The theoretical and experimental work carried out by Gregory et al. (1955) on the flow over a rotating disk signified a first important step towards the understanding of crossflow instability and ensuing transition. Using the china-clay evaporation technique, Gregory and Walker first observed clear crossflow vortices patten in an annular region, beyond the outer boundary of which the flow becomes turbulent. A convincing theoretical explanation was given in the same paper by Stuart. He derived the governing equations for the perturbation, which consisted, in their most general form, of six first-order equations. However, after neglecting the Coriolis and viscous forces, which is justified when the Reynolds number is large, they reduce to the Rayleigh equation with an effective profile U_{eff}, representing the velocity in the wavenumber vector direction. This profile would have an inflection point and thus support unstable modes if the wavenumber vector is aligned approximately with the crossflow direction. Since this pioneering work, rotating disk has become a favorite model and been extensively studied. This is because firstly the base flow is an exact solution of the N-S equations that can be easily computed, and secondly in laboratory the flow can be set up much more easily than the boundary layer over a swept wing. For the rotating disk case, the pressure gradient is absent, the boundary layer thickness is independent of the radius, and the flow does not involve a sweep angle. For the swept wing flow, the base flow is in general non-parallel, the pressure gradient is present, the boundary layer thickness depends on the downstream locations, and the sweep angle needs to be taken into account; the stability and transition of a swept wing flow is

thus more challenging.

Detailed experiments have been carried out on swept-wing boundary layers and other flows which closely resemble them. It is found that crossflow instability typically operates in the region where a favorable pressure gradient is present and the flow is still subcritical for T-S instability. The transition route has been identified. Similar to transition initiated by T-S waves in two-dimensional boundary layers, it consists of several stages including: receptivity, (i.e. excitation of cross-flow vortices), linear growth, nonlinear development and final breakdown through secondary instability (see e.g. Bippes 1999; Saric et al. 2003). Linear stability analysis has been performed, and an important finding is that both stationary and unsteady (travelling-wave) vortices are possible with the latter having larger growth rates. Theoretical predictions have broadly been confirmed by experiments (e.g. Nitschke-Kowsky and Bippes 1988; Bippes et al. 1991), but quantitative differences remain. Notwithstanding this unsatisfactory aspect of the theory, linear stability analysis has been used to correlate the transition location with the accumulated growth, measured by the so-called N-factor (Malik and Orszag 1980, Mack 1984, Arnal 1986, Arnal 1994). This so-called e^N-method, which worked rather successfully for transition in two-dimensional boundary layers, turned out to be rather unreliable for crossflow transition. The failure may be attributed to the facts that crossflow vortices are extremely sensitive to the presence of external disturbances, and undergo nonlinear saturation at a fairly low amplitude, which imply that the N factor is not the most decisive factor determining the actually strength of the vortices. Clearly, transition cannot be predicted without accounting for receptivity and nonlinearity.

In the last two decades or so, the method based on parabolised stability equations (PSE) emerged as a popular tool for studying nonlinear instability (Herbert 1997). In this approach, the disturbance is assumed to be nearly sinusoidal in the spanwise direction so that a local wavenumber can be defined in a heuristic manner, and this property is then used to deal with the pressure gradient and diffusion in the chordwise direction, thereby allowing the original elliptic equations to be parabolized. This approach was promptly adapted to predict nonlinear evolution of crossflow vortices by numerous researchers. Malik et al. (1994) (referred to as MLC hereafter) formulated the nonlinear parabolized stability equations (PSE) for a relatively simple model incompressible three-dimensional boundary layer, a swept Hiemenz flow. Since receptivity is not part of their study, the governing equations satisfy homogenous boundary conditions. In order to initiate marching, they solved the

local eigenvalue problem, and used the linear eigenmode as the initial condition. The amplification of stationary vortices is inhibited by nonlinearity when their amplitude reaches just about 4%. As vortices saturate, they roll up to form half-mushroom shaped structures, and inflectional points appear on the velocity profile, leading to secondary instability. MLC also studied nonlinear interaction between stationary and non-stationary modes. Stationary vortices were found to dominate most of the downstream development when its initial amplitude is ten times larger than that of the non-stationary mode. However, the non-stationary mode eventually acquires the same order of magnitude as the stationary one in the far downstream. When the initial amplitude of the stationary and non-stationary modes are of the same order of magnitude, the non-stationary mode dominates the downstream development. This trend of development is in agreement with the observation in experiment (Müller 1990). As a side product, the linear stability analysis shows that non-parallel flow effects destabilize crossflow disturbances, but the impact of non-parallelism depends on the value of $\bar{R} = W_f^* \delta_s / \nu$, where W_f^* denotes the free-stream velocity in the spanwise direction, δ_s denotes the (constant) boundary layer thickness, and ν is the kinematic viscosity. Their parametric study indicates that non-parallel flow effects play a more destabilizing role at lower values of $\bar{R}$.

In a subsequent paper, Malik et al. (1999) applied PSE approach to model the vortices pertaining to the experiments conducted on the 45° NLF(2)-0415 Airfoil in the Arizona State University (ASU) wind tunnel. The amplitude development of stationary vortices was predicted quite accurately by PSE. Secondary instability analysis of saturated vortices was performed, and the characteristics of growing modes are in agreement with experiments. Malik et al. (1999) suggested that transition could be correlated with the N-factor of the secondary mode rather than of the primary instability. Haynes and Reed (2000) carried out PSE analysis of the same experiments, with the aim of resolving discrepancy between the growth rate predicted by linear stability theory and measurements. They found that for the case of strong favourable pressure gradient, nonlinearity is the cause of the difference, but for weak pressure gradients, the curvature and non-parallel-flow effects are more important. Secondary instability of nonlinear travelling-wave vortices have been investigated by Wassermann and Kloker (2003) and Bonfigli and Kloker (2007) using DNS.

It has increasingly been recognised that receptivity is of crucial importance for transition. Experiments indicate that the size of the growth rate is not sufficient to determine which mode is the dominant disturbance; the occurrence of the latter depends also the

level of external disturbances. When the free-stream turbulence level is sufficiently low (typically below 0.15%), steady vortices dominate and cause transition (Müller and Bippes 1989, Deyhle and Bippes 1996) despite that they have smaller growth rates than travelling-wave modes. This was due to the extreme sensitivity to surface roughness, and further experimental studies showed that micron-sized roughness elements could generate steady vortices of considerable magnitude thereby influencing the transition process (Radeztsky et al. 1999). However, in presence of relatively high free-stream turbulence, travelling-wave vortices appear and become dominant (Nitschke-Kowsky and Bippes 1988; Bippes et al. 1991). Much of our current understanding of the role of environmental disturbances in transition process comes from the experimental work of Deyhle and Bippes (1996). They investigated the effect of different types of external disturbances on the excitation of crossflow vorticity including surface roughness, acoustic and vortical fluctuations in the free stream, or a combination of these. Their work confirmed the importance of roughness in exciting steady vortices, which are dominant distances in the boundary layer when the turbulence level is below a certain level. But as the turbulence intensity is increased from $Tu = 0.15\%$ to $Tu = 0.27\%$, the dominant mode changes from stationary to non-stationary. Interestingly, increasing the roughness height or the acoustic intensity had no appreciable impact. This is a clear indication that unsteady vortices are generated by free-stream turbulence alone without involving roughness. Free-stream acoustic fluctuations are found to have little influence.

Receptivity of three-dimensional boundary layers have been studied theoretically. The physical ideas are similar to those for two-dimensional boundary layers (e.g. Ruban 1984; Goldstein 1985), but mathematically finite-Reynolds-number formulations are adopted instead of an asymptotic approach. Crouch (1993) and Choudhari (1994) both considered excitation of stationary vortices by surface roughness which is periodic along the spanwise direction but localised in the chordwise direction. Since the time scale is absent, the mechanism is relatively straightforward: the scale matching only requires the spanwise wavelength of the roughness array to be comparable with that of steady modes. The boundary layer response is governed by an inhomogeneous boundary value problem, which can be solved by taking Fourier transform with respect the streamwise variable. The response has a continuous streamwise spectrum, from which a vortex mode would emerge. Choudhari (1994) also considered the generation of travelling-wave vortices by a free-stream acoustic wave interacting with roughness, but this mechanism turned out to be inefficient, consistent

with experimental observations. Both of these authors used in their calculations a simple model base flow, the Falkner-Skan-Cooke profile. Ng and Crouch (1999) went a step further and considered receptivity of the boundary layer over the NLF(2)-0415 with 45° sweep angle, which was used in numerous experiments at ASU. A good agreement was found between their theoretical prediction and the measurement made at ASU for roughness height up to twice the local boundary-layer displacement thickness, beyond which nonlinear effects become appreciable.

In all the work mentioned, curvature and nonparallel-flow effects are neglected. Bertolotti (1997) attempted to include the latter effect by a Taylor expansion of the mean flow about the roughness site. In order to account fully the curvature and non-parallelism, Collis and Lele (1999) carried out a DNS of crossflow vortices induced by surface roughness on a swept airfoil with a parabolic leading edge. Their numerical results indicate that receptivity is enhanced on a convex curvature. Comparing the non-parallel flow and parallel flow predictions, they concluded that parallel flow receptivity theory over predicts the receptivity considerably, contrary to the earlier conclusion of Ng and Crouch (1999) that the combined effects of non-parallelism and curvature were insignificant.

There have been very few theoretical studies of excitation of crossflow vortices by free-stream vortical disturbances. Ustinov (2001) considered the receptivity of swept wing boundary layer with a blunt leading edge to steady free-stream turbulence. The highlight of his work lies in applying the rapid distortion theory to obtain the inviscid solution, and using the method of matched asymptotic expansion to derive the initial and boundary conditions for the equations governing the induced perturbation within the boundary layer. However, the analysis assumed that the induced disturbance is periodic along the direction perpendicular to the direction of propagation rather than along the spanwise direction as it should be. The formulation is therefore not entirely correct. Recently, Schrader et al. (2009) attempted to use DNS to study the generation of non-stationary vortices by free-stream turbulence. The based flow was taken to be a Falkner-Skan-Cooke profile, which represents a swept wedge, while free-stream vortical disturbances were represented by continuous spectra of the O-S and Squire equations. These equations were solved with the resulting eigenfunctions being imposed at the inlet of the computation domain. This is the sole site where the external forcing acts on the boundary layer since a Neumann boundary condition is specified at the top of the computation domain. Numerical results indicate that unstable modes are generated, which the authors claim to describe the receptivity. However, we

think that neither the numerical set-up nor the result has much relevance to receptivity, for the following reasons. Firstly, the representation of free-stream disturbance is nonphysical. Crossflow instability occurs only when a pressure gradient is present, which means that the inviscid flow outide the boundary layer must be non-uniform. Oncoming disturbances are thus strained (distorted) when they propagate through the inviscid region. Clearly, continuous spectra, which take no account of this process and are completely local, cannot represent the true disturbance acting on the outer edge of the boundary layer. Secondly, the location of the inlet is chosen purely for computational convenience rather than for having any physical significance, which implies that the site at which the external disturbance enters the boundary layer is artificial and arbitrary. The DNS result indicates that the coupling coefficient depends on the location of the inlet, and keeps increasing as the inlet is moved upstream. This is a clear warning that vortices are actually generated near the leading edge, but as the authors concede, their numerical approach fails there. In summary, we believe that the claim of the paper is rather misleading and indeed trivialises the very issue of receptivity. Obviously, a similar simulation could be done for the familiar Blasius boundary layer, but then few would accept that as describing receptivity of T-S waves.

The aim of the present study is to provide a mathematical formulation which describes the excitation of crossflow vortices by small-amplitude free-stream vortical disturbances and their subsequent linear development. To fix the idea, we consider the base flow due to a uniform flow past a swept airfoil. The Reynolds number is assumed to be large so that the entire flow consists of an inviscid region, and a viscous boundary layer adjacent to the surface. The airfoil has a finite thickness causing a non-uniform ambient inviscid flow and a non-zero chordwise pressure gradient. The vortical disturbance in the oncoming flow is simply advected by the background mean velocity, but gets distorted by the strain field when approaching the airfoil. Our main interest is in analysing the boundary layer response to the disturbance in the inviscid region and identifying modes that can be excited.

The rest of this chapter is organized as follows. In §3.2, we formulate the problem mathematically and specify relevant scalings. In §3.3, the base flow field is calculated. Using the conformal mapping method, we first obtain the inviscid flow around a Joukowski airfoil at zero angle of attack. The slip velocity provides the far-field boundary condition for the base flow within the boundary layer. Then, the boundary-layer equations are solved numerically using Keller's box scheme. In §3.4, we formulate the initial-boundary-value problem for the unsteady perturbation. The solution in the inviscid region is derived

by applying the generalised rapid distortion theory, and the solution provides the far-field boundary condition for the unsteady boundary-layer equations governing the perturbation within the boundary layer. In order to determine the nature of the induced disturbance, the parallel and non-parallel eigenvalue problems are presented in §3.5. We show that the linear boundary-layer equations support a growing eigen mode, which will develop into fully fledge non-stationary vortices further downstream. The initial-boundary-value and eigenvalue problems are solved using numerical methods similar to those for Görtler vortices. Numerical solutions are presented in §3.6. A summary and concluding remarks are given in §3.7.

3.2 Formulation and scalings

We consider the response of a three-dimensional boundary layer over a swept Joukowski airfoil to free-stream turbulence. The oncoming mean flow is assumed to be uniform with a speed $U_\infty/\cos\phi_\infty$, where U_∞ is the free-stream velocity in the chordwise direction, and ϕ_∞ is the sweep angle. Free-stream turbulence is chosen to be stationary with a characteristic spanwise length scale Λ. The flow is described by the normalised orthogonal Cartesian coordinates

$$(x_o, y_o, z) = (x_o^*, y_o^*, z^*)/\Lambda, \tag{3.2.1}$$

and the normalised time

$$t = U_\infty t^*/\Lambda, \tag{3.2.2}$$

where x_o^* is along the chordwise direction, y_o^* is along the chord-normal direction, and z^* the spanwise direction; t^* is the dimensional time.

The oncoming mean flow, normalised by the chordwise free-stream velocity U_∞, can be written as

$$\mathbf{U_f} = (U_f, V_f, W_f) = (1, \quad 0, \quad -\tan\phi_\infty), \tag{3.2.3}$$

where the suffix f indicates the far field. As in LWG, we assume that FST is statistically stationary and homogenous, which allows us to represent it in the form of Fourier series. However, due to linearity, it suffices to consider a single Fourier component

$$\mathbf{u}_\infty = \mathbf{u}^\infty \exp\Big[\mathrm{i}(\mathbf{k}\cdot\mathbf{x} - \omega t)\Big], \tag{3.2.4}$$

where $\mathbf{k} = (k_1, k_2, k_3)$ is the non-dimensional wavenumber vector, ω is the non-dimensional frequency and

$$\mathbf{u}^{\infty} = (\hat{u}_1^{\infty}, \hat{u}_2^{\infty}, \hat{u}_3^{\infty})$$

are the normalised amplitudes of the FST in chordwise, normal and spanwise directions respectively. The normalised perturbed flow field $\mathbf{v}$ in the upstream can be written as

$$\mathbf{v} = \mathbf{U_f} + \epsilon \mathbf{u}^{\infty} \mathrm{exp}\Big[\mathrm{i}(\mathbf{k}\cdot\mathbf{x} - \omega t)\Big],$$

where $\epsilon \ll 1$ is a measure of turbulence intensity. Substituting the perturbed flow into the momentum equations, after linearisation, we obtain the governing equation for the disturbance

$$\frac{\partial \mathbf{u}_{\infty}}{\partial t} + U_f \frac{\partial \mathbf{u}_{\infty}}{\partial x_o} + W_f \frac{\partial \mathbf{u}_{\infty}}{\partial z} = 0. \tag{3.2.5}$$

Substitution of the mean flow (3.2.3) and perturbation (3.2.4) into (3.2.5) yields

$$\omega = k_1 - k_3 \mathrm{tan}\phi_{\infty}.$$

Therefore, the perturbation can be written as

$$\mathbf{u}_{\infty} = \mathbf{u}^{\infty} \mathrm{exp}\Big\{\mathrm{i}\Big[\mathbf{k}\cdot\mathbf{x} - (k_1 - k_3 \mathrm{tan}\phi_{\infty})t\Big]\Big\}.$$

Unlike streaks in a flat plate boundary layer (LWG) or Görtler vortices in the boundary layer over a concave wall, where $k_1 = \omega \ll O(1)$, we assume here $\omega, k_1 = O(1)$.

The flow domain can be divided into four asymptotic regions. Over $O(\Lambda)$ distances from the attachment line is an inviscid region, which has $O(\Lambda)$ dimensions in both the wall-normal and spanwise directions. The disturbance is treated as a small perturbation on a distorted mean flow. Beneath the inviscid region is a viscous boundary layer, where the perturbation is governed by the unsteady boundary layer equations. When the local boundary layer thickness δ grows to the same order of magnitude as the spanwise length scale Λ, a new region emerges, which will be referred to loosely as boundary region. However, the perturbation is not governed by the boundary region equations, but by linearised Euler equations or slightly more generally the Navier-Stokes equations with the streamwise diffusion terms being neglected. There is also an outer region describing the continued evolution of the oncoming disturbance, which is however of little relevance to issue ad-

dressed in this thesis. We shall therefore concentrate on the first three regions, especially the inviscid and the boundary layer regions.

3.3 The base flow

In this study, the base flow is taken to be the boundary layer over a swept Joukowski airfoil. In order to provide the appropriate far-field boundary condition, the external inviscid slip velocity u_e^* needs to be known. We apply the method of conformal mapping to obtain the value of u_e^*, and then solve the boundary layer equations numerically. The boundary layer over the airfoil will be described by the body-oriented coordinates (s^*, y^*), where s^* and y^* denote the distances alongside and perpendicular to the airfoil surface respectively. We let

$$S = s^*/L, \quad \text{and} \quad y = y^*/\delta_s,$$

where L is the chord length of the airfoil, and its value will be given in §3.3.1; δ_s denotes a characteristic boundary layer thickness at a particular streamwise location, and its value will be given when we consider the perturbation equations in §3.4.

3.3.1 The inviscid external flow

Complex potential and conformal mapping

For a two-dimensional irrotational flow, the velocity field can be described by

$$(u^*, v^*) = \Big(\frac{\partial \phi}{\partial x_o^*}, \frac{\partial \phi}{\partial y_o^*}\Big), \tag{3.3.1}$$

where the scalar function $\phi(x^*, y^*)$ is called the potential function. The velocity field can also be written as

$$(u^*, v^*) = \Big(\frac{\partial \psi}{\partial y_o^*}, -\frac{\partial \psi}{\partial x_o^*}\Big), \tag{3.3.2}$$

where the scalar function $\psi(x_o^*, y_o^*)$ is called the stream function. From (3.3.1) and (3.3.2) follow the relations between $\phi(x_o^*, y_o^*)$ and $\psi(x_o^*, y_o^*)$

$$\frac{\partial \phi}{\partial x_o^*} = \frac{\partial \psi}{\partial y_o^*}, \quad \frac{\partial \phi}{\partial y_o^*} = -\frac{\partial \psi}{\partial x_o^*}. \tag{3.3.3}$$

The above relations are called Cauchy-Riemann conditions, which are both necessary and sufficient conditions for $\phi + i\psi$ to be an analytic function of the complex argument $z = x_o^* + iy_o^*$, if the four partial derivatives in (3.3.3) are continuous. We may introduce a complex potential

$$w(z) = \phi + i\psi, \tag{3.3.4}$$

which is related to the velocity field by

$$\frac{dw}{dz} = \frac{\partial \phi}{\partial x_o^*} + i\frac{\partial \psi}{\partial x_o^*} = u^* - iv^*. \tag{3.3.5}$$

For a two-dimensional irrotational flow past a circular cylinder with its centre at $(0, 0)$, the complex potential can be written as

$$w(z) = U_\infty \Big(z e^{-i\alpha} + \frac{a_r^2}{z} e^{i\alpha} \Big) - \frac{i\Gamma}{2\pi} \log z, \tag{3.3.6}$$

where a_r is the radius of the circle, α is the attack angle of the oncoming flow, U_∞ is the free-stream velocity, and Γ is the circulation around the cylinder. As is well known, the irrotational flow field past a circle can be mapped onto the one past a symmetric Joukowski airfoil by Joukowski transformation

$$\zeta(z) = z + \frac{c^2}{z}, \tag{3.3.7}$$

where $\zeta = \xi^* + i\eta^*$ is the complex variable for the airfoil, $z = x_c^* + iy_c^*$ is the complex variable for the circle, and c is a constant. The centre of the circle is at $(-b, 0)$ with a radius $a_r = a + b$. Upon introducing the polar coordinates (r, θ) in the z plane, the circle and Joukowski airfoil can be parameterised by θ, i.e.

$$z = x_c^* + iy_c^* = -b + (a + b)e^{i\theta}, \tag{3.3.8}$$

and

$$\zeta = \xi^* + i\eta^* = -b + (a + b)e^{i\theta} + \frac{a^2}{-b + (a + b)e^{i\theta}}. \tag{3.3.9}$$

It follows that

$$\xi^*(\theta) = -b + (a + b)\cos\theta + \frac{a^2[-b + (a + b)\cos\theta]}{b^2 - 2b(a + b)\cos\theta + (a + b)^2}, \tag{3.3.10}$$

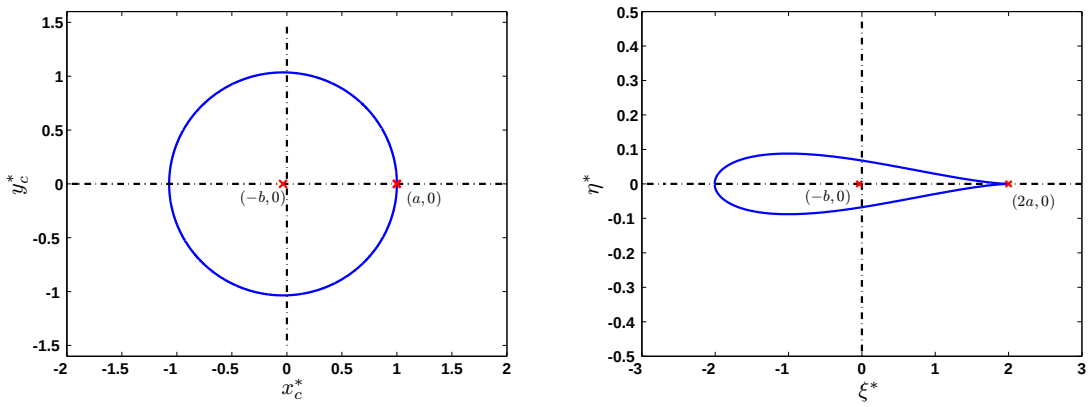


Figure 3.1: Joukowski transformation $\zeta(z) = z + c^2/z$ from the exterior of the circle to the exterior of the airfoil.

and

$$\eta^*(\theta) = (a+b)\sin\theta\Big[1 - \frac{a^2}{b^2 - 2b(a+b)\cos\theta + (a+b)^2}\Big]. \tag{3.3.11}$$

Note that the trailing and leading edges correspond to $\theta = 0, \pi$ respectively. From (3.3.10), we can obtain the chord length

$$L = \xi^*(0) - \xi^*(\pi) = 3a + 2b + \frac{a^2}{a+2b}. \tag{3.3.12}$$

Figure 3.1 shows the geometry of Joukowski airfoil through the conformal mapping (3.3.7), and figure 3.2 shows the geometry of Joukowski airfoil for different ratios of b/a. As is illustrated, an airfoil shape appears for relatively small b/a, and so we assume that $b/a \ll 1$.

Using (3.3.10) and (3.3.11), we may calculate the curvature of the airfoil , which is defined as

$$K = \frac{|\eta^{*\prime\prime}\xi^{*\prime} - \eta^{*\prime}\xi^{*\prime\prime}|}{[(\xi^{*\prime})^2 + (\eta^{*\prime})^2]^{\frac{3}{2}}}, \tag{3.3.13}$$

where a prime denotes differentiation with respect to θ, with

$$\frac{d\xi^*}{d\theta} = -(a+b)\sin\theta + \frac{a^2(a+b)[b^2 - (a+b)^2]\sin\theta}{\Big[b^2 - 2b(a+b)\cos\theta + (a+b)^2\Big]^2},$$

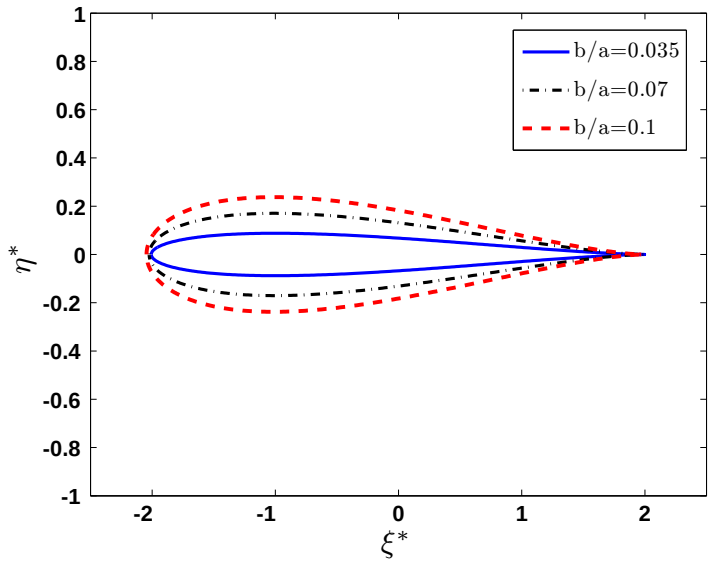


Figure 3.2: Geometry of Joukowski airfoil for different ratios of b/a.

$$\frac{d\eta^*}{d\theta} = (a+b)\cos\theta + \frac{a^2(a+b)[2b(a+b) - b^2\cos\theta - (a+b)^2\cos\theta]}{\Big[b^2 - 2b(a+b)\cos\theta + (a+b)^2\Big]^2},$$

$$\frac{d^2\xi^*}{d\theta^2} = a^2(a+b)[b^2 - (a+b)^2]\frac{[b^2 + (a+b)^2]\cos\theta - 2b(a+b) - 2b(a+b)\sin^2\theta}{\Big[b^2 - 2b(a+b)\cos\theta + (a+b)^2\Big]^3} - (a+b)\cos\theta,$$

$$\frac{d^2\eta^*}{d\theta^2} = a^2(a+b)\frac{\Big[b^2 + (a+b)^2\Big]\Big[b^2 + 2b(a+b)\cos\theta + (a+b)^2\Big] - 8b^2(a+b)^2}{\Big[b^2 - 2b(a+b)\cos\theta + (a+b)^2\Big]^3}\sin\theta - (a+b)\sin\theta.$$

Substituting the derivatives into (3.3.13) , and taking the leading-order approximation, we obtain the leading-order approximation for the curvature,

$$K = \frac{a^3(a+2b)}{16b^2(a+b)^3} = O(\frac{a}{16b^2}), \tag{3.3.14}$$

indicating that the radius of curvature is of $O(16b^2/a)$. Figure 3.3 shows the relevant char-

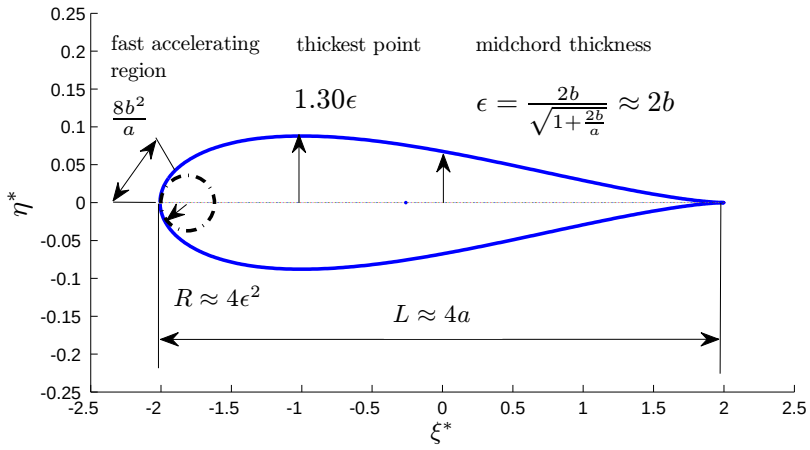


Figure 3.3: Characteristic length scales of symmetric Joukowski airfoil for $b/a = 0.035$.

acteristic length scales of a symmetric Joukowski airfoil.

When the circle is centred at $(-b, 0)$, the complex potential (3.3.6) becomes

$$w(z) = U_\infty \left[(z+b)e^{-i\alpha} + \frac{(a+b)^2}{z+b} e^{i\alpha} \right] - \frac{i\Gamma}{2\pi} \log(z+b). \tag{3.3.15}$$

Since the complex potentials for the flows past the circle and airfoil have the same value at the corresponding points of the two planes,

$$\frac{dW}{d\zeta} = \frac{dw/dz}{d\zeta/dz} = \left\{ U_\infty \left[e^{-i\alpha} - \left(\frac{a+b}{z+b} \right)^2 e^{i\alpha} \right] - \frac{i\Gamma}{2\pi(z+b)} \right\} \Big/ \left\{ 1 - \frac{a^2}{z^2} \right\} = u^*_{et} - i v^*_{et}, \tag{3.3.16}$$

where $W(\zeta)$ is the complex potential around the airfoil, u^*_{et} and v^*_{et} are the velocity components in the chordwise and normal directions respectively. Note that the velocity given by equation (3.3.16) becomes singular at $z = \pm a$ in general. The singular point $z = -a$ is inside the airfoil, and hence no special treatment for this singular point is needed. However, the singular point $z = a$ locates at the trailing edge of the airfoil. The singularity at the trailing edge must be removed by assigning the appropriate value to Γ. This is the so-called Kutta-Joukowski condition. Application of this means the value of Γ must be chosen such that the numerator of (3.3.16) tends to zero as $z \to a$, that is

$$\Gamma = -4\pi U_\infty (a+b) \sin\alpha. \tag{3.3.17}$$

Substituting (3.3.17) into (3.3.16), the flow field of the airfoil becomes singularity free (Acheson 1990). Equation (3.3.17) indicates that there is no circulation ($\Gamma = 0$) when the angle of attack α is zero, which is the case we consider in this thesis.

The slip velocity

For the special case $\Gamma = 0$, if we substitute (3.3.8) into (3.3.16), the non-dimensional chordwise and normal components of the slip velocity can be written as

$$u_{et} = 1 - \cos 2\theta + \frac{(1+p)^2}{q^2 + 2q\cos\theta + 1}\Big[q\cos\theta + \cos 2\theta + q\cos 2\theta + \cos 3\theta\Big], \tag{3.3.18}$$

$$v_{et} = \sin 2\theta - \frac{(1+p)^2}{q^2 + 2q\cos\theta + 1}\Big[q\sin\theta + \sin 2\theta + q\sin 2\theta + \sin 3\theta\Big], \tag{3.3.19}$$

where

$$u_{et} = u^*_{et}/U_\infty, \quad v_{et} = v^*_{et}/U_\infty, \tag{3.3.20}$$
$$p = \frac{-b}{b+a} = O(b/a), \qquad q = \frac{-b+a}{b+a} = O(1).$$

The total slip velocity $u^*_e \equiv \sqrt{{u^*_{et}}^2 + {v^*_{et}}^2}$ is normalised by the chordwise free-stream velocity U_∞, i.e.

$$u_e = \frac{u^*_e}{U_\infty} = \sqrt{u^2_{et} + v^2_{et}}. \tag{3.3.21}$$

Using (3.3.18) and (3.3.19), we find

$$u_e = \frac{2\sin\theta(p^2 + 2p\cos\theta + 1)}{\sqrt{2(1-\cos\theta)(q^2 + 2q\cos\theta + 1)}}, \tag{3.3.22}$$

which is the same as given in Turkyilmazoglu et al. (1999).

We now seek asymptotic approximation to u_e as $\theta \to \pi$, i.e. near the leading edge, which will be used to approximate other values within the boundary layer. Substitution of the Taylor expansions of $\sin\theta$ and $\cos\theta$ about $\theta = \pi$,

$$\sin\theta = \pi - \theta + O[(\pi-\theta)^3], \quad \text{and} \quad \cos\theta = -1 + O[(\pi-\theta)^2], \tag{3.3.23}$$

into (3.3.22) yields

$$u_e = \frac{(\pi-\theta)(p-1)^2}{|q-1|} + O[(\pi-\theta)^2]. \tag{3.3.24}$$

Equation (3.3.24) will be referred to as the first-order approximation to u_e, where $|q-1| = O(b/a)$, and $p-1 = O(1)$. Since the first term in (3.3.24) should be much larger than the second term, this first-order approximation is valid for $(\pi-\theta) \ll b/a$.

The slip velocity given by (3.3.22) may also be written as

$$u_e = 2\cos\frac{\theta}{2}\frac{p^2+2p\cos\theta+1}{\sqrt{q^2+2q\cos\theta+1}}. \tag{3.3.25}$$

Expanding $\cos\theta$ and $\cos(\theta/2)$ as Taylor series about $\theta=\pi$ up to second order,

$$\cos\theta = -1+\frac{(\theta-\pi)^2}{2}+O[(\pi-\theta)^4], \quad \text{and} \quad \cos\frac{\theta}{2} = -\frac{(\theta-\pi)}{2}+\frac{(\theta-\pi)^3}{48}+O[(\pi-\theta)^5]. \tag{3.3.26}$$

and inserting them into (3.3.25), we obtain

$$u_e = \frac{(p-1)^2(\pi-\theta)}{\sqrt{(q-1)^2+q(\pi-\theta)^2}}\Big\{1+O[(\pi-\theta)^2]\Big\}. \tag{3.3.27}$$

The two terms within the square root of equation (3.3.27) are of the same order of magnitude for $\pi-\theta = O(b/a)$. Equation (3.3.27) will be referred to as the second-order approximation to u_e, valid for $\pi-\theta = O(b/a)$. When $(\pi-\theta) \ll b/a$, Taylor expansion of the denominator of (3.3.27) can be performed to obtain

$$u_e = \frac{(p-1)^2(\pi-\theta)}{|q-1|}+\Big[\frac{p}{|q-1|}-\frac{q(p-1)^2}{2|q-1|^3}\Big](\pi-\theta)^3+O[(\pi-\theta)^5].$$

On the other hand, when $b/a \ll \pi-\theta \ll 1$, from equation (3.3.25), and retaining the $O[(\pi-\theta)^2]$ terms, the slip velocity can be written as

$$u_e = \frac{(p-1)^2+[p-(p-1)^2/48](\pi-\theta)^2}{\sqrt{q+\left(\frac{q-1}{\pi-\theta}\right)^2}}+O[(\pi-\theta)^3]. \tag{3.3.28}$$

A further Taylor expansion of the denominator for $(q-1)/(\pi-\theta) \ll 1$ gives the second-order approximation for (3.3.28),

$$u_e = \frac{1}{\sqrt{q}}(p-1)^2+\frac{p-(p-1)^2/48}{\sqrt{q}}(\pi-\theta)^2-\frac{p-1}{2q\sqrt{q}}\frac{(q-1)^2}{(\pi-\theta)^2}+O[(\pi-\theta)^3]. \tag{3.3.29}$$

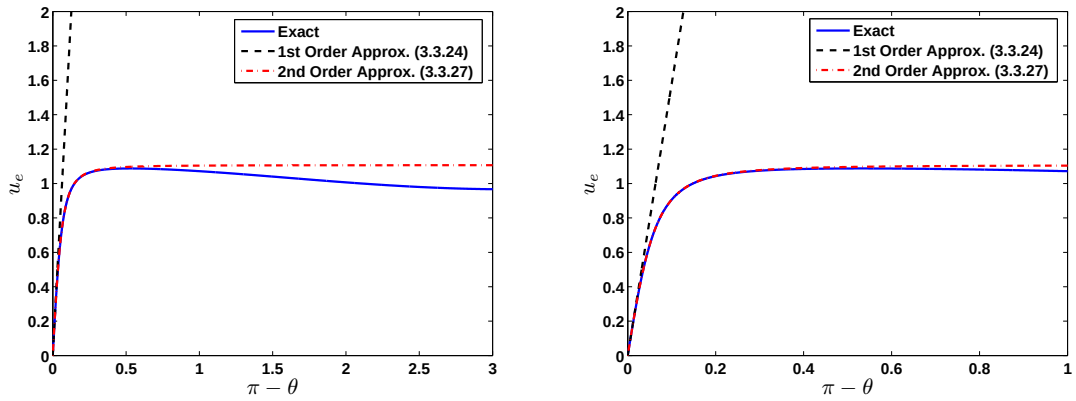


Figure 3.4: Comparison of the asymptotic approximations with the exact solution (theory) for u_e $(b/a = 0.035)$.

As $\theta \to 0$, Taylor expansions of $\cos\theta$ and $\cos(\theta/2)$ about $\theta = 0$ are

$$\cos\theta = 1 - \frac{1}{2}\theta^2 + O(\theta^4), \quad \text{and} \quad \cos\frac{\theta}{2} = 1 - \frac{1}{8}\theta^2 + O(\theta^4). \tag{3.3.30}$$

Substitution of (3.3.30) into (3.3.25) yields the approximation for the slip velocity close to the trailing edge,

$$u_e = \frac{2(p+1)}{|q+1|} + \Big[\frac{q(p+1)^2}{(q+1)^2} - \frac{8p + (p+1)^2}{4\cdot|q+1|}\Big]\theta^2 + O(\theta^4).$$

The comparison of different asymptotic approximations for u_e with the exact expression (3.3.22) is shown in figure (3.4). As expected, the second-order approximation for u_e matches the exact solution in a larger domain.

The slip velocity has been expressed in terms of θ. However for the purpose of solving the boundary layer equations, it is convenient to provide the slip velocity at each location S. This can be done by finding the relation between S and θ. Using the relation

$$\frac{dS}{d\theta} = \frac{1}{L}\frac{ds^*}{d\theta} = \sqrt{(d\xi^*)^2 + (d\eta^*)^2}\Big/ L d\theta = -\sqrt{(\frac{d\xi^*}{d\theta})^2 + (\frac{d\eta^*}{d\theta})^2}\Big/ L = -|\zeta'(\theta)|\Big/ L,$$

we have

$$S = -\int_{\pi}^{\theta} |\zeta'(\theta)| d\theta \Big/ L.$$

From equation (3.3.9) it follows that

$$|\zeta'(\theta)| = \left| i(a+b)e^{i\theta} - \frac{ia^2(a+b)e^{i\theta}}{[-b+(a+b)e^{i\theta}]^2} \right| = (a+b)\left| \frac{[-b+(a+b)e^{i\theta}]^2 - a^2}{[-b+(a+b)e^{i\theta}]^2} \right|,$$

and therefore

$$S = -\Big(\frac{a+b}{L}\Big) \int_{\pi}^{\theta} \left| \frac{[-b+(a+b)e^{i\theta}]^2 - a^2}{[-b+(a+b)e^{i\theta}]^2} \right| d\theta, \tag{3.3.31}$$

and the total length is

$$S_{\text{total}} = -\Big(\frac{a+b}{L}\Big) \int_{\pi}^{0} \left| \frac{[-b+(a+b)e^{i\theta}]^2 - a^2}{[-b+(a+b)e^{i\theta}]^2} \right| d\theta.$$

When $\theta \to \pi$, the first-order approximation for S can be found from (3.3.31) as

$$S = \Big(\frac{a+b}{L}\Big) \Big[\frac{(a+2b)^2 - a^2}{(a+2b)^2}\Big] (\pi - \theta) + O[(\pi-\theta)^2], \tag{3.3.32}$$

Combination of (3.3.24) and (3.3.32) gives an explicit relation between u_e and S,

$$u_e = \frac{S \cdot L}{2(a+b)} \cdot \Big[\frac{(a+2b)^2}{2b(a+b)}\Big]^2 + O(S^2). \tag{3.3.33}$$

Since

$$\Big[\frac{(a+2b)^2}{2b(a+b)}\Big]^2 = O(a^2/b^2), \quad \text{and} \quad L = O(a),$$

the validity of (3.3.33) is restricted to $S \ll O(b^2/a^2)$. A second-order approximation valid up to $S = O(b^2/a^2)$ can be derived by expressing S in terms of $\pi - \theta$, accurate up to $\pi - \theta = O(b/a)$. This requires us to expand the integrand in (3.3.31) to the second order. The detailed derivation is given in the appendix A1.

For a general $0 < \theta < \pi$, the relation between u_e and S has to be determined numerically. We let

$$F(\theta, S) = S + \Big(\frac{a+b}{L}\Big) \int_{\pi}^{\theta} \left| \frac{[-b+(a+b)e^{i\theta}]^2 - a^2}{[-b+(a+b)e^{i\theta}]^2} \right| d\theta.$$

The relation between S and θ is determined by $F(\theta, S) = 0$. For each given value of S, the

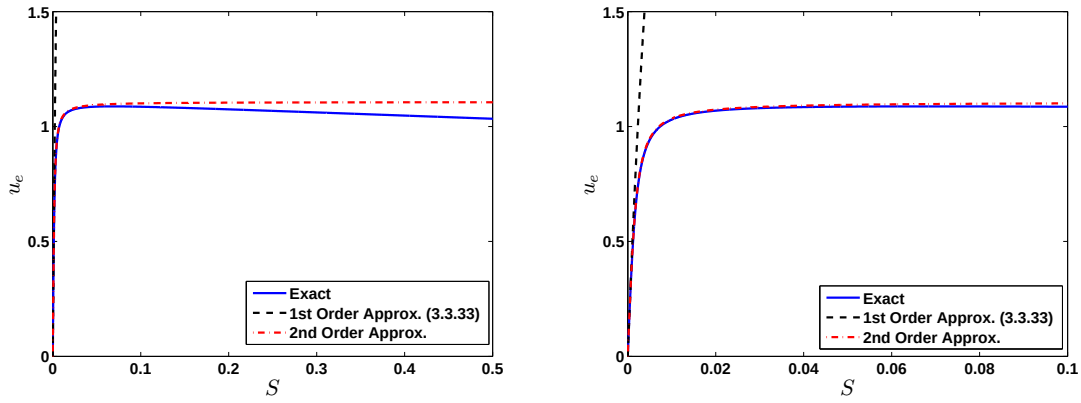


Figure 3.5: The relation between u_e and S, and comparison of the asymptotic approximation with the exact numerical solution $(b/a = 0.035)$.

corresponding value of θ can be calculated using the Newton-Raphson iteration

$$\theta^{i+1} = \theta^i - \frac{F(\theta^i, S)}{F'(\theta^i, S)},$$

where the integral term in function $F(\theta)$ is evaluated by using Simpson's Rule. When the value of θ is known, the value of u_e will be known from (3.3.22). Therefore, a relation between u_e and S is built.

Figures 3.5 and 3.6 show the slip velocity as a function of S. As is indicated, the slip velocity undergoes a rapid linear increase close to the leading edge, and then decreases slowly as S becomes larger. From figure 3.5, we note that the second-order approximation fits the numerical result in a larger domain, which is due to the fact that this approximation is valid up to $S = O(b^2/a^2)$.

3.3.2 The boundary layer flow

The steady two-dimensional boundary layer equations can be written as

$$\frac{\partial u_B^*}{\partial s^*} + \frac{\partial v_B^*}{\partial y^*} = 0, \tag{3.3.34}$$

$$u_B^* \frac{\partial u_B^*}{\partial s^*} + v_B^* \frac{\partial u_B^*}{\partial y^*} = -\frac{1}{\rho}\frac{\partial p^*}{\partial s^*} + \frac{\mu}{\rho}\frac{\partial^2 u_B^*}{\partial y^{*2}}, \tag{3.3.35}$$

where u_B^*, and v_B^* are the dimensional velocities in s^* and y^* directions respectively, and p^* is the dimensional pressure.

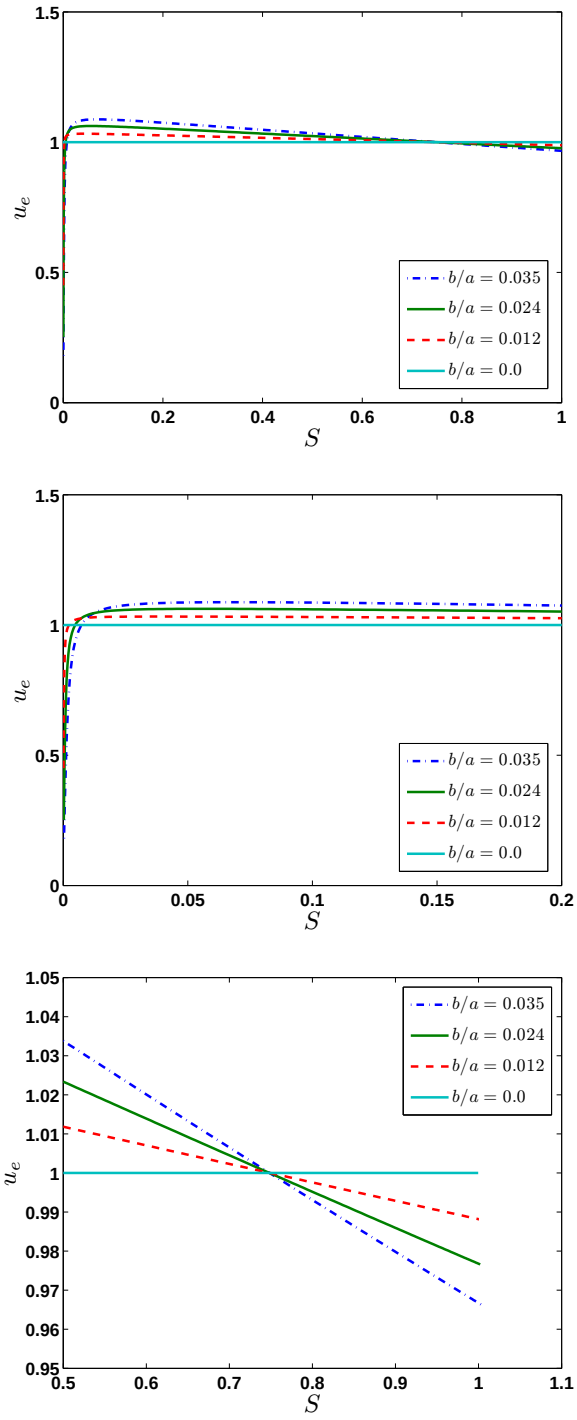


Figure 3.6: The distribution of the slip velocity along the airfoil surface for different values of b/a.

The Falkner-Skan transformation is introduced by

$$\eta = \left(\frac{u_e^*}{\nu s^*}\right)^{1/2} y^*, \tag{3.3.36}$$

where $u_e^* = u_e(S)U_\infty$, and $\nu = \mu/\rho$ is the kinematic viscosity. A dimensionless stream function $f(S,\eta)$ is introduced by

$$\psi(s^*, y^*) = (u_e^* \nu s^*)^{1/2} f(S,\eta).$$

Then the streamwise and normal velocities can be written as

$$u_B^* = \frac{\partial \psi}{\partial y^*} = (\frac{u_e^*}{\nu s^*})^{1/2} \frac{\partial \psi}{\partial \eta} = u_e f' U_\infty, \tag{3.3.37}$$

and

$$v_B^* = -\frac{\partial \psi}{\partial s^*} = -\left(\left.\frac{\partial \psi}{\partial s^*}\right|_\eta + \frac{\partial \psi}{\partial \eta}\frac{\partial \eta}{\partial s^*}\right) = -\left.\frac{\partial[(u_e^*\nu s^*)^{1/2} f]}{\partial s^*}\right|_\eta - (u_e^*\nu s^*)^{1/2} f' \frac{\partial \eta}{\partial s^*}, \tag{3.3.38}$$

where a prime denotes differentiation with respect to η. Substituting (3.3.37), (3.3.38) and

$$\frac{dp^*}{ds^*} = -\rho u_e^* \frac{du_e^*}{ds^*}$$

which comes from Bernoulli's principle, into (3.3.34) and (3.3.35), we obtain the transformed momentum equation for two-dimensional laminar flow (Cebeci and Bradshaw 1977)

$$f''' + \frac{m+1}{2} f f'' + m[1 - (f')^2] = s^*\left(f'\frac{\partial f'}{\partial s^*} - f''\frac{\partial f}{\partial s^*}\right) = S\left(f'\frac{\partial f'}{\partial S} - f''\frac{\partial f}{\partial S}\right), \tag{3.3.39}$$

where m is a dimensionless pressure gradient parameter defined by

$$m = \frac{s^*}{u_e^*}\frac{du_e^*}{ds^*} = \frac{S}{u_e}\frac{du_e}{dS}.$$

Excluding suction or blowing at the wall, the boundary conditions for (3.3.39) are

$$f' = 0 \qquad \text{and} \qquad f(S,0) = 0 \quad \text{at} \quad \eta = 0; \tag{3.3.40}$$

$$f' \to 1 \quad \text{as} \quad \eta \to \infty. \tag{3.3.41}$$

Near the leading edge ($S \to 0$), the slip velocity $u_e \sim S$ as is indicated by (3.3.33), and so $m = 1$, and the function f is independent of the coordinate S. Equation (3.3.39) then reduces to the Falkner-Skan equation,

$$f''' + \frac{m+1}{2} f f'' + m[1 - (f')^2] = 0, \tag{3.3.42}$$

which describes the boundary-layer flow in the vicinity of the stagnation point.

The solution to the Falkner-Skan equation (3.3.42) serves as the initial condition for solving (3.3.39). We apply Keller's shooting method to solve (3.3.42) (Cebeci and Bradshaw 1977; Cebeci and Cousteix 2005). According to this method, we need first to recast equation (3.3.42) into a system of three first-order ordinary differential equations,

$$f' = u, \tag{3.3.43}$$

$$u' = h_0, \tag{3.3.44}$$

$$h_0' = -\frac{m+1}{2} f h_0 - m(1 - u^2), \tag{3.3.45}$$

with the boundary conditions

$$f(0) = 0, \qquad u(0) = 0; \tag{3.3.46}$$

$$u \to 1 \quad \text{as} \quad \eta \to \infty. \tag{3.3.47}$$

In order to start the numerical integration of (3.3.43)–(3.3.45), the value of $h_0(0)$ is needed. Let an initial guess for $h_0(0)$ be denoted by g, i.e.

$$h_0(0) = g, \tag{3.3.48}$$

and the solution of Falkner-Skan equation be denoted by $\Big[f(\eta, g), u(\eta, g), h_0(\eta, g)\Big]$. Then the value of g can be determined by matching with the upper boundary condition, which is imposed by using the Newton-Raphson iteration,

$$g^{i+1} = g^i - \frac{H(g^i)}{H'(g^i)}, \tag{3.3.49}$$

where

$$H(g) = u(\eta_\infty, g) - 1,$$

a prime denotes differentiation with respect to g, and η_∞ is a large positive number suitably chosen. In order to determine

$$H'(g) = \frac{\partial u(\eta_\infty, g)}{\partial g},$$

we differentiate (3.3.43)–(3.3.45) with respect to g to obtain the so-called variational equations (Cebeci and Bradshaw 1977; Cebeci and Cousteix 2005)

$$F' = U, \tag{3.3.50}$$

$$U' = H_0, \tag{3.3.51}$$

$$H_0' = -\frac{m+1}{2}(fH_0 + h_0 F) + 2muU, \tag{3.3.52}$$

where a prime denotes differentiation with respect to η, and F, U and H_0 are defined by

$$F(\eta, g) = \frac{\partial f}{\partial g}, \qquad U(\eta, g) = \frac{\partial u}{\partial g}, \qquad H_0(\eta, g) = \frac{\partial h_0}{\partial g}.$$

The initial conditions (at $\eta = 0$) are

$$F(0) = 0, \qquad U(0) = 0, \qquad H_0(0) = \frac{\partial g}{\partial g} = 1. \tag{3.3.53}$$

For a given g^i, the Falkner-Skan equation (3.3.43)–(3.3.45) subject to the boundary condition (3.3.46) and (3.3.48) is solved using a fourth-order Runge-Kutta method to obtain $u(\eta_\infty, g)$ and $H(g)$. The variational equations (3.3.50)–(3.3.52) subject to the conditions (3.3.53) is integrated using the Runge-Kutta method to calculate $U(\eta_\infty, g) = H'(g)$. The next approximation to $h_0(0)$, g^{i+1}, can be computed from (3.3.49). This procedure is repeated until convergence is achieved, i.e. when

$$|g^{i+1} - g^i| < \epsilon,$$

where ϵ is a tolerance parameter, chosen to be 10^{-6} in our calculation (Cebeci and Bradshaw 1977; Cebeci and Cousteix 2005).

Figure 3.7 displays the profiles of the base flow velocity in the S direction for different

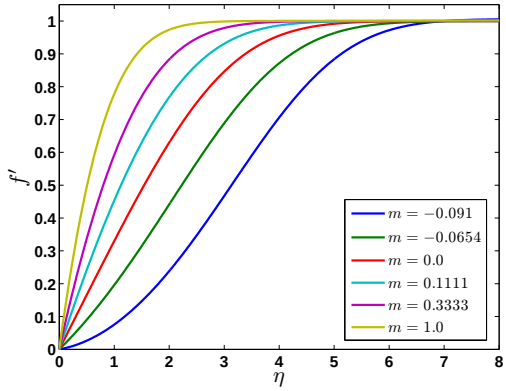


Figure 3.7: Solution to Falkner-Skan equation for different values of m.

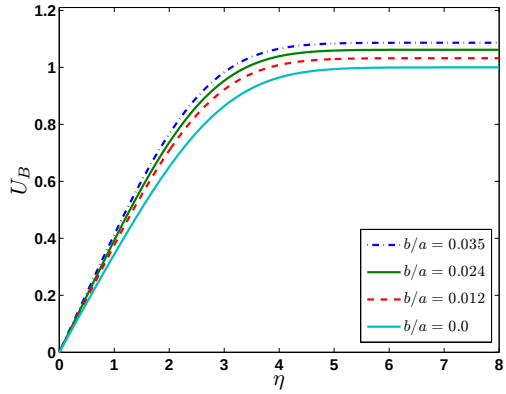


Figure 3.8: Velocity profiles for different ratios of b/a at $S = 0.05$.

m. Among these, only the one for $m = 1$ will be used as the initial condition for solving (3.3.39).

The transformed boundary layer equation (3.3.39) is solved by using Keller's box method, which is explained in detail in Cebeci and Bradshaw (1977). The solution to the Falkner-Skan equation is used as the initial condition to start the marching. With the boundary conditions given by (3.3.40) and (3.3.41), the solution to (3.3.39) can be obtained. The base flow velocity in the S direction at $S = 0.05$ and $S = 0.99$ are shown in figure 3.8 and figure 3.9 respectively. The results are in agreement with those shown in Turkyilmazoglu et al. (1999), confirming that our numerical code implements the Keller's box method correctly.

In the spanwise direction, the slip velocity $W_f^* = W_f U_\infty$ is a constant value for all S.

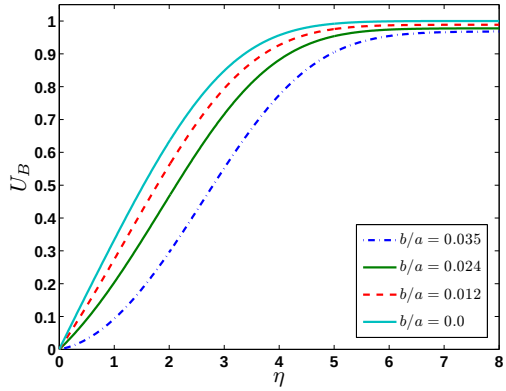


Figure 3.9: Velocity profiles for different ratios of b/a at $S = 0.99$.

From Bernoulli's principle,

$$p^* + \frac{1}{2}\rho[u_e^{*2} + W_f^{*2}] = \text{constant}, \tag{3.3.54}$$

it follows that the pressure gradient is zero in the spanwise direction, i.e. $\frac{\partial p^*}{\partial z^*} = 0$. Since the airfoil has an infinite span, the spanwise velocity w_B^* is uniform, i.e.

$$\frac{\partial w_B^*}{\partial z^*} = 0. \tag{3.3.55}$$

Therefore, the momentum equation in the spanwise direction reduces to

$$u_B^* \frac{\partial w_B^*}{\partial s^*} + v_B^* \frac{\partial w_B^*}{\partial y^*} = \frac{\mu}{\rho} \frac{\partial^2 w_B^*}{\partial y^{*2}}, \tag{3.3.56}$$

with the boundary conditions

$$\eta = 0: \qquad w_B^*(S, 0) = 0, \qquad \eta = \eta_\infty: \qquad w_B^*(S, \eta_\infty) = W_f^* = W_f \cdot U_\infty, \tag{3.3.57}$$

where $W_f = -\tan\phi_\infty$ is the non-dimensional spanwise slip velocity.

Substituting η, (3.3.37) and (3.3.38) into (3.3.56), we obtain

$$u_e f' \frac{\partial W_B}{\partial s^*} + \Big[-\frac{u_e}{2s^*} f - u_e \frac{\partial f}{\partial s^*} - \frac{1}{2} f \frac{du_e}{ds^*} \Big] \frac{\partial W_B}{\partial \eta} = \frac{u_e}{s^*} \frac{\partial^2 W_B}{\partial \eta^2}, \tag{3.3.58}$$

where

$$W_B = \frac{w_B^*}{U_\infty}. \tag{3.3.59}$$

After a rearrangement of (3.3.58), we have

$$\frac{\partial^2 W_B}{\partial \eta^2} + \Big[\frac{1}{2}f + S\frac{\partial f}{\partial S} + \frac{1}{2}f\frac{S}{u_e}\frac{du_e}{dS}\Big]\frac{\partial W_B}{\partial \eta} = Sf'\frac{\partial W_B}{\partial S}. \tag{3.3.60}$$

After solving the transformed streamwise momentum equation, f, f' and $\frac{\partial f}{\partial S}$ are already known. Equation (3.3.60) can be solved by using Keller's box method once the proper initial condition is provided. The latter can be derived by noting that as $S \to 0$, equation (3.3.60) reduces to

$$\frac{\partial^2 W_B}{\partial \eta^2} + \frac{1}{2}f(1+m)\frac{\partial W_B}{\partial \eta} = 0. \tag{3.3.61}$$

Equation (3.3.61) combined with (3.3.42) are called the Falkner-Skan-Cooke equations. The initial condition for (3.3.60) is obtained by solving (3.3.61). In order to solve (3.3.61), it is convenient to introduce a dimensionless function $h(S,\eta)$ through the relation

$$W_B = W_f h(S,\eta). \tag{3.3.62}$$

In terms of h, we can write (3.3.61) as

$$\frac{\partial^2 h}{\partial \eta^2} + \frac{1}{2}f(1+m)\frac{\partial h}{\partial \eta} = 0, \tag{3.3.63}$$

with the boundary conditions:

$$\eta = 0: \qquad h(0) = 0, \qquad \eta = \eta_\infty: \qquad h(\eta_\infty) = 1. \tag{3.3.64}$$

Keller's shooting method (Cebeci and Bradshaw 1977; Cebeci and Cousteix 2005) is applied to solve (3.3.63). In order to implement this method, we first recast the equation into two first-order ODEs,

$$h' = d, \tag{3.3.65}$$

$$d' = -\gamma_1 d, \tag{3.3.66}$$

where

$$\gamma_1 = \frac{1}{2}(1+m)f.$$

Suppose $d(0) = \bar{g}$. The value of $\bar{g}$ will be determined by imposing the boundary condition $h(\eta_\infty) = 1$ via the Newton-Raphson interaction

$$\bar{g}^{i+1} = \bar{g}^i - \frac{\bar{H}(\bar{g}^i)}{\bar{H}'(\bar{g}^i)}, \tag{3.3.67}$$

where $\bar{H} = h(\eta_\infty, \bar{g}) - 1$, and a prime denotes differentiation with respect to $\bar{g}$. The value of $\bar{H}'(g)$ is obtained by solving the variational equations

$$E' = D, \tag{3.3.68}$$

$$D' = -\gamma_1 D, \tag{3.3.69}$$

where a prime denotes differentiation with respect to η, and E and D are defined by

$$E(\eta, \bar{g}) = \frac{\partial h}{\partial \bar{g}}, \qquad D(\eta, \bar{g}) = \frac{\partial d}{\partial \bar{g}}.$$

The initial conditions (at $\eta = 0$) are

$$E(0) = 0, \qquad D(0) = 1. \tag{3.3.70}$$

We apply the same method as that for solving the Falkner-Skan equation to obtain the solution to (3.3.63). Figure 3.10 shows the velocity profiles of Falkner-Skan-Cooke boundary layer when $m = 1$.

Through the transformation (3.3.62), we can rewrite (3.3.60) as

$$\frac{\partial^2 h}{\partial \eta^2} + \Big[\frac{1}{2} f + S\frac{\partial f}{\partial S} + \frac{1}{2} f \frac{S}{u_e}\frac{du_e}{dS}\Big]\frac{\partial h}{\partial \eta} = S f' \frac{\partial h}{\partial S}. \tag{3.3.71}$$

When initial value for (3.3.71) is obtained, applying Keller's box method, equation (3.3.71) can be solved. The boundary layer velocity profiles at different downstream locations are displayed in figure 3.11.

3.4 Perturbation equations

We now consider the interaction of the perturbation with the airfoil in the $O(\Lambda)$ vicinity of the leading edge. The perturbation is governed by two regions. We first seek the per-

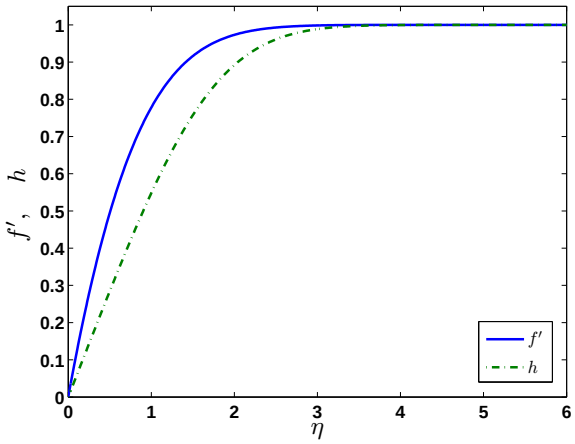


Figure 3.10: Velocity profiles of Falkner-Skan-Cooke boundary layer with $m = 1$.

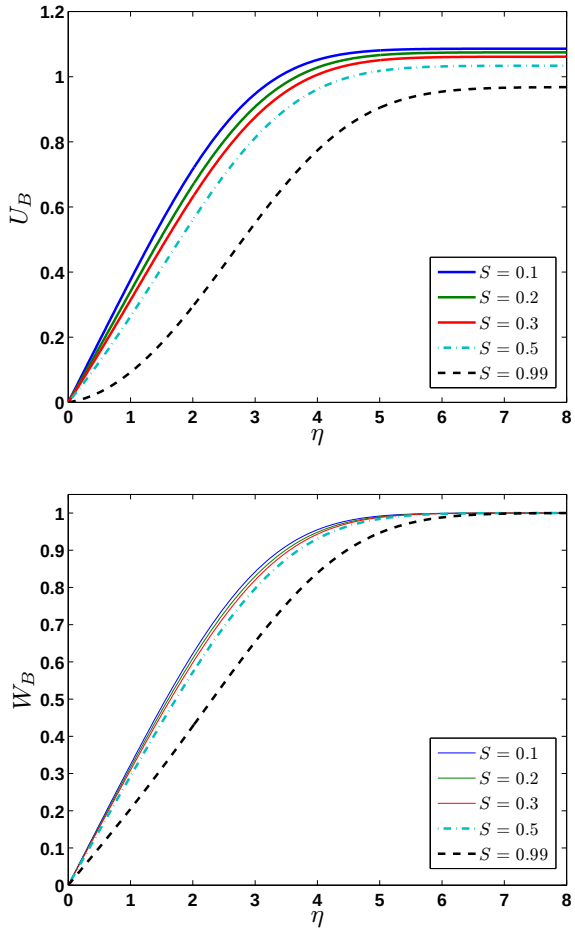


Figure 3.11: Chordwise and spanwise velocity profiles at different downstream locations with $b/a = 0.035$.

turbation solution in the inviscid region, which will be treated as the far-field condition for unsteady boundary layer equations which govern the perturbation within the boundary layer. In order to provide the initial condition, the solution for the perturbation at the stagnation point is constructed. With both the initial and boundary conditions specified, we solve the initial-boundary-value problem to calculate the amplitude and the growth rate of the perturbation.

3.4.1 General governing equations

In the inviscid region, the normalised coordinates and time t are given in (3.2.1) and (3.2.2) respectively. The velocity field is normalised by the free-stream velocity in the chordwise direction U_∞, and the pressure p^* is normalised by ρU_∞^2 , i.e.

$$(u, v, w) = (u^*, v^*, w^*)/U_\infty, \tag{3.4.1}$$

and

$$p = p^*/\rho U_\infty^2. \tag{3.4.2}$$

The governing equations in this region are the continuity equation and Euler's equations, which can, in the vector form, be written as

$$\nabla \cdot \mathbf{v} = 0, \tag{3.4.3}$$

and

$$\frac{D\mathbf{v}}{Dt} = -\nabla p, \tag{3.4.4}$$

where $\mathbf{v} = (u, v, w)$ is the velocity vector,

$$\nabla = \frac{\partial}{\partial x_o}\hat{\mathbf{i}} + \frac{\partial}{\partial y_o}\hat{\mathbf{j}} + \frac{\partial}{\partial z}\hat{\mathbf{z}}, \qquad \frac{D}{Dt} = \frac{\partial}{\partial t} + \mathbf{v} \cdot \nabla$$

with $\hat{\mathbf{i}}$, $\hat{\mathbf{j}}$, $\hat{\mathbf{z}}$ being the unit vectors in x_o, y_o, and z directions respectively.

In the viscous region, the body-oriented coordinates (s^*, y^*, z^*) are applied, where s^* and y^* measure the distance along and normal to the airfoil surface respectively, and z^*

measures the distance in the spanwise direction. The local boundary layer thickness is

$$\delta = \left(\frac{\nu s^*}{u_e^*}\right)^{\frac{1}{2}} = \left(\frac{\nu SL}{U_\infty u_e}\right)^{\frac{1}{2}}. \tag{3.4.5}$$

Close to the stagnation point, the slip velocity $u_e(S)$ is approximated by (3.3.33), i.e.

$$u_e = C \cdot S, \tag{3.4.6}$$

where

$$C = \frac{L}{2(a+b)} \cdot \left[\frac{(a+2b)^2}{2b(a+b)}\right]^2 = O(a^2/2b^2). \tag{3.4.7}$$

Use of (3.4.6) in (3.4.5) gives the stagnation point boundary layer thickness

$$\delta_s = \left(\frac{\nu L}{U_\infty C}\right)^{\frac{1}{2}}. \tag{3.4.8}$$

We introduce the normal coordinate, made dimensionless by the stagnation point boundary layer thickness δ_s ,

$$y = \frac{y^*}{\delta_s}. \tag{3.4.9}$$

The coordinates s^* and z^* are normalised by the characteristic spanwise wavelength Λ, so that

$$x = \frac{s^*}{\Lambda}, \qquad z = \frac{z^*}{\Lambda}. \tag{3.4.10}$$

In the calculation of the entire viscous base flow velocity field over the airfoil, we used variables S and η, which are normalised by L and δ respectively. The relations between the set of non-dimensional variables, (S, η) and (x, y), are

$$S = \frac{s^*}{L} = \frac{s^*}{\Lambda} \cdot \frac{\Lambda}{L} = x \cdot \frac{\Lambda}{L}, \tag{3.4.11}$$

$$\eta = \sqrt{\frac{u_e^*}{\nu s^*}} y^* = \sqrt{\frac{U_\infty u_e}{\nu SL}} y \delta_s = \sqrt{\frac{U_\infty u_e}{\nu SL}} \cdot y \sqrt{\frac{\nu L}{U_\infty C}} = y \sqrt{\frac{u_e}{CS}}. \tag{3.4.12}$$

We define the Reynolds numbers based on the spanwise wavelength and on the boundary layer thickness δ_s:

$$R_\Lambda = \frac{U_\infty \Lambda}{\nu}, \quad R_{\delta_s} = \frac{U_\infty \delta_s}{\nu} = \left(\frac{U_\infty L}{\nu C}\right)^{\frac{1}{2}}.$$

The velocities in the x and z directions are normalised by the chordwise free-stream

velocity U_∞, and the normal velocity is normalised by $R_{\delta_s}^{-1}U_\infty$ due to its small magnitude, i.e.

$$(u, v, w) = (u^*, R_{\delta_s}v^*, w^*)/U_\infty. \tag{3.4.13}$$

The normalised time and pressure are given in (3.2.2) and (3.4.2) respectively. After introducing the non-dimensional quantities, the continuity equation

$$\frac{\partial u^*}{\partial x^*} + \frac{\partial v^*}{\partial y^*} + \frac{\partial w^*}{\partial z^*} = 0$$

can be written as

$$\frac{\partial u}{\partial x} + R_0^2 \cdot \frac{\partial v}{\partial y} + \frac{\partial w}{\partial z} = 0, \tag{3.4.14}$$

where

$$R_0^2 \equiv \frac{\Lambda}{\delta_s R_{\delta_s}} = \Lambda \cdot \Big(\frac{U_\infty C}{\nu L}\Big)^{\frac{1}{2}} \cdot \Big(\frac{\nu C}{U_\infty L}\Big)^{\frac{1}{2}} = \frac{\Lambda C}{L} = \frac{\Lambda(a+2b)^4}{8b^2(a+b)^3}, \quad \text{i.e.} \quad R_0 = \sqrt{\frac{\Lambda C}{L}}.$$

If Λ is chosen to be of $O(b^2/a)$, then $R_0 = O(1)$.

For the momentum equation in the x direction

$$\frac{\partial u^*}{\partial t^*} + u^*\frac{\partial u^*}{\partial x^*} + v^*\frac{\partial u^*}{\partial y^*} + w^*\frac{\partial u^*}{\partial z^*} = -\frac{1}{\rho}\frac{\partial p^*}{\partial x^*} + \nu\Big(\frac{\partial^2 u^*}{\partial x^{*2}} + \frac{\partial^2 u^*}{\partial y^{*2}} + \frac{\partial^2 u^*}{\partial z^{*2}}\Big),$$

the non-dimensional form is

$$\frac{U_\infty^2}{\Lambda}\frac{\partial u}{\partial t} + \frac{U_\infty^2}{\Lambda}u\frac{\partial u}{\partial x} + \frac{U_\infty^2}{\delta_s R_{\delta_s}}v\frac{\partial u}{\partial y} + \frac{U_\infty^2}{\Lambda}w\frac{\partial u}{\partial z} = -\frac{U_\infty^2}{\Lambda}\frac{\partial p}{\partial x} + \nu\Big(\frac{U_\infty}{\Lambda^2}\frac{\partial^2 u}{\partial x^2} + \frac{U_\infty}{{\delta_s}^2}\frac{\partial^2 u}{\partial y^2} + \frac{U_\infty}{\Lambda^2}\frac{\partial^2 u}{\partial z^2}\Big),$$

i.e.

$$\frac{\partial u}{\partial t} + u\frac{\partial u}{\partial x} + R_0^2 v\frac{\partial u}{\partial y} + w\frac{\partial u}{\partial z} = -\frac{\partial p}{\partial x} + \frac{1}{R_\Lambda}\frac{\partial^2 u}{\partial x^2} + R_0^2\frac{\partial^2 u}{\partial y^2} + \frac{1}{R_\Lambda}\frac{\partial^2 u}{\partial z^2}. \tag{3.4.15}$$

Similarly, the non-dimensionalised normal and spanwise momentum equations are

$$\frac{\partial v}{\partial t} + u\frac{\partial v}{\partial x} + R_0^2 v\frac{\partial v}{\partial y} + w\frac{\partial v}{\partial z} = -R_\Lambda\frac{\partial p}{\partial y} + \frac{1}{R_\Lambda}\frac{\partial^2 v}{\partial x^2} + R_0^2\frac{\partial^2 v}{\partial y^2} + \frac{1}{R_\Lambda}\frac{\partial^2 v}{\partial z^2}, \tag{3.4.16}$$

and

$$\frac{\partial w}{\partial t}+u\frac{\partial w}{\partial x}+R_0^2 v\frac{\partial w}{\partial y}+w\frac{\partial w}{\partial z}=-\frac{\partial p}{\partial z}+\frac{1}{R_\Lambda}\frac{\partial^2 w}{\partial x^2}+R_0^2\frac{\partial^2 w}{\partial y^2}+\frac{1}{R_\Lambda}\frac{\partial^2 w}{\partial z^2}. \tag{3.4.17}$$

3.4.2 The linear inviscid solution

As a vortical disturbance approaches the airfoil, it is strained (distorted) by the non-uniform inviscid mean flow, which is created by the presence of the airfoil. The inviscid solution in this region may be obtained by applying the generalised rapid distortion theory (RDT) (Hunt 1973, Goldstein 1978).

Let $\mathbf{U}=(U_x,U_y,U_z)$ be the mean flow in the chordwise, normal, and spanwise directions respectively. The mean flow velocities $U_x=u_{et}$ and $U_y=v_{et}$ are obtained from conformal mapping. In the spanwise direction, the mean flow velocity $U_z=-\tan\phi_\infty$ remains constant. The perturbed flow flow field can be written as

$$\mathbf{v}=\mathbf{U}+\epsilon\mathbf{u}(\mathbf{x},t),\quad p=P_0(\mathbf{x})+\epsilon p'(\mathbf{x},t), \tag{3.4.18}$$

where the vector $\mathbf{x}=(x_o,y_o,z)$, consisting of the Cartesian coordinates along the chordwise (x_o), normal (y_o) and spanwise (z) directions respectively, and $\mathbf{u}(\mathbf{x},t)$ and $p'(\mathbf{x},t)$ denote the perturbation velocity and pressure respectively. Substituting the perturbed velocity and pressure (3.4.18) into (3.4.3)–(3.4.4), and neglecting the products of the perturbation, we obtain the linearised governing equations

$$\nabla\cdot\mathbf{u}=0, \tag{3.4.19}$$

$$\frac{\partial\mathbf{u}}{\partial t}+\mathbf{U}\cdot\nabla\mathbf{u}+\mathbf{u}\cdot\nabla\mathbf{U}=-\nabla p'. \tag{3.4.20}$$

The solution to (3.4.19)–(3.4.20) is composed of two parts, one is the complementary solution $\mathbf{u}^{(\mathbf{H})}$, which is obtained by solving the homogenous part of (3.4.20); the other part is the particular integral, which represents an irrotational fluctuation. Upon introducing a potential function $\phi(\mathbf{x},t)$, the particular solution can be expressed as $\mathbf{u_p}=\nabla\phi$. Therefore, the general solution to (3.4.19)–(3.4.20) can be written as

$$\mathbf{u}=\mathbf{u}^{(\mathbf{H})}+\nabla\phi. \tag{3.4.21}$$

Goldstein (1978) first obtained the solution to (3.4.19)–(3.4.20) in the form of (3.4.21) including a general solution form for $\mathbf{u}^{(\mathbf{H})}$. But in his work, the sweep angle is considered to be zero, and so his solution is not directly applicable to the present problem. We follow the derivation steps of Goldstein (1978), and extend the inviscid solution to the case of a nonzero sweep angle.

Consider the homogeneous part of equation (3.4.20),

$$\frac{\partial \mathbf{u}}{\partial t} + \mathbf{U} \cdot \nabla \mathbf{u} + \mathbf{u} \cdot \nabla \mathbf{U} = 0. \tag{3.4.22}$$

The original three-dimensional problem can be reduced to a two-dimensional one by introducing the substitution

$$\mathbf{u} = \hat{\mathbf{u}} \cdot \exp\Big[\mathrm{i}(k_3 z + k_3 \tan\phi_\infty t)\Big], \tag{3.4.23}$$

where $\hat{\mathbf{u}} = \Big[\hat{u}(x_o, y_o, t), \hat{v}(x_o, y_o, t), \hat{w}(x_o, y_o, t)\Big]$. Substitution of (3.4.23) into (3.4.22) yields the governing equations for the two-dimensional problem. In the chordwise direction, (3.4.22) can be rewritten as

$$\frac{\partial \hat{u}}{\partial t} + U_x \frac{\partial \hat{u}}{\partial x_o} + U_y \frac{\partial \hat{u}}{\partial y_o} + \hat{u}\frac{\partial U_x}{\partial x_o} + \hat{v}\frac{\partial U_x}{\partial y_o} = 0, \tag{3.4.24}$$

in the normal direction,

$$\frac{\partial \hat{v}}{\partial t} + U_x \frac{\partial \hat{v}}{\partial x_o} + U_y \frac{\partial \hat{v}}{\partial y_o} + \hat{u}\frac{\partial U_y}{\partial x_o} + \hat{v}\frac{\partial U_y}{\partial y_o} = 0, \tag{3.4.25}$$

and in the spanwise direction,

$$\frac{\partial \hat{w}}{\partial t} + U_x \frac{\partial \hat{w}}{\partial x_o} + U_y \frac{\partial \hat{w}}{\partial y_o} = 0. \tag{3.4.26}$$

The general solution to (3.4.24)-(3.4.25) can be constructed following the standard procedure. First, consider the equation

$$\frac{dx}{U_x} = \frac{dy}{U_y}. \tag{3.4.27}$$

This equation has an integral $Y(x_o, y_o)$ with the property that

$$y \to Y \quad \text{as} \quad x_0 \to -\infty.$$

For the present two-dimensional problem, Y is the stream function, i.e. $Y = \psi(x_o, y_o)$. This integral defines the trajectory $y_o = y_o(x_o, Y)$, which corresponds to the streamline starting from the point $(-\infty, Y)$. Each streamline is identified by Y. Next, we define the Darwin-Lighthill drift function

$$\Delta(x_o, y_o) = x_o + \int_{-\infty}^{x_o} \Big[\frac{1}{U_x(x', y_o(x', Y))} - 1\Big] dx', \tag{3.4.28}$$

where the integration is carried out along a streamline, along which Y remains constant. The second term in the integral corresponds to the time difference for a fluid particle to travel from far upstream $x_o \to -\infty$ to certain downstream location x_o in the presence and absence of the obstacle. Note that as $x_o \to -\infty$, the chordwise slip velocity tends to the upstream mean flow, i.e. $U_x \to 1$. It follows that $\Delta \to x_o$ in this limit. Introduce the vector

$$\mathbf{X}' = (\Delta, Y).$$

It can be shown that $\mathbf{X}'$ has the property that

$$\frac{D'}{Dt}\Big(\mathbf{X}' - \hat{\mathbf{i}}t\Big) = 0, \tag{3.4.29}$$

where

$$\frac{D'}{Dt} = \frac{\partial}{\partial t} + \mathbf{U} \cdot \nabla' = \frac{\partial}{\partial t} + U_x \frac{\partial}{\partial x_o} + U_y \frac{\partial}{\partial y_o}$$

is the convective derivative, and $\hat{\mathbf{i}}$ is the unit vector in the chordwise direction. The verification of (3.4.29) is given as follows. Differentiation using the chain rule shows that

$$\frac{\partial \Delta}{\partial x_o} = \frac{\partial \Delta}{\partial x_o} + \frac{\partial \Delta}{\partial Y} \cdot \frac{\partial Y}{\partial x_o} = \frac{1}{U_x} + C_r \cdot \frac{\partial Y}{\partial x_o},$$

$$\frac{\partial \Delta}{\partial y_o} = C_r \cdot \frac{\partial Y}{\partial y_o},$$

where

$$C_r = \frac{\partial \Delta}{\partial Y} = -\int_{-\infty}^{x_o} \frac{1}{U_x^2} \cdot \frac{\partial U_x}{\partial y_o} \cdot \frac{\partial y_o}{\partial Y} dx',$$

It follows that

$$\Big(\frac{\partial}{\partial t}+U_x\frac{\partial}{\partial x_o}+U_y\frac{\partial}{\partial y_o}\Big)(\Delta-t)=C_r\cdot\Big\{U_x\frac{\partial Y}{\partial x_o}+U_y\frac{\partial Y}{\partial y_o}\Big\}.$$

Now differentiation $y_o=y_o(x_o,Y)$ with respect to x_o and y_o gives

$$\left.\begin{aligned}\frac{\partial y_o}{\partial Y}\cdot\frac{\partial Y}{\partial x_o}+\frac{dy_o}{dx_o}=0,\\ \frac{\partial y_o}{\partial Y}\cdot\frac{\partial Y}{\partial y_o}=1,\end{aligned}\right\}$$

and from which it follows

$$\frac{\partial Y}{\partial x_o}=-\frac{dy_o}{dx_o}\Big/\frac{\partial y_o}{\partial Y}=-\frac{U_y}{U_x}\Big/\frac{\partial y_o}{\partial Y},\qquad \frac{\partial y_o}{\partial Y}=1\Big/(\frac{\partial Y}{\partial y_o}),$$

and

$$U_x\frac{\partial Y}{\partial x_o}+U_y\frac{\partial Y}{\partial y_o}=-U_y\frac{\partial Y}{\partial y_o}+U_y\frac{\partial Y}{\partial y_o}=0.$$

Therefore equation (3.4.29) is satisfied for the component in the chordwise direction.

For the component the normal direction, Y, the equation (3.4.29) reads

$$\Big(\frac{\partial}{\partial t}+U_x\frac{\partial}{\partial x_o}+U_y\frac{\partial}{\partial y_o}\Big)Y=U_x\frac{\partial Y}{\partial x_o}+U_y\frac{\partial Y}{\partial y_o}=0.$$

Therefore, the relation (3.4.29) is proved to be satisfied. As was stated in Goldstein (1978), equation (3.4.29) means that for an observer travelling at the same speed with the mean flow, the components of the vector $\mathbf{X}'-\hat{\mathbf{i}}t$ remain constant.

As was shown by Goldstein (1978), the solution to (3.4.24)–(3.4.25) can be constructed as

$$\hat{u}_i^{(H)}=\mathcal{A}\Big(\mathbf{X}'-\hat{\mathbf{i}}t\Big)\cdot\frac{\partial\mathbf{X}'}{\partial x_i},\quad \text{for } i=1,2, \tag{3.4.30}$$

where $\mathcal{A}$ is an arbitrary vector function of its argument $\mathbf{X}'-\hat{\mathbf{i}}t$ with $\hat{\mathbf{i}}$ denoting a unit vector in the x_o direction. That (3.4.30) satisfies (3.4.24)–(3.4.25) can be verified as follows. Since the relation (3.4.29) implies that

$$\frac{D'\mathcal{A}}{Dt}=0,$$

$$\frac{D'\hat{u}_j^{(H)}}{Dt} = \Big[\frac{D'\mathcal{A}_i}{Dt}\Big]\cdot\frac{\partial X_i'}{\partial x_j} + \mathcal{A}_i\cdot\Big[\frac{D'}{Dt}\Big(\frac{\partial X_i'}{\partial x_j}\Big)\Big] = \mathcal{A}_i\cdot\frac{D'}{Dt}\Big(\frac{\partial X_i'}{\partial x_j}\Big),$$

and

$$\begin{aligned}\frac{D'\hat{u}_j^{(H)}}{Dt} + \hat{u}_k^{(H)}\cdot\frac{\partial U_j}{\partial x_k} &= \mathcal{A}_i\cdot\frac{D'}{Dt}\Big(\frac{\partial X_i'}{\partial x_j}\Big) + \Big(\mathcal{A}_i\cdot\frac{\partial X_i'}{\partial x_k}\Big)\cdot\frac{\partial U_j}{\partial x_k}\\ &= \mathcal{A}_i\cdot\Big[\frac{\partial}{\partial t}\Big(\frac{\partial X_i'}{\partial x_j}\Big) + U_k\frac{\partial}{\partial x_k}\Big(\frac{\partial X_i'}{\partial x_j}\Big)\Big] + \Big(\mathcal{A}_i\cdot\frac{\partial X_i'}{\partial x_k}\Big)\cdot\frac{\partial U_j}{\partial x_k}\\ &= \mathcal{A}_i\cdot\Big[\frac{\partial}{\partial t}\Big(\frac{\partial X_i'}{\partial x_j}\Big) + \frac{\partial}{\partial x_j}\Big(U_k\frac{\partial X_i'}{\partial x_k}\Big)\Big] - \mathcal{A}_i\cdot\frac{\partial X_i'}{\partial x_k}\Big(\frac{\partial U_k}{\partial x_j} - \frac{\partial U_j}{\partial x_k}\Big).\end{aligned}$$

Since the mean flow is irrotational,

$$\frac{\partial U_j}{\partial x_k} - \frac{\partial U_k}{\partial x_j} = 0,$$

and

$$\frac{D'\hat{u}_j^{(H)}}{Dt} + \hat{u}_k^{(H)}\cdot\frac{\partial U_j}{\partial x_k} = \mathcal{A}_i\cdot\frac{\partial}{\partial x_j}\Big[\frac{\partial X_i'}{\partial t} + U_k\frac{\partial X_i'}{\partial x_k}\Big] = \mathcal{A}_i\cdot\frac{\partial}{\partial x_j}\Big(\frac{D'X_i'}{Dt}\Big).$$

Since

$$\frac{D'X_i}{Dt} = \begin{cases} 1 & \text{if } i = 1,\\ \\ 0 & \text{if } i = 2,\end{cases}$$

we obtain

$$\frac{D'\hat{u}_j^{(H)}}{Dt} + \hat{u}_k^{(H)}\cdot\frac{\partial U_j}{\partial x_k} = 0. \tag{3.4.31}$$

If we put $\hat{\mathbf{u}}_{\mathbf{0}}^{(\mathbf{H})} = (\hat{u}_1^{(H)}, \hat{u}_2^{(H)})$, then (3.4.31) can be written into vector form as

$$\frac{D'\hat{\mathbf{u}}_{\mathbf{0}}^{(\mathbf{H})}}{Dt} + \hat{\mathbf{u}}_{\mathbf{0}}^{(\mathbf{H})}\cdot\nabla\mathbf{U} = 0.$$

The arbitrary function $\mathcal{A}\Big(\mathbf{X}' - \hat{\mathbf{i}}t\Big)$ can be determined by matching the complementary solution $\mathbf{u}^{(\mathbf{H})}$ with the imposed free-stream turbulence $\mathbf{u}_\infty$. This requires that as $x_o \to -\infty$,

$$\mathcal{A}_j\Big(\mathbf{X}' - \hat{\mathbf{i}}t\Big)\exp\Big[\mathrm{i}(k_3 z + k_3\tan\phi_\infty t)\Big] \to \hat{u}_j^\infty\exp\Big[\mathrm{i}(\mathbf{k}\cdot\mathbf{x} - \omega t)\Big], \quad \text{for} \quad j = 1, 2, \tag{3.4.32}$$

where we use the fact that

$$\mathbf{X}' \to (x_o, y_o). \tag{3.4.33}$$

From (3.4.32) it follows that we must take the arbitrary function $\mathcal{A}$ to be

$$\mathcal{A}_j\Big(\mathbf{X}' - \hat{\mathbf{i}}t\Big) = u_j^{\infty} \exp\Big[\mathrm{i}(\mathbf{k}' \cdot \mathbf{X}' - k_1 t)\Big], \quad \text{for } j = 1, 2,$$

where $\mathbf{k}' = (k_1, k_2)$ is the wavenumber vector.

The solution to (3.4.26) can be written as

$$\hat{w}^{(H)} = \hat{u}_3^{(H)} = \mathcal{B}\Big(\mathbf{X}' - \hat{\mathbf{i}}t\Big), \tag{3.4.34}$$

where $\mathcal{B}$ is an arbitrary function. Matching with the spanwise velocity component of the imposed disturbance requires that as $x_o \to -\infty$,

$$\mathcal{B}\Big(\mathbf{X}' - \hat{\mathbf{i}}t\Big) \exp\Big[\mathrm{i}(k_3 z + k_3 \tan\phi_{\infty} t)\Big] \to \hat{u}_3^{\infty} \exp\Big[\mathrm{i}(\mathbf{k} \cdot \mathbf{x} - \omega t)\Big] \tag{3.4.35}$$

from which $\mathcal{B}$ is fixed so that

$$\hat{u}_3^{(H)} = \hat{u}_3^{\infty} \cdot \exp\Big[\mathrm{i}(\mathbf{k}' \cdot \mathbf{X}' - k_1 t)\Big]. \tag{3.4.36}$$

We now consider the particular integral of the linearised Euler's equation,

$$\mathbf{u_p} = \nabla\phi.$$

From Bernoulli's principle it follows that the pressure is

$$p' = -(\frac{\partial}{\partial t} + \mathbf{U} \cdot \nabla)\phi. \tag{3.4.37}$$

In order to determine ϕ, we substitute (3.4.21) into the continuity equation (3.4.19) to obtain

$$\nabla^2\phi = -\nabla \cdot \mathbf{u^{(H)}}. \tag{3.4.38}$$

In the far field upstream, i.e. $x_o \to -\infty$, and $\mathbf{u^{(H)}} \to \mathbf{u}_{\infty}$. Since $\mathbf{u}_{\infty}$ satisfies the solenoidal condition, i.e. $\nabla \cdot \mathbf{u}_{\infty} = 0$, equation (3.4.38) reduces to Laplace's equation. The boundary

conditions for (3.4.38) can be written as

$$\phi \to 0 \quad \text{as} \quad x_o \to -\infty, \tag{3.4.39}$$

$$\phi \to 0 \quad \text{as} \quad y_o \to \infty, \tag{3.4.40}$$

$$\hat{\mathbf{n}} \cdot \nabla\phi \to -\hat{\mathbf{n}} \cdot \mathbf{u}^{(\mathbf{H})} \quad \text{as } y_o \text{ approaches the airfoil surface,} \quad x_o > 0, \tag{3.4.41}$$

where $\hat{\mathbf{n}}$ is the unit vector in the normal direction. The condition (3.4.41) follows from the requirement that the normal component of $\mathbf{u}$ vanishes at the surface of the airfoil. The equation (3.4.38) and the boundary conditions (3.4.39)–(3.4.41) form a mixed boundary value problem, which may be solved numerically or analytically by the Wiener-Hopf technique. In the present thesis, we will omit the potential function ϕ and the associated pressure gradients in our later analysis, and consider the boundary-layer response to the slip velocity of inviscid the complementary solution only.

The inviscid solution can be written explicitly as

$$\begin{aligned} u_x &= \frac{\partial\phi}{\partial x_o} + \hat{u}_1^{\infty} \exp\left\{\mathrm{i}\Big[\mathbf{k}\cdot\mathbf{X} - (k_1 - k_3\tan\phi_\infty)t\Big]\right\} \cdot \frac{\partial\Delta}{\partial x_o} \\ &\quad + \hat{u}_2^{\infty} \cdot \exp\left\{\mathrm{i}\Big[\mathbf{k}\cdot\mathbf{X} - (k_1 - k_3\tan\phi_\infty)t\Big]\right\}\frac{\partial Y}{\partial x_o}, \end{aligned}$$

$$\begin{aligned} u_y &= \frac{\partial\phi}{\partial y_o} + \hat{u}_1^{\infty} \exp\left\{\mathrm{i}\Big[\mathbf{k}\cdot\mathbf{X} - (k_1 - k_3\tan\phi_\infty)t\Big]\right\} \cdot \frac{\partial\Delta}{\partial y_o} \\ &\quad + \hat{u}_2^{\infty} \cdot \exp\left\{\mathrm{i}\Big[\mathbf{k}\cdot\mathbf{X} - (k_1 - k_3\tan\phi_\infty)t\Big]\right\}\frac{\partial Y}{\partial y_o}, \end{aligned}$$

$$u_z = \frac{\partial\phi}{\partial z} + \hat{u}_3^{\infty} \exp\left\{\mathrm{i}\Big[\mathbf{k}\cdot\mathbf{X} - (k_1 - k_3\tan\phi_\infty)t\Big]\right\}, \tag{3.4.42}$$

where

$$\mathbf{k} = (k_1, k_2, k_3), \quad \text{and} \quad \mathbf{X} = (\Delta, Y, z).$$

3.4.3 The linearised boundary layer equations

In the present analysis, we assume that

$$R_0^2 \gg \frac{1}{R_\Lambda},$$

which implies that

$$\Lambda \gg \left(\frac{\nu L}{U_\infty C}\right)^{\frac{1}{2}} = \delta_s. \tag{3.4.43}$$

If only $O(1)$ terms are retained, equations (3.4.15) and (3.4.17) reduce to

$$\frac{\partial u}{\partial t} + u\frac{\partial u}{\partial x} + R_0^2 v\frac{\partial u}{\partial y} + w\frac{\partial u}{\partial z} = -\frac{\partial p}{\partial x} + R_0^2\frac{\partial^2 u}{\partial y^2}. \tag{3.4.44}$$

$$\frac{\partial w}{\partial t} + u\frac{\partial w}{\partial x} + R_0^2 v\frac{\partial w}{\partial y} + w\frac{\partial w}{\partial z} = -\frac{\partial p}{\partial z} + R_0^2\frac{\partial^2 w}{\partial y^2}, \tag{3.4.45}$$

while equation (3.4.16) simplifies to

$$\frac{\partial p}{\partial y} = 0,$$

which indicates that the pressure is given by the inviscid solution. The governing equations for the perturbation are the linearised boundary layer equations. The pressure gradients in (3.4.44)–(3.4.45) will be known from (3.4.37) when the solution to the potential function ϕ is known. Unfortunately, solving the mixed boundary-value problem consisting of (3.4.38) and (3.4.39)–(3.4.41), either numerically or analytically by the Wiener-Hopf technique, is a challenging task. This has to be left to a future study. In the present thesis, we will omit the potential function ϕ and the associated pressure gradients in our later analysis, and consider only the boundary-layer response to the slip velocity of the inviscid complementary solution, i.e. the solution to the homogenous equation (3.4.22). In this case, equations (3.4.44)–(3.4.45) reduces to

$$\frac{\partial u}{\partial t} + u\frac{\partial u}{\partial x} + R_0^2 v\frac{\partial u}{\partial y} + w\frac{\partial u}{\partial z} = R_0^2\frac{\partial^2 u}{\partial y^2}, \tag{3.4.46}$$

and

$$\frac{\partial w}{\partial t} + u\frac{\partial w}{\partial x} + R_0^2 v\frac{\partial w}{\partial y} + w\frac{\partial w}{\partial z} = R_0^2\frac{\partial^2 w}{\partial y^2}. \tag{3.4.47}$$

Equations (3.4.46)–(3.4.47) combined with the continuity equation (3.4.14) form the governing equations for the perturbed flow field in the boundary layer for $x^* = \Lambda = O(b^2/a)$.

In the following, we consider first the perturbation in the stagnation region, and its further development downstream.

Perturbation in the region of the stagnation point

In the vicinity of the stagnation point $x \ll 1$, the slip velocity $u_e(S) = CS$, and the base flow velocity in the x direction can be written as

$$U_S = u_e(S)f' = CSf' = C\frac{\Lambda}{L} \cdot x \cdot f' = R_0^2 f' x, \tag{3.4.48}$$

where $f = f(\eta)$is governed by (3.3.42). From (3.3.38) and the non-dimensionalisation (3.4.13), the base flow in the y direction is found as

$$\begin{aligned} V_S = \frac{v_B^*}{R_{\delta_s}^{-1} U_\infty} &= -R_{\delta_s}\left(\frac{\nu}{U_\infty L}\right)^{\frac{1}{2}} \left\{ \frac{\partial}{\partial S}\left[\left(u_e(S)\cdot S\right)^{\frac{1}{2}} \cdot f\right] + \left(u_e(S)\cdot S\right)^{\frac{1}{2}} \cdot f' \cdot \frac{\partial \eta}{\partial S} \right\} \\ &= -\frac{1}{\sqrt{C}} \left\{ \frac{\partial}{\partial S}\left[\left(u_e(S)\cdot S\right)^{\frac{1}{2}} \cdot f\right] + \left(u_e(S)\cdot S\right)^{\frac{1}{2}} \cdot f' \cdot \frac{\partial \eta}{\partial S} \right\}. \end{aligned} \tag{3.4.49}$$

Near the stagnation point, the local boundary layer thickness is the (constant) stagnation point boundary layer thickness, i.e. $\delta(S) = \delta_s$, and $\eta = y$ so that

$$\frac{\partial \eta}{\partial S} = \frac{\partial y}{\partial S} = 0. \tag{3.4.50}$$

Substitution of (3.4.50) and (3.4.6) into (3.4.49) gives the non-dimensional base flow velocity in the y direction

$$V_S = -f. \tag{3.4.51}$$

The base flow at the stagnation point is thus given by

$$(U_S, V_S, W_S) = (R_0^2 f' x, -f, -h\tan\phi_\infty), \tag{3.4.52}$$

where h, a function of η only, is governed by (3.3.63). This type of base flow is referred to as swept Hiemenz flow in the literature. The velocity $U_S(x,\eta)$ grows linearly with the coordinate x, while the normal and spanwise velocities, $V_S(\eta)$ and $W_S(\eta)$, are homogenous in the x direction.

In order to deduce the appropriate form of the boundary-layer perturbation, we consider the inviscid slip velocity. As in LWG and the Görtler problem consider in the previous chapter, we focus on the spanwise velocity. With the contribution from ϕ being neglected,

it follows from (3.4.42) that

$$u_3^{(H)} \to \hat{u}_3^{\infty} \exp\left\{ \mathrm{i}\Big[k_1\Delta - (k_1 - k_3 \tan\phi_\infty)t \Big] \right\} \quad \text{as} \quad y_o \to 0. \tag{3.4.53}$$

Close to the stagnation point, the slip velocity component U_x is also approximated by

$$U_x \to CS = R_0^2 x. \tag{3.4.54}$$

Substitution of (3.4.54) into (3.4.28) shows that the drift function

$$\Delta \to \frac{1}{R_0^2} \log x \quad \text{as} \quad x \to 0^+,$$

use of which in (3.4.53) yields

$$u_3^{(H)} \to \hat{u}_3^{\infty} \exp\left\{ \mathrm{i}\Big[k_1 \log x/R_0^2 - (k_1 - k_3 \tan\phi_\infty)t \Big] \right\} \quad \text{as} \quad y_o \to 0. \tag{3.4.55}$$

The perturbed flow within the boundary layer can be written as

$$\begin{aligned} (u, v, w) \;\; = \;\; & \Big[U_S(x,y), V_S(y), W_S(y) \Big] \\ & + \epsilon \Big[x\hat{u}(y,z,t), \hat{v}(y,z,t), \hat{w}(y,z,t) \Big] \exp\Big(i k_1 \log x / R_0^2 \Big), \end{aligned} \tag{3.4.56}$$

where $\epsilon \ll 1$ is a measure of the amplitude of the disturbance. The exponential factor appears due to the matching with (3.4.55), and the extra x factor in the velocity component in the x direction arises due to the form of U_S and the constrain of the equations.

Substituting (3.4.56) into the non-dimensional boundary layer equations (3.4.14), (3.4.46) and (3.4.47), we obtain after linearisation the leading order perturbation equations

$$\hat{u} + \frac{i k_1}{R_0^2}\hat{u} + R_0^2 \frac{\partial \hat{v}}{\partial y} + \frac{\partial \hat{w}}{\partial z} = 0, \tag{3.4.57}$$

$$\frac{\partial \hat{u}}{\partial t} + R_0^2 f' \hat{u}\Big(2 + \frac{i k_1}{R_0^2} \Big) + R_0^2 \Big(\hat{v} \cdot R_0^2 f'' - f \frac{\partial \hat{u}}{\partial y} \Big) - \tan\phi_\infty h \frac{\partial \hat{u}}{\partial z} = R_0^2 \frac{\partial^2 \hat{u}}{\partial y^2}, \tag{3.4.58}$$

$$\frac{\partial \hat{w}}{\partial t} + i k_1 f' \hat{w} - R_0^2 \Big(\tan\phi_\infty \hat{v} \frac{\partial h}{\partial y} + f \frac{\partial \hat{w}}{\partial y} \Big) - \tan\phi_\infty h \frac{\partial \hat{w}}{\partial z} = R_0^2 \frac{\partial^2 \hat{w}}{\partial y^2}. \tag{3.4.59}$$

The solution for $(\hat{u}, \hat{v}, \hat{w})$ takes the form

$$(\hat{u}, \hat{v}, \hat{w}) = \Big(\bar{u}, \bar{v}, \frac{1}{k_3}\bar{w}\Big) \exp\Big\{i(k_3 z - \omega t)\Big\},$$

where $(\bar{u}, \bar{v}, \bar{w})$ is the scaled velocity, $\omega = k_1 - k_3 \tan\phi_\infty$ is the frequency. Substitution into (3.4.57)–(3.4.59) yields

$$\bar{u} + \frac{ik_1}{R_0^2}\bar{u} + R_0^2\frac{\partial \bar{v}}{\partial y} + i\bar{w} = 0, \tag{3.4.60}$$

$$(-i\omega - ik_3 \tan\phi_\infty h)\bar{u} + R_0^2 f'\bar{u}\Big(2 + \frac{ik_1}{R_0^2}\Big) + R_0^2\Big(\bar{v}R_0^2 f'' - f\frac{\partial \bar{u}}{\partial y}\Big) = R_0^2\frac{\partial^2 \bar{u}}{\partial y^2}, \tag{3.4.61}$$

$$(-i\omega - ik_3 \tan\phi_\infty h)\bar{w} + ik_1 f'\bar{w} - R_0^2\Big(k_3 \tan\phi_\infty \bar{v}\frac{\partial h}{\partial y} + f\frac{\partial \bar{w}}{\partial y}\Big) = R_0^2\frac{\partial^2 \bar{w}}{\partial y^2}. \tag{3.4.62}$$

For computational purpose, we rewrite (3.4.60)–(3.4.62) into a first-order system,

$$\frac{\partial \bar{u}}{\partial y} = \bar{f}, \tag{3.4.63}$$

$$\frac{\partial \bar{v}}{\partial y} = -\frac{1}{R_0^2}\Big[(1 + \frac{ik_1}{R_0^2})\bar{u} + i\bar{w}\Big], \tag{3.4.64}$$

$$\frac{\partial \bar{w}}{\partial y} = \bar{g}, \tag{3.4.65}$$

$$\frac{\partial \bar{f}}{\partial y} = \frac{1}{R_0^2}\Big[-i\omega - ik_3 \tan\phi_\infty h + R_0^2 f'(2 + \frac{ik_1}{R_0^2})\Big]\bar{u} + \bar{v}\cdot R_0^2 f'' - f\bar{f}, \tag{3.4.66}$$

$$\frac{\partial \bar{g}}{\partial y} = \frac{1}{R_0^2}(-i\omega - ik_3 \tan\phi_\infty h + ik_1 f')\bar{w} - k_3 \tan\phi_\infty h'\bar{v} - f\bar{g}. \tag{3.4.67}$$

The above equations satisfy the no-slip boundary condition at the wall, and the matching condition with the spanwise velocity of the inviscid solution (3.4.55), i.e.

$$y = 0: \quad \bar{u} = \bar{v} = \bar{w} = 0; \qquad y \to \infty: \quad \bar{u} \to 0, \quad \text{and} \quad \bar{w} \to 1, \tag{3.4.68}$$

where we have taken $\hat{u}_3^\infty = 1$ without losing generality. A solution to (3.4.63)–(3.4.67) is shown in figure 3.12.

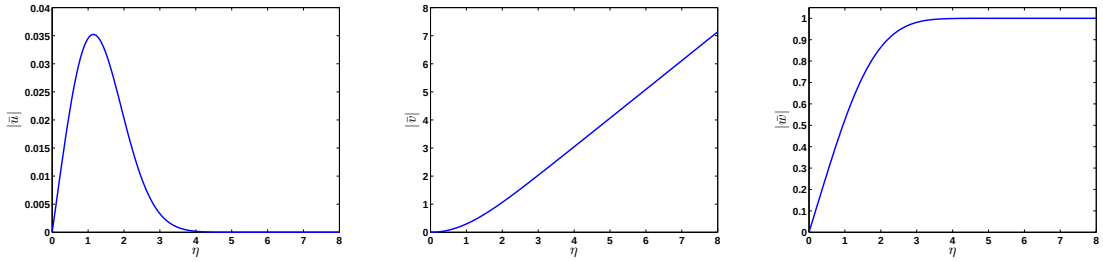


Figure 3.12: Velocity profiles at the stagnation point. The parameters used are $\omega = 0.12$, $k_3 = 1.0$, $\Lambda = 0.05$, and $b/a = 0.1$.

Development of the perturbation

Away from the stagnation point, the velocity field of the base flow is given by

$$\Big[U_B(S,\eta), V_B(S,\eta), W_B(S,\eta)\Big],$$

where the non-dimensional velocities U_B, V_B and W_B can, by using (3.3.37), (3.3.38), (3.3.62) and (3.4.13), be written as

$$U_B = u_e(S)\cdot f'(S,\eta),$$

$$\begin{aligned} V_B = \frac{v_B^*}{R_{\delta_s}^{-1}U_\infty} &= -R_{\delta_s}\Big(\frac{\nu}{U_\infty L}\Big)^{\frac{1}{2}}\left\{\frac{\partial}{\partial S}\Big[\Big(u_e(S)\cdot S\Big)^{\frac{1}{2}}\cdot f\Big] + \Big(u_e(S)\cdot S\Big)^{\frac{1}{2}}\cdot f'\cdot\frac{\partial\eta}{\partial S}\right\} \\ &= -\frac{1}{\sqrt{C}}\left\{\frac{\partial}{\partial S}\Big[\Big(u_e(S)\cdot S\Big)^{\frac{1}{2}}\cdot f\Big] + \Big(u_e(S)\cdot S\Big)^{\frac{1}{2}}\cdot f'\cdot\frac{\partial\eta}{\partial S}\right\}, \end{aligned}$$

$$W_B = -h(S,\eta)\cdot\tan\phi_\infty,$$

where a prime denotes differentiation with respect to η,

$$\frac{\partial\eta}{\partial S} = \frac{1}{2}\frac{1}{S}\Big[\frac{S}{u_e}\frac{du_e}{dS} - 1\Big]\eta,$$

with $f(S,\eta)$ and $h(S,\eta)$ being governed by (3.3.39) and (3.3.71) respectively.

Within the boundary layer, the perturbed flow can now be expressed as

$$u = U_B + \epsilon\hat{u}(x,y,z,t), \quad v = V_B + \epsilon\hat{v}(x,y,z,t), \quad w = W_B + \epsilon\hat{w}(x,y,z,t). \tag{3.4.69}$$

The perturbed flow is substituted into the non-dimensional boundary layer equations (3.4.14), (3.4.46), and (3.4.47). After linearisation, we obtain the leading-order perturbation equations

$$\frac{\partial \hat{u}}{\partial x} + R_0^2 \frac{\partial \hat{v}}{\partial y} + \frac{\partial \hat{w}}{\partial z} = 0, \tag{3.4.70}$$

$$\frac{\partial \hat{u}}{\partial t} + U_B \frac{\partial \hat{u}}{\partial x} + \hat{u}\frac{\partial U_B}{\partial x} + R_0^2\Big(V_B \frac{\partial \hat{u}}{\partial y} + \hat{v}\frac{\partial U_B}{\partial y}\Big) + W_B \frac{\partial \hat{u}}{\partial z} = R_0^2 \frac{\partial^2 u}{\partial y^2}, \tag{3.4.71}$$

$$\frac{\partial \hat{w}}{\partial t} + U_B \frac{\partial \hat{w}}{\partial x} + \hat{u}\frac{\partial W_B}{\partial x} + R_0^2\Big(V_B \frac{\partial \hat{w}}{\partial y} + \hat{v}\frac{\partial W_B}{\partial y}\Big) + W_B \frac{\partial \hat{w}}{\partial z} = R_0^2 \frac{\partial^2 \hat{w}}{\partial y^2}. \tag{3.4.72}$$

The solution for $(\hat{u}, \hat{v}, \hat{w})$ takes the form

$$(\hat{u}, \hat{v}, \hat{w}) = \Big[\tilde{u}(x,\eta), \tilde{v}(x,\eta), \frac{1}{k_3}\tilde{w}(x,\eta)\Big] \exp\Big\{i(k_3 z - \omega t)\Big\},$$

substitution of which into (3.4.70)–(3.4.72) yields

$$\frac{\partial \tilde{u}}{\partial x} + R_0^2 \frac{\partial \tilde{v}}{\partial y} + i\tilde{w} = 0, \tag{3.4.73}$$

$$-i\omega\tilde{u} + U_B \frac{\partial \tilde{u}}{\partial x} + \tilde{u}\frac{\partial U_B}{\partial x} + R_0^2\Big(V_B \frac{\partial \tilde{u}}{\partial y} + \tilde{v}\frac{\partial U_B}{\partial y}\Big) + ik_3 W_B \tilde{u} = R_0^2 \frac{\partial^2 \tilde{u}}{\partial y^2}, \tag{3.4.74}$$

$$-i\omega\tilde{w} + U_B \frac{\partial \tilde{w}}{\partial x} + k_3\tilde{u}\frac{\partial W_B}{\partial x} + R_0^2\Big(V_B \frac{\partial \tilde{w}}{\partial y} + k_3\tilde{v}\frac{\partial W_B}{\partial y}\Big) + ik_3 W_B \tilde{w} = R_0^2 \frac{\partial^2 \tilde{w}}{\partial y^2}. \tag{3.4.75}$$

For computational purpose, we rewrite (3.4.73)–(3.4.75) into a first-order system,

$$\frac{\partial \tilde{u}}{\partial y} = \tilde{f}, \tag{3.4.76}$$

$$\frac{\partial \tilde{v}}{\partial y} = -\frac{1}{R_0^2}\Big(\frac{\partial \tilde{u}}{\partial x} + i\tilde{w}\Big), \tag{3.4.77}$$

$$\frac{\partial \tilde{w}}{\partial y} = \tilde{g}, \tag{3.4.78}$$

$$\frac{\partial \tilde{f}}{\partial y} = \frac{1}{R_0^2}\Big(-i\omega + U_B\frac{\partial}{\partial x} + ik_3 W_B\Big)\tilde{u} + \frac{\tilde{u}}{R_0^2}\frac{\partial U_B}{\partial x} + \tilde{v}\frac{\partial U_B}{\partial y} + V_B\tilde{f}, \tag{3.4.79}$$

$$\frac{\partial \tilde{g}}{\partial y} = \tilde{u}\frac{k_3}{R_0^2}\frac{\partial W_B}{\partial x} + k_3\tilde{v}\frac{\partial W_B}{\partial y} + \frac{1}{R_0^2}\Big(-i\omega + U_B\frac{\partial}{\partial x} + ik_3 W_B\Big)\tilde{w} + V_B\tilde{g}. \tag{3.4.80}$$

Since the base flow is evaluated on the η grid, we need to re-write (3.4.76)–(3.4.80) in terms

of η, in order to input the corresponding base flow at each mesh point. Noting that

$$\frac{\partial}{\partial x} \to \frac{\partial}{\partial x} + \frac{\partial}{\partial \eta}\frac{\partial \eta}{\partial x}, \quad \frac{\partial}{\partial y} \to \frac{\delta_s}{\delta}\frac{\partial}{\partial \eta},$$

we convert (3.4.76)–(3.4.80) into the following system,

$$\frac{\partial \tilde{u}}{\partial \eta} = R_1 \tilde{f}, \tag{3.4.81}$$

$$\frac{\partial \tilde{v}}{\partial \eta} = -\frac{R_1}{R_0^2}\frac{\partial \tilde{u}}{\partial x} - i\frac{R_1}{R_0^2}\tilde{w} - \frac{R_1^2}{R_0^2}\frac{\partial \eta}{\partial x}\tilde{f}, \tag{3.4.82}$$

$$\frac{\partial \tilde{w}}{\partial \eta} = R_1 \tilde{g}, \tag{3.4.83}$$

$$\frac{\partial \tilde{f}}{\partial \eta} = \frac{R_1}{R_0^2}\Big(-i\omega + U_B\frac{\partial}{\partial x} + ik_3 W_B + \frac{\Lambda}{L}\frac{\partial U_B}{\partial S} + \frac{\partial U_B}{\partial \eta}\frac{\partial \eta}{\partial x}\Big)\tilde{u} + \tilde{v}\frac{\partial U_B}{\partial \eta} + \Big(\frac{R_1^2}{R_0^2}\frac{\partial \eta}{\partial x}U_B + R_1 V_B\Big)\tilde{f}, \tag{3.4.84}$$

$$\begin{aligned}\frac{\partial \tilde{g}}{\partial \eta} \;=\; & \frac{k_3 R_1}{R_0^2}\Big(\frac{\Lambda}{L}\frac{\partial W_B}{\partial S} + \frac{\partial W_B}{\partial \eta}\frac{\partial \eta}{\partial x}\Big)\tilde{u} + k_3\tilde{v}\frac{\partial W_B}{\partial \eta} + \frac{R_1}{R_0^2}\Big(-i\omega + U_B\frac{\partial}{\partial x} + ik_3 W_B\Big)\tilde{w} \\ & + \Big(\frac{R_1^2}{R_0^2}\frac{\partial \eta}{\partial x}U_B + R_1 V_B\Big)\tilde{g},\end{aligned} \tag{3.4.85}$$

where

$$R_1 = \frac{\delta}{\delta_s} = \sqrt{\frac{CS}{u_e}}, \quad \text{and} \quad \frac{\partial \eta}{\partial x} = \frac{1}{2}\frac{\Lambda}{L}\frac{1}{S}\Big[\frac{S}{u_e(S)}\frac{du_e}{dS} - 1\Big]\eta.$$

The values of

$$\frac{\partial U_B}{\partial S}, \quad \frac{\partial U_B}{\partial \eta}, \quad \frac{\partial W_B}{\partial S} \quad \text{and} \quad \frac{\partial W_B}{\partial \eta}$$

are evaluated from solving the steady boundary layer equations.

The boundary conditions for (3.4.81)–(3.4.85) are

$$\tilde{u} = \tilde{v} = \tilde{w} = 0 \quad \text{at} \quad \eta = 0; \qquad \tilde{u} \to 0, \quad \tilde{w} \to \exp(ik_1\Delta) \quad \text{as} \quad \eta \to \infty. \tag{3.4.86}$$

Note that the boundary condition at infinity comes from matching with the spanwise slip velocity. The drift function Δ needs to be evaluated numerically, and the detailed evaluation procedure is given in the appendix A2.

The initial condition for (3.4.81)–(3.4.85) is

$$(\tilde{u},\tilde{v},\tilde{w}) \to (x\bar{u},\bar{v},\bar{w}) \quad \text{as} \quad x \to 0 \tag{3.4.87}$$

with $(\bar{u},\bar{v},\bar{w})$ being obtained from solving (3.4.63)–(3.4.67) subject to the boundary condition (3.4.68). The initial-boundary-value problem consisting of equations (3.4.81)–(3.4.85) and (3.4.86)–(3.4.87) describes the receptivity and evolution of the excited perturbation.

3.5 Eigenvalue formulation

3.5.1 Non-parallel boundary-layer eigenvalue formulation

In order to see whether the perturbation evolves into a spatially growing eigenmode, we formulate a local eigenvalue problem for crossflow vortices. As usual, we seek a normal-mode solution

$$(\tilde{u},\tilde{v},\tilde{w}) = \Big[u_c(\eta), v_c(\eta), w_c(\eta)\Big] \exp\{\int^x \sigma(x)dx\},$$

where σ is in general a complex number dependent on x with its real part representing the local growth rate. Substitution of the above expression into (3.4.81)–(3.4.85), we obtain a set of ordinary differential equations

$$\frac{\mathrm{d}u_c}{\mathrm{d}\eta} = R_1 f_c, \tag{3.5.1}$$

$$\frac{\mathrm{d}v_c}{\mathrm{d}\eta} = -\frac{R_1}{R_0^2}\sigma u_c - i\frac{R_1}{R_0^2}w_c - \frac{R_1^2}{R_0^2}\frac{\partial\eta}{\partial x}f_c, \tag{3.5.2}$$

$$\frac{\mathrm{d}w_c}{\mathrm{d}\eta} = R_1 g_c, \tag{3.5.3}$$

$$\frac{\mathrm{d}f_c}{\mathrm{d}\eta} = \frac{R_1}{R_0^2}\Big(-i\omega+\sigma U_B+ik_3W_B+\frac{\Lambda}{L}\frac{\partial U_B}{\partial S}+\frac{\partial U_B}{\partial\eta}\frac{\partial\eta}{\partial x}\Big)u_c+v_c\frac{\partial U_B}{\partial\eta}+\Big(\frac{R_1^2}{R_0^2}\frac{\partial\eta}{\partial x}U_B+R_1V_B\Big)f_c, \tag{3.5.4}$$

$$\begin{aligned}\frac{\mathrm{d}g_c}{\mathrm{d}\eta} &= u_c\frac{k_3R_1}{R_0^2}\Big(\frac{\Lambda}{L}\frac{\partial W_B}{\partial S}+\frac{\partial W_B}{\partial\eta}\frac{\partial\eta}{\partial x}\Big)+k_3v_c\frac{\partial W_B}{\partial\eta}+\frac{R_1}{R_0^2}\Big(-i\omega+\sigma U_B+ik_3W_B\Big)w_c \\ &+ \Big(\frac{R_1^2}{R_0^2}\frac{\partial\eta}{\partial x}U_B+R_1V_B\Big)g_c.\end{aligned} \tag{3.5.5}$$

The system (3.5.1)–(3.5.5) along with the homogenous boundary conditions,

$$(u_c, v_c, w_c) = (0, 0, 0) \quad \text{at} \quad \eta = 0;$$

$$(u_c, w_c) \to (0, 0) \quad \text{as} \quad \eta \to \infty,$$

forms the non-parallel eigenvalue formulation. Since the pressure perturbation is absent, the ensuring eigen solution will be referred to as the 'boundary layer mode'.

3.5.2 Parallel boundary-layer eigenvalue formulation

If the nonparallel flow terms $\frac{\partial U_B}{\partial x}$, $\frac{\partial W_B}{\partial x}$, V_B, and $\frac{\partial \eta}{\partial x}$ are neglected, equations (3.5.1)–(3.5.5) simplify to

$$\frac{\mathrm{d}u_c}{\mathrm{d}\eta} = R_1 f_c, \tag{3.5.6}$$

$$\frac{\mathrm{d}v_c}{\mathrm{d}\eta} = -\frac{R_1}{R_0^2}(\sigma u_c + i w_c), \tag{3.5.7}$$

$$\frac{\mathrm{d}w_c}{\mathrm{d}\eta} = R_1 g_c, \tag{3.5.8}$$

$$\frac{\mathrm{d}f_c}{\mathrm{d}\eta} = \frac{R_1}{R_0^2}\Big(- i\omega + \sigma U_B + i k_3 W_B\Big) u_c + v_c \frac{\partial U_B}{\partial \eta}, \tag{3.5.9}$$

$$\frac{\mathrm{d}g_c}{\mathrm{d}\eta} = k_3 v_c \frac{\partial W_B}{\partial \eta} + \frac{R_1}{R_0^2}\Big(- i\omega + \sigma U_B + i k_3 W_B\Big) w_c, \tag{3.5.10}$$

with the boundary conditions

$$(u_c, v_c, w_c) = (0, 0, 0) \quad \text{at} \quad \eta = 0;$$

$$(u_c, w_c) = (0, 0) \quad \text{as} \quad \eta \to \infty.$$

The above system will be referred to as parallel boundary layer eigenvalue problem.

3.5.3 Non-parallel Navier-Stokes eigenvalue formulation

In the previous non-parallel eigenvalue formulation, the pressure gradient terms are neglected, which is justified for $x = O(1)$. However, the pressure fluctuation induced by the displacement will eventually become an $O(1)$ effect when $x = O(R_A)$. The usual Navier-Stokes eigenvalue problem will have to be considered.

Inserting $p = P_B + \epsilon\hat{p}$ along with (3.4.69) into the normalised Navier-Stokes equations (3.4.14)–(3.4.17), we obtain the linearised perturbation equations

$$\frac{\partial \hat{u}}{\partial x} + R_0^2 \frac{\partial \hat{v}}{\partial y} + \frac{\partial \hat{w}}{\partial z} = 0, \tag{3.5.11}$$

$$\frac{\partial \hat{u}}{\partial t} + U_B \frac{\partial \hat{u}}{\partial x} + \hat{u}\frac{\partial U_B}{\partial x} + R_0^2\Big(V_B \frac{\partial \hat{u}}{\partial y} + \hat{v}\frac{\partial U_B}{\partial y}\Big) + W_B \frac{\partial \hat{u}}{\partial z} = -\frac{\partial \hat{p}}{\partial x} + R_0^2 \frac{\partial^2 \hat{u}}{\partial y^2} + \frac{1}{R_\Lambda}\frac{\partial^2 \hat{u}}{\partial z^2}, \tag{3.5.12}$$

$$\frac{\partial \hat{v}}{\partial t} + U_B \frac{\partial \hat{v}}{\partial x} + \hat{u}\frac{\partial V_B}{\partial x} + R_0^2\Big(V_B \frac{\partial \hat{v}}{\partial y} + \hat{v}\frac{\partial V_B}{\partial y}\Big) + W_B \frac{\partial \hat{v}}{\partial z} = -R_\Lambda \frac{\partial \hat{p}}{\partial y} + R_0^2 \frac{\partial^2 \hat{v}}{\partial y^2} + \frac{1}{R_\Lambda}\frac{\partial^2 \hat{v}}{\partial z^2}, \tag{3.5.13}$$

$$\frac{\partial \hat{w}}{\partial t} + U_B \frac{\partial \hat{w}}{\partial x} + \hat{u}\frac{\partial W_B}{\partial x} + R_0^2\Big(V_B \frac{\partial \hat{w}}{\partial y} + \hat{v}\frac{\partial W_B}{\partial y}\Big) + W_B \frac{\partial \hat{w}}{\partial z} = -\frac{\partial \hat{p}}{\partial z} + R_0^2 \frac{\partial^2 \hat{w}}{\partial y^2} + \frac{1}{R_\Lambda}\frac{\partial^2 \hat{w}}{\partial z^2}, \tag{3.5.14}$$

where $\hat{p}$ is the perturbation pressure. Note that we have neglected the streamwise diffusion terms because they remain of a higher-order effect in the entire region of interest, over which the equations (3.5.11)–(3.5.14) serve as an composite approximation in the sense that they contain the upstream and downstream regimes in the appropriate asymptotic limits.

The solution for $\hat{u}$, $\hat{v}$, $\hat{w}$, and $\hat{p}$ may be sought of the form

$$(\hat{u}, \hat{v}, \hat{w}, \hat{p}) = \Big[\tilde{u}(x,\eta), \tilde{v}(x,\eta), \frac{1}{k_3}\tilde{w}(x,\eta), \tilde{p}(x,\eta)\Big] \exp\Big\{i(k_3 z - \omega t)\Big\}.$$

Substitution into (3.5.11)–(3.5.14) yields

$$\frac{\partial \tilde{u}}{\partial x} + R_0^2 \frac{\partial \tilde{v}}{\partial y} + i\tilde{w} = 0, \tag{3.5.15}$$

$$-i\omega\tilde{u} + U_B \frac{\partial \tilde{u}}{\partial x} + \tilde{u}\frac{\partial U_B}{\partial x} + R_0^2\Big(V_B \frac{\partial \tilde{u}}{\partial y} + \tilde{v}\frac{\partial U_B}{\partial y}\Big) + ik_3 W_B \tilde{u} = -\frac{\partial \tilde{p}}{\partial x} + R_0^2 \frac{\partial^2 \tilde{u}}{\partial y^2} - \frac{k_3^2}{R_\Lambda}\tilde{u}, \tag{3.5.16}$$

$$-i\omega\tilde{v} + U_B \frac{\partial \tilde{v}}{\partial x} + \tilde{u}\frac{\partial V_B}{\partial x} + R_0^2\Big(V_B \frac{\partial \tilde{v}}{\partial y} + \tilde{v}\frac{\partial V_B}{\partial y}\Big) + ik_3 W_B \tilde{v} = -R_\Lambda \frac{\partial \tilde{p}}{\partial y} + R_0^2 \frac{\partial^2 \tilde{v}}{\partial y^2} - \frac{k_3^2}{R_\Lambda}\tilde{v}, \tag{3.5.17}$$

$$-i\omega\tilde{w} + U_B \frac{\partial \tilde{w}}{\partial x} + k_3\tilde{u}\frac{\partial W_B}{\partial x} + R_0^2\Big(V_B \frac{\partial \tilde{w}}{\partial y} + k_3\tilde{v}\frac{\partial W_B}{\partial y}\Big) + ik_3 W_B \tilde{w} = -ik_3^2\tilde{p} + R_0^2 \frac{\partial^2 \tilde{w}}{\partial y^2} - \frac{k_3^2}{R_\Lambda}\tilde{w}. \tag{3.5.18}$$

Since the base flow is evaluated on η grid, equations (3.5.15)–(3.5.18) are re-written in terms of η,

$$\frac{\partial \tilde{u}}{\partial x} + \frac{\partial \tilde{u}}{\partial \eta}\frac{\partial \eta}{\partial x} + \frac{R_0^2}{R_1}\frac{\partial \tilde{v}}{\partial \eta} + i\tilde{w} = 0, \tag{3.5.19}$$

$$-i\omega\tilde{u} + U_B\Big(\frac{\partial\tilde{u}}{\partial x} + \frac{\partial\tilde{u}}{\partial\eta}\frac{\partial\eta}{\partial x}\Big) + \tilde{u}\Big(\frac{\partial U_B}{\partial x} + \frac{\partial U_B}{\partial\eta}\frac{\partial\eta}{\partial x}\Big) + R_0^2\Big(\frac{V_B}{R_1}\frac{\partial\tilde{u}}{\partial\eta} + \frac{\tilde{v}}{R_1}\frac{\partial U_B}{\partial\eta}\Big)$$
$$+ik_3W_B\tilde{u} = -\Big(\frac{\partial\tilde{p}}{\partial x} + \frac{\partial\tilde{p}}{\partial\eta}\frac{\partial\eta}{\partial x}\Big) + \frac{R_0^2}{R_1^2}\frac{\partial^2\tilde{u}}{\partial\eta^2} - \frac{k_3^2}{R_\Lambda}\tilde{u}, \tag{3.5.20}$$

$$-i\omega\tilde{v} + U_B\Big(\frac{\partial\tilde{v}}{\partial x} + \frac{\partial\tilde{v}}{\partial\eta}\frac{\partial\eta}{\partial x}\Big) + \tilde{u}\Big(\frac{\partial V_B}{\partial x} + \frac{\partial V_B}{\partial\eta}\frac{\partial\eta}{\partial x}\Big) + R_0^2\Big(\frac{V_B}{R_1}\frac{\partial\tilde{v}}{\partial\eta} + \frac{\tilde{v}}{R_1}\frac{\partial V_B}{\partial\eta}\Big)$$
$$+ik_3W_B\tilde{v} = -\frac{R_\Lambda}{R_1}\frac{\partial\tilde{p}}{\partial\eta} + \frac{R_0^2}{R_1^2}\frac{\partial^2\tilde{v}}{\partial\eta^2} - \frac{k_3^2}{R_\Lambda}\tilde{v}, \tag{3.5.21}$$

$$-i\omega\tilde{w} + U_B\Big(\frac{\partial\tilde{w}}{\partial x} + \frac{\partial\tilde{w}}{\partial\eta}\frac{\partial\eta}{\partial x}\Big) + k_3\tilde{u}\Big(\frac{\partial W_B}{\partial x} + \frac{\partial W_B}{\partial\eta}\frac{\partial\eta}{\partial x}\Big) + R_0^2\Big(\frac{V_B}{R_1}\frac{\partial\tilde{w}}{\partial\eta} + \frac{k_3\tilde{v}}{R_1}\frac{\partial W_B}{\partial\eta}\Big)$$
$$+ik_3W_B\tilde{w} = -ik_3^2\tilde{p} + \frac{R_0^2}{R_1^2}\frac{\partial^2\tilde{w}}{\partial\eta^2} - \frac{k_3^2}{R_\Lambda}\tilde{w}. \tag{3.5.22}$$

For the linearised Navier-Stokes eigenmode formulation, the ratio b/a, spanwise wavelength Λ/a, Reynolds number R_Λ, and the frequency ω are the four independent parameters.

We seek normal-mode solution

$$(\tilde{u},\tilde{v},\tilde{w},\tilde{p}) = \Big[u_c(\eta), v_c(\eta), w_c(\eta), p_c(\eta)\Big]\exp\{\int^x \sigma dx\},$$

where σ is in general a complex number dependent on x with its real part representing the local growth rate. We let

$$\frac{\mathrm{d}u_c}{\mathrm{d}\eta} = R_1 f_c, \quad \text{and} \quad \frac{\mathrm{d}w_c}{\mathrm{d}\eta} = R_1 g_c. \tag{3.5.23}$$

From the continuity equation (3.5.19), we have

$$\frac{\mathrm{d}v_c}{\mathrm{d}\eta} = -\frac{R_1}{R_0^2}\sigma u_c - i\frac{R_1}{R_0^2}w_c - \frac{R_1^2}{R_0^2}\frac{\partial\eta}{\partial x}f_c. \tag{3.5.24}$$

Eliminating $\frac{\mathrm{d}\tilde{p}}{\mathrm{d}\eta}$ through the operation, (3.5.20) $\times \frac{R_\Lambda}{R_1} -$ (3.5.21) $\times \frac{\partial \eta}{\partial x}$, we find

$$\begin{aligned}
\frac{\mathrm{d}f_c}{\mathrm{d}\eta} &= \frac{1}{A_1}\Bigg\{ -i\omega\frac{R_\Lambda}{R_1} + \Big[\frac{R_\Lambda}{R_1}U_B + \frac{R_1}{R_0^2}\Big(\frac{\partial\eta}{\partial x}\Big)^2 + \frac{\partial\eta}{\partial x}V_B\Big]\sigma + \frac{R_\Lambda}{R_1}\Big(\frac{\partial U_B}{\partial x} + \frac{\partial U_B}{\partial\eta}\frac{\partial\eta}{\partial x}\Big) \\
&- \frac{\partial\eta}{\partial x}\Big(\frac{\partial V_B}{\partial x} + \frac{\partial V_B}{\partial\eta}\frac{\partial\eta}{\partial x}\Big) + ik_3W_B\frac{R_\Lambda}{R_1} + \frac{k_3^2}{R_1}\Bigg\}u_c \\
&+ \frac{1}{A_1}\Big[i\omega\frac{\partial\eta}{\partial x} - \sigma U_B\frac{\partial\eta}{\partial x} + R_\Lambda\frac{R_0^2}{R_1^2}\frac{\partial U_B}{\partial\eta} - \frac{R_0^2}{R_1}\frac{\partial\eta}{\partial x}\frac{\partial V_B}{\partial\eta} - ik_3W_B\frac{\partial\eta}{\partial x} - \frac{k_3^2}{R_\Lambda}\frac{\partial\eta}{\partial x}\Big]v_c \\
&+ \frac{i}{A_1}\Big[V_B\frac{\partial\eta}{\partial x} + U_B\frac{R_1}{R_0^2}\Big(\frac{\partial\eta}{\partial x}\Big)^2\Big]w_c + \frac{R_\Lambda}{A_1R_1}\sigma p_c - \frac{i}{A_1}\frac{\partial\eta}{\partial x}g_c \\
&+ \frac{1}{A_1}\Bigg\{R_\Lambda U_B\frac{\partial\eta}{\partial x} + U_B\frac{R_1^2}{R_0^2}\Big(\frac{\partial\eta}{\partial x}\Big)^3 + \frac{R_\Lambda R_0^2}{R_1}V_B + R_1V_B\Big(\frac{\partial\eta}{\partial x}\Big)^2 \\
&\quad -\frac{\partial\eta}{\partial x}\Big[\sigma + \frac{\partial}{\partial\eta}\Big(\frac{\partial\eta}{\partial x}\Big)\Big]\Bigg\}f_c, \qquad (3.5.25)
\end{aligned}$$

where

$$A_1 = \frac{R_\Lambda R_0^2}{R_1^2} + \Big(\frac{\partial\eta}{\partial x}\Big)^2, \quad \text{and} \quad \frac{\partial}{\partial\eta}\Big(\frac{\partial\eta}{\partial x}\Big) = \frac{1}{2}\frac{\Lambda}{L}\frac{1}{S}\Big[\frac{S}{u_e(S)}\frac{du_e}{dS} - 1\Big].$$

Elimination $\frac{\mathrm{d}f_c}{\mathrm{d}\eta}$ through manipulation, (3.5.20) $\times \frac{\partial\eta}{\partial x} +$ (3.5.21) $\times \frac{R_0^2}{R_1}$, we obtain

$$\begin{aligned}
\frac{\mathrm{d}p_c}{\mathrm{d}\eta} &= -\frac{1}{A_1}\Bigg\{ -i\omega\frac{\partial\eta}{\partial x} - \frac{R_0^2}{R_1}V_B\sigma + \frac{\partial U_B}{\partial x}\frac{\partial\eta}{\partial x} + \frac{\partial U_B}{\partial\eta}\Big(\frac{\partial\eta}{\partial x}\Big)^2 + \frac{R_0^2}{R_1}\frac{\partial V_B}{\partial x} \\
&+ \frac{R_0^2}{R_1}\frac{\partial V_B}{\partial\eta}\frac{\partial\eta}{\partial x} + ik_3W_B\frac{\partial\eta}{\partial x} + \frac{k_3^2}{R_\Lambda}\frac{\partial\eta}{\partial x}\Bigg\}u_c \\
&- \frac{R_0^2}{A_1R_1}\Big[-i\omega + \sigma U_B + \frac{\partial U_B}{\partial\eta}\frac{\partial\eta}{\partial x} + \frac{R_0^2}{R_1}\frac{\partial V_B}{\partial\eta} + ik_3W_B + \frac{k_3^2}{R_\Lambda}\Big]v_c \\
&+ \frac{i}{A_1}\Big(U_B\frac{\partial\eta}{\partial x} + V_B\frac{R_0^2}{R_1}\Big)w_c - \frac{1}{A_1}\frac{R_0^2}{R_1}\Big[\sigma + \frac{\partial}{\partial\eta}\Big(\frac{\partial\eta}{\partial x}\Big)\Big]f_c - \frac{\sigma}{A_1}\frac{\partial\eta}{\partial x}p_c \\
&- i\frac{R_0^2}{A_1R_1}g_c. \qquad (3.5.26)
\end{aligned}$$

The spanwise momentum equation (3.5.22) may be written as

$$\begin{aligned}\frac{\mathrm{d}g_c}{\mathrm{d}\eta} &= u_c\frac{k_3R_1}{R_0^2}\Big(\frac{\Lambda}{L}\frac{\partial W_B}{\partial S}+\frac{\partial W_B}{\partial\eta}\frac{\partial\eta}{\partial x}\Big)+k_3v_c\frac{\partial W_B}{\partial\eta}+\frac{ik_3^2R_1}{R_0^2}p_c+\Big(\frac{R_1^2}{R_0^2}\frac{\partial\eta}{\partial x}U_B+R_1V_B\Big)g_c\\ &+ \frac{R_1}{R_0^2}\Big(-i\omega+\sigma U_B+ik_3W_B+\frac{k_3^2}{R_\Lambda}\Big)w_c \qquad (3.5.27)\end{aligned}$$

In conclusion, the classical non-parallel eigenvalue formulation consists of (3.5.23)–(3.5.27), and the boundary conditions

$$(u_c,v_c,w_c)=(0,0,0)\quad\text{at}\quad\eta=0;$$

$$(u_c,v_c,w_c,p_c)=(0,0,0)\quad\text{as}\quad\eta\to\infty.$$

The above linearised Navier-Stokes eigenvalue problem is more general than the boundary-layer eigenvalue problem. Let us now discuss the relationship between them and the respective region of validity in the context of the present problem. In the downstream region, where $S=O(1)$ and $u_e=O(1)$, we know from (3.4.7) that $C=O(a^2/b^2)$, and so

$$R_1=\frac{\delta}{\delta_s}=\sqrt{\frac{CS}{u_e}}=O(\frac{a}{b}).$$

The local boundary layer thickness

$$\delta=\sqrt{\frac{\nu s^*}{u_e^*}}\sim\sqrt{\frac{\nu L}{U_\infty}}=\frac{\Lambda}{\sqrt{R_\Lambda}}\sqrt{\frac{L}{\Lambda}}=O(\Lambda),$$

if we take the Reynolds number

$$R_\Lambda=O(\frac{a^2}{b^2}).$$

Thus

$$A_1=\frac{R_\Lambda R_0^2}{R_1^2}+\Big(\frac{\partial\eta}{\partial x}\Big)^2=O(1),$$

implying an $O(1)$ pressure variation across the boundary layer so that the instability is governed by the Navier-Stokes eigenvalue problem. A closer inspection of the asymptotic scalings suggests that the viscous terms are all of higher-order effects, that is, the eigen modes are actually governed by the Rayleigh equation with the effective profile

$$U_{eff}=U_B+\frac{ik_3}{\sigma}W_B.$$

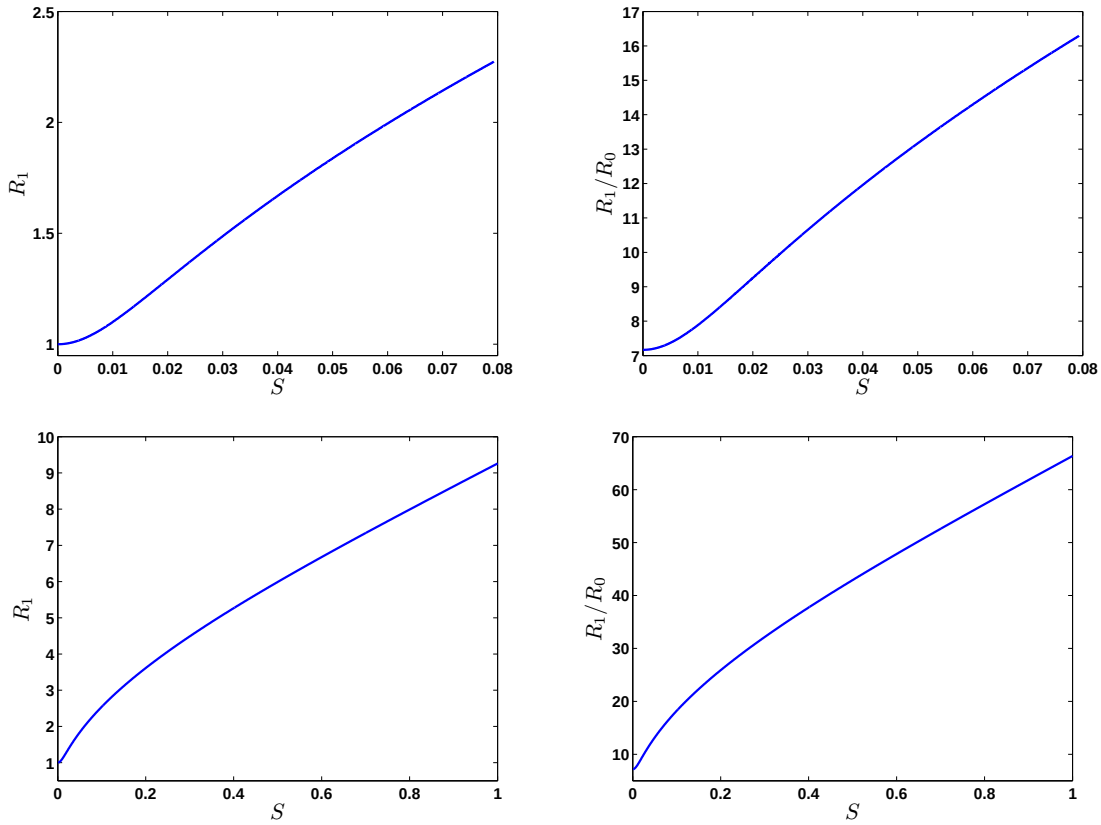


Figure 3.13: The distribution of $R_1 = \delta/\delta_s$ and R_1/R_0 along the airfoil for $b/a = 0.1$.

On the other hand, in the leading-edge region where $x = O(1)$, $S = O(\Lambda/L) = O(b^2/a^2)$ and $u_e = O(1)$. Clearly,

$$R_1 = \frac{\delta}{\delta_s} = \sqrt{\frac{CS}{u_e}} = O(1),$$

so that

$$A_1 = \frac{R_\Lambda R_0^2}{R_1^2} + \left(\frac{\partial \eta}{\partial x}\right)^2 = O(R_\Lambda),$$

implying that $\partial\tilde{p}/\partial\eta = 0$, and consequently the linearised Navier-Stokes eigenvalue reduces to the linearised boundary layer eigenvalue in this limit and the instability is of viscous nature. The 'parameter' R_1/R_0 determines different regimes of instability. It should be noted that when $R_1/R_0 = O(1)$, an eigenvalue formulation is, strictly speaking, not applicable. It is justified only when $R_1/R_0 \gg 1$, which is the case sufficiently downstream. Figure (3.13) displays the variation of R_1 and R_1/R_0 along the airfoil.

As will be shown in §3.6, between the region where $R_1/R_0 \gg 1$ and the region

where $R_1/R_0 = O(R_\Lambda)$, there exists an intermediate regime corresponding to $R_1/R_0 = O(R_\Lambda)^{1/5}$. In this region, the viscosity effect and the pressure perturbation are both important.

3.6 Numerical results

The initial-boundary-value and eigenvalue problems are solved numerically using the same numerical algorithms as in the case of Görtler vortices. However, extra terms appear due to the presence of the crossflow. Further validation of the code is needed. This is performed by comparing the growth rates obtained by solving the linearised Navier-Stokes eigenvalue problem (3.5.23)–(3.5.27) for the swept Hiemenz flow with the result presented in MLC.

3.6.1 Validation of the eigenvalue solver

MLC studied spatial crossflow instability using the swept Hiemenz flow as the base flow. The growth rates shown in their paper can be used as a reference for us to check our codes. Since the variables used in MLC are defined differently from ours, we need first to find the relations between the two sets of variables. The subscript M will be used to denote the variables in MLC.

The slip velocity in MLC's is given by

$$U_{\infty_M} = C_M \cdot s^* = C_M \cdot \frac{s^*}{\Lambda} \cdot \Lambda = C_M \cdot x \cdot \Lambda, \tag{3.6.1}$$

while in ours

$$u_e^* = C \cdot S \cdot U_\infty = C \cdot \frac{\Lambda}{L} \cdot x \cdot U_{\infty.} \tag{3.6.2}$$

Equality of the two, $U_{\infty_M} = u_e^*$, implies that

$$C_M = \frac{C}{L} \cdot U_\infty. \tag{3.6.3}$$

In MLC, the reference length scale used for non-dimensionalisation is defined as

$$l = \left(\frac{\nu}{C_M}\right)^{\frac{1}{2}}. \tag{3.6.4}$$

Substitution of (3.6.3) into (3.6.4) yields

$$l = \Big(\frac{\nu L}{C U_\infty}\Big)^{\frac{1}{2}} = \delta_s, \tag{3.6.5}$$

where δ_s refers to the stagnation point boundary layer thickness in our formulation. The Reynolds number defined in MLC is

$$R_M = \frac{U_{\infty_M} l}{\nu} = \frac{C_M \cdot s^* \cdot l}{\nu} = \frac{s^* \cdot l}{l^2} = \frac{s^*}{l} = \frac{x\Lambda}{l}. \tag{3.6.6}$$

Substituting (3.6.5) into (3.6.6), we find

$$R_M = x \cdot \Lambda \cdot \Big(\frac{U_\infty C}{\nu L}\Big)^{\frac{1}{2}} = x \cdot \Big(\frac{U_\infty \Lambda}{\nu} \cdot \frac{\Lambda C}{L}\Big)^{\frac{1}{2}} = x(R_\Lambda R_0^2)^{\frac{1}{2}}. \tag{3.6.7}$$

The normalised spanwise wavenumber in our formulation and MLC's are

$$k_3 = k_3^* \Lambda, \qquad \text{and} \quad \beta = k_3^* l \tag{3.6.8}$$

respectively. It follows that

$$\beta = \frac{k_3}{\Lambda} l = \frac{k_3}{\Lambda}\Big(\frac{\nu L}{C U_\infty}\Big)^{\frac{1}{2}} = \Big(\frac{\nu}{\Lambda U_\infty} \cdot \frac{L}{\Lambda C}\Big)^{\frac{1}{2}} = k_3 (R_\Lambda R_0^2)^{-\frac{1}{2}}. \tag{3.6.9}$$

In our formulation $k_3 = 1$, which means

$$\beta = (R_\Lambda R_0^2)^{-\frac{1}{2}}. \tag{3.6.10}$$

From the normalisation of the velocity in the x direction, we know

$$U_S = \frac{u^*}{U_\infty} = \frac{u^*}{W_{\infty_M}} \cdot \frac{W_{\infty_M}}{U_\infty} = U_M \tan\phi_\infty, \tag{3.6.11}$$

where $U_S = R_0^2 f' x$, and $U_M = x_M f'_M / \bar{R} = R f'_M / \bar{R}$ respectively. If $\tan\phi_\infty = 1$, then the base flows are identical,

$$U_S = U_M, \qquad \text{i.e.} \quad R_0^2 f' x = \frac{R}{\bar{R}} f'_M = \frac{x(R_\Lambda R_0^2)^{\frac{1}{2}}}{\bar{R}} f'_M. \tag{3.6.12}$$

Since $f' = f'_M$, the relation (3.6.12) implies that

$$R_0^2 = \frac{(R_0^2 R_\Lambda)^{\frac{1}{2}}}{\bar{R}}. \tag{3.6.13}$$

Combining (3.6.10) and (3.6.13), we get

$$R_0^2 = \frac{1}{\beta\bar{R}}, \qquad R_\Lambda = \frac{\bar{R}}{\beta}, \tag{3.6.14}$$

and

$$\Lambda/a = \frac{L}{aC} \cdot R_0^2 = \frac{L}{aC} \cdot \frac{1}{\beta\bar{R}}. \tag{3.6.15}$$

Substitution of (3.6.14) into (3.6.7) shows

$$R_M = x/\beta. \tag{3.6.16}$$

The growth rate is normalised by l in MLC, i.e.

$$\sigma_M = \sigma^* l, \tag{3.6.17}$$

while in our formualtion, the growth rate is normalised by Λ, i.e.

$$\sigma = \sigma^* \Lambda. \tag{3.6.18}$$

From (3.6.17) and (3.6.18), we have

$$\sigma = \frac{\sigma_M}{l} \cdot \Lambda = \sigma_M \cdot \left(\frac{\nu L}{C U_\infty}\right)^{-\frac{1}{2}} \Lambda = \sigma_M \cdot \left(\frac{\nu}{\Lambda U_\infty} \cdot \frac{L}{\Lambda C}\right)^{-\frac{1}{2}} = \sigma_M (R_\Lambda R_0^2)^{\frac{1}{2}} = \sigma_M/\beta. \tag{3.6.19}$$

The frequency ω in our formulation is

$$\omega = 2\pi f^* \cdot \frac{\Lambda}{U_\infty}, \qquad \text{i.e.} \quad f^* = \frac{\omega}{2\pi} \cdot \frac{U_\infty}{\Lambda}, \tag{3.6.20}$$

where f^* denotes the dimensional frequency. The frequency in MLC's formulation is

$$F_M = \frac{2\pi\nu f^*}{W_{\infty_M}^2}, \qquad \text{i.e.} \quad f^* = \frac{F_M}{2\pi\nu} \cdot W_{\infty_M}^2, \tag{3.6.21}$$

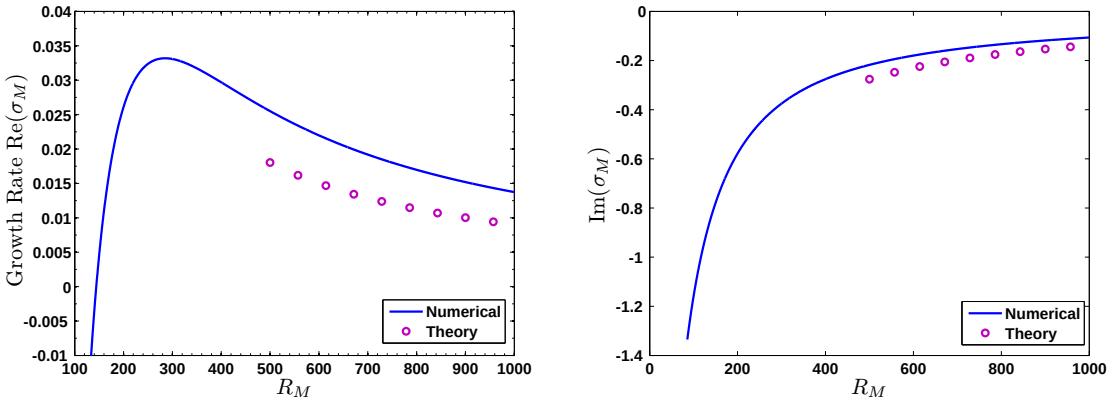


Figure 3.14: The growth rate and chordwise wavenumber of crossflow vortices at different chordwise locations. Parameter values: $\omega = 0.1071$, $R_\Lambda = 1428.57$ and $\Lambda/a = 2.9 \times 10^{-4}$.

where W_{∞_M} is the oncoming free-stream velocity in the spanwise direction. From (3.6.20) and (3.6.21), it follows

$$\frac{\omega}{2\pi} \cdot \frac{U_\infty}{\Lambda} = \frac{F_M}{2\pi\nu} \cdot W_{\infty_M}^2, \qquad \text{i.e.} \quad \omega = F_M \cdot R_\Lambda \cdot \frac{W_{\infty_M}^2}{U_\infty^2} \tag{3.6.22}$$

From the definition

$$\bar{R} = \frac{W_{\infty_M} l}{\nu},$$

we have

$$W_{\infty_M} = \frac{\bar{R} \cdot \nu}{l}. \tag{3.6.23}$$

Substitution of (3.6.23) and (3.6.5) into (3.6.22) leads to

$$\omega = F_M \cdot R_0^2 \cdot \bar{R}^2 = F_M \bar{R}/\beta. \tag{3.6.24}$$

From figure 5 in MLC, we can extract the value of $\sigma_M = i\alpha = -\alpha_i + i\alpha_r$. The value of α_i can be read directly from the figure. From the relation

$$\tan(\theta + \psi) = \frac{\beta}{\alpha_r}, \tag{3.6.25}$$

where θ is the local sweep angle in MLC defined as $\theta = \arctan(\bar{R}/R)$, and ψ is the orientation angle, which can be read from the figure directly, the value of α_r can be obtained. When frequency $F = 0.75 \times 10^{-4}$ and $\beta \approx 0.35$, we have $-\alpha_i = 0.032$, and $\alpha_r = -0.36289472$. Using (3.6.16) and (3.6.19), we find the corresponding location

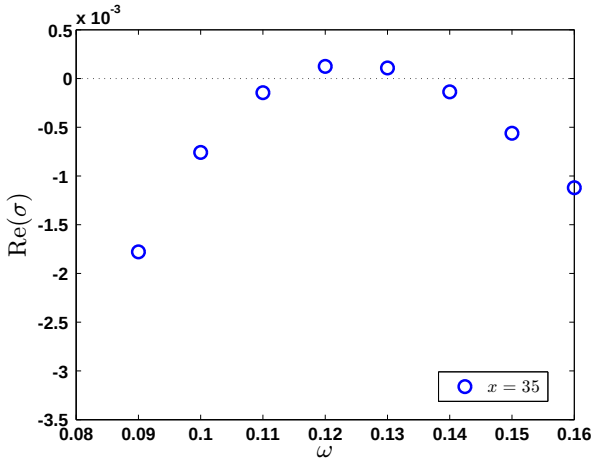


Figure 3.15: Non-parallel eigenvalue calculation for different frequencies at $x = 35$ with $\Lambda/a = 0.005$, $k_3 = 1.0$, and $b/a = 0.1$.

$x = 105$ and the initial guess for $\sigma = (0.09143, -1.03684)$ with $\omega = 0.1071$ to start the Newton-Raphson iteration. From (3.6.14), we get $R_0^2 = 5.714 \times 10^{-3}$, and $R_\Lambda = 1428.57$, while using (3.6.15) with $b/a = 0.1$, we have $\Lambda/a = 2.9 \times 10^{-4}$. The convergent value after the Newton-Raphson iteration turns out to be (0.09452, -1.07230).

With the parameters given above, we calculate the growth rates at different locations (i.e. R_M values) using our eigenvalue solver. The results are shown in figure 3.14, and are found to be quite close to those in figure 7(b) in MLC (see figure **??**) . There is a slight difference between the two since $\beta = 0.4$ in figure 7(b) of MLC. But overall, the result is convincing enough to indicate both our formulation and eigenvalue solver are reliable.

3.6.2 Initial-value and eigenvalue solutions

Figure 3.15 shows boundary-layer eigenmodes at $x = 35.0$ for different frequencies with $\Lambda/a = 0.005$. When the frequency $\omega = 0.12$, the unstable mode acquires its maximum growth rate. This result fits the linear stability theory (Reed and Saric 1989) that unsteady disturbances are more amplified than steady ones. Although, unsteady disturbances are more amplified, eigenmodes with a frequency ω exceeding a certain value are damped. In the following computation, the value $\omega = 0.12$ will be used as the suitable frequency value to perform other unsteady initial-value and eigenvalue calculations. Figure 3.16 shows the non-parallel eigenvalues for different spanwise wavelengths. As the wavelength decreases,

the eigenmode becomes more amplified, indicating that crossflow vortices of short wavelength are more likely to occur. This trend echoes the finding of Saric and his coworker (Dagenhart and Saric 1999), who observed in their experiment that stationary vortices of smaller wavelength exhibit a larger growth rate in the region close to the leading edge. Presumably, the same trend holds for non-stationary vortices. In our calculations, the growth rate for $\Lambda/a = 0.001$ is quite appreciable, and so the value $\Lambda/a = 0.001$ will be used for other initial-value and eigenvalue calculations.

We now discuss the nature of the instability. It should be emphasised that the instability is governed by the linearised boundary layer equations, and occurs without any pressure fluctuation. This instability is similar to that identified by Cowley et al. (1985) for a two-dimensional boundary-layer type of flows. They showed that if the base flow profiles U_B is non-monotonic such that there exists a local maximum or minimum at η_c, i.e. $U_B'(\eta_c) = 0$, then there exists a temporally amplifying mode with $\omega_r/\alpha = U_B(\eta_c)$ to leading order, where ω_r is the real part of the complex frequency $\omega = \omega_r + i\omega_i$. The characteristic wavelength of the mode is much shorter than the streamwise length scale of the mean flow, but much longer than the local boundary-layer thickness. Recently, Riley et al. (2009), and Hewitt and Duck (2011) analysed spatial instability of such flows, and showed that a spatially amplifying mode exists with its frequency ω and wavenumber satisfying the relation $\omega/\alpha = U_B(\eta_c)$

The result mentioned above can be generalised to a generic three-dimensional boundary layer. For the problem under consideration, the eigenvalue formulation can formally be justified in the downstream region corresponding to $x \gg 1$, where $R_1/R_0 \gg 1$. In this limit, we may seek an an asymptotic solution with

$$\sigma = \sigma_0 + (R_0/R_1)\sigma_1 + \dots . \tag{3.6.26}$$

and similar expansions for the eigenfunction $(\tilde{u}, \tilde{v}, \tilde{w})$. It can be shown that at leading order

$$\tilde{v} = \bar{A}^{\pm}\Big[U_B + \frac{k_3}{\sigma}W_B - \frac{\omega}{\sigma}\Big], \qquad \sigma\tilde{u} + ik_3\tilde{w} = -\bar{A}^{\pm}\frac{R_0^2}{R_1}\Big[U_B' + \frac{k_3}{\sigma}W_B'\Big], \tag{3.6.27}$$

where $\bar{A}^{\pm}$ is an $O(1)$ constant which may take different values above or below η_c (Cowley et al., 1985). It can be shown that σ_0 is purely imaginary, i.e. $\sigma_0 = i\sigma_i$, and the instability

is equivalent to that for a two-dimensional flow with an effective profile

$$U_{eff} = U_B + \frac{k_3}{\sigma_i} W_B.$$

The skewed profile has a maximum at η_c, $U'_{eff} = 0$, i.e.

$$\sigma_i \frac{\partial U_B(\eta_c)}{\partial \eta} + k_3 \frac{\partial W_B(\eta_c)}{\partial \eta} = 0. \tag{3.6.28}$$

The frequency ω and σ_i satisfy the relation

$$\frac{\omega}{\sigma_i} = U_B + \frac{k_3}{\sigma_i} W_B,$$

i.e.

$$\omega = \sigma_i U_B(\eta_c) + k_3 W_B(\eta_c). \tag{3.6.29}$$

From (3.6.28) and (3.6.29) it follows

$$-\frac{\omega}{k_3} + [\frac{W_B(\eta_c)}{U_B(\eta_c)} - \frac{W'_B(\eta_c)}{U'_B(\eta_c)}] U_B(\eta_c) = 0. \tag{3.6.30}$$

The relations (3.6.28) and (3.6.30) allow us to determine σ_i. At a given downstream location, the values of the base flow U_B, W_B, and their derivatives U'_B, and W'_B are all known. We are able to find the location of η which satisfies the relation (3.6.30). When the value of η_c is known, the imaginary part of the eigenvalue, i.e. σ_i will be obtained from (3.6.28). An analysis of the viscous critical layer, which has a width of $O[(R_0/R_1)^{1/2}]$, gives the value of

$$\sigma_1 = -\frac{(-i\sigma_i U''_{eff})^{1/2}}{\sqrt{2} U_B(\eta_c)},$$

and so the real part of σ

$$\sigma_r = \frac{(\sigma_i U''_{eff})^{1/2}}{2 U_B(\eta_c)} R_0/R_1. \tag{3.6.31}$$

In figure 3.17, the value of σ computed by solving the non-parallel eigenvalue problem is compared with the theoretical result. As illustrated in figure 3.17, for σ_i the numerical result matches with the theoretical prediction quite well. The theoretical value for σ_r is about twice the numerical value. The discrepancy arises because R_0/R_1 is not large enough, merely 0.2. But the general trend is consistent. The overall agreement reassures

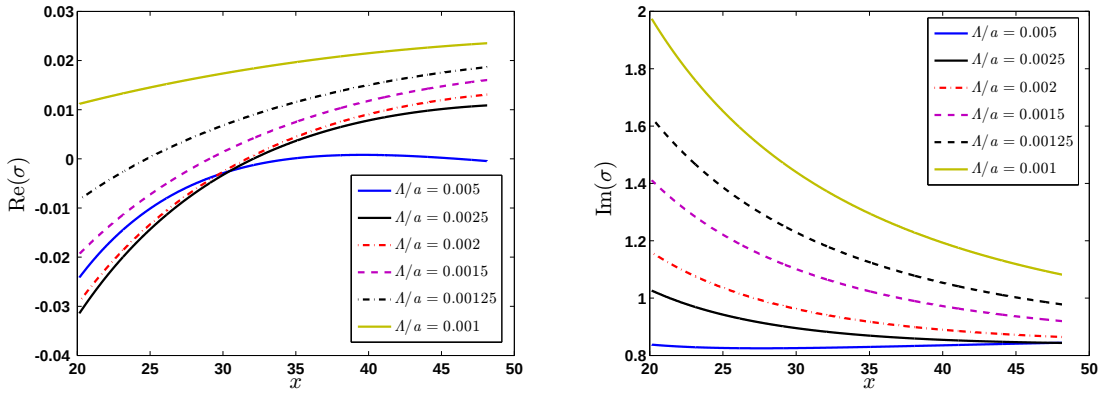


Figure 3.16: The growth rates $(\mathrm{Re}(\sigma))$ and chordwise wavenumber $(\mathrm{Im}(\sigma))$ of the non-parallel eigenmodes for different spanwise wavelengths for $\omega = 0.12$, $k_3 = 1.0$, and $b/a = 0.1$.

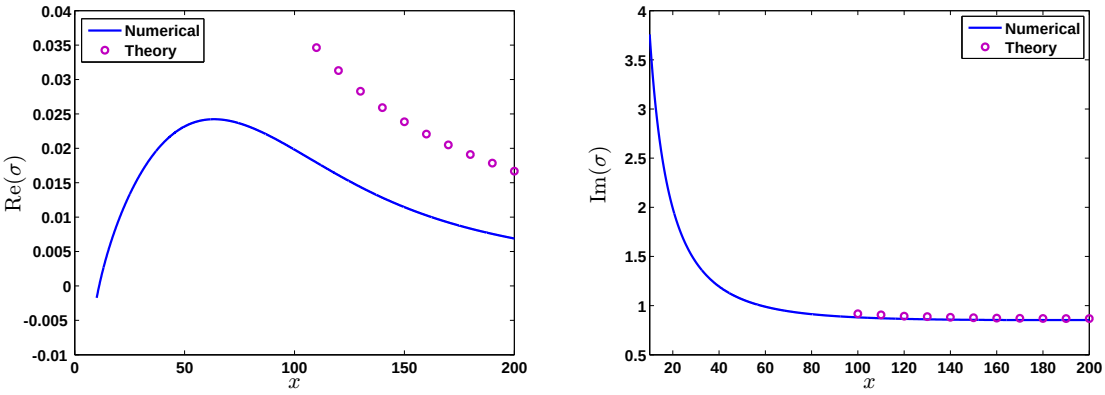


Figure 3.17: Non-parallel eigenvalue and comparison with the theoretical result . Parameter values: $\omega = 0.12$, $\Lambda/a = 0.001$, $k_3 = 1.0$, and $b/a = 0.1$.

us that the numerical results are reliable. We also apply the theory to the swept Hiemenz flow. The result is shown in figure 3.14, and a reasonable agreement is obtained.

Both non-parallel and parallel eigenvalues calculations are carried out, and the results are compared with the theoretical results in figure 3.18. Figure 3.18 indicates that non-parallel flow effects destabilize the flow. In the upstream region where $x = O(1)$, there is significant difference. But the eigenvalue formulation in this region is *ad hoc*, and the result should probably be rejected. In the downstream region where the character of the asymptotic mode is established, the difference between parallel and non-parallel predictions is rather small.

We solved the initial-boundary-value problem (3.4.81)–(3.4.85) with (3.4.86)–(3.4.87)

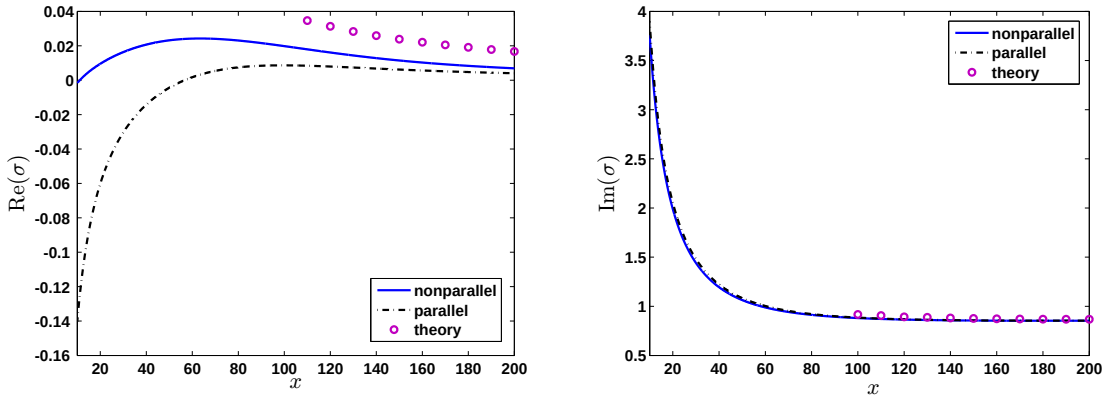


Figure 3.18: Comparison between non-parallel and parallel eigenvalue calculations with the theoretical result for $\omega = 0.12$, $\Lambda/a = 0.001$, $k_3 = 1.0$, and $b/a = 0.1$.

pertaining to the free-stream turbulence. The local growth rate, $\frac{1}{\tilde{u}}\frac{d\tilde{u}}{dx}$, is computed and shown in figure 3.19. We note that $\frac{1}{\tilde{u}}\frac{d\tilde{u}}{dx}$ remains positive, indicating that the induced disturbance amplifies monotonically. We also compared $\frac{1}{\tilde{u}}\frac{d\tilde{u}}{dx}$ with the eigenvalue σ. The two solutions converge as x increases, suggesting that the perturbation gradually develops into an eigen mode.

We performed the calculation of boundary layer receptivity to suction imposed on the surface. For this case, the initial condition is taken to be $\tilde{u} = \tilde{v} = \tilde{w} = 0$. The boundary conditions are

$$\eta = 0: \quad \tilde{u} = \tilde{w} = 0, \quad \tilde{v} = x\mathrm{e}^{-x}; \qquad \eta = \eta_\infty: \quad \tilde{u} = \tilde{v} = \tilde{w} = 0.$$

The local growth rates obtained are compared with the non-parallel eigenvalues in figure 3.20. The result shows that the induced perturbation eventually develops into an eigenmode, i.e. crossflow vortices are excited by suction. As can be seen from the figure, the form of the initial disturbance affects the response in the region relatively close to the leading edge, but the induced motion acquire the same behaviour at large distances.

3.6.3 The intermediate regime

In this subsection, we analyse the development of boundary-layer modes farther downstream, and show that the mode will enter an intermediate regime where the induced pressure will eventually balance the inertia and viscous effects.

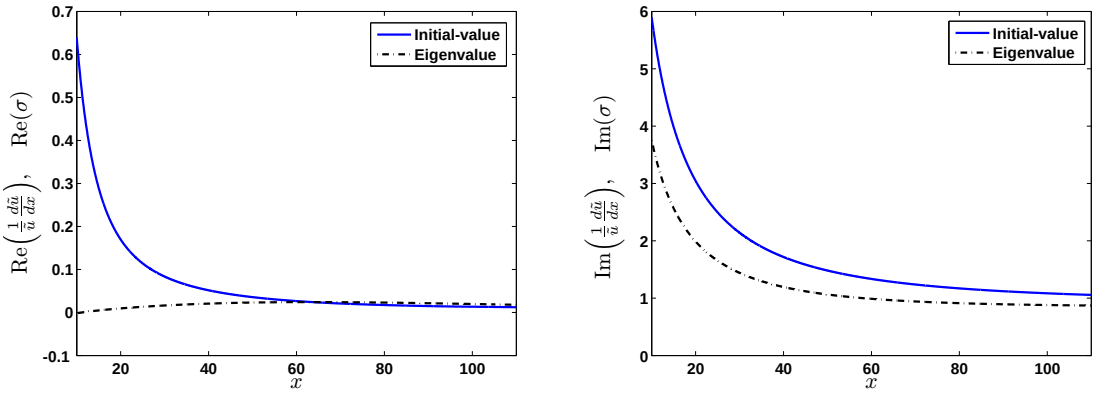


Figure 3.19: The local growth rate predicted by the initial-value calculation for FST and comparison with the non-parallel eigenvalues. Parameter values: $\omega = 0.12$, $\Lambda/a = 0.001$, $k_3 = 1.0$, and $b/a = 0.1$.

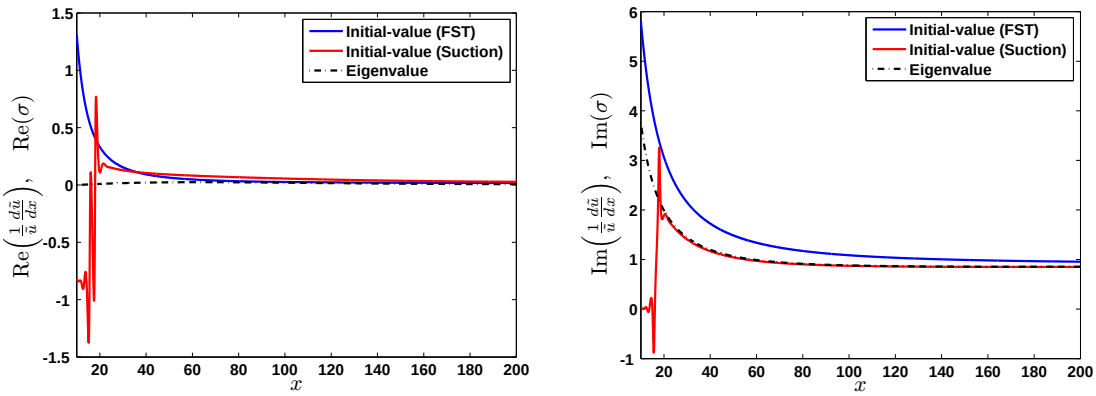


Figure 3.20: The local growth rate predicted by the initial-value calculation for suction and comparison with the non-parallel eigenvalues. Parameter values: $\omega = 0.12$, $\Lambda/a = 0.001$, $k_3 = 1.0$, and $b/a = 0.1$.

In order to estimate the induced pressure, we note that the first equation in (3.6.27) shows that as $\eta \to \infty$,

$$\tilde{v} \to \bar{A}^{\pm}\Big[1 + \frac{k_3}{\sigma}\tan\phi_\infty - \frac{\omega}{\sigma}\Big] = O(1).$$

Since $\tilde{v}$ does not vanish at the edge of the boundary layer, an outer layer has to be introduced, where a pressure is induced by $\tilde{v}$. The pressure is governed by the Laplace equation (in the $y-z$ plane)

$$\nabla^2\tilde{p} = \Big[(R_1^2/R_0^2)\partial^2/\partial\eta^2 - k_3^2/R_\Lambda\Big]\tilde{p} = 0.$$

The balance of the two terms indicates that the width of the outer layer corresponds to

$$\eta = O\Big[\frac{R_0}{R_1}\sqrt{R_\Lambda}\Big]. \tag{3.6.32}$$

The balance between the inertial term and the pressure gradient in the normal momentum equation (3.5.21) implies that

$$\frac{R_\Lambda}{R_1}\frac{\partial\tilde{p}}{\partial\eta} = O(1).$$

By using (3.6.32) in the above relation, the induced pressure is estimated as

$$\tilde{p} = O\Big[(R_1/R_\Lambda)\frac{R_0}{R_1}\sqrt{R_\Lambda}\Big] = O(R_0/\sqrt{R_\Lambda}). \tag{3.6.33}$$

Now we consider the dominant balance in the critical layer corresponding to $\eta - \eta_c = O[(R_0/R_1)^{1/2}]$. The streamwise and spanwise momentum equations (3.5.20) and (3.5.22) can be combined to show that

$$i\sigma_i U_{eff}(\sigma\tilde{u} + \mathrm{i}k_3\tilde{w}) - \frac{R_0^2}{R_1^2}\frac{\partial^2}{\partial\eta^2}(\sigma\tilde{u} + \mathrm{i}k_3\tilde{w}) = (-\sigma^2 + k_3^2)\tilde{p} + \ldots,$$

where higher-order terms are omitted. Since $U_{eff} = O(R_0/R_1)$, and

$$\sigma\tilde{u} + ik_3\tilde{u} = O[(R_0^2/R_1)(R_0/R_1)^{1/2}] = O(R_0^{5/2}/R_1^{3/2})$$

as can be inferred from the second equation of (3.6.27), the pressure will be comparable

with the inertia if $(R_0/R_1)R_0^{5/2}/R_1^{3/2} \sim R_0/\sqrt{R_\Lambda}$, i.e. if

$$R_1 \sim R_0 R_\Lambda^{\frac{1}{5}}, \tag{3.6.34}$$

which signifies the region where the pressure gradient comes into play. The viscous effect remains at leading order, and thus this intermediate regime links the upstream viscous boundary-layer mode and the downstream inviscid Rayleigh mode.

3.7 Summary and discussion

Transition initiated by crossflow instability on a swept wing is of great practical importance for aeronautic technology. Although, the problem has been studied for several decades, there are still quite a lot of unsolved issues. One of these is the receptivity to external disturbances. Much of the previous work considered excitation of steady vortices by surface roughness, or of unsteady vortices by free-stream disturbance interacting with surface roughness elements. In the present study, we consider a possible new and more effective receptivity mechanism: excitation of crossflow vortices by free-stream vortical disturbances directly without any involvement of surface roughness. In the present work, we have assumed that the intensity of free-stream turbulence is sufficient low so that the excitation and the subsequent growth of crossflow vortices remains linear. An initial-boundary-value problem describing the excitation and evolution of crossflow vortices was derived. The initial-boundary-value problem was solved numerically for appropriate values of relevant parameters. The result showed the induced perturbation amplifies downstream.

In order to identify the character of the induced motion, we formulated the 'boundary-layer eigenvalue problem'. An interesting growing mode was found to exist despite that the pressure gradient is absent. The instability is associated with the existence of a maximum of the skewed mean-flow profile, and is essentially a generalisation to the three-dimensional flows of the instability identified by Cowley et al. (1985) for two-dimensional flows. The solution of the initial-boundary-value problem was found to converge to this mode downstream, indicating that the latter was excited by FST alone without interacting with surface roughness. The boundary-layer mode develops into a usual N-S (or more precisely inviscid Rayleigh) mode further downstream. This new receptivity mechanism is much more effective as it does not need a quadratic interaction between the unsteady vortical disturbance

and steady mean-flow distortion caused by roughness elements.

The response to the spanwise slip velocity was found to be monotonically increasing, but it should be pointed out that the contribution from both the unsteady pressure gradients and from the potential part of the fluctuation are ignored. Further work is needed in order to obtain the complete response.

Chapter 4

Further discussions and future work

4.1 Summary of conclusions and further discussions

In this thesis, we have studied receptivity of boundary layers on a concave wall and a swept wing to oncoming free-stream turbulence. The underlying instabilities are Görtler and crossflow instabilities respectively, which lead to formation of Görtler and crossflow vortices. The FST was represented by small-amplitude vortical disturbances. In each case, an initial-boundary-value problem was formulated and then solved numerically. Numerical solutions showed that both types of vortices can be excited by FST directly without the need of surface roughness. The specific conclusions for each problem are already drawn in chapter 2 and 3 respectively. Rather than repeating them here, we now give a brief summary of the main findings and insights, and discuss the main common features as well as differences of the two problems.

Crucial to both receptivity problems is the proper specification of disturbances in the free stream. For the Görtler problem, the instability has a long streamwise length scale, and so the relevant free-stream disturbances must have long streamwise wavelengths and low frequencies. Since the inviscid mean flow is uniform, these disturbances are not strained near the leading edge, but sufficient downstream they are affected by the displacement produced by the viscous motion in the boundary layer. This effect can be accounted for by a suitable shift of the transverse coordinate. The long-wavelength disturbances are entrained into the boundary layer over an extended region. For the crossflow problem, the instability in the majority of the flow field has streamwise and spanwise length scales comparable with the local boundary thickness δ^*, and it is receptive to disturbances having wavelengths

comparable with a typical δ^*. Because a pressure gradient is present (due to the finite thickness of the airfoil), the inviscid mean flow is non-uniform so that the disturbances are strained as they propagate through this region. The generalised rapid distortion theory has to be applied to account for this process in order to obtain the slip velocity. Because of their relatively short streamwise wavelength, the disturbances entrain into the boundary layer near the leading edge.

The initial-boundary-value problem for the Görtler instability can describe the receptivity and the entirely linear development. The concept of eigenvalue is redundant, and indeed is not even tenable unless the Görtler number $G_\Lambda \gg 1$. However, in typical experiments and practical applications, G_Λ turns out to be a large number of $O(10^2)$ at least, for which initial-value solutions approach the local eigenfunction rather quickly, but the growth rate is not accurately predicted by the eigenvalue until very large distances downstream. Useful insights into the instability and receptivity has been gained from the asymptotic analysis assuming $G_\Lambda \gg 1$. An important finding is the growing asymptotic modes, which link the pre-modal phase to the modal stage of the disturbance development. Because of these modes, the induced vortices amplify monotonically without exhibiting transient decay.

For crossflow vortices, receptivity and instability have to be considered in two distinct (but asymptotically overlapping) regions. Near the leading edge, the boundary layer response to free-stream disturbances is described by an inhomogeneous initial-boundary-value problem, consisting of the linearised boundary layer equations. We show that these equations support a growing asymptotic mode despite that no pressure fluctuation is present. This mode has a viscous origin, and exists because the effective velocity profile in the direction of propagation has a maximum. In the downstream limit of this region, the asymptotic mode develops out of the overall response, and evolves into usual inviscid crossflow vortices.

In each problem, the respective asymptotic modes, identified for the first time, are instrumental to receptivity. They play a similar role as the well-known Lam-Rott modes for T-S receptivity. The importance of the present asymptotic modes is arguably more significant because they are all amplifying. This implies that the lower branches of the respective neutral curves do not exist, and that Görtler and crossflow vortices are extremely receptive to free-stream vortical disturbances.

Finally, it should be pointed out that while a local eigenvalue problem can be readily formulated at any streamwise location, it is important to determine where it is applicable

and where it is not. For both problems, there always exist regions close to the leading edge where the eigenvalue approach cannot be justified, and may give incorrect predictions such as a superficial lower branch of the neutral curve.

4.2 Topics for future study

The work undertaken in the thesis points to several topics for future study. In the Görtler problem, we have assumed that FST intensity is sufficiently low that the excitation and the subsequent growth of Görtler vortices remain linear. Further more, it was assumed that the free-stream disturbance consists of a single Fourier mode and is periodic in the spanwise direction. In reality, the disturbance may have a continuous spectrum, and the resulting Görtler vortices may not exhibit a strictly periodic patten (e.g. Finnis and Brown 1997). The calculation can be generalized to such more general cases, for which one could compute the root-mean-square of the induced boundary-layer signature and then compare it with experimental data (e.g. Volino and Simon 2000).

When FST is high, the excitation and evolution of unsteady Görtler vortices are governed by the nonlinear boundary-region equations. Unsteady vortices of sufficient amplitude may undergo secondary instability to cause transition to turbulence as it occurs in the case of steady Görtler vortices (Saric 1994). The secondary instability of steady Görtler vortices, developed from an arbitrarily imposed upstream perturbation or from roughness, has been studied by a number of researchers (e.g. Hall and Horseman 1991, Li and Malik 1995). However, nonlinear unsteady vortices generated by strong FST and their secondary instability have not yet been studied. Both problems are of particular practical importance to turbo-machinery, where the pre-transitional flow over the blade features streaks or vortices due to the combined effects of high turbulence intensity Tu and the centrifugal force, and the onset location of transition is strongly dependent on both Tu and the surface curvature (Schultz and Volino 2003). With this application in sight, a future task is to solve the nonlinear boundary-region equations, which govern nonlinear excitation and evolution of unsteady Görtler vortices, and perform related secondary instability analysis. Investigation along this line may allow us to correlate, on a physical basis, the transition location with Tu and the geometry feature of blades.

In the Görtler problem studied in the present thesis, the pressure gradient of the mean flow is absent. However, in applications such as turbo-machinery, a pressure gradient is

usually present because of the geometry of the blade. This means that the inviscid mean flow must be non-uniform and the ensuing distortion of the turbulence will complicate the receptivity analysis. This is another topic for further research.

In the crossflow problem, we have shown that the response to the spanwise slip velocity is monotonically increasing. However, as has been pointed out in chapter 3, the contribution from the unsteady pressure and the potential part of the fluctuation have been neglected. These have to be taken into account by solving the mixed boundary-value problem (formulated in chapter 3) so that the complete response can be predicted.

In many application, the airfoil may be both concave and swept. This means that Görtler and crossflow instability mechanisms operate simultaneously. The receptivity in this more complicated setting is of interest. Bassom and Hall (1991) showed that a small amount of crossflow may produce an $O(1)$ effect on Görtler instability. In this weak sweep limit, a receptivity theory may be formulated by combining the analyses in chapters 2 and 3.

Finally, the receptivity result may be used to improve some of current transition prediction methods. A popular method for correlating transition location is the e^N-method. Typically, the N factor is calculated by integrating the local growth rate from the first neutral point, which is, in the case of crossflow instability, very close to the leading edge. But the present study indicates that near the leading edge, eigenvalue approach is not applicable, and the predicted growth rate and the neutral point are both suspected. This observation may explain why the e^N-method does not work well. A simple remedy would be to exclude a suitable region near the leading edge in the calculation of N, but an improved and physics-based method is to use the receptivity analysis to provide the correct initial amplitude, and then use the e^N and/or PSE to account for the subsequent development. The transition location may be decided by an amplitude criterion: transition occurs once the amplitude reaches a certain threshold. If the nonlinear PSE is used, the location where saturated crossflow vortices become unstable to high-frequency perturbations may be taken as an approximation for the transition location.

Appendix A

Approximation for $S-\theta$ relation for $\pi-\theta=O(b/a)$

We first expand the term within the modulus of (3.3.31) at $\theta=\pi$ to second order:

$$1-\frac{a^2}{[-b+(a+b)e^{i\theta}]^2}=I-iI'\varphi+\frac{1}{2}I''\varphi^2, \tag{A.0.1}$$

where we have put $\varphi=\pi-\theta$,

$$I=1-\frac{a^2}{(a+2b)^2}=\frac{4b(a+b)}{(a+2b)^2},\quad I'=\frac{2a^2(a+b)}{(a+2b)^3},\quad I''=\frac{2a^2(a+b)(2a+b)}{(a+2b)^4}.$$

It follows that

$$\begin{aligned}\left|1-\frac{a^2}{[-b+(a+b)e^{i\theta}]^2}\right| &= \sqrt{\left[I+\frac{1}{2}I''\varphi^2\right]^2+\left[I'\varphi\right]^2}\\ &= \sqrt{I^2+\frac{1}{4}[I''\varphi^2]^2+II''\varphi^2+[I'\varphi]^2}.\end{aligned} \tag{A.0.2}$$

For $a=O(1)$ and $b/a\ll 1$,

$$I=1-\frac{a^2}{(a+2b)^2}=\frac{4b(a+b)}{(a+2b)^2}=O(b/a),\quad I'=O(1)\quad\text{and}\quad I''=O(1).$$

Since $\varphi=O(b/a)$, we may neglect terms which are smaller than $O(b^2/a^2)$ within the

square root of (A.0.2), so that

$$\left|1-\frac{a^2}{[-b+(a+b)e^{i\theta}]^2}\right| = \sqrt{I^2+[I'\cdot\varphi]^2} = I\sqrt{1+\Big(\frac{I'}{I}\varphi\Big)^2}.$$

Use of this approximation in (3.3.31) gives ,

$$\begin{aligned} S(\theta) &= -\Big(\frac{a+b}{L}\Big)\int_{\pi}^{\theta}\left|1-\frac{a^2}{[-b+(a+b)e^{i\theta}]^2}\right|d\theta \\ &= \Big(\frac{a+b}{L}\Big)I\int_0^{\varphi}\sqrt{1+\Big(\frac{I'}{I}\varphi\Big)^2}\,d\varphi. \end{aligned} \tag{A.0.3}$$

By performing integration by parts, we find that

$$\begin{aligned} \int_0^{\varphi}\sqrt{1+\Big(\frac{I'}{I}\varphi\Big)^2}d\varphi &= \frac{1}{2}\Big(\sqrt{1+\Big(\frac{I'}{I}\varphi\Big)^2}\cdot\varphi+\int_0^{\varphi}\frac{1}{\sqrt{1+\Big(\frac{I'}{I}\varphi\Big)^2}}d\varphi\Big) \\ &= \frac{1}{2}\left\{\sqrt{1+\Big(\frac{I'}{I}\varphi\Big)^2}\cdot\varphi+\frac{I}{I'}\ln\Big[\frac{I'}{I}\varphi+\sqrt{1+\Big(\frac{I'}{I}\varphi\Big)^2}\Big]\right\}. \end{aligned} \tag{A.0.4}$$

Substituting the integration values of (A.0.4) into (A.0.3) yields

$$S=\frac{1}{2}\Big(\frac{a+b}{L}\Big)\frac{I^2}{I'}\left\{\sqrt{1+\Big(\frac{I'}{I}\varphi\Big)^2}\cdot\Big(\frac{I'}{I}\varphi\Big)+\ln\Big[\frac{I'}{I}\varphi+\sqrt{1+\Big(\frac{I'}{I}\varphi\Big)^2}\Big]\right\}. \tag{A.0.5}$$

Equations (A.0.5) and (3.3.27) give the $u_e\sim S$ relation valid for $S=O(b^2/a^2)$.

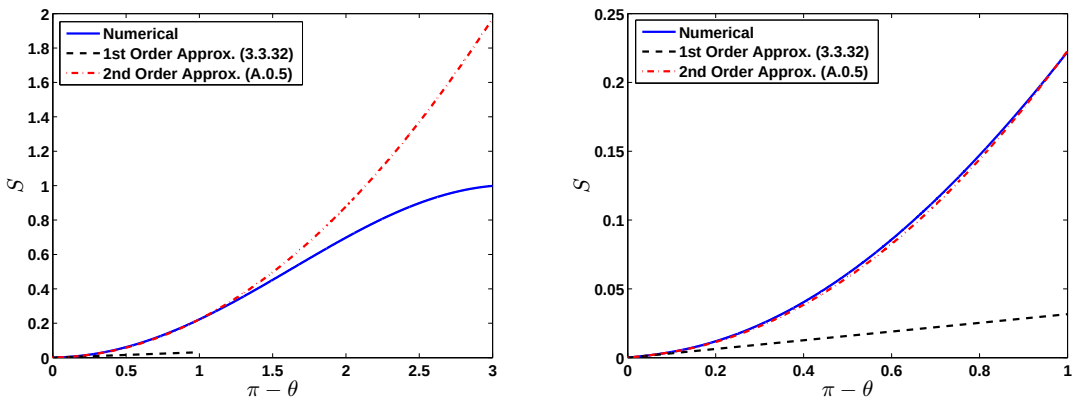


Figure A.1: Comparison of the $s-\theta$ relation obtained by numerical integration with the asymptotic approximation (A.0.5) $(b/a=0.035)$.

Appendix B

Evaluation of drift function

We re-write the drift function (3.4.28) as

$$\Delta = \frac{1}{\Lambda}\Big[\xi^* + \int_{-\infty}^{\xi^*}\Big(\frac{1}{U_\xi} - 1\Big)\mathrm{d}\xi^*\Big], \tag{B.0.1}$$

where U_ξ is the inviscid velocity in the ξ^* direction, and the form of ξ^* is given in (3.3.10). As the streamline approaches the surface of the airfoil, U_ξ is the slip velocity component in the ξ^* direction, i.e. $U_\xi = u_{et}$. From equation (3.3.18), we have

$$U_\xi = 1 - \cos2\theta + \frac{(1+p)^2}{q^2 + 2q\cos\theta + 1}\Big[q\cos\theta + \cos2\theta + q\cos2\theta + \cos3\theta\Big] \equiv G(\theta), \tag{B.0.2}$$

where θ is the polar angle parameterising the circle on the z^*-plane; ξ^* is related to θ via equation (3.3.10). The expression (B.0.2) is valid when $0 \leq \theta \leq \pi$, i.e. $-(a+2b) - [a^2/(a+2b)] \leq \xi^* \leq 2a$.

The inviscid velocity in the η^* direction is zero along the streamline $\eta^* = 0$ upstream of the airfoil, i.e. $v_{et} = 0$. Corresponding to $\eta^* = 0$, $y_c^* = 0$ in the z^*-plane. From equation (3.3.16), we obtain the inviscid velocity upstream of the airfoil

$$U_\xi = \Big[1 - \Big(\frac{a+b}{x_c^* + b}\Big)^2\Big] \Big/ \Big[1 - \frac{a^2}{x_c^{*2}}\Big], \tag{B.0.3}$$

which is valid when $\xi^* < -(a+2b) - [a^2/(a+2b)]$. The validity limits for U_ξ can in terms

of x_c^*, be written as

$$U_\xi = \begin{cases} \Big[1-\Big(\dfrac{a+b}{x_c^*+b}\Big)^2\Big]\Big/\Big[1-\dfrac{a^2}{x_c^{*2}}\Big] & x_c^* < -(a+2b), \\ \\ G(\theta) & x_c^* \geq -(a+2b), \end{cases}$$

where $x_c^* = -(a+2b)$ corresponds to the forward stagnation point on the circle.

Upstream of the airfoil, it follows from Joukowski transformation (3.3.7) that

$$\xi^* = x_c^* + \frac{a^2}{x_c^*}, \quad d\xi^* = (1-\frac{a^2}{x_c^{*2}})dx_c^*. \tag{B.0.4}$$

Along the airfoil, we can write $d\xi^*$ as

$$d\xi^* = \frac{d\xi^*}{d\theta}\cdot d\theta, \tag{B.0.5}$$

where

$$\frac{d\xi^*}{d\theta} = -(a+b)\sin\theta + \frac{a^2(a+b)[b^2-(a+b)^2]\sin\theta}{\Big[b^2-2b(a+b)\cos\theta+(a+b)^2\Big]^2}.$$

Substituting (B.0.2), (B.0.3), and (B.0.4) into (B.0.1), we write the drift function as

$$\Delta \;=\; \Big[(x_c^*+\frac{a^2}{x_c^*})\Big/\Lambda\Big] + \bar{\Delta}_1 + \bar{\Delta}_2 + \Delta_1 + \Delta_2, \tag{B.0.6}$$

where

$$\bar{\Delta}_1 = \frac{1}{\Lambda}\int_{-\infty}^{-(a+2b)+\delta}\left\{\Big[(1-\frac{a^2}{x_c^{*2}})\Big/\Big(1-\Big(\frac{a+b}{x_c^*+b}\Big)^2\Big)\Big]-1\right\}\Big[1-\frac{a^2}{x_c^{*2}}\Big]dx_c^*, \tag{B.0.7}$$

$$\bar{\Delta}_2 = \frac{1}{\Lambda}\int_{\pi-\bar{\delta}}^{\theta}\Big[\frac{1}{G(\theta)}-1\Big]\xi^{*\prime}(\theta)d\theta, \tag{B.0.8}$$

$$\Delta_1 = \frac{1}{\Lambda}\int_{-(a+2b)+\delta}^{-(a+2b)}\left\{\Big[(1-\frac{a^2}{x_c^{*2}})\Big/\Big(1-\Big(\frac{a+b}{x_c^*+b}\Big)^2\Big)\Big]-1\right\}\Big[1-\frac{a^2}{x_c^{*2}}\Big]dx_c^*, \tag{B.0.9}$$

$$\Delta_2 = \frac{1}{\Lambda}\int_{\pi}^{\pi-\bar{\delta}} \Big[\frac{1}{G(\theta)} - 1\Big]\xi^{*\prime}(\theta)d\theta, \tag{B.0.10}$$

where a prime denotes differentiation with respect to θ, δ and $\bar{\delta}$ are small positive constants introduced to deal with the singularity at the leading edge, and $G(\theta)$ is defined in (B.0.2).

The first two integral terms in the drift function will be evaluated numerically using Simpson's rule. The last two integral terms in the drift function are singular at $\theta = \pi$, and $x_c^* = -(a+2b)$ respectively. They will be interpreted as Hadamard's principal values, and evaluated accordingly.

By using the software of Mathematica, we can evaluate the indefinite integral

$$\begin{aligned}
&\int \Big(1 - \frac{a^2}{x_c^*}\Big)\cdot\Big[\frac{1-\frac{a^2}{x_c^{*2}}}{1-(\frac{a+b}{x_c^*+b})^2} - 1\Big]dx_c^* \\
= \;& \frac{b}{3x_c^{*3}(a+2b)^4}\Big\{a(a+2b)\Big[6ab^2(b-3x)x - 12b^3x^2 + a^4(b+3x) \\
&+a^2b(4b^2+15bx-15x^2) + 2a^3(2b^2+6bx-3x^2)\Big] \\
&+24bx_c^{*3}(a+b)^3\ln|x_c^*| - 24(a+b)^3bx_c^{*3}\ln|a+2b+x_c^*|\Big\},
\end{aligned} \tag{B.0.11}$$

which is used to calculate the finite part of Δ_1.

$$\Delta_1 = \frac{1}{\Lambda}\int_{-(a+2b)+\delta}^{-(a+2b)} \Big(1 - \frac{a^2}{x_c^*}\Big)\cdot\Big[\frac{1-\frac{a^2}{x_c^{*2}}}{1-(\frac{a+b}{x_c^*+b})^2} - 1\Big]dx_c^* \to \frac{8b^2(a+b)^3}{\Lambda(a+2b)^4}\ln|\delta|. \tag{B.0.12}$$

As $\theta \to \pi$, $\cos\theta$, $\cos 2\theta$, and $\cos 3\theta$ can be expanded as

$$\cos\theta = -1 + \frac{1}{2}(\theta-\pi)^2 + O[(\theta-\pi)^4], \tag{B.0.13}$$

$$\cos 2\theta = 1 - 2(\theta-\pi)^2 + O[(\theta-\pi)^4], \tag{B.0.14}$$

$$\cos 3\theta = -1 + \frac{9}{2}(\theta-\pi)^2 + O[(\theta-\pi)^4]. \tag{B.0.15}$$

Substitution of (B.0.13), (B.0.14) and (B.0.15) into (B.0.2) gives

$$U_\xi = 2(\theta-\pi)^2 + \frac{(1+p)^2}{(q-1)^2+q(\theta-\pi)^2}\Big(-\frac{3}{2}q + \frac{5}{2}\Big)(\theta-\pi)^2 + O[(\theta-\pi)^4]. \tag{B.0.16}$$

The leading-order term of equation (B.0.16) is

$$U_\xi \to \Big[2+\Big(\frac{1+p}{q-1}\Big)^2\Big(\frac{5}{2}-\frac{3}{2}q\Big)\Big](\theta-\pi)^2. \tag{B.0.17}$$

As $\theta \to \pi$, the leading order approximation for $d\xi^*/d\theta$ is

$$\frac{d\xi^*}{d\theta} \approx (a+b)\Big[1+\frac{a^3}{(a+2b)^3}\Big](\theta-\pi). \tag{B.0.18}$$

If we substitute (B.0.17) and (B.0.18) into the fourth integral in (B.0.6), we get the leading-order approximation for the above integral,

$$\begin{aligned}\Delta_2 &\to \frac{(a+b)}{\Lambda}\Big[1+\frac{a^3}{(a+2b)^3}\Big]\int_\pi^{\pi-\bar\delta}\left\{\frac{1}{\Big[2+\Big(\frac{1+p}{q-1}\Big)^2\Big(\frac{5}{2}-\frac{3}{2}q\Big)\Big](\theta-\pi)^2}-1\right\}(\theta-\pi)d\theta\\ &= \frac{(a+b)}{\Lambda}\Big[1+\frac{a^3}{(a+2b)^3}\Big]\left\{\frac{1}{\Big[2+\Big(\frac{1+p}{q-1}\Big)^2\Big(\frac{5}{2}-\frac{3}{2}q\Big)\Big]}\int_\pi^{\pi-\bar\delta}\frac{1}{\theta-\pi}d\theta-\frac{1}{2}\bar\delta^2\right\}.\end{aligned} \tag{B.0.19}$$

The integral

$$\int_\pi^{\pi-\bar\delta}\frac{1}{\theta-\pi}d\theta$$

is singular, but we take its finite part in the sense of Hadamard, and so

$$\int_\pi^{\pi-\bar\delta}\frac{1}{\theta-\pi}d\theta = \ln|\bar\delta|.$$

Therefore equation (B.0.19) can be written as

$$\begin{aligned}\Delta_2 &\to \frac{a+b}{\Lambda}\Big[1+\frac{a^3}{(a+2b)^3}\Big]\left\{\frac{1}{\Big[2+\Big(\frac{1+p}{q-1}\Big)^2\Big(\frac{5}{2}-\frac{3}{2}q\Big)\Big]}\ln|\bar\delta|-\frac{1}{2}\bar\delta^2\right\}\\ &\to \frac{8b^2(a+b)^3}{\Lambda(a+2b)^4}\ln|\bar\delta|.\end{aligned} \tag{B.0.20}$$

Substitution of (B.0.20) and (B.0.12) into (B.0.6), finally gives

$$\Delta = \Big[(x_c^*+\frac{a^2}{x_c^*})\Big/\Lambda\Big]+\bar\Delta_1+\bar\Delta_2+\frac{8b^2(a+b)^3}{\Lambda(a+2b)^4}\ln|\bar\delta|+\frac{8b^2(a+b)^3}{\Lambda(a+2b)^4}\ln|\delta|. \tag{B.0.21}$$

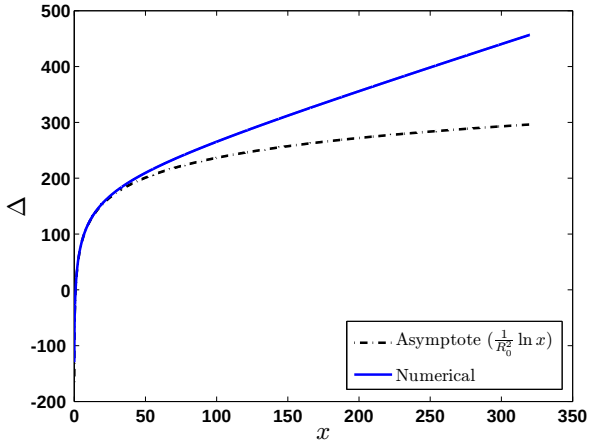


Figure B.1: Drift function for $b/a = 0.1$, and $\Lambda/a = 0.001$.

For calculation, we take $b/a = 0.1$, $\Lambda/a = 0.001$, and $\bar{\delta} = \delta = 1.0 \times 10^{-4}$. The solution to the drift function is shown in figure B.1.

References

D. J. Acheson. *Elementary Fluid Dynamics*. Oxford University Press, 1990.

D. Arnal. Three-dimensional boundary layers: Laminar-turbulent transition. AGARD Rep. 741, Von Kármán Inst., Rhode-St.-Genese, Belg., 1986. Special course on calculation of three-dimensional boundary layers with separation.

D Arnal. Predictions based on linear theory. *Progress in transition modelling. AGARD Rep. No.709*, 1994.

A. P. Bassom and P. Hall. Vortex instabilities in three-dimensional layers: the relationship between Görtler vortices and crossflow vortices. *J. Fluid Mech.*, 232:647–680, 1991.

A. P. Bassom and P. Hall. The receptivity problem for $O(1)$ wavelength Görtler vortices. *Proc. R. Soc. Lond. A*, 446:499–516, 1994.

A. P. Bassom and S. O. Seddougui. Receptivity mechanisms for Görtler vortex modes. *Theor. Comput. Fluid Dyn.*, 7:317–339, 1995.

G. K. Batchelor. *An Introduction to Fluid Mechanics*. Cambridge University Press, 1967.

F. P. Bertolotti. Response of the Blasius boundary layer to free stream vorticity. *Phys. Fluids*, 9:2286–2299, 1997.

H. Bippes. Basic experiments on transition in three-dimensional boundary layers dominated by crossflow instability. *Prog. Aerosp. Sci.*, 35:363–412, 1999.

H. Bippes and H. Görtler. Dreidimensionale störungen in der grenzschicht an einer könkaven wand. *Acta Mech.*, 14:251–267, 1972.

H. Bippes, B. Müller, and M. Wagner. Measurements and stability calculations of the disturbance growth in an unstable three-dimensional boundary layer. *Phys. Fluids*, 3: 2371–2377, 1991.

A. V. Boiko, Y. S. Kachanov, and D. A. Mischenko. Quasi-steady and unsteady Görtler vortices on a concave wall: experiment and theory. In J. M. L. M. Palma and A. Silva Lopes, editors, *Advances in Turbulence XI: Proc. 11th Euromech Euro. Turbulence Conf., Porto*, pages 173–175. Springer, 2007.

A. V. Boiko, Y. S. Kachanov, and D. A. Mischenko. Steady and unsteady Görtler boundary-layer instability on concave wall. *Euro. J. Mech. B/Fluids*, 29:61–83, 2010.

G. Bonfigli and M. Kloker. Secondary instability of crossflow vortices: validation of the stability theory by direct numerical simulation. *J. Fluid Mech.*, 583:229–272, 2007.

A. Bottaro and P. Luchini. Görtler vortices: are they amenable to local eigenvalue analysis? *Euro. J. Mech. B/Fluids*, 18:47–65, 1999.

T. Cebeci and P. Bradshaw. *Momentum Transfer in Boundary Layers*. McGraw-Hill, 1977.

T. Cebeci and J. Cousteix. *Modeling and Computation of Boundary-Layer Flows (2nd Edition)*. Horizons Publishing Inc., 2005.

M. Choudhari. Roughness-induced generation of crossflow boundary vortices in three-dimensional boundary layers. *Theor. Comput. Fluid Dyn.*, 6:1–30, 1994.

S. S. Collis and S. K. Lele. Receptivity to surface roughness near a swept leading edge. *J. Fluid Mech.*, 380:141–168, 1999.

S. J. Cowley, L. M. Hocking, and O. R. Tutty. The stability of solutions of classical unsteady boundary layer equation. *Phys. Fluids*, 28(2):441–443, 1985.

R. I. Crane and J. Sabzvari. Laser-doppler measurements of Görtler vortices in laminar and low-reynolds number turbulent boundary layers. In *Proc. Int. Symp.Applications of Lase Doppler Anemometry to Fluid Mechanics*, Lisbon, 1982.

J. D. Crouch. Receptivity of three-dimensional boundary layers. *AIAA Pap.No. 93-0074*, 1993.

J. R. Dagenhart and W. S. Saric. Crossflow stability and transition experiments in swept wing flow. TP 209344, NASA, 1999.

R. T. Davis and S. G. Rubin. Non-Navier-Stokes viscous flow computations. *Comput. Fluids*, 8:101–131, 1980.

H. P. Day, T. Herbert, and W. S. Saric. Comparing local and marching analyses of Görtler instability. *AIAA J.*, 28(6):1010–1015, 1990.

J. P. Denier, P. Hall, and S. O. Seddougui. On the receptivity problem for Görtler vortices: vortex motions induced by wall roughness. *Phil. Trans. R. Soc. Lond. A*, 335:51–85, 1991.

H. Deyhle and H. Bippes. Disturbance growth in an unstable three-dimensional boundary layer and its dependence on environmental conditions. *J. Fluid Mech.*, 316:73–113, 1996.

P. G. Drazin and W. H. Reid. *Hydrodynamic Stability*. Cambridge University Press, 1981.

P. W. Duck, A. I. Ruban, and C. N. Zhikharev. The generation of Tollmien-Schlichting waves by freestream turbulence. *J. Fluid Mech.*, 312:341–371, 1996.

M. V. Finnis and A. Brown. The linear growth of Görtler vortices. *J. Heat Fluid Flow*, 18: 389–399, 1997.

J. M. Floryan. On the Görtler instability of boundary layers. *Prog. Aerospace Sci.*, 28: 235–271, 1991.

J. M. Floryan and W. S. Saric. Stability of Görtler vortices in boundary layers. *AIAA J.*, 20 (3):316–323, 1982.

J. M. Floryan and W. S. Saric. Wavelength selection of Görtler vortices. *AIAA J.*, 22(11): 1529–1538, 1984.

M. Gaster. A note on the relation between temporally-increasing and spatially-increasing disturbances in hydrodynamic stability. *J. Fluid Mech.*, 14:222–224, 1962.

M. Gaster. On the effects of boundary-layer growth on flow stability. *J. Fluid Mech.*, 66: 465–480, 1974.

M. E. Goldstein. Unsteady vortical and entropic distortions of potential flows round arbitrary obstacles. *J. Fluid Mech.*, 89:433–468, 1978.

M. E. Goldstein. The evolution of Tollmien-Schlichting waves near a leading edge. *J. Fluid Mech.*, 127:59–81, 1983.

M. E. Goldstein. Scattering of acoustic waves into Tollmien-Schlichting waves by small streamwise variations in surface geometry. *J. Fluid Mech.*, 154:509–529, 1985.

M. E. Goldstein and L. S. Hultgren. Boundary-layer receptivity to long-wave free-stream disturbances. *Annu. Rev. Fluid Mech.*, 21:137–166, 1989.

H. Görtler. Über eine dreidimensionale instabilität laminarer grenzschichten an konkaven wanden. *des. d. wiss. göttingen, nachr.* 1(2); translated as 'on the three-dimensional instability of laminar boundary layers on concave walls'. TM 1375(1954), NACA, 1940.

N. Gregory, J. T. Stuart, and W. S. Walker. On the stability of three-dimensional boundary layers with application to the flow due to a rotating disk. *Philos. Trans. Roy. Soc. Lond. Ser. A*, 248:155–199, 1955.

A. N. Gulyaev, V. E. Kozlov, V. R. Kuzenetsov, B. I. Mineev, and A. N. Sekundov. Interaction of a laminar boundary layer with external turbulence. *Izv. Akad. Nauk. SSSR Mekh. Zhid. i Gaza*, 24(5):700–710, 1989.

P. Hall. Taylor–Görtler vortices in fully developed or boundary-layer flows: linear theory. *J. Fluid Mech.*, 124:475–494, 1982.

P. Hall. The linear development of Görtler vortices in growing boundary layers. *J. Fluid Mech.*, 130:41–58, 1983.

P. Hall. The nonlinear development of Görtler vortices in growing boundary layers. *J. Fluid Mech.*, 193:243–266, 1988.

P. Hall. Görtler vortices in growing boundary layers: The leading edge receptivity problem, linear growth and the nonlinear breakdown stage. *Mathematika*, 37:151–189, 1990.

P. Hall and N. J. Horseman. The linear inviscid secondary instability of longitudinal vortex structures in boundary layers. *J. Fluid Mech.*, 232:357–375, 1991.

T. S. Haynes and H. L. Reed. Simulation of swept-wing vortices using nonlinear parabolized stability equations. *J. Fluid Mech.*, 405:325–349, 2000.

W. Heisenberg. Über Stabilität und Turbulenz von Flussigkeitsströmen. *Ann. Phys., Lpz.* (4)74,577–627. (translated as 'On stability and turbulence of fluid flows ', *Tech. Memor. Nat. Adv. Comm. Aero, Wash.*, No. 1291(1951)). 1924.

T. Herbert. Parabolized stability equations. *Annu. Rev. Fluid Mech.*, 29:245–283, 1997.

R. E. Hewitt and P. W. Duck. Pulsatile jets. *J. Fluid Mech.*, 670:240–259, 2011.

J. C. R. Hunt. A theory of turbulent flow round two-dimensional bluff bodies. *J. Fluid Mech.*, 61:625–706, 1973.

Lord Kelvin. On a disturbing infinity in lord rayleigh's solution for waves in a plane vortex stratum. *Nature*, 23:45–46, 1880.

N. Kemp. The laminar three-dimensional boundary layer and a study of the flow past a side edge. Macs thesis, Cornell University, 1951.

J. Kim, T. W. Simon, and S. G. Russ. Free-stream turbulence and concave curvature effects on heated transitional boundary layers. *ASME J. Heat Transfer*, 114:338–347, 1992.

V. Kottke. On the instability of laminar boundary layers along concave walls towards Görtler vortices. In *Propagation in Nonequilibrium Systems*, pages 390–398, Berlin, 1988. Springer.

L. S. G. Kovasznay. Turbulence in supersonic flow. *J. Aero. Sci.*, 20:657–682, 1953.

S. J. Leib, D. W. Wundrow, and M. E. Goldstein. Effect of free-stream turbulence and other vortical disturbances on a laminar boundary layer. *J. Fluid Mech.*, 380:169–203, 1999.

F. Li and M. R. Malik. Fundamental and subharmonic secondary instabilities of Görtler vortices. *J. Fluid Mech.*, 297:77–100, 1995.

C. C. Lin. On the stability of two-dimensional parallel flows. *Quart. Appl. Math.*, 3: 117–142,218–234,277–301, 1945.

C. C. Lin. *The theory of Hydrodynamic Stability*. Cambridge University Press, 1955.

L. M. Mack. Boundary-layer linear stability theory. *Spec. Course Stab. Transit. Laminar Flows, AGARD Rep. 709*, pages 3.1–81, 1984.

M. R. Malik, F. Li, and C.-L. Chang. Crossflow disturbances in three-dimensional boundary layers: nonlinear development, wave interaction and secondary instability. *J. Fluid Mech.*, 268:1–36, 1994.

M. R. Malik, F. Li, and C. L. Chang. Secondary instability of crossflow vortices and swept-wing boundary layer transition. *J. Fluid Mech.*, 399:85–115, 1999.

M. R. Malik and S. A. Orszag. Comparison of methods for prediction of transition by stability analysis. *AIAA J.*, 18:1485–1489, 1980.

M. V. Morkovin. On the many faces of transition. In *Viscous Drag Reduction*, pages 1–31. 1969.

B. Müller. *Experimentelle Untersuchung der Querströmungsinstabilität im linearen und nichtlinearen Bereich des Transitionsgebietes*. Dissertation zum dr.-ing., Universität Fridericiana zu Karlsruhe, 1990.

B. Müller and H. Bippes. Experimental study of instability modes in a three-dimensional boundary layer. *Fluid Dyn. Three-Dimens Turbul. Shear Flows Transit., AGARD CP 438*, pages 13.1–15, 1989.

L. L. Ng and J. D. Crouch. Roughness-induced receptivity to crossflow vortices on a swept wing. *Phys. Fluids*, 11(2):432–438, 1999.

P. Nitschke-Kowsky and H. Bippes. Instability and transition of a three-dimensional boundary layer on a swept flat plate. *Phys. Fluids*, 31:786–795, 1988.

S. A. Orszag. Accurate solution of the Orr-Sommerfeld stability equation. *J. Fluid Mech.*, 50:689–703, 1971.

R. H. Jr Radeztsky, Reibert M. S., and W. S. Saric. Effect of isolated micron-sized roughness on transition in swept wing flows. *AIAA J.*, 37:1371–1377, 1999.

Lord Rayleigh. On the stability, or instability, of certain fluid motions. *Proc. Lond. Math. Soc.*, 11:57–70, 1880.

H. L. Reed and W. S. Saric. Stability of three-dimensional boundary layers. *Annu. Rev. Fluid Mech.*, 21:235–284, 1989.

H. L. Reed, W. S. Saric, and D. Arnal. Linear stability theory applied to boundary layers. *Annu. Rev. Fluid Mech.*, 28:389–428, 1996.

E. Reshotko. Boundary-layer stability and transition. *Annu. Rev. Fluid Mech.*, 8:311–349, 1976.

O. Reynolds. An experimental investigation of the circumstances which determine whether the motion of water shall be direct or sinuous, and of the low of resistance in parallel channels. *Phil. Trans. Roy. Soc.*, 174:935–982, 1883.

N. Riley, M. Sánchez-sanz, and E. J. Watson. A planar pulsating jet. *J. Fluid Mech.*, 638: 161–172, 2009.

A. I. Ruban. On the generation of Tollmien-Schlichting waves by sound. *Izv. Akad. Nauk SSSR, Mech. Zhidk. & Gaza.*, 5:44–52, 1984.

W. S. Saric. Görtler vortices. *Annu. Rev. Fluid Mech.*, 26:379–409, 1994.

W. S. Saric and A. H. Nayfeh. Non-parallel stability of boundary layer flows. *Phys. Fluids*, 18(8):945–950, 1975.

W. S. Saric, H. L. Reed, and E. B. White. Stability and transition of three-dimensional boundary layers. *Annu. Rev. Fluid Mech.*, 35:413–440, 2003.

H. Schlichting. Zur Entstehung der Turbulenz bei der Plattenströmung. *Nachr. Ges. Wiss Göttingen, Math.-phys. Kl.*, pages 181–208, 1933.

H. Schlichting. *Boundary Layer Theory*. McGraw-Hill, 1955.

L. U. Schrader, L. Brandt, and D. S. Henningson. Receptivity mechanisms in three-dimensional boundary-layer flows. *J. Fluid Mech.*, 618:209–241, 2009.

L. U. Schrader, L. Brandt, and T. A. Zaki. Receptivity, instability and breakdown of Görtler flow. *J. Fluid Mech.*, 682:362–396, 2011.

G. B. Schubauer and H. Skramstad. Laminar boundary-layer oscillations and transition on a flat plate. *J. Res. Nat. Bur. Stand.*, 38:251–292, 1947.

M. P. Schultz and R. J. Volino. Effects of concave curvature on boundary layer transition under high freestream turbulence conditions. *ASME J. Turbomach.*, 125:18–27, 2003.

A. M. O. Smith. On the growth of Taylor-Görtler vortices along highly concave walls. *Quart. J. Math.*, 13(3):233–262, 1955.

F. T. Smith. On the nonparallel flow stability of the Blasuis boundary layer. *Proc. Roy. Soc. A*, 366:91–109, 1979.

J. D. Swearingen and R. F. Blackwelder. The growth and breakdown of streamwise vortices in the presence of a wall. *J. Fluid Mech.*, 182:255–290, 1987.

I. Tani. Production of longitudinal vortices in the boundary layer along a concave wall. *J. Geophys. Res.*, 67(8):3075–3080, 1962.

I. Tani and Y. Aihara. Görtler vortices and boundary-layer transition. *ZAMP*, 20:609–618, 1969.

I. Tani and J. Sakagami. Boundary-layer instability at subsonic speeds. In *Proc. Intl. Council Aerosp. Sci., 3rd Cong.*, pages 391–403, Washington: Spartan, 1962.

G. I. Taylor. Stability of a viscous liquid contained between two rotating cylinders. *Phil. Tran. Roy. Soc. A*, 223:289–343, 1923.

V. Theofilis. Advances in global linear instability analysis of nonparallel and three-dimensional flows. *Prog. Aerosp. Sci.*, 39:249–315, 2003.

V. Theofilis. Global linear instability. *Annu. Rev. Fluid Mech.*, 43:319–352, 2011.

S. N. Timoshin. Asymptotic analysis of a spatially unstable Görtler vortex spectrum. *Izv. Akad. Nauk. SSSR Mekh. Zhid. i Gaza*, 25(1):25–33, 1990.

M. Tobak. On local Görtler instability. *ZAMP*, 22:130–143, 1971.

W. Tollmien. Über die Entstehung der Turbulenz. *Nachr. Ges. W.iss Göttingen, Math.-phys. Kl.*,21–44. (translated as 'The production of turbulence', *Tech. Memor. Nat. Adv. Comm. Aero, Wash.*, No. 609(1931)). 1929.

W. Tollmien. Ein allgemeines Kriterium Instabilität laminarer Geschwindigkeitsverteilungen. *Nachr. Wiss. Fachgruppe, Göttingen, Math.-Phys. Kl.* 1, 79–114. (Translated as 'General instability criterion of laminar velocity distributions' *Tech. Memor. Nat. Adv. Comm. Aero., Wash.* No. 792 (1936)). 1935.

M. Turkyilmazoglu, J.S.B. Gajjar, and A.I. Ruban. The absolute instability of thin wakes in an incompressible compressible fluid. *Theoret. Comput. Fluid Dynamics*, 13:91–114, 1999.

M. V. Ustinov. Receptivity of the swept wing boundary layer to a steady flow inhomogeneity. *Fluid Dynamics*, 36(3):437–447, 2001.

R. J. Volino and T. W. Simon. Bypass transition in boundary layers including curvature and favourable pressure gradient effects. *ASME J. Turbomach.*, 117:166–174, 1995.

R. J. Volino and T. W. Simon. Spectral measurements in transitional boundary layers on a concave wall under high and low free-stream turbulence conditions. *ASME J. Turbomach.*, 122:450–457, 2000.

P. Wassermann and M. Kloker. Transition mechanisms induced by travelling crossflow vortices in a three-dimensional boundary layer. *J. Fluid Mech.*, 483:67–89, 2003.

S. H. Winoto and R. I. Crane. Vortex structure in laminar boundary layers on a concave wall. *Int. J. Heat Fluid Flow*, 2:221–231, 1980.

F. X. Wortmann. Visualizaton of transition. *J. Fluid Mech.*, 38:473–480, 1969.

X. Wu. On local boundary-layer receptivity to vortical disturbances in the free stream. *J Fluid Mech.*, 449:373–393, 2001a.

X. Wu. Receptivity of boundary layers with distributed roughness to acoustic and vortical disturbances: a second order asymptotic theory and comparison with experiments. *J. Fluid Mech.*, 431:91–133, 2001b.

X. Wu, D. Zhao, and J. Luo. Excitation of steady and unsteady Görtler vortices by free-stream vortical disturbances. *J. Fluid Mech.*, 682:66–100, 2011.